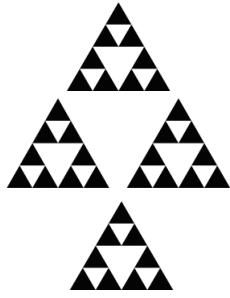


**FRACTAL ANALYSIS OF  
MICROSTRUCTURAL AND FRACTOGRAPHIC IMAGES  
FOR EVALUATION OF MATERIALS**

Thesis submitted for the degree of  
**Doctor of Philosophy (Engineering)**  
of  
**Jadavpur University, Kolkata**

**Mita Tarafder  
2008**





## **Supervisors**

Prof. Mita Nasipuri  
Professor  
Computer Science and Engineering Department  
Jadavpur University  
Kolkata-700032  
Email: [mnasipuri@cse.jdvu.ac.in](mailto:mnasipuri@cse.jdvu.ac.in)

Dr. Indranil Chatteraj  
Scientist-F  
National Metallurgical Laboratory  
Jamshedpur-831007  
Email: [ichatt@nmlindia.org](mailto:ichatt@nmlindia.org)



## **Certificate from the Supervisors**

This is to certify that the thesis entitled “*Fractal analysis of microstructural and fractographic images for evaluation of materials*” submitted by *Smt. Mita Tarafder*, who got her name registered on 09 June 2004 for the award of Ph.D. (Engineering) degree of Jadavpur University, is absolutely based upon her own work under our supervisions and that neither her thesis nor any part of the thesis has been submitted for any degree / diploma or any other academic award anywhere before.

---

Prof. Mita Nasipuri  
Signature of the Supervisor  
and date with Official Seal

---

Dr. Indranil Chatteraj  
Signature of the Supervisor  
and date with Official Seal



## List of Publications and Presentations

### Papers (International=5, National=1)

1. M. Tarafder, I. Chattoraj, M. Nasipuri and A. Mitra, Magnetic characterization of HSLA steel by power-law decay exponents of Barkhausen Emission signal, *Journal of Magnetism and Magnetic Materials*, available on-line 2008
2. Mita Tarafder, I. Chattoraj, S. Tarafder and M. Nasipuri, Fractal analysis to determine self-similar characteristics in microstructures of HSLA steel, *International Journal of Materials and Manufacturing Processes*, in Press (to be published in Vol.24, Issue 2, February 2009)
3. Mita Tarafder, I. Chattoraj, S. Tarafder and M. Nasipuri, Self-similar and self-affine characteristics of microstructural images of HSLA steel, *Material Science and Technology*, available on-line, 2008
4. Mita Tarafder, S.K. Das, S. Tarafder and I. Chattoraj, Fractal characteristics of microstructures of HSLA steels, *Proceedings of the International Conference on Microalloyed Steel: Emerging Technologies & Applications*, Vitasta Publishers, New Delhi, Eds: D. Bhattacharjee, U.K. Chatterjee, S. Chatterjee, M. Dutta and K.K. Ray, pp.1-6, Vol.3, 2007
5. Mita Tarafder, Swati Dey, S. Sivaprasad and S. Tarafder, A novel technique for extracting stretch zone features from fractographs, *Proceedings of the 16th European Conference of Fracture (ECF16)*, Alexandroupolis, Greece, July 2006 (in CD)
6. Mita Tarafder, Swati Dey, S. Sivaprasad, S. Tarafder and M. Nasipuri, Stretch zone analysis by image processing for the evaluation of initiation fracture toughness of a HSLA steel, *Zeitschrift für Metallkunde*, 96 (2005), pp.924-932

Only papers available in print or on-line in web-media are listed. A number of other manuscripts are under consideration for publication or at an advanced stage of preparation.

### Presentations (National Conferences)

1. Mita Tarafder, S.K. Das, S. Tarafder and Amitava Mitra, Correlation of MBE signal with the fractal characteristics of aged microstructure of HSLA material, National Seminar on Non-Destructive Evaluation (NDE-2006), Hyderabad, 7-9 Dec 2006
2. Mita Tarafder, Tapasi Das, S.K. Das and S. Tarafder, Fractal characteristics of fracture behaviour of HSLA steel, 60th ATM of Indian Institute of Metals, Jamshedpur, 14-16 Nov 2006

### Presentations (International Conferences)

1. Mita Tarafder, I. Chattoraj, S. K. Das, Arpan Das, Soumitra Tarafder, Fractal analysis of tensile fracture surfaces of HSLA steel, 17<sup>th</sup> European Conference on Fracture, ECF17, Brno, Czech Republic, 2-6 September 2008
2. Mita Tarafder, S.K. Das, I. Chattoraj and S. Tarafder, Fractal characteristics of microstructures of HSLA steel, International Conference on Microalloying 2007, Kolkata, 9-11 March 2007
3. Mita Tarafder, I. Chattoraj, S. Tarafder and M. Nasipuri, Fractal analysis to determine self-similar characteristics in the microstructure of HSLA steel, International Conference on Neural Network and Genetic Algorithm (NGMS-2008), January 2008, Kolkata



# Acknowledgement

I would like to express my heartfelt gratitude to my supervisors Prof. Mita Nasipuri and Dr. Indranil Chattoraj for their guidance and extended help. During the course of this research, I have received invaluable suggestions and comments from them. I am indebted to them for their generosity.

I am sincerely thankful to Prof. S.P. Mehrotra, Director, National Metallurgical Laboratory (NML), for granting me permission to register for the PhD programme at Jadavpur University, Kolkata. I wish to thank the present and past Heads of the Mathematical Modelling and Simulation (MMS) Division of NML, Dr. S.K. Das, Dr. K.M. Godiwalla and Dr. R.N. Ghosh, who have always encouraged my work. I appreciate the support received from the other members of the MMS Division and the faculty members of the Computer Science and Engineering Department of Jadavpur University. I am particularly thankful to Prof. Nandini Mukherjee of Jadavpur University for her assistance and advice, whenever necessary.

During my research, I had an opportunity to interact and share my thoughts with many eminent persons whose knowledge has enriched me tremendously. I am grateful to Prof. D.P. Mukherjee (ISI, Kolkata), Prof. P. Ramachandra Rao (Former Director, NML), Prof. K.K. Ray (IIT, Kharagpur), Dr. Baldev Raj (Director, IGCAR), Dr. D.K. Bhattacharya (Scientist G, CGCRI), and Prof. H.K.D.H. Bhadeshia (Cambridge University, UK) for patiently listening to my ideas and problems and offering help when I have approached them.

I fondly remember Dr. Placid Rodriguez (Former Director, IGCAR), who has passed away recently, for his constructive comments on this work and giving me the opportunity to interact with medical professionals involved in fractal quantification of X-ray radiographic images.

My colleagues were the most important support in the accomplishment of this work. Dr. Swapan Das, Dr. Amitava Mitra, Dr. S. Sivaprasad, Mr. Arpan Das, Dr. N. Narasaiah and Mr. Byomkesh Dash, who have worked with me in generating images, acquiring signals, carrying out experiments and keeping my workstation running. I specially thank Dr. Sukomal Ghosh and Mr. M. Madan for their generous support at the last minute. Without their participation, it would not have been possible to complete this work. I am thankful for their kind help and suggestions. I acknowledge the help of several students who did projects on fractal analysis with me, especially Ms. Swati Dey (presently working in IBM, Kolkata) for assisting me in various assignments.

I am grateful to my parents, parents-in-law, our daughter Rini and other family members for their kindness, love and affection. Lastly I would like to offer my gratitude to my husband Soumitra who taught me fracture mechanics, criticized my theories and made me work hard till I perfected them. I am deeply indebted to him.

18 November 2008, Jamshedpur.

Mita Tarafder  
Scientist-EII, National Metallurgical Laboratory



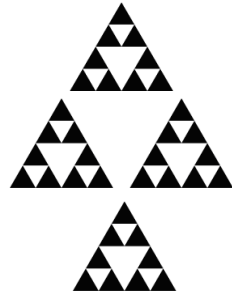
# Contents

<b>1.0 Introduction</b>	
1.1 Fractals for evaluation of damage in materials	5
1.2 Fractals for studying fracture mechanisms	5
1.3 Fractals for non-destructive signal analysis	6
1.4 Motivation of work	7
1.5 Fractal analysis in other areas and the gap in material science research	7
1.6 Objectives	8
1.7 Thesis outline	9
1.8 References	10
<b>2.0 Basic concepts and background</b>	
2.1 Fractal property	14
2.1.1 Fractal dimension	14
2.1.2 Self similarity and self affinity	18
2.1.3 Hurst exponent: a quantifier of complexity	21
2.2 Available methods for computation of fractal dimension	23
2.3 Image rendering by scanning electron microscope (SEM)	32
2.3.1 Basic principle of SEM	32
2.3.2 Signal to noise ratio in SEM images	35
2.3.3 Resolution and contrast in SEM images	37
2.3.4 Secondary electron images	38
2.3.5 Backscattered electron images	39
2.4 SEM image and surface roughness	39
2.5 Basic image processing techniques	42
2.5.1 Histogram equalization	42
2.5.2 Binarization	44
2.6 Mechanical and fracture properties of materials	45
2.6.1 Mechanical properties	45
2.6.2 Fracture properties	49
2.7 Microstructural images	53
2.7.1 Microstructural phases of steel	54
2.8 Fractographic images	57
2.9 Magnetic Barkhausen emission signal	58
2.10 References	60
<b>3.0 Fractal analysis of microstructure, fracture surface and magnetic Barkhausen signal: a brief review</b>	
3.1 Fractal analysis of microstructures	69
3.2 Fractal analysis of fracture surfaces	72
3.3 Fractal analysis of magnetic Barkhausen emission signals	79
3.4 References	84
<b>4.0 Fractal analysis of synthetic signals and images</b>	
4.1 Generation of synthetic signals and images	90
4.1.1 Weierstrass cosine function (WCF)	90
4.1.2 Fractional Brownian motion (fBm)	91



4.1.3	Fractional Gaussian noise (fGn)	95
4.2	Results and discussion	98
4.2.1	Verification of fractal analysis codes using WCF	99
4.2.2	Verification of fractal analysis codes using fBm images	103
4.3	Conclusions	107
4.4	References	108
<b>5.0</b>	<b>Fractal analysis of microstructural images</b>	
5.1	Preparation of metallographic samples	110
5.2	Results and discussion	111
5.2.1	Effect of magnification, spatiality and image preprocessing	112
5.2.2	Self-similar & self-affine characteristics of microstructural images	115
5.2.3	Fractal analysis of microstructural images	121
5.2.4	Correlations between fractal dimensions and material properties	126
5.3	Conclusions	129
5.4	References	130
<b>6.0</b>	<b>Fractal analysis of fractographic images</b>	
6.1	Materials and fractographs	134
6.2	Results and discussion	134
6.2.1	Effect of magnification, spatiality and image preprocessing	135
6.2.2	Fractal analysis of fractographic images	139
6.2.3	Correlations between fractal dimensions and mechanical properties	145
6.3	Conclusions	154
6.4	References	156
<b>7.0</b>	<b>Fractal analysis of magnetic Barkhausen emission signals</b>	
7.1	MBE signal acquisition	160
7.2	Standard magnetic properties from MBE signal	164
7.3	Results and discussion	165
7.3.1	Probability density function for the MBE signals	165
7.3.2	Fractal analysis of MBE signals	169
7.3	Conclusions	176
7.4	References	177
<b>8.0</b>	<b>Conclusions</b>	
8.1	Future direction of work	183
<b>A</b>	<b>Appendices</b>	
A1	HSLA steel and its properties	185
A2	Algorithms for fractal analysis	188
A3	Expression for the void volume fraction	193





Nature keeps her secrets in all her creations. Manmade logic and perceptions attempt to decode and decipher these secrets. Our limited range of observations may have been extended by technological advancement; however there is much to unveil. Fractal is Nature's own logic—the method of self-generation, the pattern of self-similarity. Images and signals from materials may have signatures waiting to be discovered and fractal could be the answer to unraveling them.

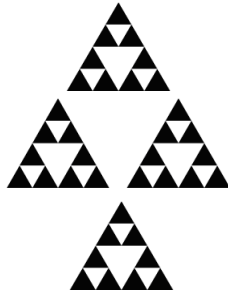


# CHAPTER 1

## 1.0 Introduction

1.1	Fractals for evaluation of damage in materials	5
1.2	Fractals for studying fracture mechanisms	5
1.3	Fractals for non-destructive signal analysis	6
1.4	Motivation of work	7
1.5	Fractal analysis in other areas and the gap in material science research	7
1.6	Objectives	8
1.7	Thesis outline	9
1.8	References	10





# 1

## INTRODUCTION

Materials have hierarchically organized complex structures at different length scales. Quantitative description of material behaviour is dependent on four fundamental length scales [1], which are of concern to materials scientists. These are (1) nano scale,  $1-10^3$  nm, (2) micro scale,  $1-10^3$   $\mu$ m, (3) macro scale,  $1-10^3$ mm, and (4) global size scale,  $1-10^6$  m. While the nano scale corresponds to, often, highly ordered atomic structures, the global size scale relates geophysical phenomena and large man made engineering structures. Micro scale and macro scale correspond to size of material samples used in laboratories, for designing and for fabrication of miniature to small machineries.

Materials researchers have been attempting to find the correspondence between two or more length scales so as to predict material behaviour at a desired scale from information available at another scale. For example, since it is often difficult to evaluate mechanical properties of components of global size due to measurement limitations, the same has to be predicted from tests done on small proto-type engineering structures or, even better, from the behaviour of the material at a still smaller specimen level. An important concern for scientists is to devise

computational methodologies for information extrapolation where measurements made in micro or nano scale can be used for assessment of engineering components at global scale. The assessment is usually to ensure safety, integrity and reliability.

For morphological characterization of materials in micro and nano scales, optical and electron imaging is popularly used to identify characteristic features of material structures. For engineering structural materials, a class that is of immense technological importance, typified by metallic materials, the fundamental morphological feature that is frequently measured is the grain size ( $\sim 1-150\mu\text{m}$ ), which is known to govern macro-properties like strength and hardness. The functional formulation of the two quantifiable entities, popularly known as the Hall-Petch [2, 3] relation, is given by

$$\sigma_y = \sigma_i + \frac{K}{\sqrt{D_g}} \quad (1.1)$$

where  $\sigma_y$  is the yield stress,  $\sigma_i$  is the “frictionless stress”, representing the overall resistance of the crystal lattice to deformation,  $K$  is the “locking parameter” that measures the relative hardening (difficulty in deforming) contribution of the grain boundaries, and  $D_g$  is the grain diameter. This equation is valid for a certain range of grain size, below which other equations [4] need to be considered. The yield stress, a macro-property estimated using micro-scale grain diameter, is one of the most important mechanical properties of materials essential for design and fabrication of engineering structures. Similar correlations, generically known as structure-property correlations for materials, are available in literature, which provide the correspondence between morphological characteristics, including the distribution of micro and nano constituents, and the physical properties of materials at the macro level. Appropriate correlation of structure and property demands that the parameters used encompass a wide range of length scales, and hence exhibit scale invariance.

Our general perception of scale invariance comes from the concept of Euclidean geometry, the mathematical foundation of which permits the transformation of a one dimensional object to higher dimensions using integer power law exponents. This transformation is applicable to *smooth* object space, where self-similar copies of length create a surface, and several self-similar surfaces create volume, the self-similarity ensuring scale invariance. However for uneven or *rough* objects like complex grain boundaries or fracture surface roughness, the assumption of planer geometry for quantification is often found unacceptable, primarily because invariance of

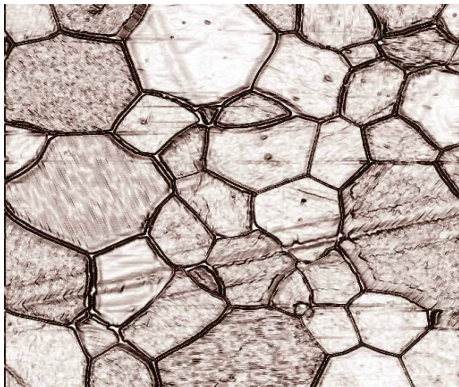
scale is not preserved. To quantify the uneven, complex and non-planer geometrical nature of micro and nano constituents of materials, it is necessary therefore to devise and use suitable scale invariant parameters. Advancement in mathematics and of computational techniques and resources has led to considerable development in this respect. Fractal, for example, is a promising tool, particularly for quantifying patterns and complex shapes that contain fine details discernible at high magnifications, indistinguishable at higher length scales.

To represent hierarchically organized material systems [5] through a unified framework, fractal mathematics, which naturally permits transitioning between length scales, is found to be a most suitable computational tool. Fractal is defined as “a rough or fragmented geometric shape that can be split into parts, each of which is (at least approximately) a reduced-size copy of the whole” [6,7]. Fractal dimension quantifies a fractal object and the dimension represents fractional or non-integer exponent of the power law correlation for representing irregular but self-similar pattern and shape of the object. The quantification gives the true measurement within a wide range of length scales. Scale invariant self-similar fractal patterns are often found in the microstructures and fracture surfaces of materials; hence fractal dimension may be an option to interlink morphological properties at micro-scale with the macro level mechanical properties like strength, hardness and toughness of a material.

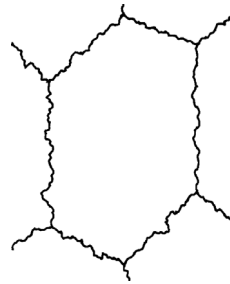
Polycrystalline materials, particularly the metallic variety that is considered important from the point of view of structural applications, consist of aggregates of grains; each grain having elementary crystallographic cell structure. To reveal microstructural features in materials, images of the material surfaces, suitably prepared, are captured using optical and electron microscopes. High resolution microstructural images of polycrystalline materials may show features like distinct grains and grain boundaries, precipitates, inclusions, second phase particles, defects or discontinuities in the form of dislocations (line defects), slip bands, porosities, micro-cracks, *etc.* Fractals can be used to model some of these features. For instance, Figure 1.1 shows the microstructural image of an aluminium alloy with typical “hexagonal” grain structures [5]; the grain boundaries are rough which can be modeled using self-affine fractal Koch curve [8], as shown.

Like non-planer grain boundaries in microstructure, the geometry of crack paths, crack fronts, and fracture surface texture demonstrate fractal characteristics [9, 10]. However classical fracture mechanics assumes smooth fracture surfaces or planer cracks and the formulation of material properties like fracture energy, stress intensity factors (SIF), *etc* is based on the planer Euclidean

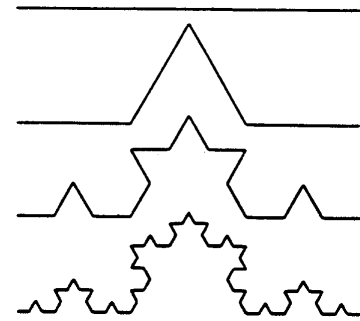
geometry. Thus the fracture energy calculated using Euclidean surface concepts is often found to be lower than the experimentally measured values.



Grain boundary structure of aluminium alloy (<http://www.cmu.edu/mrsec/>)



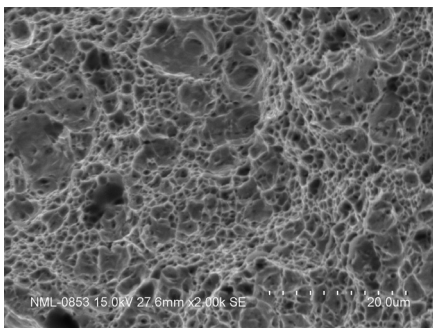
A single grain with complex grain boundaries [1]



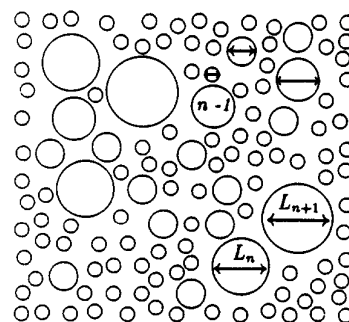
Attempt to model grain boundary by fractal Koch curve [1]

Figure 1.1: Fractal Koch curve model of grain boundaries of polycrystals.

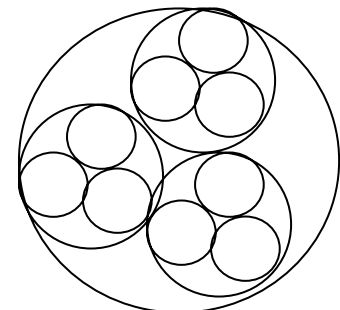
Similarly, the SIF of planar cracks is less than the same estimated for actual fractal crack paths. Fracture features like voids, tortuosity of crack path, crack branching, manifestations of fracture surface undulations like striations, riverlines and other such microductilities are responsible for increasing the actual fracture surface area and creating fracture surface roughness. Analysis of fractographic images can identify these features and fractal models of these features can be employed to find out the true fracture surface area for calculation of surface energy. In Figure 1.2, the fractographic image of a ductile fracture surface is represented by circular void features of a homeomorphic (regular) fractal model [1, 11]. Fractal dimensions quantify such fracture models, and the non-integer exponents can be used for estimating the roughness of the fracture surfaces.



Fractograph of ductile fracture surface



Schematic representation [11]



Fractal model of the ductile fracture surface

Figure 1.2: Homeomorphic (regular) fractal model for fractographic image of fracture surface

The sub-sections that follow highlight some specific instances where fractals may be employed for modelling of materials and their behaviour.

### **1.1 Fractals for evaluation of damage in materials**

Fractal quantification of microstructural images or micrographs has immense potential for evaluation of damage in materials which can help in developing technology and protocols for remaining life assessment (RLA) of engineering components and structures. Detection of cracks, measurement of the crack size, quantification of damage proliferation, assessment of material properties, and finally prediction of remaining lives of engineering components are parts of RLA studies. Size of a crack or defect and the extent of damage that has been manifested have profound significance in RLA investigations. When defects are small in nano to micro scale they are collectively called damage, whereas in micro to macro scale they can further be defined as defects if they develop into typical forms. Damage mechanics, which primarily deals with the behaviour of damaged material, proposes that materials are initially damage free and, as they put in service, gradually over the period of time, develop microstructural damages in the form of cracks and crack-like defects, micro pores and voids, precipitations of second phase particles, coarsening and modification of precipitates, characteristic dislocation configurations etc. Damaged areas and defects are often irregular in shapes. High resolution microstructural images of materials contain complex morphological signatures of these damages and defects. The accumulation of micro damages in the matrix of materials alters the intrinsic macro mechanical properties like strength and hardness of materials. These properties may show size dependence depending upon the size or extent of damage and the size or volume of material probed during determination of properties. Quantification of damage state by fractal analysis of microstructural images can lead to the generation of scale invariant parameters that may help in overcoming limitations of structure-property correlation over a wider scale range.

### **1.2 Fractals for studying fracture mechanisms**

When an object is broken into pieces, fracture surfaces are generated. Fracture surfaces contain valuable information with regard to the type of material, the load history it has been subjected to and the mechanism of fracture operative. Generally, a flat fracture surface indicates brittle fracture, whereas roughness of the surface and tortuosity in the crack path (or the profile of a

fracture surface) signify ductile fracture processes are active. Examination of fracture surfaces, using high resolution images known as fractographs, is routinely carried out for quality assurance of engineering materials as well as to study the fracture behaviour of materials.

Microscopic features like cleavage patterns, voids, striation marks, stretch zone, *etc* are the signature of various fracture processes which can be identified in fractographs. These fractographic features are responsible for the variations of fracture surface roughness that is represented by contrast variations in fractographic images. Quantification of fracture surface roughness by fractal analysis of fractographic images may help in gaining greater insight into mechanical and fracture behaviour of materials, so as to understand the mechanisms liable to cause morphological variations or roughness on the fracture surface. Thus, a fractal based quantification tool for analysis of fracture surface would assist in devising mathematical models for correlating with macro-mechanical properties like toughness, strength and hardness of materials.

### **1.3 Fractals for non-destructive signal analysis**

Evaluation of materials through determination of mechanical properties is a destructive procedure. Small amounts of material need to be removed from components for preparation of specimens for mechanical testing. Evaluation of materials based on microstructures (and fracture surfaces, if available) are invasive in the sense that sufficient *in situ* (and often *ex situ*) preparations are necessary prior to microscopic observation. When components are operational, and when on-site and quick evaluations are necessary in industrial scenarios, it is imperative to employ non-destructive methods for assessment of materials. Magnetic Barkhausen emission (MBE) is an upcoming non-destructive method for evaluating microstructural damage in certain classes of materials. The signal obtained by MBE is a high frequency burst type temporal signal. Fractal dimension of the MBE signal may detect microstructural changes accompanying damage so that variations of material behaviour may be indexed and material degradation during service predicted.

## **1.4 Motivation of work**

The motivation of this investigation comes from major research activities taken up at the National Metallurgical Laboratory, Jamshedpur, under an initiative entitled “Component Integrity Evaluation Programme” (CIEP). In this programme various methodology and techniques were developed and implemented for structural integrity and remaining life assessment of engineering components. In a sequel project called “Technology for Assessment and Refurbishment of Engineering Materials and Components” (TAREMaC), sponsored by the Council of Scientific and Industrial Research (CSIR), India, currently being executed in network mode, emphasis has been given to development of advanced computational techniques for evaluation of microstructural damage in materials. Quantification of microstructural and fractographic images and non destructive signals is required for evaluation of damage in materials. Fractal quantification is a non-conventional method that can be used as a complementary technique for microstructural characterization and signal analysis which can lead to important advancement in understanding of structure-property correlations of materials. To appreciate and develop these correlations it is necessary to take up interdisciplinary research in areas like metallurgical engineering, computer science and applied mathematics. The current endeavour is an effort along these lines. The outcome of this work is expected to generate knowledge in the area of signal and image processing with particular emphasis on the microstructural and fractographic images and MBE signals.

## **1.5 Fractal analysis in other areas and the gap in materials science research**

Fractal dimension as a scale invariant quantitative tool has been used extensively in medical imaging like X-ray radiography, ultra-sonography, etc [12-15]. It has been used to quantify 1D temporal signal like EEG for assessing neurological aspects of the brain [16]. However fractal analysis of intensity images of microstructure and fracture surfaces for evaluation of materials has not received much attention. The standard stereological measurement procedures available for characterizing material microstructures are found to be over simplification for quantifying complex morphological structural properties. Fractal based quantification refines the measurement which can be implemented within a wider range of length scales.

Previous investigators have quantified fracture surface by generating 3D structure by techniques like slit island method, stereo photogrammetry *etc* to quantify the surface roughness by fractal

dimensions. Direct quantification of microstructural and fractographic image has raised the question whether the gray level intensity image is the true representation of the surface roughness since the intensity image may contain noise which can limit the accuracy of the fractal analysis. Kube and Pentland [17] and later McGunnigle [18] have shown that surface roughness can be represented by fractal dimension estimated from its image spectra since fractal dimension is a differential parameter insensitive to high frequency noise. Their work, primarily in the area of image processing, needs to be introduced in materials fraternity for estimation of fractal dimension from intensity images directly.

## 1.6 Objectives

This thesis investigates scale invariant property of microstructural and fractographic intensity images and MBE signals of metallic materials and attempts to quantify them using fractal dimensions for evaluation of macro mechanical properties. In order to achieve this goal, following objectives are defined:

- To study fractal properties of high resolution images of microstructures and fracture surfaces of materials obtained by the SEM. The images are obtained in secondary and back scattered electron emission modes, which are captured and converted to appropriate digital format.
- To devise application routines and to carry out extensive validation study of three methods, namely Rescaled Range (R/S) analysis, Power Spectral Density (PSD) analysis and Wavelet analysis, that are employed for fractal analysis in this work. For validation of these analysis procedures, synthetic 1D signals and 2D images are simulated. While the Weierstrass cosine function, a standard function for generating fractal curve, is used for simulating fractal 1D signal, for simulating 2D images, fractional Brownian motion (fBm) surfaces are considered.
- To examine whether microstructures and fractographs of High Strength Low Alloy (HSLA) steel aged at various tempering temperatures have fractal behaviour, and to investigate if different aging conditions change the fractal behaviour in a way similar to the manner of variation of material properties like hardness, yield strength and fracture

toughness. To develop appropriate structure-property correlations based on fractal mathematics for evaluation of materials.

- To investigate whether MBE signal has fractal properties and to establish a non-destructive protocol for quantifying microstructural damage by quantitative evaluation of MBE signals by fractal analysis.

## 1.7 Thesis outline

This thesis is organised into four parts: the first part is the *theoretical background and literature review* addressed in chapters 2 and 3 respectively; the second part is the *image analysis module* presented in three chapters from chapter 4 to chapter 6; the third part is the *signal analysis module* addressed in chapter 7. Finally, the last part contains the *conclusions and future direction of research* in chapter 8.

Chapter 2 discusses the theoretical background of fractal mathematics and the definitions of parameters like the fractal dimension,  $D$ , or the Hurst exponent,  $H$ , for quantifying fractal objects. The  $H$  exponent represents self-similar or self-affine behaviour of images or signals. Concepts of self-similarity and self-affinity have been discussed in details. Available methods for fractal analysis are discussed briefly in this chapter. Since the scanning electron microscope (SEM) has been used for acquiring high resolution images used in this work, electron imaging techniques and signal-to-noise ratio for rendering the images on display devices have been discussed. Conventional methods for evaluating mechanical and magnetic behaviour of materials are also explained. A brief account of microstructural and fractographic images and their applications in materials research for evaluation of materials has been discussed. MBE signal analysis is one of the recently developed non-destructive material evaluation techniques. Discussion on MBE signal generation has been included in a separate section in this chapter. Chapter 3 reviews the related work in the area of fractal analysis of microstructures, fractographs and MBE signals.

The second part of the thesis is the image analysis modules which are discussed in the next three chapters. Validation of the fractal analysis algorithms using synthetic signals and images are addressed in chapter 4. Comparisons of various fractal analysis methods are presented in chapter 4, highlighting the robustness of the algorithms used in this investigation. Fractal analyses of

fractographs and microstructural images and the correlations between fractal dimensions and material properties are described in chapters 5 and 6 respectively.

Part III deals with the time domain 1D MBE signal analysis. Fractal dimensions computed from the signals for the HSLA steel have been correlated with the magnetic and mechanical properties in chapter 7.

Conclusions and future direction of research have been presented in the final part of this thesis in chapter 8.

## 1.8 References

1. A. Balankin: Physics of fracture and mechanics of self-affine cracks, *Engineering Fracture Mechanics*, 57, 2/3, 135 – 203(1997).
2. E. O. Hall: The deformation and aging of mild steel, *Proc. Phys. Soc. London*, 643, 747-753(1951).
3. N. J. Petch: The cleavage strength of polycrystals, *J. Iron Steel Inst. London*, 173, 25-28(1953).
4. R. W. Armstrong, Y. T. Chou, R. M. Fisher and N. Louat: The Limiting Grain Size. Dependence of the Strength of a Polycrystalline Aggregate, *Philos. Mag.*, 14, 943-951(1966).
5. E. Saether and S. Taasan: A Hierarchical approach to fracture mechanics, NASA Final report, NASA/TM-2004-213499, 2004.
6. B. B. Mandelbrot: *The Fractal Geometry of Nature*, 1983, W. H. Freeman, New York.
7. Fractal. (2008, May 30). In *Wikipedia, The Free Encyclopedia*. Retrieved 10:25, June 5, 2008, from <http://en.wikipedia.org/w/index.php?title=Fractal&oldid=215876991>.
8. P. Streitenberger, D. Forster , G. Kolbe and P. Veit: The fractal geometry of grain boundaries in deformed and recovered zinc, *Scripta Metallurgica et Materiala*, 33, 541-546(1995).
9. L. T. Dougan, P. S. Addison and W. M. C. McKenzie: Fractal analysis of fracture: A comparison of dimension estimates, *Mech. Res. Commun*, 27, 383-392(2000).
10. E. Hornbogen: Fractals in microstructure of metals, *Int. Materials Reviews*, 34, 277-296(1989).

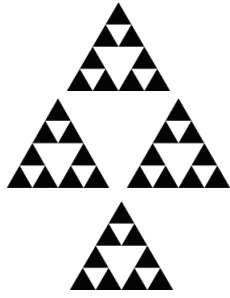
11. V. S. Ivanova, A. S. Balankin, I. J. Bunin and A. A. Oksogoev: Synergetics and Fractals in Materials Science, Nauka, Moskow, 1994 (in Russian); in English by Gordon and Beach, 1997.
12. P. Zioupos, C. Kaffy and J. D. Currey: Tissue heterogeneity, composite architecture and fractal dimension effects in the fracture of aging human bone, International Journal of Fracture, 139, 407–424(2006).
13. Andrzej Materka, Piotr Cichy: Texture analysis of X-ray images for detection of changes in bone mass and structure, [http://www.eletel.p.lodz.pl/programy/cost/pdf\\_3.pdf](http://www.eletel.p.lodz.pl/programy/cost/pdf_3.pdf)
14. D. Chappard , F . Pascaretti-Grizon , Y . Gallois , P . Mercier , M . Baslé , M . Audran: Medullar fat influences texture analysis of trabecular microarchitecture on X-ray radiographs, European Journal of Radiology, 58, 3, 404 – 410(2003).
15. E. K. Kerut, M. Given and T. D. Giles: Review of methods for texture analysis of Myocardium from Echocardiographic Images: A means of tissue characterization, Echocardiography: A journal of CV Ultrasound & Allied Tech., 20, 8, 727-736(2003).
16. Paolo B. DePetrillo, Qingfeng Yang, Jamie Rackoff, Anitza SanMiguel, Kamran Karimullah: Surface fractal computation and its application to immunofluorescent histochemical studies of calpain and calpastatin in PC12 cells, Journal of Neuroscience Methods, 103, 191–197(2000)
17. P. Kube and A. P. Pentland: On the imaging of fractal surfaces, IEEE Trans. Pattern Anal. Machine Intell., 10, 704–707(1988).
18. G. McGunnigle and Mike J. Chantler: Evaluating Kube and Pentland’s Fractal Imaging Model, IEEE Transactions of image processing, 10, 4, 534-542(2001).



# CHAPTER 2

<b>2.0 Basic concepts and background</b>	
2.1 Fractal property	14
2.1.1 Fractal dimension	14
2.1.2 Self similarity and self affinity	18
2.1.3 Hurst exponent: a quantifier of complexity	21
2.2 Available methods for computation of fractal dimension	23
2.3 Image rendering by scanning electron microscope (SEM)	32
2.3.1 Basic principle of SEM	32
2.3.2 Signal to noise ratio in SEM images	35
2.3.3 Resolution and contrast in SEM images	37
2.3.4 Secondary electron images	38
2.3.5 Backscattered electron images	39
2.4 SEM image and surface roughness	39
2.5 Basic image processing techniques	42
2.5.1 Histogram equalization	42
2.5.2 Binarization	44
2.6 Mechanical and fracture properties of materials	45
2.6.1 Mechanical properties	45
2.6.2 Fracture properties	49
2.7 Microstructural images	53
2.7.1 Microstructural phases of steel	54
2.8 Fractographic images	57
2.9 Magnetic Barkhausen emission signal	58
2.10 References	60





# 2

## BASIC CONCEPTS AND BACKGROUND

The term “Fractal” was first coined by Mandelbrot [1, 2] in 1975. The word originated from the adjective “Fractus”, from the verb “frangere”, meaning *to break* in Latin. Since fractal dimension is the non-integral fractional dimension, the word “Fractus” is rhymed with “Fractional” to form the word “Fractal” for representing irregular and non-linear phenomenon be it a shape or an event. The degree of irregularity exhibited by the fractal is represented by the fractal dimension  $D$  and it remains the same at all scales in the mathematical sense. The scale independent behaviour of  $D$  makes it a useful tool for representing any forms of irregularity in nature.

Fractal [1] and chaos [2] are the two sides of the same coin of a non-linear stochastic behaviour of any natural process. While fractal determines the inherent order, chaos represents disorder. There are fractals in chaos. Many natural processes which are presumably chaotic show fractal behaviour. For examples changes in weather, turbulence and oscillations, growth and propagation of biological species, satellite images of earth surface, images of microstructures, all

show fractal behaviour within certain scales of observations. However more orderly signals used for medical diagnostics or to check structural health of engineering components may contain chaotic properties. It is the self-similar or self-affine characteristic [3] that makes an event or an object *fractal*.

This chapter presents the definition of fractal dimension and the self-similar and self-affine property of the fractal objects. Physical significance of self-similarity and self-affinity in terms of surface roughness are discussed in details. An overview of the popular estimator of self-similarity and self-affinity known as Hurst exponent [4] has been outlined here. A review report on various methods for computing fractal dimensions has been included.

The accuracy of any computational method depends upon the quality of input data. In the present work, high resolution images captured by the Scanning Electron Microscope (SEM) are used as the input data. This chapter addresses the factors that affect the contrast variations in the SEM images and the rationale for using SEM images for fractal analysis. Morphologies of various structural phases present in the microstructures of steel have been described and the effects of these on the mechanical properties are illustrated. Discussion on images of fracture surface also highlights the types of fracture in micro-scale and the typical fracture features in fractographic images have been highlighted. Additionally basic concepts of Magnetic Barkhausen Emission (MBE) signals, a Non Destructive Evaluation (NDE) method for material evaluation, have been included.

## **2.1 Fractal property**

### **2.1.1 Fractal dimension**

Dimension signifies correlation between measured quantities and the unit of measurement. It can be seen that there is an inverse correlation between unit or scale ( $k$ ) and the measured quantity ( $N$ ). As the size of the measurement scale decreases, the measured quantity increases. This can be understood from the data presented in Table 2.1. The  $\log(k)$  vs.  $\log(N)$  data, when plotted, shows the linear property with the magnitude of slope equal to 1 signifying the topological dimension of the length.

Mathematically the correlation between the scale ( $k$ ) and the measured quantity ( $N$ ) can be written as

$$N.k = N_0.(k)^{1-D} \quad (2.1)$$

where  $N_0$  is the constant which is obtained for  $k=1$ .

Table 2.1: Correlation between scale and measured quantity for distance of 23 km.

Scale	$k$	Quantity, $N$	$\text{Log}(k)$	$\text{Log}(N)$
km	1000	23	3	1.361728
m	1	23000	0	4.361728
cm	0.01	2300000	-2	6.361728
mm	0.001	23000000	-3	7.361728
micron	0.000001	23000000000	-6	10.36173
nano	0.000000001	23000000000000	-9	13.36173

In the same mathematical framework, fractal dimensions can be estimated for fractal objects. Fractal is defined as "a rough or fragmented geometric shape that can be split into parts, each of which is (at least approximately) a reduced-size copy of the whole," [1]. Fractal objects are generated by iteration to achieve precise geometrical fineness. For example, a triangle is transformed to non-linear shape using the principle constituent (PC) given in Figure 2.1 (a). Each side of the triangle is divided and reshaped using the PC to get 4 lines. This can be continued infinitely, by taking reduced PC, and the complex fine geometrical fractal in Figure 2.1 (b) can be generated. The correlation between scale and the measured quantity for this fractal object is given in Table 2.2.

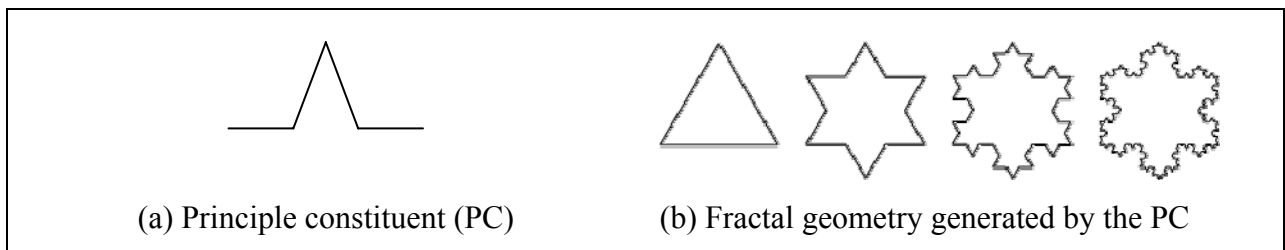


Figure 2.1: Non-linear principle constituent and evolution of fractal object

Table 2.2: Correlation between scale and measured quantity for the fractal object in Figure 2.2(b)

k	N	$\log(k)$	$\log(N)$
1	3	0	0.477121
0.333333	12	-0.47712	1.079181
0.111111	48	-0.95424	1.681241
0.037037	192	-1.43136	2.283301

The correlation between the scale ( $k$ ) and the measured quantity ( $N$ ) can be obtained using equation (2.1). The value for  $D$  is found to be 1.2619 and this is independent of  $k$ . Hence the length of the curve can be given by

$$L = N.k = N_0.(k)^{-0.2619} \quad (2.2)$$

Similar to Euclidean or Topographic geometry, fractal geometry allows measured quantity to change inversely with the unit of measurement scale; but the dimension,  $D$ , is always a non-integer. The non-integer dimension is called fractal dimension. Objects having fractal dimension are called the fractal objects. These objects have the property that finer self-similar or self-affine (reduced-size copies of the whole) structure is revealed as we magnify them. This property makes the fractal function (used for generating fractal object) a non-differentiable function. In addition to self-similar or self-affine property, it is stated that fractal dimension should always remain between Topological dimension,  $D_T$ , and Euclidean dimension,  $D_E$ . While the topological dimension represents the lowest complexity, the Euclidean dimension signifies the highest complexity for any irregular shape or object.

For determination of fractal dimension from a signal or image, following steps are followed:

- A signal or image is read
- Using a particular scale,  $k$ , a quantity,  $N$ , is measured for the signal or image
- The data representing  $\log(N)$  vs.  $\log(k)$  is plotted. This log-log plot is called the Richardson plot.
- A linear fitting of the Richardson plot within certain scale range gives the slope of the plot.
- From the slope, fractal dimension  $D$  is computed.

There are many variants of fractal dimension for characterizing fractal objects. Table 2.3 presents definitions and mathematical formulations of some important variants of fractal dimensions [5]. It may be pointed out that Capacity dimension ( $D_0$ ), Information dimension ( $D_I$ ) and Correlation Dimension ( $D_2$ ) can be derived from the q-Dimension taking  $q$  as 0, 1 and 2 respectively.

Table 2.3: Definitions and mathematical formulations of some important variants of fractal dimension

Name	Equations	Remarks
q-Dimension	$D_q = \frac{1}{1-q} \lim_{k \rightarrow 0} \frac{\ln I(q, k)}{\ln\left(\frac{1}{k}\right)}$ <p>where</p> $I(q, k) = \sum_{i=1}^N \mu_i^q$ <p>where <math>k</math> is the box size, and <math>\mu_i</math> is the natural measure which states the probability that element “<math>i</math>” is populated.</p>	Based on $q^{\text{th}}$ order statistics.
Capacity dimension or Box-counting dimension	$D_0 = - \lim_{k \rightarrow \varepsilon^+} \frac{\ln(N)}{\ln(k)}$ <p>where <math>N</math> is the measured quantity and <math>k</math> is the scale of measurement.</p>	Also called Housdorff dimension, Hausdorff-Besicovitch dimension or Matric dimension
Information dimension	$D_1 = - \lim_{k \rightarrow \varepsilon^+} \frac{I}{\ln(k)}$ <p>where <math>I = - \sum_{i=1}^N P_i(k) \ln[P_i(k)]</math></p>	$P_i(k)$ , is the probability that element “ $i$ ” is populated. Called probabilistic dimension.
Correlation dimension	$D_2 = \lim_{k, k' \rightarrow 0^+} \frac{\ln \left[ \frac{C(k)}{C(k')} \right]}{\ln\left(\frac{k}{k'}\right)}$ $C(k) = \lim_{N \rightarrow \infty} \frac{1}{N^2} \sum_{\substack{i, j=1 \\ i \neq j}}^{\infty} H_v(k -  x_i - x_j )$ <p>Heaviside step function, <math>H_v(x)</math> is defined as</p> $H_v(x) = \begin{cases} 0 & x < 0 \\ \frac{1}{2} & x = 0 \\ 1 & x > 0 \end{cases}$	Based on second order statistics for representing q-Dimension when $q=2$ .
Minkowski-Bouligand dimension	$D_M = \lim_{r \rightarrow 0} \frac{\ln F(r)}{-\ln(r)} + 2$ <p><math>F(r)</math> is the area traced out by a small circle with radius <math>r</math> following a fractal curve.</p>	For all strictly self-similar fractals, the Minkowski-Bouligand dimension is equal to the Hausdorff dimension; otherwise $D_M > D$ .

### 2.1.2 Self similarity and self affinity

The terms self similarity and self affinity can be defined using the mathematical tool called Iterative Function System (IFS) [6] which was invented by J. Hutchinson [7]. IFS is used for constructing fractal objects, which essentially mean self similar objects. A self-similar set,  $E$ , can be infinite or finite copies of itself which can be expressed as

$$E = \bigcup_{i=1}^m f_i(E) \quad (2.3)$$

In equation (2.3),  $E$  is the invariant set or attractor of the IFS,  $f_i$  is the transformation function describing the relationship between the invariant set and the constituent parts. If there are contractive similarities between  $E$  and  $f_i(E)$ , then  $E$  is called self-similar. If  $f_i$  are affine functions, then  $E$  is called self-affine.

Two objects are said to be self similar if one is a union of a number of smaller similar copies of itself. Figure 2.2 illustrates construction of the invariant set  $E$ . The initial geometry was a square,  $E$ . The transformation function  $f_i$  defines a scalar transformation reducing its size and the shifting of origin inside  $E$ . Here  $f_1$  defines the top-left shift and  $f_2$  defines the bottom-right shift.

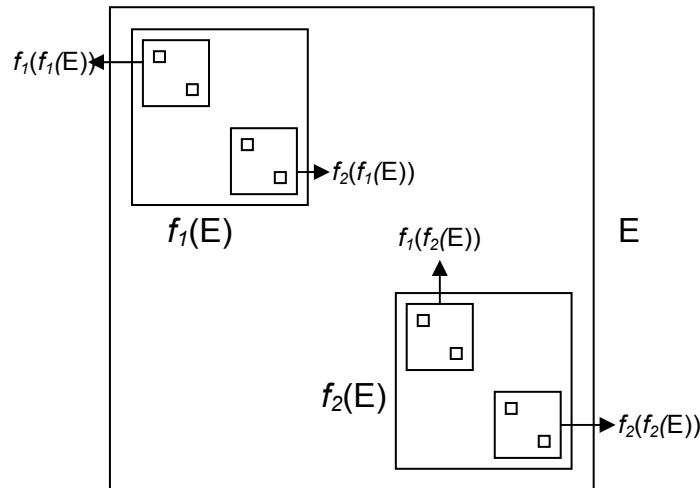


Figure 2.2: Construction of the invariant set  $E$

The affine function [8] is defined as a function  $A: \mathbb{R}^m \rightarrow \mathbb{R}^m$  if there is a linear function  $L: \mathbb{R}^m \rightarrow \mathbb{R}^m$  and a vector  $\mathbf{b}$  in  $\mathbb{R}^m$  such that

$$A(\mathbf{x})=L(\mathbf{x})+\mathbf{b} \quad (2.4)$$

for all  $\mathbf{x}$  in  $\mathbb{R}^m$ . An affine function is the summation of a linear function and a translation. A linear function  $L: \mathbb{R}^m \rightarrow \mathbb{R}^m$  has following properties for any vectors  $\mathbf{x}$  and  $\mathbf{y}$  in  $\mathbb{R}^m$ ,

- (1)  $L(\mathbf{x}+\mathbf{y})=L(\mathbf{x})+L(\mathbf{y})$
- (2)  $L(a\mathbf{x})=aL(\mathbf{x})$  for scalar  $a$ .

Figure 2.3 illustrates the self-similar and self-affine transformation of a square. Self-affine transformation is also called shearing transformation. It may be noted that self-similarity is the subset of self-affinity.

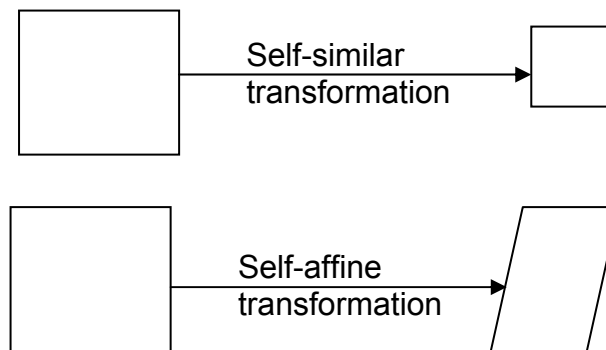


Figure 2.3: Self-similar and self-affine transformation

Self affine including self-similar geometry can be classified into three groups [9]: exactly self affine, quasi self affine and statistically self affine. Exactly self affine objects can be generated mathematically using the IFS as in equation (2.2); they are structurally and statistically same at different levels of spatial isotropic transformation. Quasi self similar objects found in natural objects like plants, biological organs, *etc.* exhibit a degree of irregularity, however they are exception rather than the rule. Statistical self affinity is abundant in natural objects. Satellite images of the Earth surface, microstructural and fractographic images are the examples of statistical self affinity within certain range of magnification. Figures 2.4 (a)-(d) illustrate different kinds of self affine fractal objects.

For modeling self-similar or self-affine fractal objects, the Hurst exponent,  $H$  [10] is used as the quantifier of complexity. The structural function describing self affinity can be written as

$$F_I(x)-F_I(y) \sim (x-y)^H \quad (2.5)$$

Where  $F_I(x)$  and  $F_I(y)$  are the two fractal objects, indistinguishable copies of the original object  $x$  and  $y$  respectively as shown in Figure 2.2. In equation (2.5), the structural function correlates the Euclidean distance in two successive generations of fractal objects. When  $H$  is equal to 1, the object is exactly self similar otherwise it is self-affine. It is therefore understood that self-similarity is a special case of self-affinity.

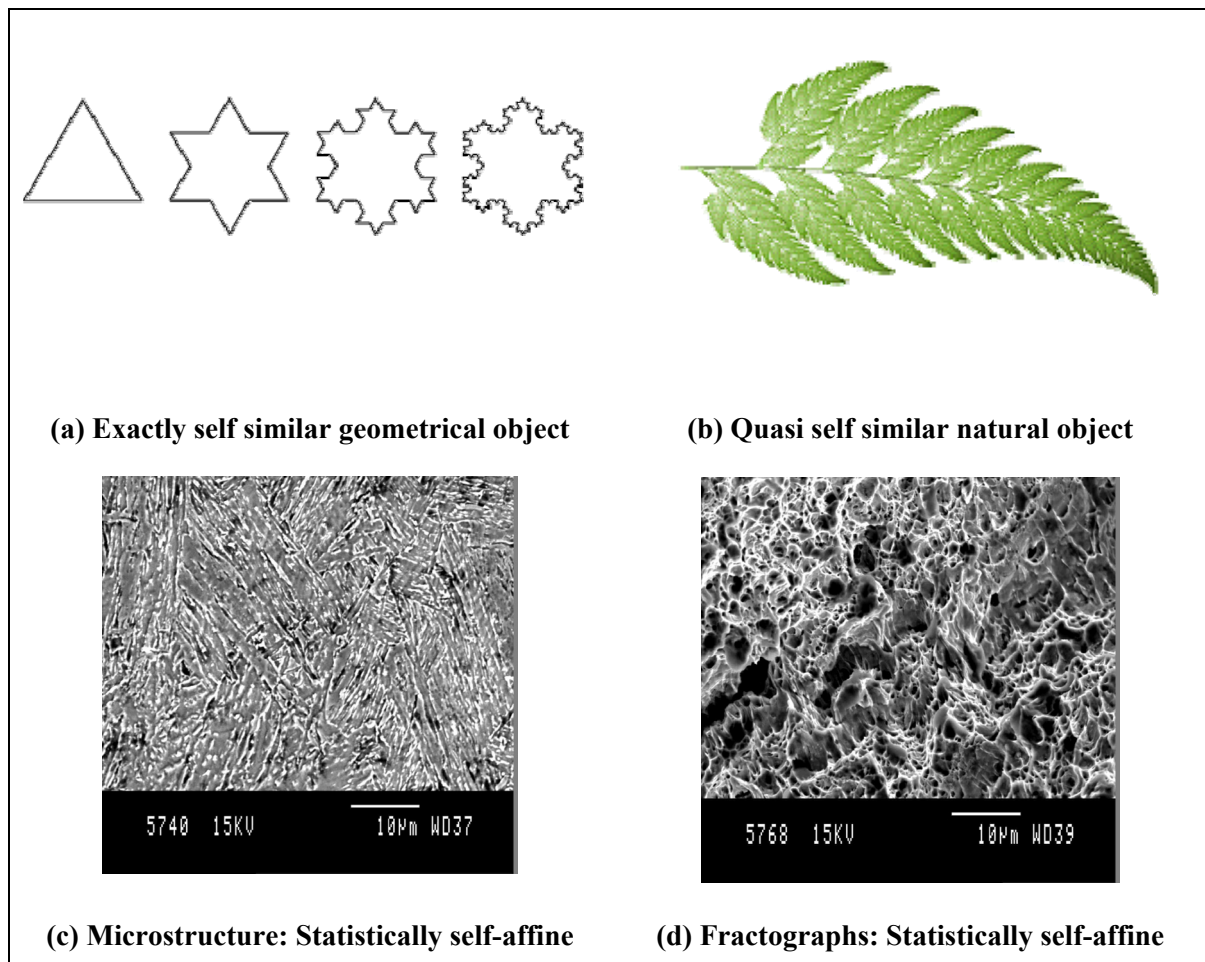


Figure 2.4: Types of self-similar fractal objects

### 2.1.3 Hurst exponent: A quantifier of complexity

Self-similarity represents order or symmetry whereas complexity identifies the chaos or entropy in a system. One is an inverse function of other. For quantifying complexity, Hurst exponent was proposed by Harold Edwin Hurst in 1951. It measures the linear volatility, trend or roughness of an observed geometric form, including time series data. Originally developed in hydrology to estimate optimum dam size for the Nile River based on the rain fall data over a long period of time; the work was reported in a classic paper by Hurst [11]. Hurst exponent,  $H(q)$ , is defined as  $H_q = H(q)$ , where  $q$  is the order of the moment of the statistical time series,  $g(t)$ , where  $t = \Delta t, 2\Delta t, \dots, N\Delta t$  and  $N$  is the number of data in the time series. The definition of the structure functions  $S_q(k)$  [12] is given as

$$S_q(k) = \left\langle |g(t+k) - g(t)|^q \right\rangle \quad (2.6)$$

where  $k$  is the lag and  $\langle \rangle$  is used to denote the average taken over a time window  $T \gg k$ . Here,  $T$  is the maximum time attained by the system.

Considering self-similar or self-affine property as given in equation (2.5), the structure function  $S_q(k)$  reduces to

$$S_q(k) = \left\langle |g(t+k) - g(t)|^q \right\rangle = C_q k^{qH(q)} \quad (2.7)$$

where the coefficient  $C_q$  and the exponent  $qH(q)$  are independent of  $k$ , but depend on the order  $q$  and the parameter  $H(q)$ .

When  $q=1$ , the 1<sup>st</sup> order structure function,  $S_1(k)$ , defines the correlation between the lag  $k$  and the absolute mean relief,  $\langle |g(t+k) - g(t)| \rangle$  whereas the 2<sup>nd</sup> order structure function,  $S_2(k)$ , represents the correlation with semivariance,  $\Delta(k)$ , as

$$\Delta(k) = \frac{1}{2} \left\langle |g(t+k) - g(t)|^2 \right\rangle \quad (2.8)$$

The scaling behaviour of  $S_q(k)$  can be expressed [13,14] as

$$S_q(k) \propto k^{qH(q)} \quad (2.9)$$

When  $H(q)$  is independent of  $q$ , then a unique  $H$  can quantify a process. This is the characteristics of uni-fractal process. However, when  $H(q)$  is a function of  $q$ , the process is called multifractal. Simple Brownian motion is the process which will have  $H=0.5$  irrespective of the order of moment  $q$ . However the fractional Brownian motion (fBm) will have  $H$  varying with the order of moment. When  $q=1$ ,  $H(1)$  describes the scaling behaviour of the absolute values of the increments which is expected to be closely related to the original Hurst exponent. When  $H(1)>0.5$ , the trend of the time series is said to be persistent and for  $H(1)<0.5$  it is antipersistent in nature.

Physical significance of the parameter  $H$  can be appreciated by examining the affine transformation in three dimensions [15]. In practical sense, this transformation takes place during the creation of rough surface. This anisotropic affine transformation is represented as:  $x' \rightarrow \lambda_x x; y' \rightarrow \lambda_y y; z' \rightarrow \lambda_z z$ , where  $(x,y,z)$  is the Cartesian co-ordinate of a point which is transformed to  $(x',y',z')$ . To maintain structural continuity, the transformation co-efficient  $(\lambda_y, \lambda_z)$  are correlated to  $\lambda_x$  by the scaling law

$$\lambda_y \propto \lambda_x^{\nu_y}; \lambda_z \propto \lambda_x^{\nu_z} \quad (2.10)$$

When  $\nu_z \neq \nu_y$ , the Hurst exponent is given as

$$H = \frac{\nu_z}{\nu_y}; \nu_z < \nu_y \quad (2.11)$$

In case of self similar surface  $\nu_z = \nu_y$  when the value of  $H$  becomes 1 resulting to a constant fractal dimension. This makes quantification of surface roughness using  $H$  or  $D$  meaningless. Therefore to quantify surface roughness for exactly self-similar surface,  $H$  has to be considered as either  $\nu_z$  or  $\nu_y$  [15].

The Hurst exponent,  $H$  is directly related to fractal dimension,  $D$  [9] by the following formula

$$D = D_T + 1 - H \quad (2.12)$$

For one dimensional time series data  $D_T = 1$  hence  $D = 2 - H$ . For an image,  $D = 3 - H$ .

## 2.2 Available methods for computation of fractal dimension

There are numerous methods for computing fractal dimensions for 1D spatial or temporal data series and 2D images. These methods can be classified into four broad groups:

Categories	Methods
Covering methods	Dividers (Compass) method, Box-counting method
Geometrical methods	Slit Island method using Area-perimeter relationships
Statistical methods	Probability-density function, Information theory based method, Rescaled range analysis (R/S analysis)
Spectral methods	Power spectral density (PSD) Method, Wavelet method

Different methods estimate different quantities and fractal dimension is the exponent of the power-law variations between the measured quantities and scales. For examples dividers method estimates length ( $L$ ), box counting method counts number of boxes, slit island method needs area verses perimeter correlation. In case of statistical methods, different statistical parameters like semivariance, range, standard deviation, probability density functions are the estimated quantities. For spectral methods, power and energy components are computed. While many of these methods compute Capacity Dimension ( $D_0$ ) or Box counting or Housdroff dimension, some of them compute information and correlations dimensions. Description of these methods, the areas of applications, and their limitations are discussed in review literatures [16, 17]. A few important methods are presented in the following sections.

**M.1: Method Name:** Dividers (Compass) method [18-23]

**Applicable to:** Curves e.g. cell membrane, coastline, grain boundary, and landscape edge.

**Formulation:** The estimated length of the coastline is the product of  $N$  (number of rulers required to 'cover' the object) and the scale factor  $k$ . The power-law relationship between the measuring scale  $k$  and the length  $L$  is:

$$L = N_0 k^{(1-D)} \quad (2.13a)$$

$$\log(L) = \log(N_0) + (1 - D) \log(k) \quad (2.13b)$$

where  $N_0=L$  when  $k=1$ . The fractal dimension ( $D$ ) is estimated by measuring the length  $L$  of the curve at various scale values  $k$ .

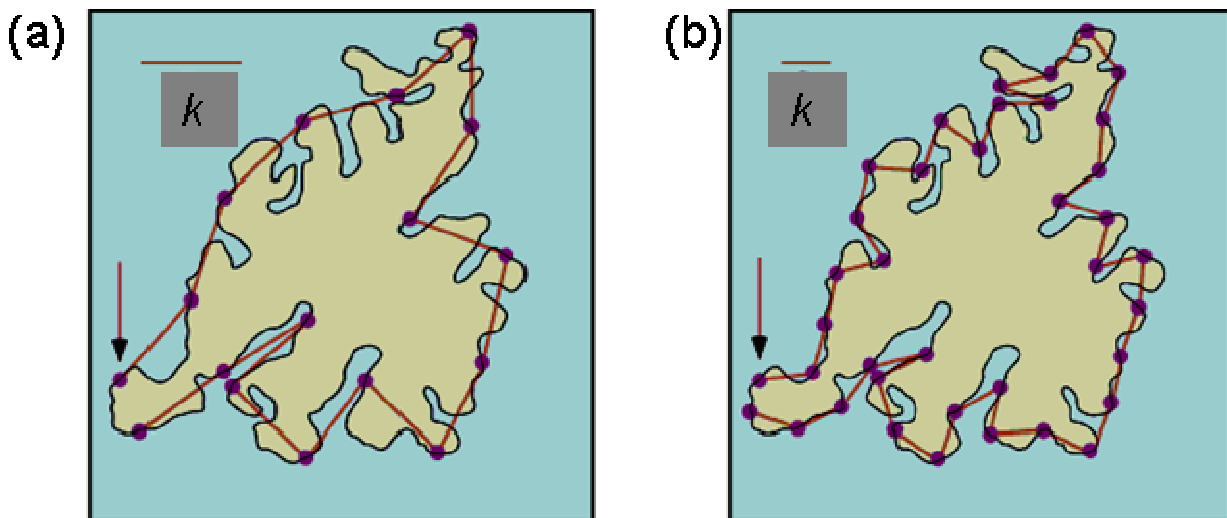


Figure 2.5: Dividers (compass) method. Two ruler lengths ( $k$ ) are shown in (a) and (b). The starting position is indicated by an arrow.

**Limitations:**

- This method is not well-founded theoretically, and furthermore it is exact only for statistically self-similar curves
- Results will vary for different starting points
- Log ( $L$ )-log ( $k$ ) plot using equation (2.13b) may not have constant slope.
- Variable slope either indicates the operational scale of different generative processes or reflects the limited spatial resolution of the data being analyzed.

**M.2: Method Name:** Box-counting method [24-30]

**Applicable to:** Overlapping curves, structures lacking strict self-similar properties.

**Formulation:** Number of boxes,  $N$ , of size  $k$  covering an object is the function of the size of the box. The correlation can be written as

$$N = N_0 k^{-D} \quad (2.14a)$$

$$\log(N) = \log(N_0) - D * \log(k) \quad (2.14b)$$

where  $N_0 = N$  when  $k=1$ . The fractal dimension ( $D$ ) is estimated by counting the number of boxes at various box sizes,  $k$ .

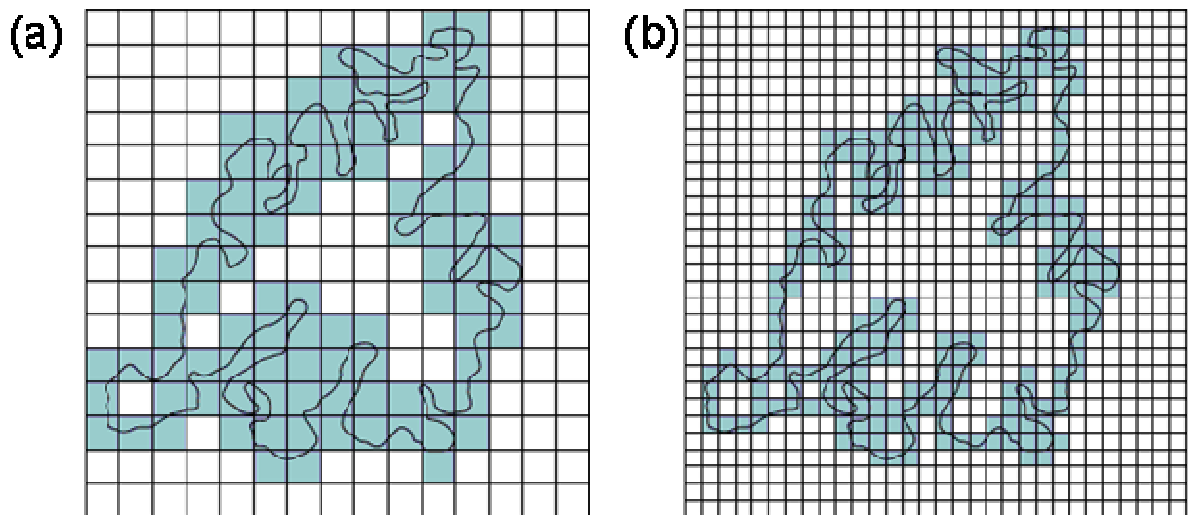


Figure 2.6: Two box 'lengths' are shown in (a) and (b). Box size,  $k$  in (a) is greater than the same in (b).

**Limitations:**

- Placement of boxes will change the total count  $N$ , hence statistical variations of  $D$  needs to be estimated by randomly placing the boxes.
- Limited resolution of data affects  $D$  values.
- Gives inaccurate results for surfaces.
- $\log(N)$ - $\log(k)$  plot by equation (2.14b) may not have constant slope.
- Variable slope either indicates the operational scale of different generative processes or reflects the limited spatial resolution of the data being analyzed.

**M.3: Method Name:** Slit island method using area-perimeter relationships [31-41]

**Applicable to:** Black & White images

**Formulation:** Shaded object in Figure 2.7 is considered as island and white is lake. Island area,  $A$ , is computed by counting number of black pixels. Perimeter,  $P$ , is estimated by counting the number of pixels covering the perimeter. The area perimeter relationship is given as

$$P = P_0 A^{D/2} \quad (2.15a)$$

$$\log(P) = \log(P_0) + \frac{D}{2} * \log(A) \quad (2.15b)$$

where  $P_0$  is the scaling constant and  $D$  is the fractal dimension of the coastline of the island.



Figure 2.7: Area-perimeter relationships. Landscape of pixel 'islands'. The area of each island is shaded, and its perimeter is indicated by a solid black line.

**Limitations:**

- Pixel of the digital image is rectangular resulting in biased estimates of  $D$  due to this 'rectangularization' for small island ( $A < 30$ ).
- Edge effects are also a problem. Islands touching the edges of the image gives biased estimates of  $D$ .
- "Staircase" effect of perimeter of  $45^\circ$  orientation since number of pixels required is more.

**M.4: Method Name:** Probability-density function [28,42-43]

**Applicable to:** Black & white image

**Formulation:** A square grid of size ( $k \times k$ ) is slid over the image from left to right, top to bottom by shifting its position by one pixel from its previous one. Let  $N(k)$  be the number of black pixels at a particular position of the square grid where  $N(k) \leq k^2$ . The first order moment,  $M(k)$ , of the probability density function  $P(k)$  of the  $N(k)$  values for different positions of the square grid can be derived by using the following formula

$$M(k) = \sum_{i=1}^{N(k)} i.P_i(k) \text{ where } \sum_{i=1}^{N(k)} P_i(k) = 1 \quad (2.16a)$$

$M(k)$  is often termed the 'mass dimension'. The relationship between the first order moment value  $M(k)$  and  $k$  may be given by

$$M(k) \propto k^D \quad (2.16b)$$

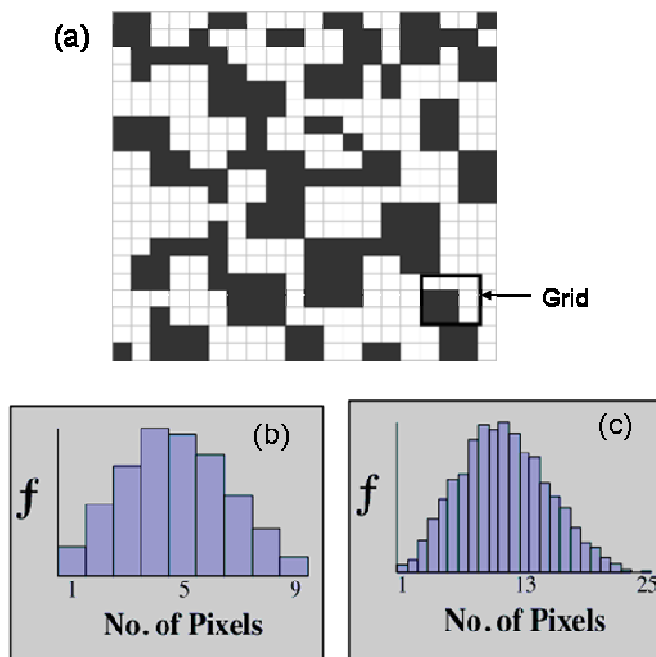


Figure 2.8: Probability-density function. (a) Pixel map (black regions), showing a representative 3x3 sliding grid for which the count,  $N(k) = 4$ ; (b) Frequency distribution of pixel counts for a 3x3 window; (c) Frequency distribution of pixel counts for a 5x5 window.

**Limitations:**

- Gives poor estimates of fractal dimension more than 2.5.
- Edge effects are a problem. Increases in the window size ( $k$ ) result in exclusion of a greater proportion of pixels along the periphery of the map.

**M.5: Method Name:** Information Theory based method [44-48]

**Applicable to:** 1D spatial or temporal series; Binary images

**Formulation:** This method is similar to the previous method M.4 where square box of size  $k$  is convoluted on a binary image or a set of data series. Within each box, numbers of dark pixels are counted as  $n_i$ . Each count is expressed in terms of probability

$$P_i(k) = \frac{n_i(k)}{N} \quad (2.17)$$

where  $N$  is the total number of points in the set. Shannon entropy,  $S(k)$ , and Simpson diversity index,  $C(k)$ , are computed to estimate Information dimension,  $D_1$ , and Correlation dimension,  $D_2$ .

Shannon entropy and the power law correlation	Simpson diversity index and the power law correlation
$S(k) = -\sum_{i=1}^{N_k} P_i(k) \log P_i(k)$ $S(k) \propto k^{D_1}$ <p><math>D_1</math> is the information dimension.</p>	$C(k) = \sum_{i=1}^{N_k} P_i(k)^2$ $C(k) \propto k^{D_2}$ <p><math>D_2</math> is the so-called correlation dimension.</p>

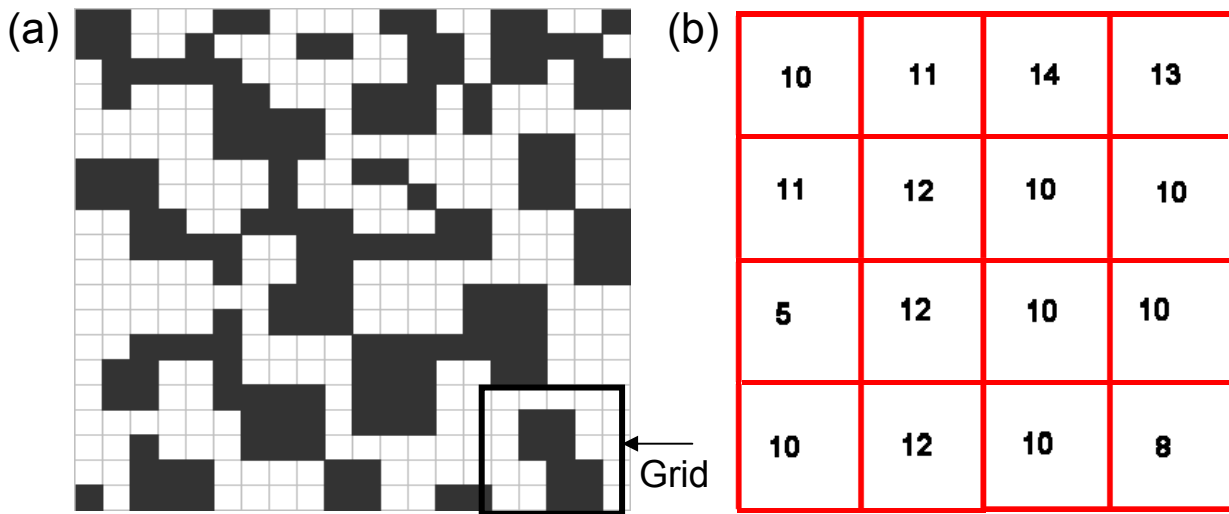


Figure 2.9: Point pattern analysis: information and correlation dimension. (a) A self-similar point pattern (b) Number of points per box for box size 5 x 5.

**Limitation:**

- Edge effects are a problem. Increases in the window size ( $k$ ) result in exclusion of a greater proportion of pixels along the periphery of the map

**M.6: Method Name:** Rescaled range analysis (R/S analysis) [49-59]

**Applicable to:** 1D spatial or temporal series, 2D images

**Formulation:** For 1D spatial or temporal series,  $X(t)$ , average deviation is computed for a segment of length,  $k$ , of the data series as  $Y(t,k) = X(t,k) - \bar{X}$ ,  $t=1,2,3,4,\dots,k$  where  $\bar{X} = \frac{1}{k} \sum_{t=1}^k X(t)$ . Range,  $R(k)$ , and standard deviation,  $S(k)$ , for the data segment,  $Y(t,k)$  are given as

$$\left. \begin{aligned} R(k) &= \text{Max}(Y(t,k)) - \text{Min}(Y(t,k)) \\ S(k) &= \sqrt{\frac{1}{k} \left( \sum_{t=1}^k (X(t) - \bar{X})^2 \right)} \end{aligned} \right\} \quad (2.18)$$

The rescaled range of an irregular time series  $X(k)$  can be defined as

$$\left. \begin{aligned} R/S(k) &= \frac{R(k)}{S(k)} \\ \langle R/S(k) \rangle &= C.k^H \end{aligned} \right\} \quad (2.19)$$

where fractal dimension,  $D=D_T+1-H$ . For 1D spatial or time series  $D_T=1$  and for 2D image  $D_T=2$ .

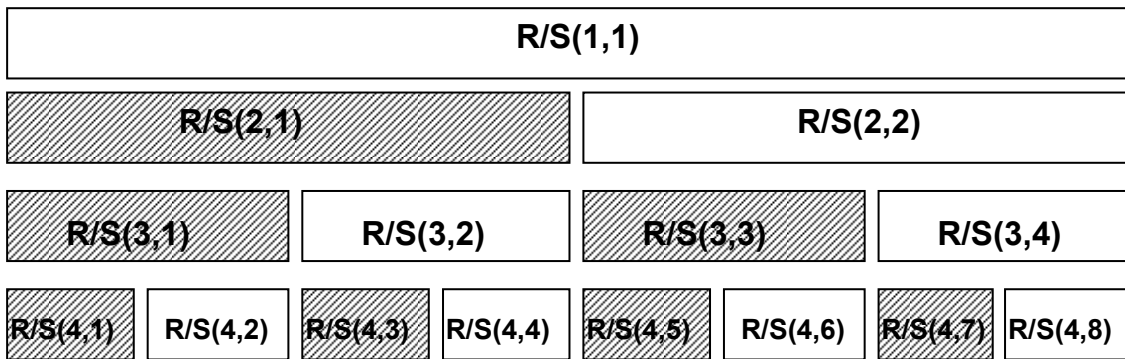


Figure 2.10: Binary segmentation of data series for the RS analysis

**Limitations:**

- Removal of average trend of the data eliminates low frequency components.
- Higher  $k$  has greater effect on R/S analysis than the smaller scale.

**M.7: Method Name:** Power Spectral Density (PSD) Method [60-65]

**Applicable to:** 1D spatial or temporal series, 2D images

**Formulation:** For 1D spatial or temporal series,  $X(t)$ , the Fourier transform,  $G(f)$ , is given as

$$G(f) = \int_{-\infty}^{\infty} X(t)e^{-i2\pi ft} dt \quad (2.20)$$

For a finite time interval,  $N$  where  $0 < t < N$ , the power spectral density,  $P(f)$ , is computed as

$$P(f) = \frac{|G(f)|^2}{N} \quad (2.21)$$

For 2D image, frequency  $f$  has two orthogonal components  $f_x$  and  $f_y$ .

For fractal object, PSD can be expressed as a function of frequency by

$$P(f) \propto \frac{1}{(f)^{(2H+D_T)}} \quad (2.22)$$

where  $D_T$  is the topological dimension and the fractal dimension,  $D = D_T + 1 - H$ .

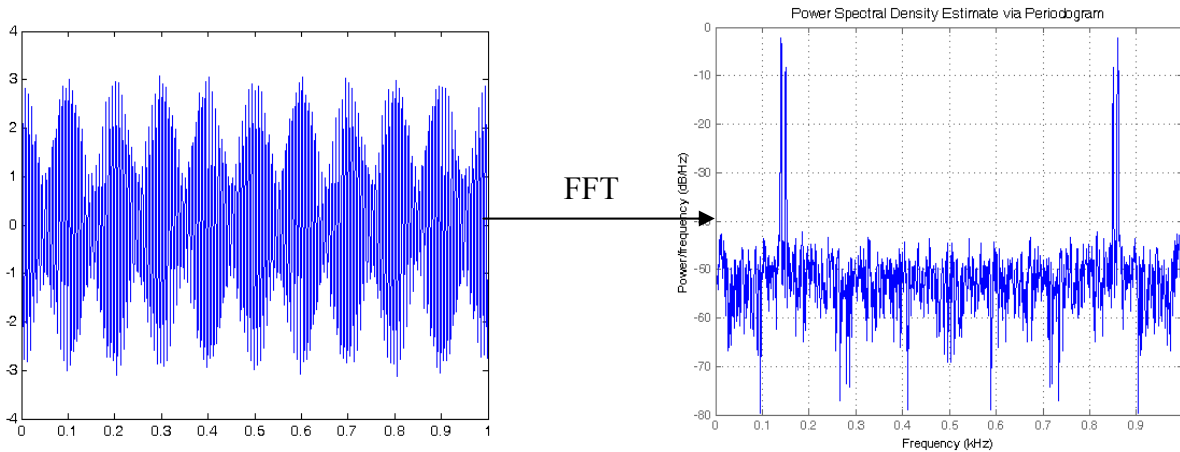


Figure 2.11: Frequency vs power spectral density

**Limitations:**

- Often finite size effect is seen in low frequency level or large length scale.
- At high frequency, the power spectrum contains high level of noise.

**M.8: Method Name:** Wavelet Method [66-75]

**Applicable to:** 1D spatial or temporal series, 2D images

**Formulation:** For 1D spatial or temporal series,  $X(t)$ , can be expressed as

$$X(t) = \sum_k c_{j_0}(k) \phi_{j_0,k}(t) + \sum_{j=j_0}^{\infty} \sum_k d_j(k) \psi_{j,k}(t) \quad (2.23)$$

where  $j_0$  is the arbitrary starting scale,  $c_{j_0}(k)$  is the average (scaling) coefficient and  $d_j(k)$  is the detailed (wavelet) coefficient and  $j$  is the level of decomposition. Average energy for a 1D series of finite duration ( $1 \leq t \leq N_j$ ) is computed as

$$E_x(j) = \frac{1}{N_j} \sum_{k=0}^{N_j-1} (d_j(k))^2 \quad (2.24)$$

The correlation between average energy,  $E(j)$ , computed by the Wavelet analysis and the level,  $j$ , is given as

$$E_x(j) \propto \frac{1}{j^{2H+D_T}} \quad (2.25)$$

where  $D_T$  is the topological dimension and the fractal dimension,  $D = D_T + 1 - H$ .

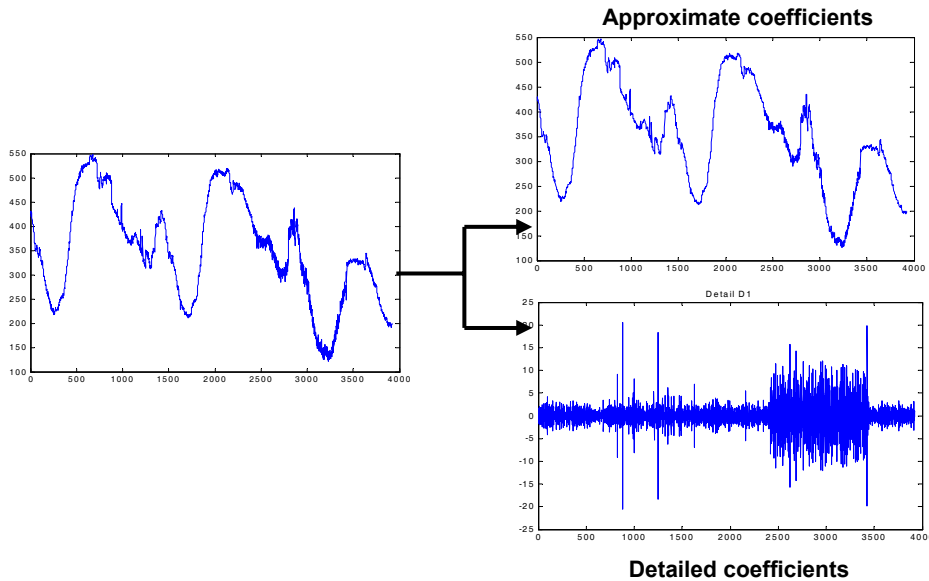


Figure 2.12: Wavelet transformation

**Limitations:**

Poor discrimination capability since data averaging takes place with the level of decomposition

## 2.3 Image rendering by Scanning Electron Microscope

This section gives a brief overview of the Scanning Electron Microscope (SEM) which is used for generating intensity images of metallic materials surfaces. High resolution images of microstructure of materials are known as micrographs. It is important to have a clear understanding of the input data (image) especially the approximations and assumptions being considered for final image rendering. Since, in this investigation, the contrast variations of these images are used for devising the quantification procedure, correlations between image intensity variations and low level electron signals have been presented.

### 2.3.1 Basic principle of SEM

The SEM generates micrographs by scanning the surface of a specimen with small electron beam synchronously with the electron beam in a cathode ray tube (CRT). The image contrast is due to topographic variations and atomic number differences in the specimen.

The instrument produces finely focused electron beam to irradiate flat specimens. During irradiation, the specimen releases several types of radiation such as

- Secondary electrons
- Backscattered electrons
- Low pass electrons
- Auger electrons
- Light
- Characteristics x-rays
- Continuous x-ray spectrum

The shape, chemical composition and the crystal orientation of the irradiated volume determines the intensity of these radiation signals.

Detailed discussion of all these radiation signals can be found elsewhere [76,77]. Only the relevant part *i.e.* the signals generated due to the secondary electrons and the backscattered electrons has been included here. In both the cases the generated electron beam scans over an area of a specimen; the radiated electrons are capture by detectors and then converted into electrical signals. These signals are amplified, processed and finally sent to the display unit for rendering. Figure 2.13 shows the block diagram indicating the signal path.

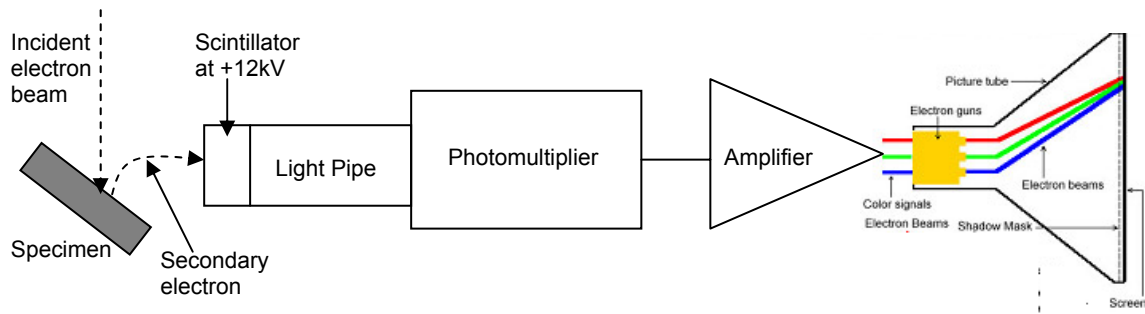


Figure 2.13: Signal path in SEM

The intensity of the signals, contrast variations as well as the amount of information contained in the image depend upon the following factors

- Beam diameter
- Magnification
- Depth of focus.

**Beam diameter** determines the amount of incident energy of the probe electrons. Controlling the beam diameter, minimum resolution of the SEM can be achieved. The total beam diameter,  $d$ , is estimated by

$$d^2 = d_0^2 + d_s^2 + d_c^2 + d_f^2 \quad (2.26)$$

where  $d_0$  is aberration less beam diameter at specimen,  $d_s$  is diameter of disk of confusion due to spherical aberration,  $d_c$  is diameter of disk of confusion due to chromatic aberration and  $d_f$  is diffraction effect or the Airy disk diameter. Considering  $\alpha$  as half the aperture angle of illumination and  $\lambda$  as the wavelength of the electron beam,  $d_f$  can be expressed as

$$d_f = \frac{1.22\lambda}{\alpha} \quad (2.27)$$

As the beam diameter decreases, the current carrying capacity of the beam also decreases. Typically  $10^{-11}$  amp current is required to have a beam diameter of 100 Å to focus the same area on the specimen. To achieve higher resolution, it is not possible to minimize the beam diameter greatly as for the smaller beam diameter; electron energy carried by the beam also gets reduced. The wavelength  $\lambda$  of the electron beam is inversely proportional to the energy carried by them *i.e.*

$$eV = \frac{h}{2\pi\lambda} \quad (2.28)$$

where  $h$  is the Plank's constant.

It can be seen from equations (2.26), (2.27) and (2.28) that, for the smallest beam diameter, the wavelength is reduced for which the electron energy increases. To accommodate high electron energy, beam diameter subsequently increases. Therefore beam diameter can not be reduced indiscriminately to achieve better resolution since it is limited by the wavelength of the energy quanta carrying by the beam.

**Magnification** is controlled by varying the size of the area that is scanned on the specimen. It can be varied from 15 to 100,000 times or more. Low magnification micrographs can not be photographically enlarged or zoomed to obtained detailed information. This is because the magnification is controlled by changing the beam diameter. For lower magnification, beam diameter is enlarged. Hence the resolution of the image formed on the display unit decreases.

**Depth of focus** determines the range (FD in Figure 2.14) within which the image remains focused. Since the angle of incidence ( $A/2W$ ) can be lowered substantially for the electron beam with the smaller wave lengths, the depth of focus gets increased. This gives a good range of contrast or intensity variations which shows the topographic 3D view of the SEM images. In Figure 2.14, P is the ratio between the pixel diameter and magnification,  $Mx$ , which is  $100 \mu\text{m}/Mx$  for SEM. Figure 2.15(a) shows the optical image and (b) the SEM image. The clearly visible topographic variations in (b) are due to the larger depth of focus of the SEM.

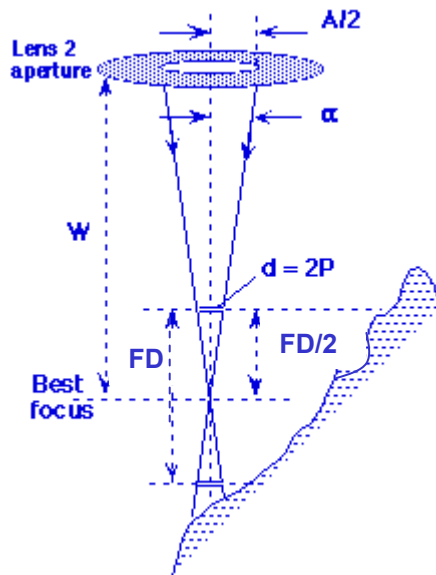


Figure 2.14: Depth of focus (FD)

(Image take from <http://www.emal.engin.umich.edu/courses/semlectures/focus.html>)

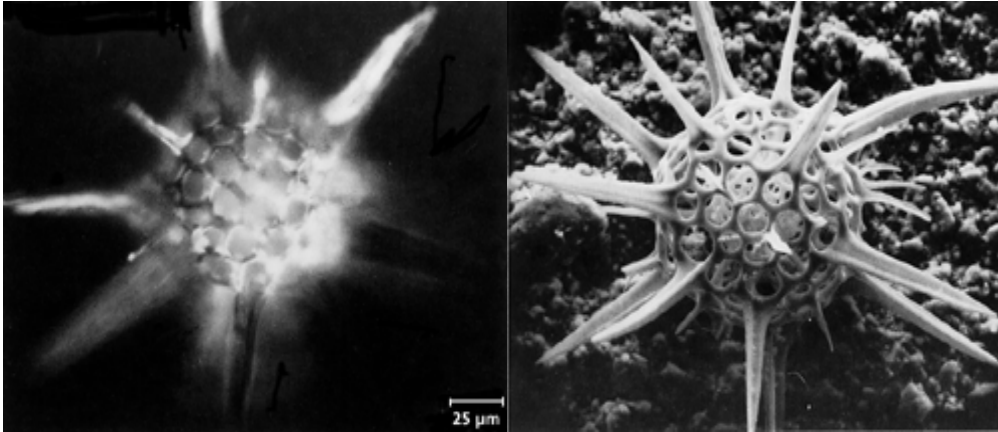


Figure 2.15: (a) Limited depth of focus in optical image (b) Large depth of focus in SEM image

(Taken from J.I. Goldstein et al., eds., Scanning Electron Microscopy and X-Ray Microanalysis, (Plenum Press, NY, 1980).)

### 2.3.2 Signal to noise ratio in SEM images

For generating image signals, the radiated electrons are detected by the noise free scintillator-photomultiplier detector system. The number of detected electrons determines the amount of current generated in the detector which is the raw signal prior to the allocation of gray level intensity values. In case of low magnification image, the beam diameter is increased. The detected electron count increases and the noise pulse can be easily reduced. However, for high magnification image, since the beam diameter is small, the detected electron count is of limited range. Reducing the noise level will further reduce the count resulting in a very dark image. Thus a minimum level of noise pulses is accepted for generating the electron image with acceptable contrast variations.

An image is a 2D spatial signal of size  $M \times N$  with  $G$  discernable grey levels. For  $n$  bit image  $G$  is equal to  $2^n$ . The minimum resolution of the image depends upon the size of a pixel or the picture element on the display unit. The intensity value realized by a pixel contains actual signal quanta and the noise pulse. Allocation of gray levels is therefore made on the basis of equal reliability levels *i.e.* keeping the signal-to-noise ratio (SNR) constant from the darkest (0) to the brightest ( $2^n$ ) zones of the image.

The SNR is defined as the ratio between the root mean square(rms) signal and the rms fluctuation due to noise. The probable error,  $P(e)$  for one unit gray level change on account of noise is related to the SNR by the equation

$$P(e) = \frac{1}{2} \left[ 1 - \operatorname{erf} \left( \frac{K}{2\sqrt{2}} \right) \right] \quad (2.29)$$

where the error function is defined as

$$\operatorname{erf}(x) = \frac{1}{\sqrt{\pi}} \int_0^x e^{-y^2} dy \quad (2.30)$$

In equation (2.29),  $K$  is the SNR ratio between the signal quanta ( $\bar{n}_i$ ) and the rms fluctuation ( $\sqrt{\bar{n}_i}$ ) caused by noise, where “ $i$ ” subscript is used to specify the position along the signal path within the SEM. For instant  $n_i$  signifies the number of electron in the incident beam and  $n_5$  the number of signal quanta in the photomultiplier as illustrated in Figure 2.13. The position at which minimum  $n_i$  is obtained is called the noise bottleneck. Solving equation (2.29), it can be found that for  $K=5$ , the gray level fluctuation is 1 in 160, which is acceptable for a low magnification micrographs. For higher magnification micrographs, poorer SNR ( $K<5$ ) may be acceptable to get an image on the CRT.

For assigning contrast variations in the image displayed at the CRT, the minimum and maximum signal quanta are considered at the location where noise is maximum *i.e.* at the noise bottleneck. The minimum is referred as  $\bar{n}_{black}$  and maximum is referred as  $\bar{n}_{white}$ . The range between black and white ( $\bar{\delta}_A$ ) is defined by

$$\bar{\delta}_A = \frac{\bar{n}_{white} - \bar{n}_{black}}{\bar{n}_1} \quad (2.31)$$

where  $\bar{n}_1$  refers to the number of electrons in the incident beam. The background range ( $\bar{\delta}_B$ ) is given as

$$\bar{\delta}_B = \frac{\bar{n}_{black}}{\bar{n}_1} \quad (2.32)$$

To maintain equal reliability levels, the SNR is kept constant which is expressed in terms of  $\bar{n}_{black}$ ,  $\bar{n}_{white}$  and the maximum grey level  $G$ . The SNR,  $K$  is written as

$$K = \frac{2}{G} \left( \sqrt{\bar{n}_{white}} - \sqrt{\bar{n}_{black}} \right) \quad (2.33)$$

It is possible to find out the ratio between beam current ( $i_{beam}$ ) required for an image and the minimum beam current ( $i_{min}$ ) in terms of  $\bar{n}_{white}$  and  $\bar{n}_{black}$  as

$$i_{beam} = i_{min} \frac{1}{\bar{\delta}_A} \text{ if } \bar{\delta}_B \ll \bar{\delta}_A \quad (2.34)$$

$$= i_{min} \frac{4\bar{\delta}_B}{\bar{\delta}_A} \text{ if } \bar{\delta}_B \gg \bar{\delta}_A \quad (2.35)$$

where

$$i_{min} = \frac{K^2 G^2 N^2 e}{4t_1} \quad (2.36)$$

where  $t_1$  is the total time available for recording the image,  $N^2$  is the number of picture elements and  $e$  is the electron charge.

It may be noted from equation (2.36) that for larger image ( $N$ ), high SNR ( $K$ ), high definition image ( $G$ ) and faster scan rate ( $t_1$ ), minimum beam current will increase. If the background range,  $\bar{\delta}_B$ , is less than the available range,  $\bar{\delta}_A$ , of allocated gray levels, it can be understood from equation (2.34), that the beam current is reduced.

### 2.3.3 Resolution and contrast in SEM images

Resolution and contrast in an SEM image give the morphological and structural variations in the microstructure of the specimen. How closely the surface morphology and the image signal are interlinked, depends upon the beam diameter. To obtain a noise less image, beam diameter needs to be standardized. The convention is that for a particle size of diameter  $d_1$  and beam diameter of  $d_2$ , the apparent size of the particle in the image will be  $\sqrt{d_1^2 + d_2^2}$ . To get a noise less image the beam diameter should be equal to or greater than the particle size. Hence for a particle size and beam diameter of  $d$ , the apparent size of the particle will be  $\sqrt{2} d$ .

There are many ways by which the video waveform can be reconstructed to form an image. Intensity modulated image is the commonly used method in which the brightest part corresponds to the part of the specimen where the signal quanta is the highest. Conversely the lowest signal

gives the darkest spot on the image. For showing the surface topography, secondary and backscattered or low-pass images are obtained. To observe the shape of a rough surface, like fracture surface, secondary electron image is better than the other two. However for viewing the flat surface like microstructure of materials backscattered or low pass images are better.

### 2.3.4 Secondary electron image

Secondary electron image provides high-resolution imaging of topography of the specimen surface. The electron beam striking on the surface causes scattering of electrons of different energy bands. The low energy secondary electrons are collected by the positively charged collector and transformed to image signal. Larger the area of interaction between electron beam and the specimen surface, greater the possibility of scattering of electrons resulting to brighter area on the micrographs. The secondary electrons are of energies less than 50eV. Secondary electrons escape from the top 15nm of the specimen independent of the accelerating voltage. The orientation of surface features influences the number of electrons that reach the secondary electron detector. Sharp edges or corners will appear brighter because of the additional secondary electron emission due to low angle of incidence between incident beam and the surface. The secondary electron image resolution for an ideal sample is about 3.5 nm.

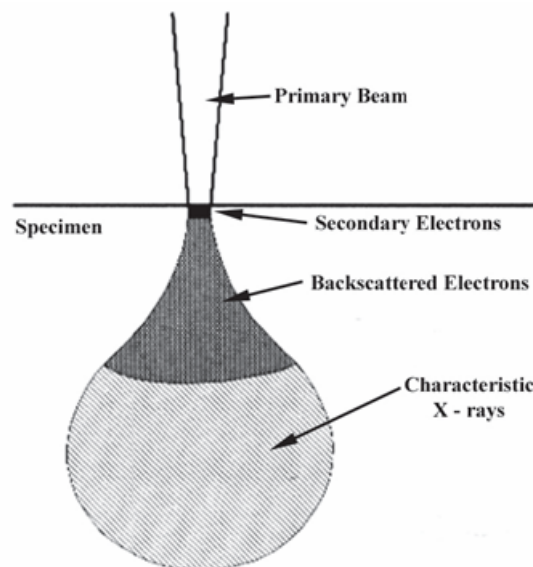


Figure 2.16: A schematic drawing of the beam-specimen interaction volume (Ref: R. Johnson, Environmental Scanning Electron Microscopy - An introduction to ESEM, Robert Johnsson Associates, El Dorado Hills, CA, 1996)

### **2.3.5 Back scattered electron image**

Back scattered electron (BE) image provides information about composition of elements as well as surface topography. BE images can be obtained from a relatively flat surface by the elastic interactions between the sample and the incident electron beam. These high-energy electrons, more than 50eV, can escape from much deeper than secondary electrons and collected by a pair of detectors. Image contrast for the BE image is determined by the intensity (number) of elastically scattered electrons collected by the detectors. To get elemental information, signal acquired by the pair of detectors are added. For higher atomic number material back scattered electrons are more than low atomic number material. Hence high atomic number elements are seen brighter in the BE image. Excellent topographic information of the specimen surface can be obtained in BE mode by using the difference between two signals captured by the detectors. Backscattered electrons escape from approximately 40% of the total electron penetration. The optimum image resolution for backscattered electron imaging is about 5.5 nm.

### **2.4 SEM image and surface roughness**

SEM images are formed due to the scattering of electrons from the surface of the sample. It was mentioned that the image intensity depends upon the beam current which is proportional to the variations in the number of electrons captured by the detectors, as given in equations (2.34) and (2.35). The perception of the shape of an object, thus, comes from the differential electron scattering and detection in the SEM. There is a similarity between electron imaging and optical imaging. While in optical imaging, light is the source and photon is captured for the image formation, in electron microscopy, electrons are the image forming units. The scattered electrons are analogous to photons reflected at the surface. In optical imaging, reflected light intensity is maximum when the reflected ray is perpendicular to the surface whereas in electron imaging it should be parallel. The mathematical formulations for image formation in both the systems are same. In SEM, the formulation is simplified as there is uniform illumination and the projection is often near orthogonal.

The shape of a surface is perceived due to the differential reflectance of light rays or electrons from the surface which depends upon the angle of incidence ( $i$ ), angle of emergence ( $e$ ) and the phase angle ( $g$ ) between the incident ray and the emergent ray as given by the Lambertian

reflection geometry [78] shown in Figure 2.17. In the context of SEM, rays are analogous to the paths of electrons.

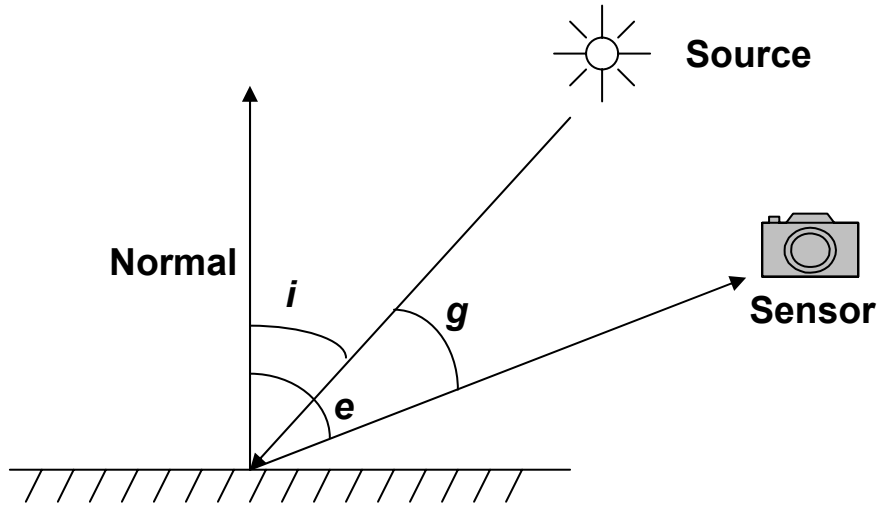


Figure 2.17: Lambertian reflection geometry showing incident ( $i$ ), emittance ( $e$ ), and phase ( $g$ ) angles

Considering  $I, E, G$  are the cosine of the angles  $i, e$  and  $g$  respectively the reflectivity function,  $\phi(I, E, G)$  is written as

$$\phi(I, E, G) = \frac{b(r')}{A(r)} \quad (2.37)$$

where  $b(r')$  is the intensity measured at the image point,  $A(r)$  is the incident light intensity. Here  $\phi(I, E, G)$  is a functions of  $x, y, z, p$  and  $q$ , where  $(x, y, z)$  are the spatial co-ordinates of the object,  $r$  is the corresponding polar coordinate,  $r'$  is the polar coordinate at image plane,  $p = \frac{\partial z}{\partial x}$ ,  $q = \frac{\partial z}{\partial y}$  and  $z$  is the elevation of the surface at  $(x, y)$ . The surface gradients  $p$  and  $q$  can be used to specify the surface orientation. The surface height represented by  $z(x, y)$  has a unique normal,  $n$ , with the components of surface gradient  $p$  and  $q$ . A unit step along  $x$  direction ( $\partial x = 1$ ), when  $\partial y = 0$  will give the surface elevation  $p$  ( $\partial z = p \cdot \partial x$ ), similarly for  $\partial x = 0, \partial y = 1, \partial z = q$ . Thus the unit surface normal,  $n$ , vector is the cross product of the two tangent of the vectors  $[1, 0, p]^T$  and  $[0, 1, q]^T$ , given as

$$n = \frac{1}{\sqrt{1 + p^2 + q^2}} \begin{bmatrix} -p \\ -q \\ 1 \end{bmatrix} \quad (2.38)$$



For the SEM, the set of five differential equations in (2.40) simplified to

$$\left. \begin{aligned} \dot{x} &= p \\ \dot{y} &= q \\ \dot{z} &= p^2 + q^2 \\ \dot{p} &= b_x \frac{n^3}{A\phi_I} \\ \dot{q} &= b_y \frac{n^3}{A\phi_I} \end{aligned} \right\} \quad (2.41)$$

In equation (2.41),  $n$  is the inward normal to the surface at the point  $O$  given by equation (2.38),  $b_x$  and  $b_y$  are the two components of the surface elevation related to the object plane,  $A$  is the incident intensity of the electron beam and  $\phi_I$  is the reflectivity of the electrons. The surface elevation at object plane in Cartesian coordinate  $(b_x, b_y, b_z)$  is related to the image intensity  $(b'_x, b'_y, b'_z)$  and the correlation can be given as

$$(b_x, b_y, b_z) = \left( \frac{f}{z} \right) \left[ b'_x, b'_y, - \left\{ \left( \frac{x}{z} \right) b'_x + \left( \frac{y}{z} \right) b'_y \right\} \right] \quad (2.44)$$

It may be noted that the intensities measured from the image do not locally determine the normal. The intensity is related to the magnitude of the first derivatives, and the gradient of the intensity is related to the second derivatives of the distance to the surface.

## 2.5 Basic image processing techniques

Digital images captured by the SEM are often pre-processed to enhance image quality for discrimination and classification of features. Two basic preprocessing methods such as histogram equalization and binarization have been used in this investigation to observe the effect of preprocessing on the fractal dimensions estimated by image analysis. While histogram equalization enhances the image quality, binarization converts the gray scale image to black and white image. An account of these two basic image processing techniques is given below.

### 2.5.1 Histogram Equalization

Image histogram is the plot of gray level values along the x-axis versus the frequency of occurrence of the gray level values along the y-axis. When the image histograms were plotted

for the fractographs, it was found that the image brightness range did not cover the entire 0-255 range, which is available for a gray-scale image. This means the available gray levels are not used efficiently. Therefore, in order to use the available gray levels efficiently, histogram equalization is employed. Histogram equalization method presumes that an image looks better if the gray levels of the pixels are distributed uniformly over the available gray level range, i.e. the histogram of the image is flat. For applying histogram equalization method on digital images, probability density function is used in discrete form which is given by the expression [79]

$$P_r(r_k) = \frac{n_k}{n} \tag{2.45}$$

where  $n_k$  is the number of pixels having a particular gray level  $r_k$ ,  $k$  varies between 0 to  $(L-1)$  and  $n$  is the total number of pixels in the image. Here,  $L$  is the total number of possible gray scale in the image. Figure 2.19 shows the original image, the histogram equalized image and the plot showing the corresponding histograms.

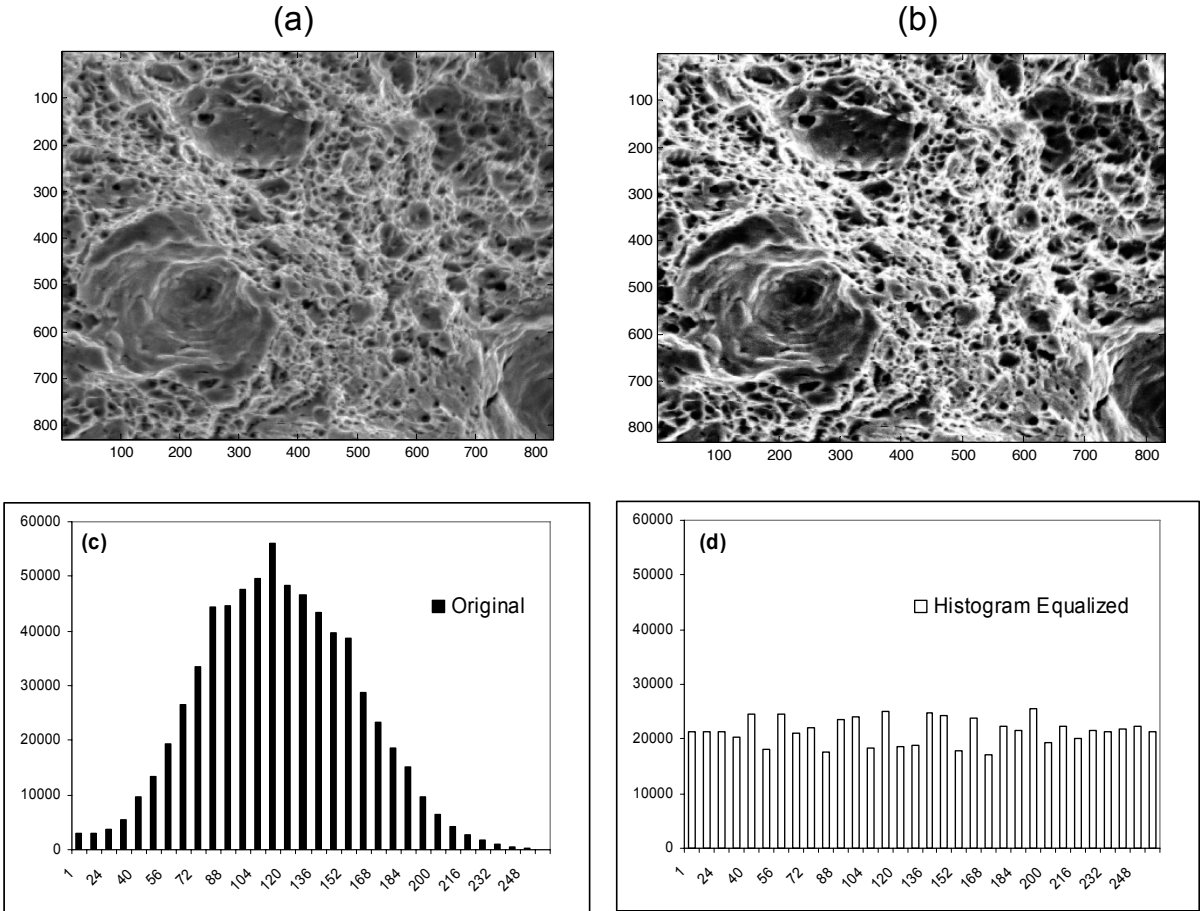


Figure 2.19: (a) The original fractographic image, (b) The histogram equalized fractographic image, (c) Histogram of (a), (d) Histogram of (b).

The original gray level  $r_k$  can be mapped to a discrete version of the new gray level  $s_k$  by using the following cumulative summation formula:

$$s_k = T(r_k) = \sum_{j=0}^k P_r(r_j) = \sum_{j=0}^k \frac{n_j}{n} \quad (2.46)$$

The equation (2.46) maps the gray level  $r_k$  of the input image to the discrete gray level  $s_k$  of the output image. It may be pointed out that both the gray levels  $r_k$  and  $s_k$  are normalized and presented in the domain of [0,1]. To get the actual gray levels, they are to be mapped within [0,L]. The plot of  $P_r(r_k)$  versus  $r_k$  is called the histogram and the transformation given in equation (2.46) is called histogram equalization.

### 2.5.2 Binarization

The most common way of converting gray scale image to binary image is by discrimination or thresholding. This is called binarization. Figure 2.20 shows the original fractographic image and the binarized image obtained using MATLABs “*im2bw*” function.

Manual setting of thresholds is most often accomplished interactively in standard image analysis software and it is the user’s responsibility to select appropriate threshold values to delineate the features of interest. Error in such threshold settings is liable to cause bias in the measured parameters. For instance, if the manual threshold is set lower than the actual threshold value then the size of the object will be reduced. Use of the same settings on different images from the same or similar samples may not be appropriate if the overall brightness level or contrast changes, or if the sample preparation is different. This can be a major source of error in the final results. Automatic thresholding [79] functions are available in standard image processing software to avoid such errors.

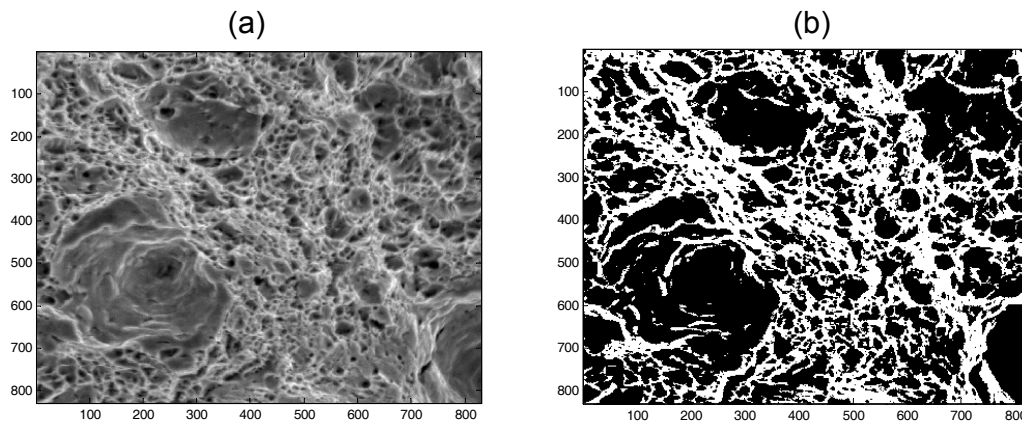


Figure 2.20: (a) The original fractographic image; (b) The binarized image obtained using MATLABs “*im2bw*” function.

## 2.6 Mechanical and fracture properties of materials

This section describes various macro-mechanical and fracture properties [80-83] which have direct relevance to this thesis. Some popular models addressing the effect of microstructural characterizing parameters such as grain size, micro cracks, dislocations, voids and distribution of second phase particles on the macro properties have been highlighted. Brief discussion on fractographs and micrographs are included to highlight the effectiveness of these images in material research.

### 2.6.1 Mechanical properties

When a force ( $F$ ) is applied on an object, displacement  $\Delta L$  takes place. In the elastic case, there is a linear correlation between force and displacement, which can be written as  $F = k\Delta L$ , where  $k$  is the stiffness of the material.

The force per unit area is the stress ( $s=F/A$ ) and the increment of displacement per unit original length ( $L$ ) of the object is the strain ( $e = \Delta L/L$ ). The mechanical properties comprise of hardness, various stresses and strains; the fracture properties deal with the energy required for a material to fracture and to its ability to resist propagation of cracks.

For determining mechanical properties of materials, engineering tensile test is performed on laboratory specimen. For continually applied uniaxial tensile load ( $F$ ), elongation ( $\Delta L$ ) are monitored using strain gauge attached to the specimen. Data obtained from this test is used to generate load-elongation curve from which engineering stress-strain curve is constructed. The stress used in the curve is the average longitudinal stress in the tensile specimen which is obtained by dividing  $F$  by the original area ( $A_0$ ) of the cross section of the specimen. The strain used for the engineering stress-strain curve is the average linear strain obtained by dividing the elongation of the gauge length of the specimen ( $\Delta L$ ) by the original length ( $L_0$ ). The engineering stress ( $s$ ) and strain ( $e$ ) relations are given as

$$\begin{aligned} s &= \frac{F}{A_0} \\ e &= \frac{\Delta L}{L_0} = \frac{L - L_0}{L_0} \end{aligned} \tag{2.47}$$

The relations given in equation (2.47) are based on the original length ( $L_0$ ) or area ( $A_0$ ) which does not correctly represent the true deformation behaviour of materials since during deformation cross sectional area gets reduced or gauge length increases. For representing true stress-strain behaviour, the engineering stress and strain need to be transformed to true stress ( $\sigma$ ) and strain ( $\epsilon$ ) using the following equations:

$$\sigma = \frac{P}{A_0}(e+1) = s(e+1) \quad (2.48a)$$

$$\epsilon = \ln(e+1) \quad (2.48b)$$

Mechanical properties that are estimated from an engineering stress-strain curve are ultimate tensile strength (UTS), yield strength (YS), percentage elongation ( $e_f$ ) and reduction of area ( $q$ ). In addition Modulus of Elasticity ( $E$ ) or Young's modulus, fracture stress ( $\sigma_f$ ), fracture strain ( $\epsilon_f$ ), necking strain ( $\epsilon_n$ ), strain hardening coefficient ( $n$ ) and hardness ( $Hv$ ) are some of the useful mechanical properties addressed in this work. Figure 2.21 shows engineering stress-strain curve where four distinct regions can be identified. The initial zone up to yield strength is elastic region. Beyond the elastic region, the plastic region consists of the yielding, strain hardening and necking regions. Uniform elongation of the specimen is found up to UTS after which necking or thinning out of the specimen starts and continues up to fracture.

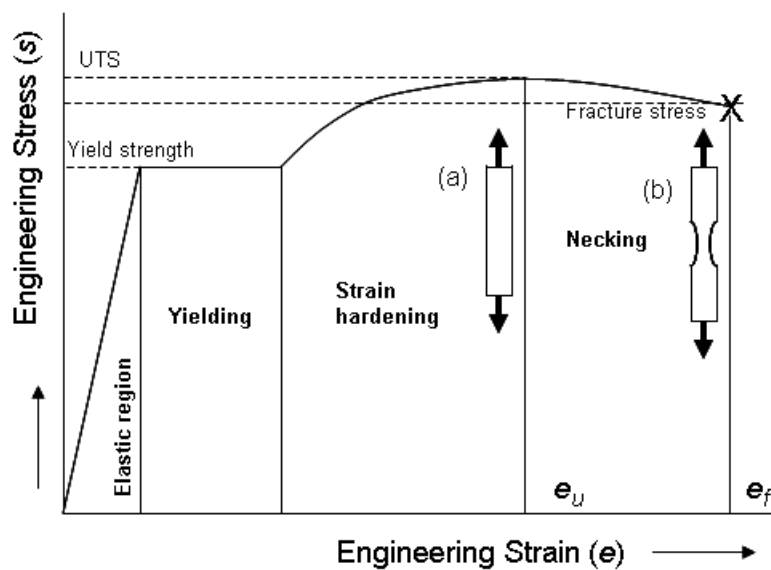


Figure 2.21: Engineering stress-strain curve showing tensile specimen during (a) strain hardening and (b) necking.

*Modulus of elasticity (E)*: The slope of initial linear part of the stress-strain curve is the modulus of elasticity or Young's modulus. It can be given by the expression-

$$E = \frac{S}{e} \quad (2.49)$$

*Ultimate tensile strength (UTS)*: Ultimate strength ( $s_u$ ) of the material subjected to tensile loading. It is the maximum engineering stress developed in the tension test given by

$$s_u = \frac{F_{\max}}{A_0} \quad (2.50)$$

*Yield strength (YS)*: Indication of the maximum stress that can be developed without causing any plastic deformation shown in Figure 2.21. Up to yielding, material follows linear stress-strain behaviour within the elastic region. It is also known as yield stress.

*Percent Elongation ( $e_f$ ) and Reduction of area ( $q$ )*: These are the measure of ductility which shows the extent of deformation a material can withstand without fracture. These properties indicate the plastic flow behaviour of material. Both the properties are estimated after the specimen has fractured when the change of gauge length is  $\Delta L_f$  and the change of area is  $\Delta A_f$ .

Percent elongation and the reduction of area are given as

$$e = \frac{\Delta L_f}{L_0} = \frac{L_f - L_0}{L_0} \quad (2.50a)$$

$$q = \frac{\Delta A_f}{A_0} * 100 = \frac{A_0 - A_f}{A_0} * 100 \quad (2.50b)$$

*True Fracture stress ( $\sigma_f$ )*: The stress that is applied to fracture the tensile specimen. This stress is well below the UTS of the material when expressed on an engineering stress-strain curve. The reason is, beyond the UTS there are local stress intensification leading to formation of necks and a consequent load drop due to a fast reduction of the cross sectional area. Subsequently the necked area experiences stress triaxiality and the specimen is no longer under a truly uniaxial load.

*True uniform strain ( $\epsilon_u$ )*: The uniform strain is the strain up to the maximum load (prior to necking), when the cross sectional area is  $A_u$ . The strain is given as

$$\epsilon_u = \ln \frac{A_0}{A_u} \quad (2.51)$$

*True Fracture strain ( $\varepsilon_f$ ):* The maximum true strain that the material can withstand before fracture. In a highly deformable or plastic material, the fracture strain is high. For brittle materials, the fracture strain is nearly the same as the uniform strain ( $\varepsilon_u$ ).

$$\varepsilon_f = \ln \frac{A_0}{A_f} = \ln \left( \frac{1}{1-q} \right) \quad (2.52)$$

*True local necking strain ( $\varepsilon_n$ ):* The true local necking strain is the difference between  $\varepsilon_f$  and  $\varepsilon_u$  which can be estimated from the cross sectional area  $A_u$  when the load is maximum. The relationship of fracture strain and uniform strain are given below:

$$\varepsilon_n = \varepsilon_f - \varepsilon_u = \ln \frac{A_u}{A_f} \quad (2.53)$$

*Strain hardening exponent ( $n$ ):* The stress-strain behaviour of materials which is represented by the stress-strain curve has three regions. The first region up to the yield point, is the elastic region; the next region is the uniform plastic deformation region up to UTS, and beyond this and up to fracture is the unstable plastic deformation region. In the uniform plastic region, the true stress-strain curve can be expressed using simple power curve relation given as

$$\sigma = K_x \varepsilon^n \quad (2.54)$$

where  $n$  is the strain hardening exponent and  $K_x$  is the strength co-efficient. The strain hardening exponent is found to be equal to true uniform strain  $\varepsilon_u$ .

*Hardness ( $H_v$ ):* This property implies resistance to permanent or plastic deformation for a material. Hardness can be of different types. Here indentation hardness is addressed and the test to measure hardness is called Vickers hardness. The standard test method generates Vickers hardness ( $H_v$ ) which is given as

$$H_v = \frac{1.854F}{L_x^2} \quad (2.55)$$

where  $F$  is the applied load and  $L_x$  is the average length of the diagonals of the indent produced by the square base diamond pyramid indenter.

## 2.6.2 Fracture properties

Fracture properties presented in this section are  $K_{IC}$ , fracture toughness for brittle material,  $J_{IC}$ , fracture toughness for ductile material estimated from experimental  $J$ - $R$  curve often called  $R$ -curve and impact toughness ( $K_d$ ).

Cracks or defects in materials are responsible for stress intensification. The stress fields ahead of the crack tip at distance at point X with polar co-ordinate  $(r, \theta)$  and crack tip radius  $\rho$  shown in Figure 2.22 can be given as

$$\left. \begin{aligned} \sigma_x &= \frac{K_I}{\sqrt{2\pi r}} f_x(\theta, \rho) \\ \sigma_y &= \frac{K_I}{\sqrt{2\pi r}} f_y(\theta, \rho) \\ \tau_{xy} &= \frac{K_I}{\sqrt{2\pi r}} f_{xy}(\theta, \rho) \end{aligned} \right\} \quad (2.56)$$

where  $\sigma_x, \sigma_y$  and  $\tau_{xy}$  are the normal and shear components of 2D stress fields and  $K_I$  is the mode I stress intensity factor.

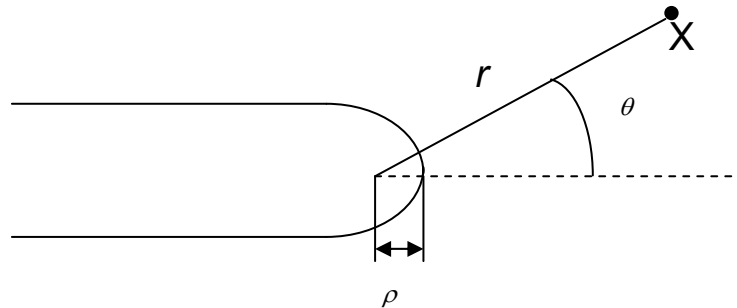


Figure 2.22: Crack tip with tip radius  $\rho$

Ahead of the crack tip, there are three zones which signify three different fracture mechanisms. Figure 2.23 shows the three distinct stress intensification zones ahead of the crack tip. Just ahead of the crack tip, there is the region of intense plastic zone which is called fracture process zone (FPZ). The next region is the plastic zone (PZ) and beyond this is the elastic zone (EZ). When there is very insignificant plastic deformation or yielding in the material ( $EZ \gg PZ$ ), the fracture is in the linear elastic fracture mechanics (LEFM) domain. For large plastic zone ( $PZ \gg EZ$ ), the fracture is governed by the elastic plastic fracture mechanic (EPFM) principles.

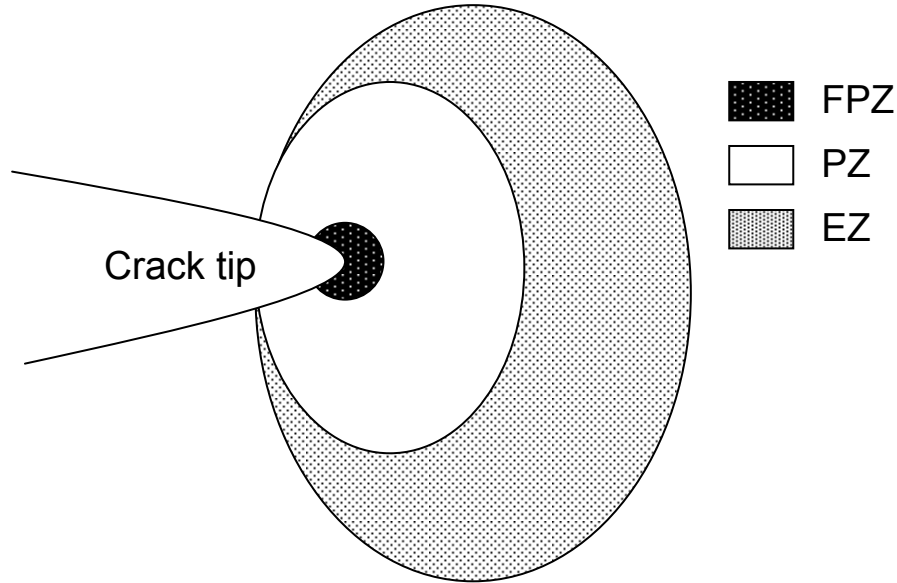


Figure 2.23: Three distinct zones ahead of the crack tip

Mainly two types of fracture have been found in various materials, i.e., *cleavage fracture* and *ductile fracture*. Cleavage fracture generally occurs through formation of steps like cleaves. Since a cleavage fracture is usually associated with little plastic deformation, it is called brittle fracture. But the term brittle fracture is often generalised to all fractures with little plastic deformation, although the final separation may occur in a ductile manner. Ductile fracture generally occurs when the PZ is significantly large.

In case of brittle fracture, PZ is insignificant compared to the EZ and the fracture toughness [83] is expressed by the following equation

$$K_C = \sigma_c \sqrt{\pi a_c} f\left(\frac{a_c}{W}\right) \quad (2.57)$$

where  $\sigma_c$  is the critical stress,  $a_c$  is the critical crack length at which the specimen has fractured and  $f(a_c/W)$  is a factor related to the geometry of the specimen having width,  $W$ . Typical three point bend (TPB) geometry is shown in Figure 2.24.

For ductile fracture,  $J$ -integral (fracture energy per unit crack extension) is defined as the strain energy ( $dU$ ) required for an infinitesimal crack ( $da$ ) to grow

$$J = -\frac{dU}{B.da} \quad (2.58)$$

where  $B$  is the thickness of the specimen. The  $J$  signifies the fracture resistance of a material in the EPFM domain.

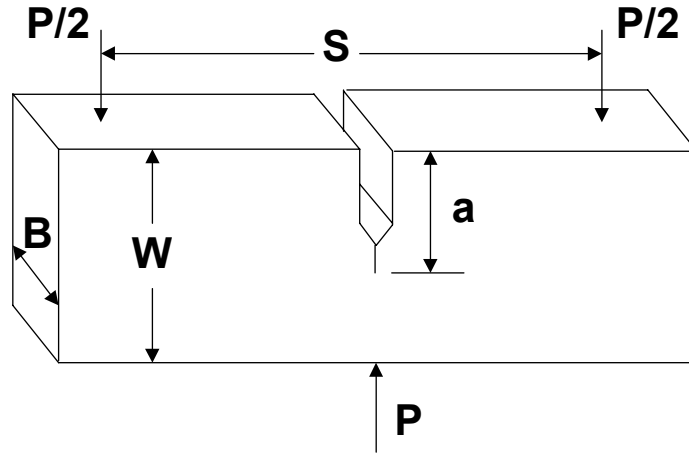


Figure 2.24: Typical three point bend (TPB) geometry

The fracture behaviour of a material including crack initiation and propagation can be described by the  $R$ -curve which is essentially  $J$  versus  $da$  (extension of crack length) plot. This method provided a way to analyze fracture behaviour of an elastic-plastic (ductile) material. The ASTM [84] procedure for  $J$ - $R$  analysis divides  $J$ -resistance of a material into elastic and plastic components:

$$J_R = J_{el} + J_{pl} \quad (2.59)$$

where the elastic component  $J_{el}$  is given by

$$J_{el} = \frac{K_a^2 (1 - \gamma)}{E} \quad (2.60)$$

where  $K_a$  is the stress intensity factor for crack length  $a$  determined by equation (2.57),  $\gamma$  is the Poisson's ratio and  $E$  is the modulus of elasticity. The  $J_{pl}$  is determined for TPB specimen using

$$J_{pl} = \frac{2A}{Bb} \quad (2.61)$$

where,  $A$  is the area under load-displacement curve during the  $J$ -integral test,  $b$  is the remaining ligament ( $W-a$ ) of the specimen. Typical load displacement curve and corresponding  $R$  curve are shown in Figure 2.25.

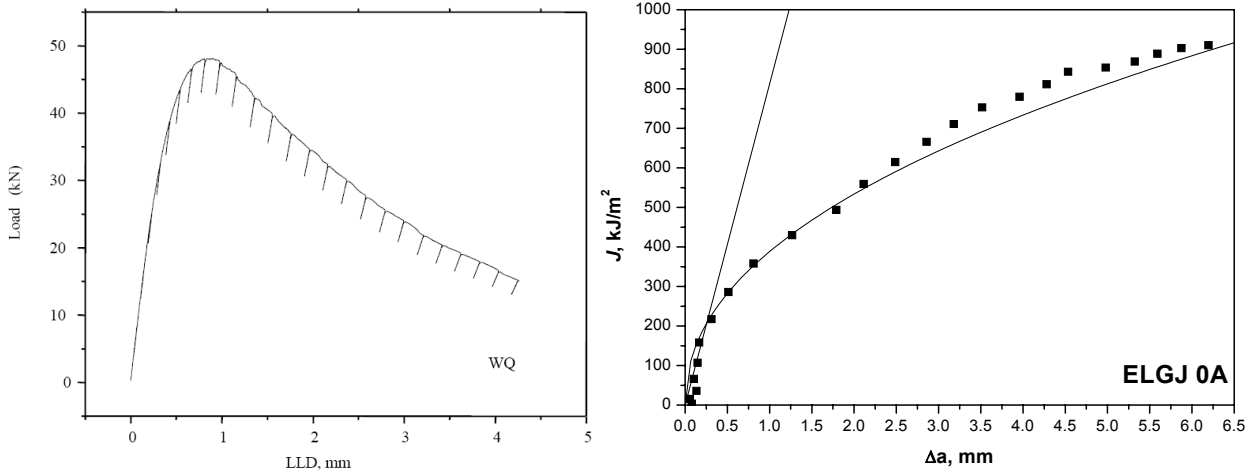


Figure 2.25: Load-displacement plot and corresponding J-R curve. LLD stands for load line displacement.

When  $K_c$  and  $J_c$  satisfy some predefined criteria related to minimum specimen size requirement [82,83], they are called  $K_{IC}$  and  $J_{IC}$  fracture toughnesses of brittle and ductile materials respectively. While  $J_{IC}$  denotes the energy required for a crack to initiate propagation,  $K_{IC}$  is related to the critical stress and critical crack length at fracture.

The ductile fracture toughness,  $J_{IC}$  is correlated with the micro structural parameters like characteristics length,  $l_0$ , which is the average spacing between microvoids ahead of the crack tip, local fracture strain,  $\epsilon_f^*$  and yield stress,  $\sigma_y$ . The correlation [80] is given as

$$J_{1C} = \sigma_y \epsilon_f^* l_0 \quad (2.62)$$

The above equation shows the scaling behaviour of the  $J_{IC}$  fracture toughness, since the available local strain energy is scaled down by the factor  $l_0$ . Thus selection of scale or ruler for the measurement of  $l_0$  plays a crucial role for the determination of  $J_{IC}$  from the microstructural parameters.

Impact toughness test is performed to determine the tendency of a material to behave in a brittle manner. Charpy V-notch specimen type is often used for the impact toughness test. The specimen is forced to bend and fractured at a high strain rate of the order of  $10^3$  /sec by a heavy swinging pendulum. The result obtained by the impact toughness test is the energy absorbed in fracturing the specimen. The energy absorbed in fracture is read from the calibrated instrumented tester. The toughness measured by the impact toughness test often referred to as the Charpy test known as  $C_v$  impact toughness, and is usually expressed in joules.

## 2.7 Micro structural image

To reveal microstructural features in materials, images of the material surfaces are captured using optical and electron microscopes. A typical microstructure of metallic materials may contain one or some of the following:

- Grains and grain boundaries
- Crystallographic orientations
- Defects in the form of dislocations (line defects), slip bands, porosities, micro cracks
- Coherent and/or incoherent precipitations
- Grain boundary precipitations
- Second phase particles

Figure 2.26 shows the schematic of microstructural features [84] in metallic materials. Each of these features has effect on mechanical as well as fracture properties of materials. The Hall-Petch relation [85,86] is the most popular structure-property correlation mentioned in the previous chapter.

Crystallographic orientations refer to the relative orientations of crystallite grains, the collective nature of which is often called texture. Grain orientations may manifest as low angle grain boundaries (LAGB) and high angle grain boundaries (HAGB). Since strain is caused by smooth motion of dislocations (unit of defects), HAGB impedes dislocation motion, for which ductility is reduced and strength increases.

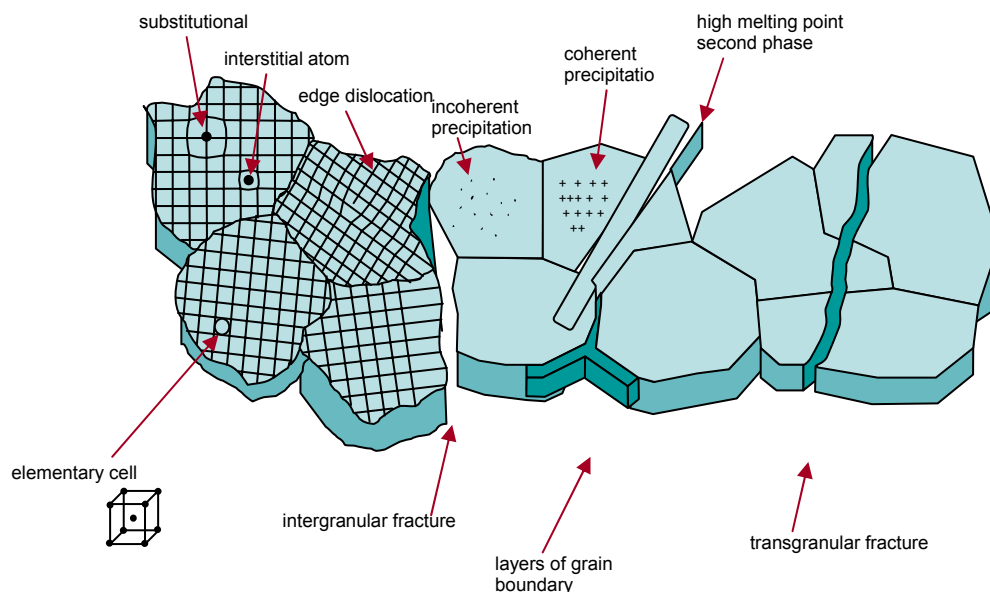


Figure 2.26: Microstructural constituents [84]

Coherent, incoherent (coarse) and grain boundary precipitations as well as second phase particles alter the mechanical as well as morphological properties in metallic materials. Addition of alloying elements, heat treatment, cooling rate, *etc.*, control the precipitation mechanisms, dispersion of second phase particles and formation of new phases, which create materials with new microstructural compositions and properties.

### 2.7.1 Microstructure phases of steel

For steel, different morphological structures like austenite, pearlite, bainite, ferrite, cementite (iron carbide) and martensite are formed depending upon the cooling rate. These phases occur depending upon the temperature and solubility of carbon (in weight percent) in iron. The temperature vs solubility of carbon showing various phases are known as iron-carbon phase diagram shown in Figure 2.27 up to 1000°C. Morphological characteristics of these phases are shown in the figure in five distinct regions (A to E). There are four critical temperatures for pure iron:  $A_1$  temperature (723°C) when eutectoid reaction occurs,  $A_2$  (769°C) temperature when iron changes from ferro-to paramagnetic condition,  $A_3$  temperature(910°C) when alpha iron transform to gamma iron, and  $A_4$  temperature (1390°C) at which gamma iron transforms to delta iron. Solubility of carbon is higher in austenite than ferrite in a given temperature. Addition of alloying elements in steel changes the iron-carbon diagram by altering the critical temperatures and phases.

Austenite (or gamma phase iron) is a metallic non-magnetic solid solution of iron [87]. In plain-carbon steel, austenite exists above the critical eutectoid temperature of 723°C; other alloys of steel have different eutectoid temperatures. The rate of cooling determines the phases that will occur in the final microstructure as shown in Figure 2.28. Slow cooling transforms austenite into pearlite phase which is the combination of ferrite, cementite and a proeutectoid phase that forms (on cooling) before the eutectoid austenite decomposes. Depending upon the carbon content in the steel, microstructure will be either ferrite-perlite (A) or perlite-cementite (B). Moderate cooling transforms austenite into bainite phase which is the combination of ferrite and cementite and it forms between 250-550°C. Bainite also occurs during athermal treatments at cooling rates too fast for pearlite to form, yet not rapid enough to produce martensite.

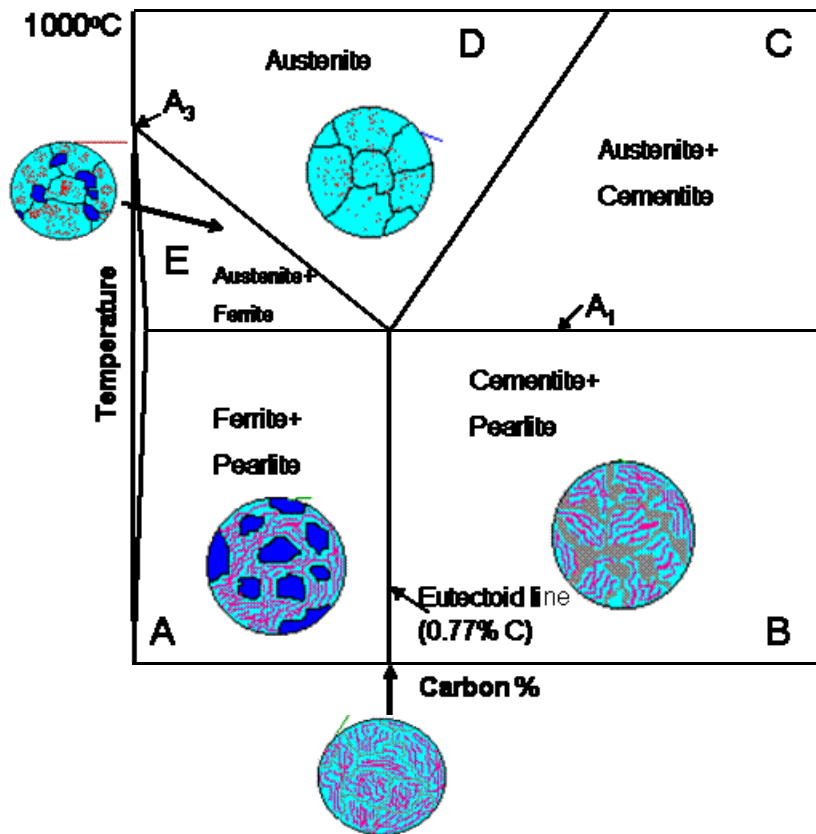


Figure 2.27: Iron-carbon phase diagram up to 1000°C  
 (Source: <http://www.rmutphysics.com/CHARUD/scibook/crystal-structure/iron%20section.htm>)

The martensite is formed by rapid cooling (quenching) of austenite which traps carbon atoms that do not have time to diffuse out of the crystal structure [88]. Thus it forms by a sudden diffusionless shear process. This martensitic reaction begins during cooling when the austenite reaches the martensite start temperature ( $M_s$ ) and the parent austenite becomes mechanically unstable. At a constant temperature below  $M_s$ , a fraction of the parent austenite transforms rapidly, then no further transformation will occur. When the temperature is decreased, more of the austenite transforms to martensite. Finally, when the martensite finish temperature ( $M_f$ ) is reached, the transformation is complete. In practice, depending upon the alloying element, a small proportion of austenite is retained in the matrix which is called retained austenite. Reheating of martensite generates tempered martensite which is again shown as a combination of ferrite and cementite phase (Figure 2.29).

Microstructural phases of steel described above have different mechanical properties. For example martensite alone is harder than austenite. Desired mechanical properties can be obtained by combining two or more phases which create new morphological structures. The effect of these phases on mechanical properties like strength and ductility is shown in Figure 2.30. By

selecting appropriate cooling rate, carbon content and alloying elements in iron, steel with desired mechanical properties can be obtained.

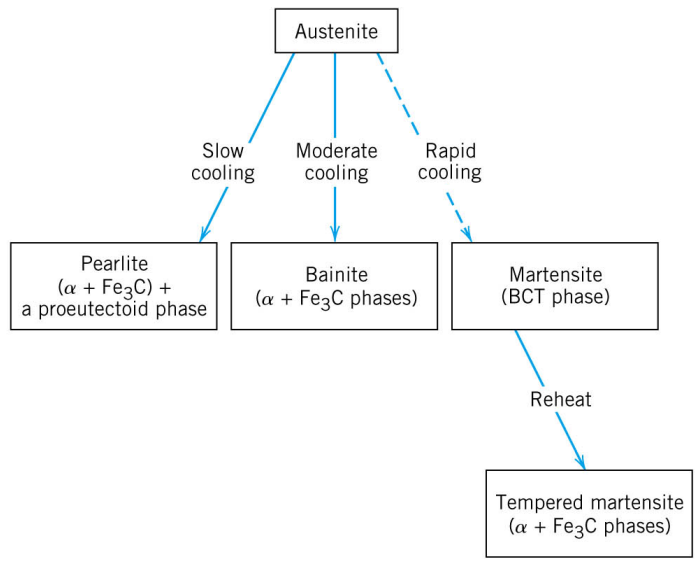


Figure 2.28: Various phases of steel [89]

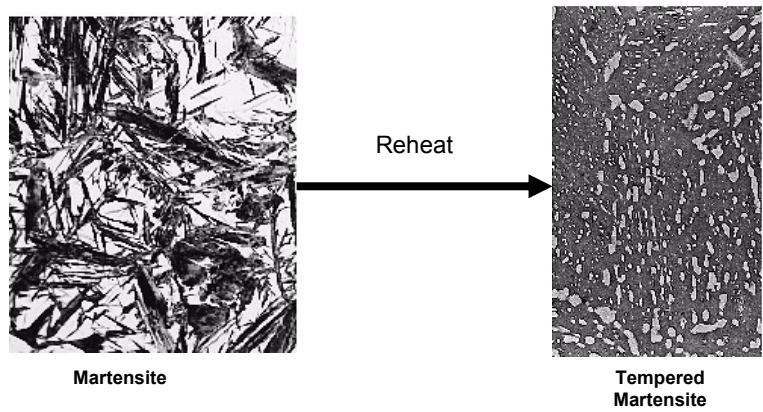


Figure 2.29: Reheating transform martensite into tempered martensite

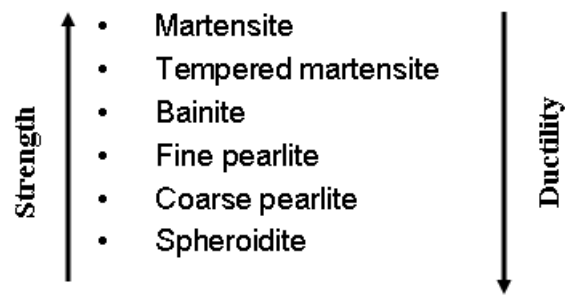


Figure 2.30: Phases of steel and their effect on mechanical properties

## 2.8 Fractographic images

For analyzing and assessing various fracture mechanisms, high resolution images of fractured surfaces are used. These surfaces may be created after fracturing standard specimens in the laboratory, primarily to investigate the fracture mechanisms. The fracture surfaces, obtained as a result of catastrophic failure of engineering components, may be used for failure analysis. Fracture surface can be viewed in macroscale and microscale. At different length scales, different fracture features are revealed which corresponds to various operative fracture mechanisms. Depending upon the crack path, fracture mechanism is classified into two broad groups: Transgranular fracture and Intergranular fracture. Cleavage or brittle fracture and ductile fracture are types of transgranular fracture, when the crack path breaks through the grains. Intergranular fracture takes place due to grain boundary separation. Figure 2.31 shows SEM fractographs of transgranular and intergranular fractured surfaces. While the crack path corresponding to the ductile fracture is found to be less tortuous, this is not so for intergranular fracture when grains have HAGB. Effect of crack path tortuosity on the energy required for crack initiation and growth is being investigated by fractal analysis of crack path geometry.

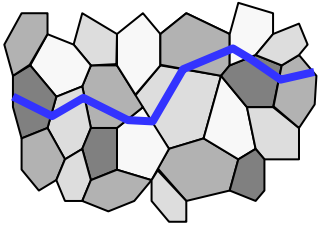
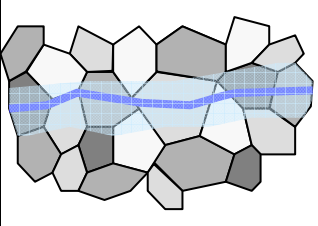
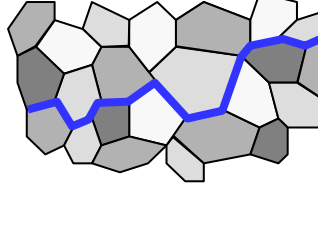
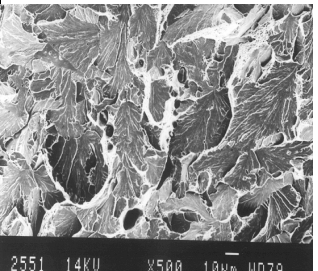
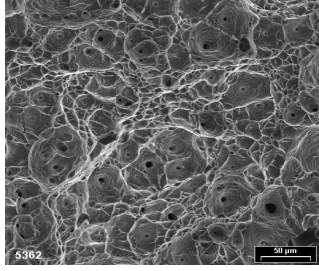
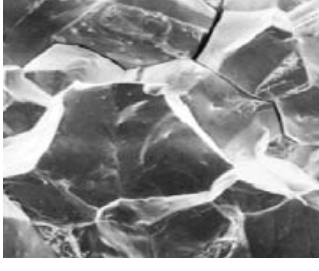
Type	Cleavage fracture	Ductile fracture	Intergranular fracture
Schematic			
SEM Fractographs			

Figure 2.31: Morphology of fractographs

## 2.9 Magnetic Barkhausen Emission Signal

Magnetic Barkhausen Emission (MBE) signals are the time domain burst type signals. This emission occurs in a ferromagnetic material when it is subjected to varying magnetizing force. This phenomenon is known as Barkhausen effect [90] and the emission is also called Magnetic Barkhausen Noise (MBN). To observe Barkhausen effect and to acquire MBN signal, a ferromagnetic material, wound by surface pick-up coil, is magnetized by an electromagnet at a certain magnetizing frequency typically in the range of 0.2 Hz to 50Hz. The detected pick-up voltage is then amplified and filtered using band pass filter, which is then sent to the data acquisition card of a computer for storage and analysis. Typical Barkhausen Emission signals, shown in Figure 2.32, are like acoustic signals. These signals are essentially magnetic noise, which is produced due to the abrupt jump causing the stepped increments in the B-H curve. The burst is maximum at the coercivity point ( $H_c$ ), when the flux density ( $B$ ) is zero and the change of flux density due to the applied magnetic field is maximum. The width of the burst corresponds to the width of the hysteresis loop.

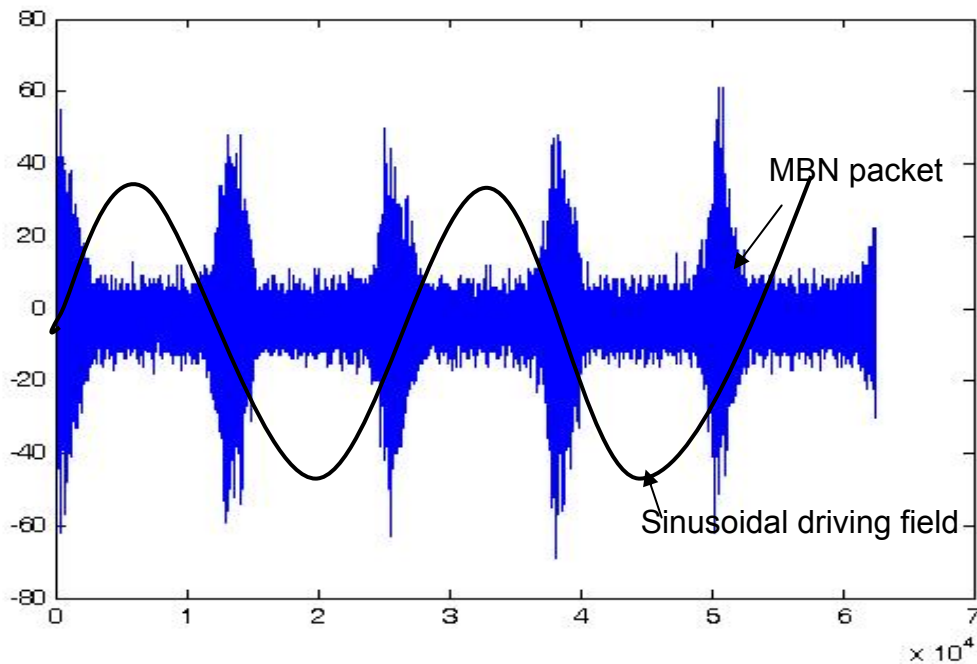


Figure 2.32: Packets of MBE signal

A typical magnetization curve showing the effect of the magnetic field,  $H$  on the magnetization strength  $M$  or  $B$ , is illustrated in Figure 2.33 along with the acquired MBE signal. The magnetization strength is the magnetic dipole moment per unit volume of the specimen which is

the function of magnetic flux density  $B$ . The apparently smooth continuous curve looks stepped [91] when examined more closely as shown in inset of Figure 2.33(a). The Barkhausen effect causes small, discontinuous changes of  $M$  or  $B$  as  $H$  varies.

During magnetization, a large number of magnetic moments align in one direction in small regions called domains. The region between two domains having opposite domain orientations is known as domain wall (DW) shown in Figure 2.34. Each DW consists of several hundred atom layers where the magnetic orientation is random. When a magnetic field is applied, domains favourably aligned with the field, tend to grow by domain wall motion at the expense of the unfavourably aligned domains. The amount of growth or the distance, that a domain wall travels, depends on the strength and direction of applied magnetic field, microstructures, composition and stress state of the material.

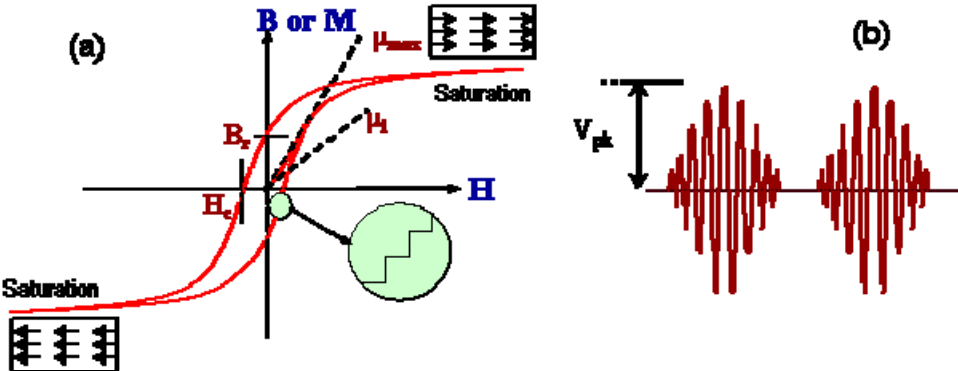


Figure 2.33 : (a) Magnetic hysteresis loop showing important properties, Remanence ( $B_r$ ), Coercivity ( $H_c$ ), initial permeability ( $\mu_i$ ) and maximum differential permeability ( $\mu_{max}$ ) (b) Magnetic Barkhausen emissions signal for full magnetizing cycle

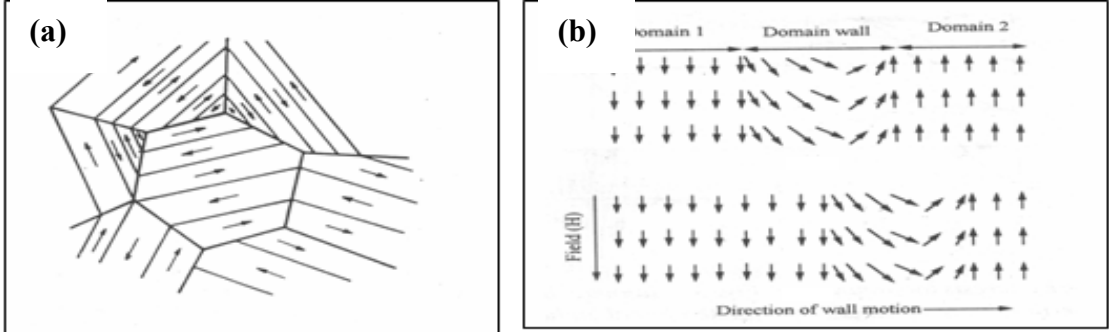


Figure 2. 34: (a) Schematic representation of magnetic domain in polycrystalline materials like steel (b) the movement of the domain wall under applied magnetic field

During magnetization, the movement of domain walls is obstructed or pinned by the presence of grain boundaries, second phase particles, and non-metallic inclusions in ferromagnetic materials. Presence of these microscopic obstacles keeps the flux density invariant even when the magnetizing force ( $H$ ) is increased. When the applied  $H$  is sufficiently large, which can overcome the effect of the obstruction, unpinning of DWs take place and the material gets magnetized. This causes the stepped hysteresis loop when seen at a microscopic level.

Since the characteristics of MBE signals are related to the microstructural features, which control the mechanical properties of material, the signal can be used for quantifying internal stress [92-96] and extent of damage in a material due to the variation in the service conditions, like stress, temperature or aggressive environment under which the material is operational. Thus characterization of MBE is proven to be a useful non-destructive evaluation tool for magnetic materials.

## 2.10 References

1. B. B. Mandelbrot: *The Fractal Geometry of Nature*, 1983, W. H. Freeman, New York.
2. James Gleick: *Chaos: Making a New Science*, 1987, Viking Penguin, New York.
3. A. Yavari, S. Sarkani and E.T. Moyer: The mechanics of self-similar and self-affine fractal cracks, *International Journal of Fracture*, 114, 1, 1-27 (2002).
4. H. E. Hurst: Long term storage capacity of reservoirs, *Trans. Am. Soc. Civil Eng.* 116, 770 – 808 (1951).
5. Weisstein, Eric W. "Fractal Dimension." From *MathWorld*--A Wolfram Web Resource. <http://mathworld.wolfram.com/FractalDimension.html>.
6. K. Falconer: *Fractal geometry- Mathematical Foundations and Applications*, John Wiley & Sons Ltd., Baffins Lane, Chichester, West Sussex PO19 1UD, England (1990).
7. J. E. Hutchinson: Fractals and Self-similarity, *Indiana Univ. Math. J.*, 30, 713-747(1981).
8. O.I. Yordanov and I.S. Atanasov: Self-affine random surfaces, *Eur. Phys. J. B* 29, 211–215 (2002).
9. Fractal. (2008, May 30). In *Wikipedia, The Free Encyclopedia*. Retrieved 10:25, June 5, 2008, from <http://en.wikipedia.org/w/index.php?title=Fractal&oldid=215876991>.

10. Hurst exponent. (2008, January 28). In *Wikipedia, The Free Encyclopedia*. Retrieved 10:27, June 5, 2008, from [http://en.wikipedia.org/w/index.php?title=Hurst\\_exponent&oldid=187539864](http://en.wikipedia.org/w/index.php?title=Hurst_exponent&oldid=187539864).
11. H. E. Hurst, R. P. Black, Y. M. Simaika: *Long-Term Storage: An Experimental Study*, Constable, London, 1965.
12. Xinxia Jiang: *Fractal analysis of topography and reflectance surfaces*, PhD thesis, 1998, University of Southampton, UK.
13. B. B. Mandelbrot and J. R. Wallis: Some long-run properties of geophysical records, *Water Resour. Res.*, 5, 321 – 340 (1969).
14. J. K. Weissel, L. F. Pratson and A. Malinverno: The length-scaling property of topography, *J. Geophys. Res.*, 99, B7, 13997-14012 (1994).
15. A. Balankin: Physics of fracture and mechanics of self-affine cracks, *Engineering Fracture Mechanics*, 57, 2/3, 135 – 203(1997).
16. N.C. Kenkel and D.J. Walker:  
<http://www.umanitoba.ca/faculties/science/botany/LABS/ECOLOGY/FRACTALS/fractal.html>.
17. John Hitchcock: <http://www.cs.uwyo.edu/~jhitchco/bib/dim.shtml>.
18. F. Normant and C. Tricot: Methods for evaluating the fractal dimension of curves using convex hulls, *Phys. Rev. A*, 43, 6518-6525(1991).
19. G. Sugihara and R.M. May: Applications of fractals in ecology, *Trends Ecol. Evol.*, 5, 79-86(1990).
20. C. Kent and J. Wong: An index of littoral zone complexity and its measurement, *Can. J. Fish. Aquat. Sci.*, 39, 847-853(1982).
21. J.A. Wiens: Spatial scaling in ecology, *Funct. Ecol.* 3, 385-397(1989).
22. S.K. Hamilton, J.M. Melack, M.F. Goodchild and W.M. Lewis: Estimation of the fractal dimension of terrain from lake size distributions. 1992, In: P.A. Carling and G.E. Petts (eds.). *Lowland floodplain rivers: geomorphological perspectives*. pp. 145-163. J. Wiley and Sons, New York.
23. N.C. Kenkel and D.J. Walker: Fractals and ecology, *Abst. Bot.*, 17, 53-70(1993).

24. P.A. Longley and M. Batty: On the fractal measurement of geographical boundaries, *Geogr. Anal.*, 21, 47-67(1989).
25. H.-O. Peitgen, H. Jürgens and D. Saupe: *Fractals for the classroom*, 1992 Springer, New York.
26. S. Appleby: Multifractal characterization of the distribution pattern of the human population, *Geographical Analysis* 28,147-160(1996).
27. J. Tatsumi, A. Yamauchi and Y. Kono: Fractal analysis of plant root systems, *Ann. Bot.*, 64, 499-503(1989).
28. B.T. Milne: Spatial aggregation and neutral models in fractal landscapes, *Am. Nat.* 139, 32-57(1992).
29. C.C. Taylor and S.J. Taylor: Estimating the dimension of a fractal, *J. R. Statist. Soc B*, 53, 353-364(1991).
30. Nirupam Sarkar and B. B. Chaudhuri: An efficient approach to estimate fractal dimension of textural images, *Pattern Recognition*, 25, 9, 1035–1041(1992).
31. C. S. Pande, L. R. Richards and S. Smith: Fractal characteristics of fractured surfaces, *J Mater Sci Lett*, 6, 295-302(1987).
32. D. A. Lange, H. M. Jennings and S.P. Shah: Analysis of surface roughness using confocal microscopy, *J Mater Sci*, 28, 3879-3884(1993).
33. T. G. Smith, W. B. Marks, G. D. Lange, W. H. Sheriff, and E. A. Neale: A fractal analysis of cell images, *Journal of Neuroscience Methods*, 27, 173–180(1989).
34. B.B. Mandelbrot, D.E. Passoja and A.J. Paullay: Fractal character of fracture surfaces of metals, *Nature*, 308, 721-722(1984).
35. Z.H. Huang, J. F. Tian and Z.G. Wang: A study of the slit island analysis as a method for measuring fractal dimension of fractured surface, *Scripta Metall Mater*, 24, 967-972(1990).
36. P. McAnulty, LV Meisel, PJ Cote: Hyperbolic distributions and fractal character of fracture surfaces, *Phys Rev, A* 46, 63523-63526(1992).
37. A. Imre: Problems of measuring the fractal dimension by the slit-island method, *Scripta Metall Mater*, 27, 1713-1716(1992).

38. Hui Su and Zhenqi Yan: Fractal analyses of microstructure and properties of HSLA steels, *Journal of Materials Science Letters*, 14, 1436-1439 (1995).
39. J. C. Hsiung and Y. T. Chou: Fractal characterization of the fracture surface of a high-strength low-alloy steel, *Journal of Materials Science*, 33, 2949- 2953(1998).
40. Lucas M'aximo Alvesa, Rosana Vilarim da Silvab , Bernhard Joachim Mokross: Influence of crack fractal geometry on elastic–plastic fracture mechanics, *Physica A* 295, 144–148(2001).
41. Sérgio Francisco dos Santos and José de Anchieta Rodrigues: Correlation Between Fracture Toughness, Work of Fracture and Fractal Dimensions of Alumina-Mullite-Zirconia Composites, *Materials Research*, 6, 2, 219-226(2003).
42. R.F. Voss: Fractals in nature:from characterization to simulation. In: Peitgen, H.-O. and D. Saupe (eds.).*The science of fractal images*. pp. 21-70(1988) Springer, New York.
43. James M. Keller and Susan Chen: Texture description and segmentation through fractal geometry, *Computer Vision, Graphics, and Image Processing*, 45, 2, 150–166(1989).
44. B.T. Milne: Measuring the fractal geometry of landscapes, *Appl. Math. Comp.* 27: 67-79(1988).
45. P. Grassberger and I. Procaccia: Characterization of strange attractors. *Phys. Rev. Letters* 50, 346-349(1983).
46. I. Scheuring and R.H. Riedi: Application of multifractals to the analysis of vegetation pattern, *J. Veg.Sci.*, 5, 489-496(1994).
47. J.D. Farmer, E. Ott and J.A. Yorke: The dimension of chaotic attractors, *Physica 7D*, 153-180(1983).
48. H.G.E. Hentschel and I. Procaccia: The infinite number of generalized dimensions of fractals and strange attractors, *Physica 8D*, 435-444(1983).
49. W.C. Strahle, R.K. Sigman, W.L. Meyer: Stagnating turbulent flows. *AIAA J*, 25, 1071–1077( 1987).
50. M.S. Taqqu, V. Teverovsky, W. Willinger: Estimators for long-range dependence: An empirical study, *Fractals*, 3, 785–798( 1995).

51. J. Beran, R. Sherman , M. S. Taquq, W. Willinger: Long-range dependence in variable-bit-rate video traffic, *IEEE T Commun* , 43,1566–1579( 1995).
52. Chun-Feng Li: Rescaled –range and power spectrum analyses on well-logging data, *Int. Journal of Geophysics*, 153, 201-212(2003).
53. Michael R. King: Fractal analysis of eight glacial cycles from an Antarctic ice core, *Chaos, Solitons and Fractals*, 25, 5–10(2005)
54. H. E. Hurst, R. P. Black, Y. M. Simaika: *Long-Term Storage: An Experimental Study*, Constable, London, 1965.
55. M. V. Berry and Z. V.Lewis: On the Weierstrass-Mandelbrot fractal function, *Proc. Roy. Soc. London, Ser. A.*, 370, 459-484(1980).
56. S.M. Kay and S.L. Marple: Spectral analysis- a modern perspective, *Proceedings of IEEE* 69, 1381–1419(1981).
57. A. P Pentland: Fractal-Based Description of Natural Scenes, *IEEE Trans. Pattern Anal. Machine Intell.*, 6, 661–674(1984).
58. S. R. Brown and C. H. Scholz : Broad bandwidth study of the topography of natural rock surfaces. *Jour. Geophys. Res.*, 90, B14, 12575-12582(1985).
59. J. S. Y.Wang , T. N.Narasimhan and C. H. Scholz: Aperture correlation of a fractal fracture. *Jour. Geophys. Res.*, 93, B3, 2216-2224 (1988).
60. M.F. Barnsley, R.L. Devaney, B.B. Mandelbrot, H.O. Peitgen, D. Saupe, R.F. Voss: *The Science of Fractal Images*, 1988, Springer-Verlag, New York.
61. D. L. Turcotte: *Fractals and chaos in geology and geophysics*, 1992, Cambridge University Press, New York.
62. J. R.Carr: *Numerical Analysis for the Geological Sciences*, 1995, Prentice Hall, Inc, NJ.
63. Rajat Bindlish and Paula Barros: Aggregation of digital terrain data using a modified fractal interpolation scheme: *Computers & Geosciences*, 22, 8, 907-917(1996).
64. A.A. Likhachev, J. Pons, E. Cesari, A.Yu. Pasko, V.I. Kolomytsev: Observation and analysis of scaling behaviour in surface martensite-austenite relief during the reverse martensitic transformation in Cu-Al-Ni single crystal by using 2D Fourier processing method, *Scrip. Mat*, 43, 765-769(2000).

65. Ernesto Trujillo, Jorge A. Ramírez, and Kelly J. Elder: Topographic, meteorologic, and canopy controls on the scaling characteristics of the spatial distribution of snow depth fields, *Water Resources Research*, 43, W07409, doi:10.1029/2006WR005317(2007).
66. A. Arneodo, E. Bacry and J.F. Muzy: The thermodynamics of fractals revisited with wavelets, *Physica A*, 213, 232–275(1995).
67. C.J. Jones, G.T. Loneragan and D.E. Mainwaring: Wavelet packet computation of the Hurst exponent. *Journal of Physics A*, 29, 2509–2527(1996).
68. I. Simonsen, A. Hansen, O.M. Nes: Determination of the Hurst exponent by use of wavelet transforms, *Physical Review E*, 58, 2779–2787(1998).
69. Fausto Espinal, Bjorn D. Jawerth, Toshiro Kubota: Wavelet-based fractal signature analysis for automatic target recognition, *Opt. Eng.*, 37, 1, 166–174(1998).
70. Ashutosh Chamoli, Abhey Ram Bansal and V.P. Dimri: Wavelet and rescaled range approach for the Hurst coefficient for short and long time series, *Computers & Geosciences*, 33, 83–93 (2007).
71. Ed Bullmore, Jalal Fadili, Voichita Maxim, Levent Xendur, Brandon Witcher, John Suckling, Michael Brammer and Michael Breakspear: Wavelets and functional magnetic resonance imaging of the human brain, *NeuroImage*, 23, S234–S249(2004).
72. S. Soltania, P. Simarda and D. Boichub: Estimation of the self-similarity parameter using the wavelet transform, *Signal Processing*, 84, 117 – 123(2004).
73. Stilian Stoev, Murad S Taqqu, Cheolwoo Park and J.S. Marron: On the wavelet spectrum diagnostic for Hurst parameter estimation in the analysis of Internet traffic, *Computer Networks*, 48, 423–445 (2005).
74. A.L. Wang, C.X. Yang and X.G. Yuan: Evaluation of the wavelet transform method for machined surface topography I: methodology validation, *Tribology International*, 36, 517–526 (2003).
75. A.L. Wang, C.X. Yang, X.G. Yuan: Evaluation of the wavelet transform method for machined surface topography 2: fractal characteristic analysis, *Tribology International*, 36, 527–535(2003).
76. O. .C. Wells, A. Boyde, E. Lifshin, A. Rezanowich: *Scanning Electron Microscopy*, 1974, McGraw-Hill Book Company, USA.

77. M. A. Hayat, Principles and Techniques of Scanning Electron Microscopy-Biological applications, 1974, Van Nostrand Reinhold Company, New York.
78. B.K.P. Horn, and M.J. Brooks: Shape from shading, MIT Press, Cambridge Massachusetts, 1989 ISBN 0-262-08183-0  
[http://people.csail.mit.edu/bkph/articles/Shape\\_from\\_Shading.pdf](http://people.csail.mit.edu/bkph/articles/Shape_from_Shading.pdf)
79. Rafael C. Gonzalez, Richard E. Woods: 'Digital Image Processing', 2002, 2nd Edition Pearson Education (Singapore) Pvt Ltd. India
80. G. E. Dieter: Mechanical Metallurgy, SI Metric Edition/adapted by David Bacon, 1988 McGraw-Hill Book Company, UK.
81. David Broek: Elementary Engineering Fracture Mechanics, Third revised edition, 1982, Martinus Nijhoff Publishers, The Netherlands.
82. H. L. Ewalds and R.J.H. Wanhill: Fracture Mechanics, 1983, Edward Arnold (Publishers) Ltd, UK.
83. J. F. Knott: Fundamentals of Fracture Mechanics, 1973, Butterworth, London.
84. R. W. K. Honeycomb: Steels Microstructure and Properties, 1980, Edward Arnold (Publishers) Ltd, UK.
85. E. O. Hall: The deformation and aging of mild steel, Proc. Phys. Soc. London, 643, 747-753(1951).
86. N. J. Petch: The cleavage strength of polycrystals, J. Iron Steel Inst. London, 173, 25-28(1953).
87. Austenite. (2008, October 5). In *Wikipedia, The Free Encyclopedia*. Retrieved 07:23, October 23, 2008, from  
<http://en.wikipedia.org/w/index.php?title=Austenite&oldid=243278241>
88. Martensite. (2008, September 11). In *Wikipedia, The Free Encyclopedia*. Retrieved 12:45, October 22, 2008, from  
<http://en.wikipedia.org/w/index.php?title=Martensite&oldid=237739267>
89. [www.ims.uconn.edu/~alpay/Courses/MMAT%20201/Topic10-PhaseTransformations.ppt](http://www.ims.uconn.edu/~alpay/Courses/MMAT%20201/Topic10-PhaseTransformations.ppt)
90. Gianfranco Durin and Stefano Zapperi: The Barkhausen effect, arXiv:cond-mat/0404512v1 [cond-mat.mtrl-sci] "The Science of Hysteresis", vol. II, G. Bertotti and I. Mayergoyz eds, Elsevier, Amsterdam(2006)181.

91. D. C. Jiles: Review of magnetic methods for nondestructive evaluation, *NDT & E International*, 21, 5, 311-319( (1988).
92. M. Soultan, X. Kleber, J. Chicois and A. Vincent: Mechanical Barkhausen noise during fatigue of iron, *NDT&E International* 39, 493–498(2006).
93. E. S. Gorkunov, Yu. N. Dragoshanskii, and M. Mikhovski: Barkhausen Noise and Its Utilization in Structural Analysis of Ferromagnetic Materials (Review Article V). Effects of Volume and Surface Thermal Processing *Russian Journal of Nondestructive Testing*, 36, 6(2000) 389. Translated from *Defektoskopiya*, 6(2000) 3.
94. D.O’Sullivan, M.Cotterell, S.Cassidy, D.A. Tanner and I. M!esz!aros: Magneto-acoustic emission for the characterisation of ferritic stainless steel microstructural state, *Journal of Magnetism and Magnetic Materials* 271, 381–389 (2004).
95. A. Mitra, L.B. Sipahi, M.R. Govindaraju , D.C. Jiles and V.R.V. Ramanan : Effects of tensile stress on magnetic Barkhausen emissions in amorphous Fe-Si-B alloy, *Journal of Magnetism and Magnetic Materials* 153, 231-234 (1996).
96. R. D. McMichael, L.J. Swartzendruber and L. H. Bennett: Langevin Approach to Hysteresis and Barkhausen Modeling in Steel, *J. Appl. Phys*, 73, 5848-5850(1993).

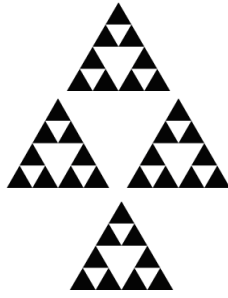


# CHAPTER 3

## **3.0 Fractal analysis of microstructure, fracture surface and magnetic Barkhausen signal: a brief review**

3.1	Fractal analysis of microstructures	69
3.2	Fractal analysis of fracture surfaces	72
3.3	Fractal analysis of magnetic Barkhausen emission signals	79
3.4	References	84





# 3

## **FRACTAL ANALYSIS OF MICROSTRUCTURE, FRACTURE SURFACE, AND BARKHAUSEN SIGNAL: A BRIEF REVIEW**

Over the last three decades, applications of fractal mathematics are found in various fields of science, engineering, arts, medicines, finance and commerce [1-5]. This chapter highlights fractal research carried out in material science with particular emphasis in the areas of quantitative metallography, fracture mechanics, and magnetic Barkhausen emission signal analysis.

### **3.1 Fractal analysis of microstructures**

Fractal analysis of microstructure is an advanced quantitative metallographic technique which may be needed when the standard practice is found inadequate to describe microstructures by standard parameters like particle diameter and spacing. The *Metals Handbook Desk Edition* [6] defines metallography as "The science dealing with the constitution and structure of metals and

alloys as revealed by the unaided eye or by such tools as low-powered magnification, optical microscopy, electron microscopy and diffraction or x-ray techniques."

While extensive research for characterizing fracture surfaces by fractal dimensions has been carried out in the last three decades, very little effort has been made to quantify microstructures of metallic surface by fractal dimensions. The reason may be that the preparation of metallic samples for viewing microstructural features is more an art than science. Since quality of microstructure depends upon the skill of the expert metallographers, finding out a reproducible quantifier for microstructure is a challenging task. Nevertheless research have been carried out for quantifying soil microstructures by fractal dimensions [7,8], characterizing textures in fabrics [9], tissue characterization [10], bone mass quantification and texture characterization[10,11], etc. The input data for the fractal analysis was clinical CT, X-ray radiography, optical microscopic and SEM images. In quantitative metallography, limited literature on fractal dimension for characterization of microstructure of metallic materials has been found. A review of these is presented here.

Spatial self-similarity, a subset of self-affine property, and scaling behavior are observed in microstructures of multiphase steel, and shape memory alloys [12-13]. Distribution of various phases and their morphological characteristics are responsible for the scaling and self-similar or fractals [14] like behaviour in microstructures. For example, the scaling properties of the distribution of martensite [15-16] indicate the macroscopic change in the material characteristics. Similarly an individual bainite sheaf in the microstructure of bainitic steel shows scaling properties since the topology of the interfaces is not smooth [14, 17]. Fractal nature of acicular ferrite, a highly sub-structured non-equiaxed ferrite, is evident for a range of more than one order of magnitude [18].

Figure 3.1 shows the fractal growth of martensite in steel which is similar to the fractal generation of Sierpinski triangles shown in Figure 3.2. It demonstrates that transformation from austenite to martensite starts at the austenite grain boundaries. The transformation begins at the martensite start temperature ( $M_s$ ) and is completed at the martensite finish temperature ( $M_f$ ). Distinguishable fractal pattern can be found in the third generation of the transformation, this would continue till the transformation is complete. During this period the fractal dimension will remain constant.

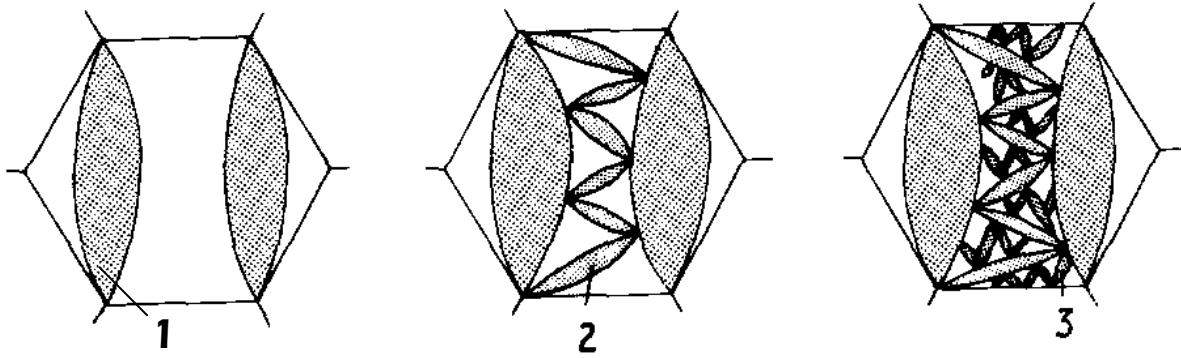


Figure 3.1: Fractal growth of martensite in steel [21]

Likhachev et al. [12] analysed optical images of microstructure of Cu-Al-Ni single crystal alloys and demonstrated that martensitic domain distribution in the image has two different scaling or frequency regions with a cross over point. The small spatial length scale (high frequency) region corresponds to the distribution of the self accommodating groups of plates and the large scale corresponds to the thickness distribution of martensitic crystals. Su et al [13] analysed optical images of the microstructures of ferrite-martensite steels by progressively aging the materials and obtained a positive correlation with the grain size. It was concluded by the authors that ferrite is fractal in nature.



Figure 3.2: Fractal generation of Sierpinski-triangle

In the review paper, Hornbogen [15] stressed that for representing microstructures by fractal dimensions, self similarity or self-affinity has to be established. It was highlighted that formation of martensitic microstructure undergoes fractal growth of different martensitic morphologies. For characterizing martensitic microstructure, it was pointed out that two fractal dimensions can be obtained. The dimension in between  $1.7 > D > 1.3$  characterizes true microstructure. However the second fractal dimension  $D < 1$  represent the length of the martensite crystals and the spacing of the islands of residual austenite. Colas [16] analyzed microstructure of different grain sizes for the AISI type 316L austenitic stainless steel and estimated fractal dimensions using box counting method. The fractal dimension was found to be varying inversely with the grain size. Similar correlation between fractal dimension and pearlite size was reported by Su et al [17] for HSLA

steel. The fractal dimensional increment  $D^*$  range was found to be 0.48-0.58. Using a different method, the same author obtained the range for  $D^*$  as 0.09-0.13; however the same positive correlation was obtained between the fractal dimension and pearlite size. For bainitic steel, it was reported by Kang and Bhadeshia [18, 19] that bainite sheaf, shown in Figure 3.3, has a fractal character with fractal dimensional increment 0.59.

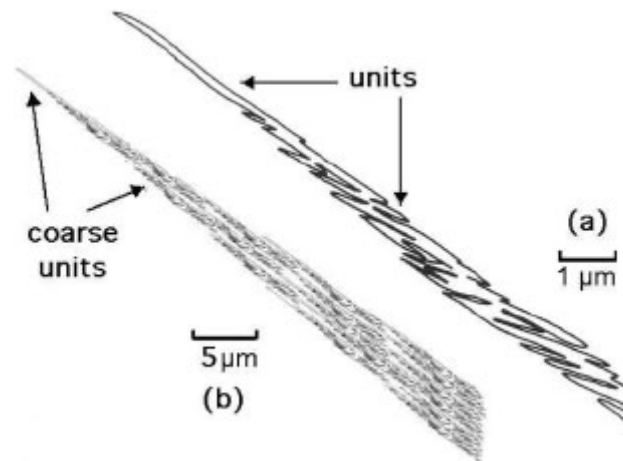


Figure 3.3: (a) Tracing diagram of a bainite sheaf (b) Regenerated a larger sheaf using (a) as unit (reproduced from ref[19])

Villegas et al investigated [20] fractal characteristics of acicular ferrite phase in medium carbon micro-alloyed forging steels. At different cooling rates, SEM images of microstructure were analysed and fractal dimensional increment  $D^*$  was obtained between 0.11 and 0.41. Skrotzki [21] characterized a martensitic microstructure of a Fe-Ni alloy by fractal analysis. The author used Sierpinski-triangle (Figure 3.2) to describe the stepwise transformation from austenite to martensite phase. Rybaczuk [22] proposed an approach employing fractal geometry to describe martensite phase in austenitic steel.

### 3.2 Fractal analysis of fracture surfaces

Fracture surfaces of metallic materials are rough. The extent of roughness depends upon the amount of surface energy used for creating the surface, and the availability of surface energy subsequently depends upon the mechanical properties of the materials. There can be dynamic variations of material properties due to various loading conditions and environment. Progressive changes in the materials thus affect the fracture mechanisms for which the fracture surface will

have morphological variations in terms of roughness and waviness. Since fractal dimension quantifies surface roughness, the dimension will vary with the loading history, environment and material being investigated. It has already been discussed in chapter 2 that fractal dimensions depend upon the methods by which the dimensional estimates are made. Different methods give different fractal dimensions for the same surface. With regard to the analysis of fracture surfaces, the most popular method was the slit island method (SIM) considering area-perimeter correlation. In fact SIM is the way to capture the surface elevation by progressively eliminating the surface coated with nickel or chromium for revealing new structural features. Table 3.1 summarizes the research carried out for evaluating fractal dimensions from fracture surfaces, the fractal analysis methods, materials used and the range obtained.

Mandelbrot, Passoja and Paullay [23] analysed fracture surfaces of tempered 300-grade Maraging steel by SIM and estimated fractal dimensions to be between 1.1 and 1.3. An inverse correlation between the fractal dimension and the impact energy was obtained. Later Pande and Richards [25] estimated fractal dimensions of tensile fracture surfaces of titanium 6211 tensile test specimen by three methods: vertical sectioning (VS), secondary electron line scanning (SEL) and slit island and got the values 1.126, 1.171 and 1.32 respectively. In VS method, fractured surface was mounted in carbon bakelite, the mount was cut vertically to produce two complementary fracture surface cross sections. These cross sections were mechanically polished and observed by the SEM to capture high resolution images of the profile. This profile of the vertical cross-section of the fracture surface was used for computation of fractal dimension. In the second method (SEL), secondary electron signal was directly used for computing fractal dimensions. Huang [30] obtained the value of  $D$  of the impact fractured surfaces for CK45 steel at different heat treatment temperatures by the SEL scanning analysis and the VS method. They reported that the  $D$  by the SEL scanning analysis is greater than the same by the VS method. However,  $D$  by both the methods show similar trend which was found to be directly proportional to the impact toughness.

For computing fractal dimension of fracture surface, the logarithmic correlation between scale and measured quantity, referred as fractal plot here, needs to be used. For natural surface this correlation can be presented by reversed sigmoidal (RS) curve since the correlation between scale and measured quantity is negative. Since the RS curve has different slope at different length scale, a unique fractal dimension can not quantify the surface correctly. Multifractal concept was required for representing the full RS curve as reported by Williford [29]. While the

length scale of  $10^{-5}$  m corresponds to the fracture process,  $10^{-15}$  m,  $10^{-20}$  m and  $10^{-23}$  m correspond to the grain boundary cavitations, dislocations and bond breaking processes respectively. Fracture surface roughness shows similar RS behaviour (roughness is positive in the secondary Y-axis) as shown in Figure 3.4. It can be seen in the same plot that fracture energy is directly proportional to the scale of measurement whereas surface roughness is inversely correlated.

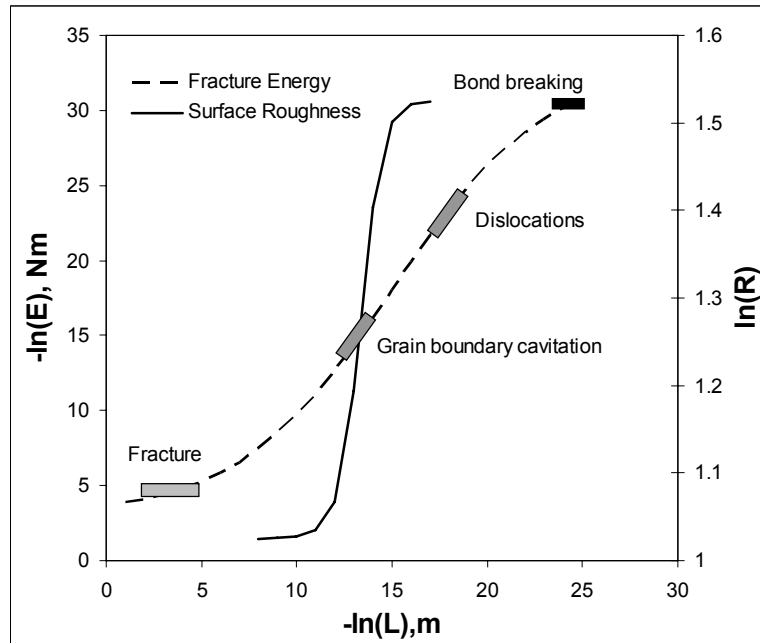


Figure 3.4: Multiscaling behaviour of fracture energy and surface roughness plotted against scale of observation [13].

Underwood and Banerji [24] reported the same RS nature of the fractal plot and suggested an alternative procedure for linearizing the plot. The alternative fractal dimensions from the profile and surface obtained from the fracture surface of AISI 4340 steel show minima at  $500^{\circ}\text{C}$  which correlate the embrittlement phenomenon at this temperature associated with this steel.

Huang [30] recommended that the true fractal dimension can only be obtained if the area of the fracture surface could be measured with area scale directly. In a later paper by Huang et al [34], slit island method was used where it was shown that the variation with the toughness depends upon the object being measured. When the object “lake” was measured within “island”, fractal dimension decreases whereas for measuring “island” within “lake”, the value increases.

Krupin Yu. A. [33] investigated the statistical properties of the fractal dimensions estimated by the SIM and the VS methods. The fracture surfaces were generated by stress corrosion cracking in low-alloy steel. It was observed that the values of fractal dimension obtained by two methods

for the same specimen are different and not correlated. Krupin Yu. A. further investigated the correctness of the fractal dimensions by confluent analysis and obtained them within the range of 2.668 to 2.957 for the same type of corrosion fracture surfaces of low alloy high strength steel. They have reported the lowest value 2.65 for cleavage, intermediate value of 2.7-2.75 for intergranular, 2.8-2.85 for ductile and 2.6-2.9 for mixed fracture surfaces.

Su, Zhang and Yan [36] carried out fractal analysis of microstructures and reported direct correlations between fractal dimension,  $D_m$  estimated from the microstructure of ferrite-martensite steel and the grain size ( $R$ ). They have used SIM and carried out image analysis to compute fractal dimensions using area-perimeter correlation. The fractal dimension,  $D_f$  from the fracture surface and its correlation with the logarithmic values of the impact toughness ( $K_d$ ) was reported by the authors. It was found that the value of  $D_f$  increases as the impact toughness decreases exponentially, contrary to the findings of Mandelbrot et al [23]. The correlations of  $D_m$  and  $D_f$  as reported by Su et al are of the following forms

$$D_m = 1.36R - 1.12 \quad (3.1)$$

$$\log(K_d) = -0.67D_f + 2.87 \quad (3.2)$$

Hsiung and Chou [41] characterised the fracture surface of an HSLA steel by SIM and computed  $D_f$  by area-perimeter correlation. They had used three ruler lengths or magnifications and found out that the correlation between  $D_f$  and the impact energy ( $K_d$ ) varied with the ruler lengths. For larger ruler length at low magnification the correlation is inversely proportional whereas it is direct when the magnification is higher. They have proposed a correlation based on fractal dimension increment  $D^*$  (fractional part of  $D_f$ ) as

$$K_d = 25K_{d0}D^* \quad (3.3)$$

In the above equation  $K_{d0}$  is the impact toughness determined experimentally.

Annamaria Celli [49] analyzed the crack paths generated by Vickers indentation in composite materials by fractal geometry and reported the correlation between the fractal dimension  $D$  of the geometric pattern of the crack path and the roughness. The crack profile was captured by SEM at high magnification and the images of the crack paths were analyzed to estimate fractal dimension. This correlation indicates the extent of anisotropy of the microstructure due to the presence of clusters of whiskers in the composites.

A correlation between fracture toughness ( $K_c$ ) and fracture surface energy ( $\gamma_c$ ) and the fractal dimension for brittle material like ceramic was reported [40] as

$$K_c = K_0 + E.a^{0.5}D^{*0.5} \quad (3.4)$$

$$\gamma_c = \gamma_0 + \frac{a_0 D^*}{2} E \quad (3.5)$$

where  $E$  is the elastic modulus,  $a_0$  is the characteristic length (the minimum length scale used for measuring an object) involved in the fracture process *i.e.* the value of the order of the atomic radii, and  $D^*$  is the fractional part of the fractal parameter.  $K_0$  and  $\gamma_0$  are the fracture toughness and fracture surface energy respectively for a flat fracture surface which is found to be zero for ceramic.

The correlation between fractal dimension and the theoretical strength,  $\sigma_t$ , has been presented by Mecholsky [50] by considering the stress distribution at a point( $r, \theta$ ) near the crack tip during fracture as

$$\sigma_{r,\theta} = \frac{K_c}{(2\pi r)^{0.5}} f(\theta) \quad (3.6)$$

Combining equations (3.4) and (3.6) and considering  $f(\theta)=1$ ,  $r=a$  and  $K_0=0$ , the theoretical strength of brittle material is obtained as

$$\sigma_t = \frac{ED^{*0.5}}{(2\pi)^{0.5}} \quad (3.7)$$

The theoretical strength computed by the above equation was found to be between  $E/8$  and  $E/\pi$  when fractal dimensional values collected from the literatures were used. The theoretical strength values are found to be acceptable particularly for brittle materials. The author concluded that theoretical strength of materials can be estimated based on the geometry of the crack tip and the generated fracture surface.

The main emphasis of fractal quantification was to obtain a correlation between the fractal dimension,  $D$ , and the fracture toughness of the material. In many cases fractal has been considered as the roughness property which eventually correlates the toughness of the materials. For a fracture surface such as those observed in single crystal or in glass, the driving force for crack initiation,  $G_{IC}$ , can be represented by

$$G_{IC} = 2.\gamma_0 = \frac{(1-\eta^2)(K_{IC})^2}{E} \quad (3.8)$$

where  $\gamma_0$  is the surface energy per unit area, expressing only the thermodynamic surface energy *i.e* the energy necessary to break chemical bonds. In equation (3.8)  $\eta$  is the Poisson's ratio and  $K_{IC}$  is the plane strain fracture toughness of the material. At room temperature, even a ceramic material exhibit some micro-plasticity near the crack tip, which causes stress release. Taking into account this extra energy for plastic deformation,  $\gamma_p$ , the total energy for fracture becomes  $(\gamma_0 + \gamma_p)$ . Increasing fracture energy creates more surface area and the surface roughness enhances. This can be accounted for by incorporating fractal dimension in the model represented by equation (3.8). Previous investigators [51, 52] have presented such model where the area increment due to tortuosity (or roughness) has been incorporated in the surface energy. Therefore, effectively the crack propagation initiates when

$$G_{1c} = 2.(\gamma_0 + \gamma_p)k^{1-D} \geq \frac{(1-\eta^2)(K_{IC})^2}{E} \quad (3.9)$$

where  $k$  is related to the scale of measurement and the characteristic length of the material.

Rodrigues & Pandolfelli [51] proposed fractal theory for ceramic materials in which the crack deflection was suggested as the geometric toughening mechanism. The total energy of fracture and the average value of the crack propagation resistance were correlated with the fractal dimension. Presenting the correlation between roughness of the fracture surface and the fractal dimension, it was pointed out that the average difficulty for crack propagation calculated from the J-R curve within an interval of certain crack extension could be expressed as a function of fractal dimension when a purely geometric toughening mechanism took place. In concrete, a direct correlation between the fracture toughness and fractal dimension was observed by Issa et al [53]. They recommended a simple linear relation between fractal and fracture energy for concrete.

Charkaluk et al [4] reviewed various methods for the determination of fractal dimension and its correlations with the mechanical properties. It was found, as discussed earlier, that different methods generate different  $D$  values for the same fracture surface. In some work a positive correlation between  $D$  and the  $K_{IC}$  fracture toughness was reported for materials like cement [54], Ocala chert [55], Alumina and glass ceramics [56] and  $AlN$  ceramic [57]. A negative correlation was observed in case of 24SiMnCrNi2A and 30CrMnSiNi2A [28], concrete [58] and dental porcelains [59]. No correlation [60] was obtained for concrete. The authors concluded that the difference between fractal dimensions computed by different methods is greater than the

variations with the material properties. The algorithms were not found to be precise in many cases. Malcai et al [61] carried out statistical analysis of values of  $D$  in order to find out the scaling range and cutoffs in computing the slope of the reverse sigmoidal curve. They summarised that for self-similar fractals, width of the scaling range is within 2 decades ( $10^2$ ). It was recommended that for computing the fractal dimension, the sensitivity of the scaling range with the experimental variables required to be assessed.

Fractal behaviour of brittle materials has been studied extensively where correlations between fracture toughness, denoted by  $K_C$  or  $K_{1C}$ , and fractal dimensions had been presented. In the case of ductile fracture, void initiation, coalescence and growth determine the fracture toughness,  $J_{1C}$ , by arresting or decelerating crack propagation rate. The energy dissipation (ED) rate is related to the amount of plastic energy that is necessary to propagate a crack. Three mechanisms that contribute to ‘ED’ during crack propagation are the lateral necking, deformation within the plastic zone and formation of voids in the process zone in case of tensile fracture. The energy required for the formation of void is responsible for the fracture surface formation and the morphology that is created on the fracture surface. Since the fractal dimension,  $D$ , correlates the surface irregularities caused primarily due to this void energy the correlation between  $D$  and  $J_{1C}$  may be found when the number of voids is large *i.e.* the void energy is maximum.

Thomson and Ashby [62] found a relation between  $J_{1C}$  and the fractal dimension of the surface:

$$J_{1C} = \frac{\sigma_y}{3} \ln \left[ \frac{4^{(1-D^{-1})} - 1}{12f_p} \right] l_0^* \quad (3.10)$$

where  $\sigma_y$  is the tensile strength of the material,  $f_p$  is the volume fraction of voids and  $l_0^*$  is the characteristic length. A direct correlation between the fractal dimension and  $J_{1C}$  is observed according to the above equation.

The analytical relationship between roughness parameter and fractal dimension has been obtained for different types of materials by previous investigators [24, 63]. Roughness can be measured for profiles as well as surfaces in terms of profile roughness parameter ( $R_L$ ) and surface roughness parameter ( $R_S$ ). The  $R_L$  is defined as the real length ( $L_R$ ) divided by the projected length ( $L_P$ ) of the profile. Whereas,  $R_S$  is defined as real area ( $A_R$ ) of the fracture surface divided by the projected area of fracture ( $A_P$ ). The equations for the profile and surface roughness can be written as:

$$R_L(k) = \frac{L_R(k)}{L_p} = C_1(k)^{-D^*} \quad (3.11)$$

$$R_S(k^2) = \frac{A_R(k^2)}{A_p} = C_2(k)^{-D^*} \quad (3.12)$$

where  $C_1$  and  $C_2$  are the constants. The measurement scale  $k$  defines that, as the value of  $k$  decreases, the roughness increases since  $D^*$  (fractional part of  $D$ ) is always negative. It is relatively difficult to find  $R_S$  experimentally. A simple linear parametric equation proposed by Underwood [63], which fits a large amount of experimental data, is given as

$$R_S = \frac{4}{\pi}(R_L - 1) + 1 \quad (3.13)$$

Using the profile and surface roughness data in equation (3.11), (3.12) and (3.13) fractal dimension can be computed. It was reported that roughness and fractal dimension has strong dependence on magnification [64]. Too small or too large magnification will generate insufficient roughness information which would not be correct representation of fracture surface morphology.

### 3.3 Fractal analysis of magnetic Barkhausen emission signals

MBE signal is a non-stationary time domain signal which is generated due to the change of domain wall (DW) velocity. Fractal characteristics of Barkhausen effect due to the unpinning of the DW or Barkhausen Jumps (BJ), was investigated by several authors [65-68]. Durin et al [65] highlighted that MBE signal exhibit self-similarity properties at sufficiently low domain wall velocity. They estimated fractal dimension,  $D_c$  based on random Cantor dust and had shown  $D_c=1-c$ , where  $c$  is the average normalised DW velocity less than 1. Here  $c$  is proportional to the applied field rate, given in equation (3.14), and is correlated with two exponents  $\gamma$  and  $\beta$  to express the duration (T) and size distribution (s) of the DW respectively.

The average DW velocity is given as:

$$c = \langle v \rangle = \left( \frac{\sigma.G}{AS\mu} \right) \langle \dot{\Phi} \rangle = \left( \frac{\sigma.G}{A} \right) \langle \dot{H}_a \rangle = \dot{h}_a \quad (3.14)$$

In equation (3.14),  $\sigma$  is the electrical conductivity,  $G$  is a constant 0.1357,  $S$  is the cross sectional area,  $\mu$  is the permeability,  $\phi$  is the induced flux per coil turn,  $A$  is the parameter measuring the strength of the local pinning interactions,  $\dot{H}_a$  is the applied magnetic field.

Zapperi & Durin [70] highlighted the power law variation of the signal amplitude distribution considering velocity ( $v$ ), size ( $s$ ) and time duration ( $T$ ) of the DW as

$$\begin{aligned} P_\tau(v) &\sim v^{-(1-c)} e^{\frac{-v}{v_0}} \\ P(s) &\sim s^{-\beta} f\left(\frac{s}{s_0}\right) \\ P(T) &\sim T^{-\gamma} g\left(\frac{T}{T_0}\right) \end{aligned} \quad (3.15)$$

where the exponents of the above equations are estimated from  $c$  and the correlations are given as

$$\begin{aligned} \gamma &= 2 - c \\ \beta &= \frac{3 - c}{2} \end{aligned} \quad (3.16)$$

The  $P(v)$  distribution reflects the characteristics of BJ's at different rate of applied magnetic field,  $\dot{h}_a$ . When  $c > 1$ , the DW motion is continuous; when  $c < 1$ , the BJ's are separated in time and widely distributed in duration and size. The  $P(s)$  distribution is expressed as a function of the average area under a typical BJ, termed as avalanche size  $s$ . To express the temporal distribution,  $P(T)$ , a power law correlation with  $T$  is also used, where  $T$  is the time duration for each BJ event.

Equation (3.15) is the stationary amplitude distribution from the MBE signals which was obtained by solving Fokker-Plank equation given as

$$\begin{aligned} \frac{dv}{du} + (v - c) &= -\frac{dh_p}{du} \\ v &= \left(\frac{\sigma \cdot G}{AS\mu}\right) d\Phi; \quad u = \frac{t}{\sigma \cdot GS\mu}; \quad h_p = \frac{H_p}{AS\mu}; \end{aligned} \quad (3.17)$$

In equation (3.17),  $v$  is the normalized DW velocity,  $u$  is the normalized time duration, and  $h_p$  is the normalized local DW pinning field ( $H_p$ ). Zapperi et al [70] highlighted various approaches for the prediction of Barkhausen noise (BN) pulses and discussed their advantages and limitations in interpreting the experimental results. The models are primarily focused on explaining the statistical properties of the Barkhausen effect. It was highlighted that the properties of power

spectrum for experimental results need to be explained in the light of the physical phenomenon observed in DW motion.

Elementary signals of Barkhausen noise of the commercial VITROVAC 6025 X metal glass sample, were extracted by Spasojevic et al [71]. They have computed power law exponents from an elaborate formula for the power law spectrum. The formulation included probability distribution function, a correlation factor determining the signal duration and the power law spectrum of the elementary signal. The role of BN elementary signal, power laws, scaling relations to understand the criticality of BN was highlighted there.

Tidac [72] explored the scaling behaviour of BN and found it to be non-universal. When the degree of disorder is varied through non-equilibrium phase transition, the scaling exponent also varies. They reviewed experimental and theoretical investigation of the BN, in which the power spectrum was shown to decay with frequency as  $\sim f^{-\phi}$ , where  $1.5 < \phi < 2$  and the distribution of size, duration and energy associated with BJ exhibit a power law behaviour over a few decade with a cutoff.

The characteristics of BN signals and their power spectrums elucidated by previous researchers were classified into three groups by Plewka et al [73]. These are

- Noise in BN treated as a stochastic element [73] can be modeled using desired parameters to get a known shape of the power spectra
- The evidence of  $1/f$  power spectrum signifies self-organised criticality [74] in which BN was considered as a collective phenomenon of several degrees of freedom. An avalanche like propagation of domain wall takes place for a small perturbation due to a single BJ. The effect of BJ may decay gradually generating a point of self organized criticality in spatial as well as time domains.
- Chaos in the BN pulses can be treated as deterministic rather than stochastic [75-77]. A single domain may show random disorder, however the presence of long range magnetostatic interactions orchestrated the random disorder in synchronized deterministic forms.

Using correlation dimension, a method to represent self-similar fractal behaviour in signals, Plewka et al [73] demonstrated that Barkhausen effect exhibits low dimensionality and, therefore can be treated as a deterministic chaotic phenomenon.

Table 3.1: Fractal analysis of fracture surface\*

Ref No	Reference	Year	Methods	Materials	Range for D*	Remarks
23.	Mandelbrot B. B. et al	1984	SIM/PSD	300-grade Maraging steel	0.1-0.27	Impact energy is inversely proportional to the D*.
24.	Underwood EE, Banerji K.	1986	VSM+R	AISI 4340	0.072-0.091	Fractal dimension plot for different tempering temperatures show a minima at 500°C indicating embrittlement.
25.	Pande CS et al	1987	VSM SEL SIM	Ti Alloy 6211	0.087-0.126 0.171 0.32	Tensile fracture surfaces were used for estimating fractal dimension.
26.	Pande CS et al	1987	SIM VSM	TA6V2XZr	0.41-0.46 0.03-0.11	No correlation was found between material properties and D*.
27.	Richards LE, Dempsey BD.	1988	SIM	Ti Alloy	0.78-0.91	No correlation was found between material properties and D*.
28.	Mu ZK, Lung CW	1988	SIM	24SiMnCrN2A 30CrMnSiNi2A	0.12-0.22 0.11-0.18	$K_{Ic}$ fracture surface is inversely proportional with D*.
29.	Williford R. E.	1988	-	Brittle(ZnSe, Al <sub>2</sub> O <sub>3</sub> ) Ductile(Maraging steel, Ti alloys)	0.1-0.3 0.3-0.1	For brittle fracture, D* has direct correlation with the surface energy. Inverse correlation is true for ductile materials.
30.	Huang Z. H. et al	1989	VSM SE	CK45	0.12-0.16 0.2-0.3	D* and impact toughness increase with increasing temperature.
31.	Davidson DL. F	1989	R	Al-SiC	0.084-0.248	No correlation between D* and Material properties reported.
32.	Bouchaud E et al	1990	Corr Func	Al alloy	0.18-0.25	D* remains constant
33.	Krupin YA, Kiselev I K	1990	SIM/VSM	4340 steel	0.063-0.753	Correlation not defined
34.	Huang Z H. et al	1990	SIM (island) SIM(lake)	CK45	0.32-0.4 0.22-0.3	Inverse correlation with impact toughness for lake-in-island. Direct correlation for island-in-lake.
35.	Dauskart et al.	1990		Mn steel	0.28	Intergranular failure
36.	Su H et al	1991	SIM	Dual Phase Dual Phase	0.2-0.8 0.09-0.22	Inverse correlation obtained between Impact toughness and D*. Direct correlation obtained between D* and fatigue threshold.
37.	Long QY et al	1992	VSM+R	30CrMnSiNi2	0.08-0.12	Direct correlation with toughness.
38.	Ray K K and Mandal G	1992	SIM/P	HSLA	0.01-0.53	Direct correlation with impact toughness.

Ref No	Reference	Year	Methods	Materials	Range for D*	Remarks
39.	Jiang XG et al.	1993	VSM	7475 Al alloy	0.143-0.362	No correlation defined
40.	Hilders and A., Pilot D.	1997	SIM	A commercial medium-carbon ferrite-pearlite steel.	0.05-0.8	Positive correlation between D* and impact toughness.
41.	Hsiung J.C. & Caou Y. T.	1998	SIM	HSLA from Temp. of -20 to -145oC	0.02-0.2	Positive correlation between D* and impact toughness.
42.	Kurt Wiencek et al	2001	VSM	A high carbon steel	0.09-0.1	No correlation. Independent of the impact toughness.
43.	Maria Sozanska et al	2001	P	Carbon steels	0.08-0.11	Surface roughness as well as D* is strictly correlated with an increase in hydrogen embrittlement.
44.	Sebastian Stach et al	2001	PCM & BC	Ductile (SW7M+0.057N steel) Brittle (10H2M steel)	0.08/0.15 (ductile) 0.01/0.02 (Brittle)	D* for ductile fracture surface is more than the same for brittle fracture surface.
45.	A.L. Horovistiz and Hein	2004	MB	Aluminium alloy	0.03-0.11	D* measures local morphological entropy. D* depends upon the local microstructure as well as the state of stress fields.
46.	O. A. Hilders et al	2004	SIM	Aluminum alloys	0.08 – 0.25	Phase I: D* is inversely proportional to fracture strain. Phase II: D* is constant Phase III: D* is directly proportional to fracture strain.
47.	Katarzyna Klyk-Spyra and Maria Sozańska	2006	P	Duplex stainless steel 2205	0.13-0.25	External loading affect the roughness of the fracture surfaces. A direct correlation between D* and external loading was observed. Fracture mechanism changes from brittle to ductile as the load increases.
48.	I. Dlouhy and B. Strnadel	2008	P	Ni–Cr steel	0.06-0.18	D* for intergranular fracture > 0.12 else transgranular fracture

P: Profilometry; VSM: Vertical sectioning method; SEL: Secondary electron line scanning; PCM: Projected covering method; SIM: Slit Island Method; R: Richardson Plot; Corr. Func: Correlation function; BC: Box counting; MB: Modified box counting; R/S: Rescaled range analysis; PSD: Power spectral density method; Wave: Wavelet analysis  
\*(23-35: from ref [4])

### 3.4 References

1. W.Sun, G. Xu, P. Gong and S. Liang: Fractal analysis of remotely sensed images: A review of methods and applications, *International Journal of Remote Sensing* 27, 22, 4963–4990(2006).
2. Brendt Wohlberg and Gerhard de Jager: A Review of the Fractal Image Coding Literature, *IEEE transactions on Image processing*, 8, 12, 1716-1729(1999).
3. Chaoxin Zheng, Da-Wen Sun and Liyun Zheng: Recent applications of image texture for evaluation of food qualities—a review, *Trends in Food Science & Technology* 17,113–128(2006)
4. E. Charkaluk, M. Bigerelle, A. Iost : Fractals and fracture, *Engineering Fracture Mechanics* 61, 119-139(1998).
5. N.C. Kenkel and D.J. Walker: <http://www.umanitoba.ca/faculties/science/botany/LABS/ECOLOGY/FRACTALS/fractal.html>
6. *Metals Handbook Desk Edition*, By ASM, ASM International / Amer. Soc. of Metals edited by Joseph R. Davis, 1998
7. Dathe, S. Eins, J. Niemeyer, G. Gerold: The surface fractal dimension of the soil–pore interface as measured by image analysis *Geoderma* 103, 203-229(2001).
8. D. E. Pendleton, A. Dathe, and P. Baveye: Influence of image resolution and evaluation algorithm on estimates of the lacunarity of porous media *Physical Review E* 72, 041306:1-9(2005).
9. T.J. Kang, S.C. Kim, I.H. Sul, J.R. Youn and K. Chung: Fabric Surface Roughness Evaluation Using Wavelet-Fractal Method Part I: Wrinkle, Smoothness and Seam Pucker, *Textile Res. J.* 75(11), 751–760 (2005).
10. P. Ziouposi, C. Kaffy and J.D. Currey: Tissue heterogeneity, composite architecture and fractal dimension effects in the fracture of aging human bone, *International Journal of Fracture*, 139, 407–424(2006).
11. Geoffrey Dougherty, Geoffrey M. Henebry: Fractal signature and lacunarity in the measurement of the texture of trabecular bone in clinical CT images, *Medical Engineering & Physics*, 23, 369–380 (2001).
12. A.A. Likhachev, J. Pons, E. Cesari, A.Yu. Pasko, V.I. Kolomytsev: Observation and analysis of scaling behavior in surface martensite-austenite relief during the reverse martensitic transformation in Cu-Al-Ni single crystal by using 2D Fourier processing method, *Scrip. Mater.*, 43, 765-769(2000).
13. Su Hui, Z. Yugui, Y. Zhenqi: Fractal analysis of microstructures and properties in ferrite-martensite steels, *Scrip. Mat.*, 25,651-654(1991).
14. J.M. Li, L. Lu, M.O. Lai, B. Ralph: *Image-based Fractal Description of Microstructures*, 2003, Kluwer Academic Publishers, UK.
15. E. Hornbogen, Fractals in microstructure of metals, *Int. Materials Reviews*, 34, 277-296((1989).
16. R. Colas: On the variation of grain size and fractal dimension in an austenitic stainless steel, *Material Characterisation*, 46, 353-358(2001).

17. Su. Hui and Yan Zhenqi: Fractal analysis of microstructures and properties in HSLA steels, *J. of Materials Science*, 14, 1436-1439(1995).
18. Y. Kang, H.K.D.H. Bhadeshia, *Materials Science and Technology*, 22(2006) 650.
19. H.K.D.H. Bhadeshia: The dimensions of steel, *Ironmaking and Steelmaking*, 34, 194-199(2007).
20. R. Villegas, A. Redjaimia, M. Confente, M.T. Perrot-Simonetta: On the Fractal Nature of Acicular Ferrite, and V(C,N) Precipitation in Medium Carbon Microalloyed Steels, *Material Science and Technology*, 6, 401-410(2006).
21. B. Skrotzki: Fractal analysis of martensite in an Fe-Ni alloy, *J. of materials science*, 26, 1073-1077(1991).
22. M. Rybaczuk and G. Zietek: Fractal model of the cold martensite transformation in steels, *Archives of Civil and Mechanical Engineering*, Vol II, No. 2 (2002).
23. B.B.Mandelbrot, D.E. Passoja, A.J. Paullay: Fractal character of fracture surfaces of metal, *Nature*, 308, 19, 721-722(1984).
24. E. E. Underwood and K. Banerji: Fractal Analysis of Fracture Surfaces, Formerly Ninth Edition, *Metal Handbook*, 12, Fractography, 211-215(1987).
25. C.S Pande, L.E.Richards, S.Smith: Fractal characteristics of fracture surfaces, *J Mater Sci Lett*, 6, 295-297(1987).
26. CS Pande, L E Richards, N Louat, B D Dempsey, AJ Schwoeble: Fractal characterization of fractured surfaces, *Acta Metall*, 35(7),1633-1640(1987).
27. LE Richards, BD Dempsey: Fractal characterization of fractured surfaces in Ti-4.5 Al-5.0 Mo-1.5 Cr (CORONA 5), *Scripta Met*, 22, 687-696 (1988).
28. Z.K. Mu and C.W. Lung: Studies on the fractal dimension and fracture toughness of steel, *J Phys D, Appl Phys*, 21, 848-850(1988).
29. R. E. Williford: Scaling similarities between fracture surfaces, energies, and a structure parameter, *Scr. Metall.*, 22, 197-200(1988).
30. Z. H. Huang, J. F. Tian and Z.G.Wang: Analysis of Fractal Characteristics of Fractured Surfaces by Secondary Electron Line Scanning, *J Marerial Science and Engineering A*, 118, 19-24(1989).
31. D.L. Davidson: Fracture surface roughness as a gauge of fracture toughness: aluminium-particulate SiC composites, *J Mater Sci*, 24,681-688(1989).
32. E. Bouchaud, G. Lapasset, J. Planes: Fractal dimension of fractured surfaces: a universal value?, *Europhys Lett*, 13,1,73-82(1990).
33. Yu. A. Krupin, I. K. Kiselev: On statistical properties of the estimation of fractal dimension of the corrosion fracture surface of low alloy high strength steel, *Scr. Metall*, 24, 2113-2118(1990).
34. Z H., Huang, J.F., Tian and Z.G. Wang: A study of the slit island analysis as a method for measuring fractal dimension of fractured surface, *Scr. Metall*, 24, 967-972(1990).
35. R.H. Dauskardt and F. Haubensak, R.O. Ritchie: On the interpretation of the fractal character of fracture surfaces, *Acta Metall Mater*, 38,143-159(1990).

36. Hui Su, Yugui Zhang and Yan Zhenqi: Fractal analysis of microstructures and properties in ferrite-martensite steels, *Scr. Metall*, 25, 651-654(1991).
37. Q.Y. Long, J. Chen, J. Chen, Z.Q. Mu, C.W. Lung: A study on fractal dimension of fracture surface created by stress corrosion cracking in high strength steels, *Scripta Metall Mater*, 27, 1319-1343(1992).
38. K. K. Ray and G. Mandal: Study of correlation between fractal dimension and impact energy in a high strength low alloy steel, *Acta Metall Mater*, 40, 3, 463-469(1992).
39. X. G. Jiang, J. Z. Cui, L.X. Ma: Fractal dimension of fracture surface and superplasticity of 7475 Al alloy, *J Mater Sci Lett*, 12, 1616-1624(1993).
40. Hilders and D. Pilot: On the Development of a Relation between Fractal Dimension and Impact Toughness, *Materials Characterisation*, 38, 121-127 (1997).
41. J.C. Hsiung and Y. T. Chou: Fractal characterization of fracture surface of a high-strength low-alloy steel, 33, 2949-2953(1998).
42. Kurt Wiencek, Andrzej Czarski, Tadeusz Skowronek: Fractal characterization of fractured surfaces of a steel containing dispersed Fe<sub>3</sub>C carbide phase, *Materials Characterization*, 46, 235– 238(2001).
43. Maria Sozanskaa, Jaroslav Sojkab, Petra Betřa'kova'b, Catherine Dagbertc, Ludmila Hyspecka'b, Jacques Gallandc, Miroslav Tvrđy': Examination of hydrogen interaction in carbon steel by means of quantitative microstructural and fracture descriptions, *Materials Characterization* 46, 239– 243(2001).
44. Sebastian Stach, Jerzy Cybo, Jerzy Chmiela: Fracture surface — fractal or multifractal?, *Materials Characterization* 26,163– 167(2001).
45. A.L. Horovistiz and Hein: Fractal analysis along stretch zone for an aluminium alloy, *Materials Letters*, 9, 7, 790-794(2005).
46. O. A. Hilders, M. Ramos, N. D. Peřa, L. Saenz, R. A. Caballero: Plasticity Fractal-Behavior Trends for Different Aluminum Alloys Tested in Tension, *Materials Forum*, 28, Edited by J.F. Nie, A.J. Morton and B.C. Muddle(2004).
47. Katarzyna Klyk-Spyra , Maria Sozańska: Quantitative fractography of 2205 duplex stainless steel after a sulfide stress cracking test, *Materials Characterization* 56, 384–388(2006).
48. Dlouhy and B. Strnadel: The effect of crack propagation mechanism on the fractal dimension of fracture surfaces in steels, *Engineering Fracture Mechanics* 75,726–738(2008).
49. Annamaria Celli, Antonella Tucci, Leonardo Esposito: Quantitative Evaluation by Fractal Analysis of Indentation Crack Paths in Si<sub>3</sub>N<sub>4</sub> – SiCw, *J European Ceramic Society*,19, 441-449(1999).
50. J. J. Mecholsky: Estimating theoretical strength of brittle materials using fractal geometry, *Materials Letters*, 60, 2485-2488(2006).
51. J.A.A Rodrigues and V. C. Pandolfelli: Insights on the Fractal-fracture behaviour relationship, *Materials research*, 1, 47-52 (1998).
52. Santos Sergio Francisco dos & J.D.A Rodrigues: Correlation between fracture toughness, work of fracture and fractal dimensions of Alumina-mullite-zirconia composite, *Materials Research*, 6, 219-226(2003)

53. Mohsen A. Issa, Mahmoud A. Issa, Islam Md. S. and A. Chudnovsky: Fractal dimension-a measure of fracture roughness and toughness of concrete, *Engineering Fracture Mechanics*, 70, 125-137(2003).
54. D.A.Lange, H.M. Jennings and S.P. Shah: Analysis of surface roughness using confocal microscopy, *J Mater Sci*, 28, 3879–3884(1993).
55. J.J. Mecholsky and T.J. Mackin: Fractal analysis of fracture in Ocala chert, *J Mater Sci Lett*, 7, 1145–1147(1988).
56. J. J. Mecholsky, D. E. Passoja and K. S.Feinberg-Ringel: Quantitative analysis of brittle fracture surfaces using fractal geometry, *Journal of American Ceramic Society*, 72, 60-65 (1989).
57. M. Tanaka: Fracture toughness and crack morphology in indentation fracture of brittle materials, *J. Mat. Sci.*, 31, 749-755(1996).
58. V.E. Saouma and C. Barton: Fractals, fractures, and size effects in concrete, *J Engg. Mech*, 120, 4, 835–854(1994).
59. G.R. Baran, C. Roques-Carmes, D. Wehbi and M. Degrange: Fractal characteristics of fracture surfaces, *J Am Ceram Soc*, 75 ,10, 2687–2691 (1992).
60. A.M. Brandt and G. Prokopski: On the fractal dimension of fracture surfaces of concrete elements, *J Mater Sci*, 28, 4762–4766(1993).
61. O. Malcai, A. D. Lidar, O. Biham and D. Avnir: Scaling range and cutoffs in empirical fractals, *Physical Review E*, 56, 3, 2817-2828(1997).
62. A.W. Thompson, M.F. Ashby: Fracture surface micro-roughness, *Scripta Met*, 18,127-130(1984).
63. E.E. Underwood: Quantitative fractography, *Applied Metallography*, G.F. vander Voort, Ed., Van Nostrand Reinhold, 101-122(1986).
64. Xiao Wu Li, JiFeng Tian, Yan Kang and ZhongGuang Wang: Quantitative analysis of fracture surface by roughness and fractal method, *Scripta Metallurgica et Materialia*, 33, 5, 803-809(1995).
65. G. Durin, A. Magni and G. Bertotti, Fractal properties of the Barkhausen effect, *J. Mag. Mag. Mat.*, 140-144, 1835-1836(1995).
66. P.J. Cote and L.V. Meisel: Self-organized criticality and the Barkhausen effect, *Phys. Rev. Lett*, 67, 1334-1337(1991).
67. L.V. Meisel and P.J. Cote: Power law, flicker noise and Barkhausen effect, *Phys. Rev. Lett*, B46, 10882-10827(1992).
68. R. D. McMichael, L.J. Swartzendruber and L. H. Bennett: Langevin Approach to Hysteresis and Barkhausen Modeling in Steel, *J. Appl. Phys*, 73, 5848-5850(1993).
69. C. Beatrice Magni , G. Durin and G. Bertotti: Stochastic approach to domain wall dynamics and ferromagnetic hysteresis, *J. Mag. Mag. Mat*, 157/158, 353-354(1996).
70. S. Zapperi and G. Durin: New perspectives for the Barkhausen effect, *Comp. Materials Science*, 20, 436-442(2001).

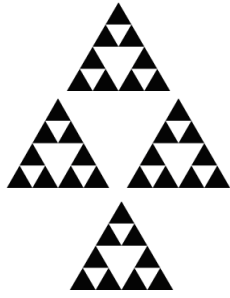
71. D. Spasojevic, S. Bukvic, S. Milosevic and H. E. Stanley: Barkhausen signals, power laws and scaling relations, *Phy Review E*, 54, 3, 2531-2546(1996).
72. B. Tidac: Nonuniversal scaling behaviour of Barkhausen noise, *Phy Review E*, 77, 18, 3843-3846(1996).
73. P. Plewka, J.J. Zebrowski and M. Urbanski: Determinism and correlation dimension of Barkhausen noise, *Physical Review E*, 57, 6, 6422-6430(1998).
74. P. Bak, C. Tang and K. Wiesenfeld: Self-organised criticality, *Physical Review A*, 38,1, 364-374(1988).
75. J. S. Urbach, R. C. Madison, and J. T. Markert: Interface Depinning, Self-Organized Criticality, and the Barkhausen Effect, *Phys. Rev. Lett.*, 75, 276 - 279 (1995).
76. J. R. Petta, M. B. Weissman, and K. P. O'Brien: Multiple magnetization paths in Barkhausen noise, *Phys. Rev.*, E54, R1029-R1031(1996).
77. J. R. Petta, M. B. Weissman, and G. Durin: Barkhausen pulse structure in an amorphous ferromagnet: Characterization by high-order spectra, *Phys. Rev.*, E 57, 6363-6369(1998).

# CHAPTER 4

## **4.0 Fractal analysis of synthetic signals and images**

4.1	Generation of synthetic signals and images	90
4.1.1	Weierstrass cosine function (WCF)	90
4.1.2	Fractional Brownian Motion (fBm)	91
4.1.3	Fractional Gaussian Noise (fGn)	95
4.2	Results & discussion	98
4.2.1	Verification of fractal analysis codes using WCF	99
4.2.2	Verification of fractal analysis codes using fBm images	103
4.3	Conclusions	107
4.4	References	108





# 4

## FRACTAL ANALYSIS OF SYNTHETIC SIGNALS AND IMAGES

This chapter introduces the initial steps for carrying out fractal analysis of images and signals. Fractal analysis requires selection of appropriate algorithms for computing fractal dimension and their implementation for generating accurate results. Review of various algorithms for fractal analysis of images and signals has been discussed in chapter 2. In this work, three algorithms selected for implementation are: Rescaled Range analysis, known as R/S analysis, Power Spectral Density (PSD) and Wavelet analyses. As an initial step, prior to carrying out fractal analysis of real signals (here signals mean both 1D signal and 2D image), fractal quantification needs to be done for synthetically generated signals with known fractal dimensions. When the input dimensions match with the estimated dimensions for the synthetic signals, the codes are validated. It may be noted that exact agreement *i.e.* zero error may not be possible if the synthetic signals are generated using random functions. However an empirical correlation within a wide

data range would make the fractal estimator a useful technique for quantification of images as well as any one dimensional signals.

For generation of synthetic signals, various methods like Random Midpoint Displacement (RMD) algorithm [1,2], Fourier Filtering (FF) algorithm [1,2], *etc* are available. In addition functional formulation like Weierstrass Cosine Function (WCF) [3,4] is available for simulating 1D signals. The simulated synthetic images and signals presented in this chapter are of fractional Brownian motion (fBm) and fractional Gaussian noise (fGn) [3,4] type, which are generated synthetically by FF algorithm and using WCF.

Implementation of methodologies and algorithms are presented in this chapter along with the results for validation of the fractal codes. Extensive error analysis has been performed to assess the quality of results.

## 4.1 Generation of synthetic signals and images

Mathematical formulations for generating synthetic signals and images based on fBm and fGn functions are given in this section. While the 1D synthetic signals are based upon Weierstrass cosine function (WCF), synthetic images are based upon fBm and fGn types. For simulating the synthetic images, only Fourier Filtering method based on stochastic random variables has been implemented since this method (FF) is compatible with other methods as reported [5].

### 4.1.1 Weierstrass cosine function (1D)

This function is continuous everywhere however differentiable nowhere. The typical WCF [6] is given as

$$f(x) = \sum_{i=0}^{\infty} a^i \cos(b^i \pi x) \quad (4.1)$$

where  $0 < a < 1$ , and  $ab > 1 + 1.5\pi$  and  $b$  is a positive odd integer. Weierstrass function shows the typical fractal nature where the self similarity is observed at all measurable resolutions.

Mathematically continuous functions,  $f(x)$  can be defined as

$$\lim_{x \rightarrow \varepsilon^+} f(x) = \lim_{x \rightarrow \varepsilon^-} f(x) \quad (4.2)$$

where  $\varepsilon$  is the infinitesimally small value and the non-differentiability is expressed as

$$\lim_{x \rightarrow \varepsilon^+} \frac{f(x) - f(\varepsilon)}{x - \varepsilon} = \lim_{x \rightarrow \varepsilon^-} \frac{f(x) - f(\varepsilon)}{x - \varepsilon} \quad (4.3)$$

For algorithmic implementation of Equation (4.1) for a given value of the Hurst exponent,  $H$ , the WCF can be rewritten as

$$f_H(x) = \sum_{i=0}^M Y^{-iH} \cos(2\pi Y^i x) \quad (4.4)$$

where  $H=2-D$  and  $D$  is the fractal dimension. To generate temporal signals, the input variable,  $x$ , needs to be converted to the sampled time by multiplying it with  $(1/f_s)$ , where  $f_s$  is the sampling frequency. Figures 4.1(a-d) show the curves generated by the Weierstrass cosine function for  $M=25$ ,  $Y=5$  and  $H=0.9, 0.5, 0.3$  and  $0.1$  respectively.

#### 4.1.2 Fractional Brownian Motion (fBm)

As one of the representations of the statistical self-similarity or statistical fractals, this function is known as fractional Brownian motion (fBm). The 1D fBm function is a continuous-time Gaussian process bounded between  $[0, T]$  where  $T \in \mathfrak{R}$ , where  $\mathfrak{R}$  is the set of real numbers. The function typically has zero mean which can be determined by its covariance or auto correlation function. For this zero mean time varying Gaussian process  $\{B_H(t)\}_{t \in \mathfrak{R}}$ , the covariance function is written as

$$\text{Cov}(B_H(s), B_H(t)) = \frac{\sigma^2}{2} (|t|^{2H} + |s|^{2H} - |t-s|^{2H}) \quad (4.5)$$

where  $\sigma^2$  is the variance of  $B_H(t)$  function. The standard fBm refers to the condition when  $\sigma^2=1$ . The extent of complexity in  $B_H(t)$  is given by the  $H$  exponent. Similar to Weierstrass function, fBm is a continuous function but not the differentiable iterative function system (IFS).

The increment of fBm is given as

$$\langle B_H(t) - B_H(t + \Delta t) \rangle = c \sigma^2 |\Delta t|^{2H} \quad (4.6)$$

where  $c$  is a constant. The curve represented by  $B_H(t)$  becomes smoother as  $H$  increases. When  $0 < H < 0.5$ , the increments of fBm have opposite signs and their covariance becomes negative, hence the function is anti persistent. For  $0.5 < H < 1$ , positive covariance is obtained, so the function becomes persistent. For  $H=0.5$ , the function shows complete random behaviour.

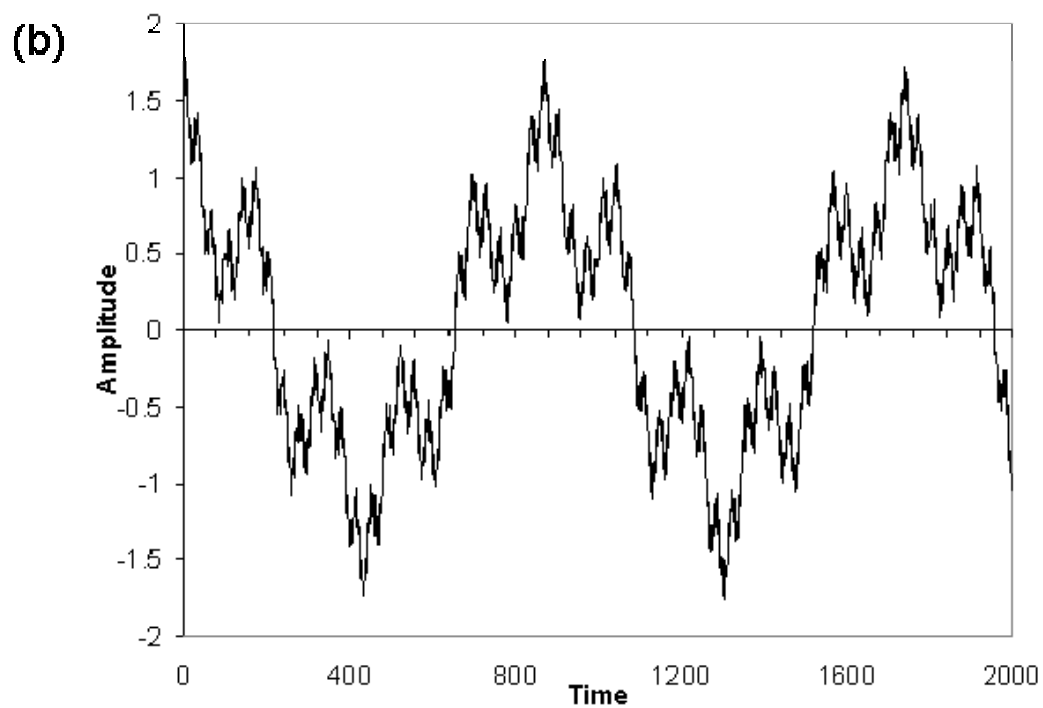
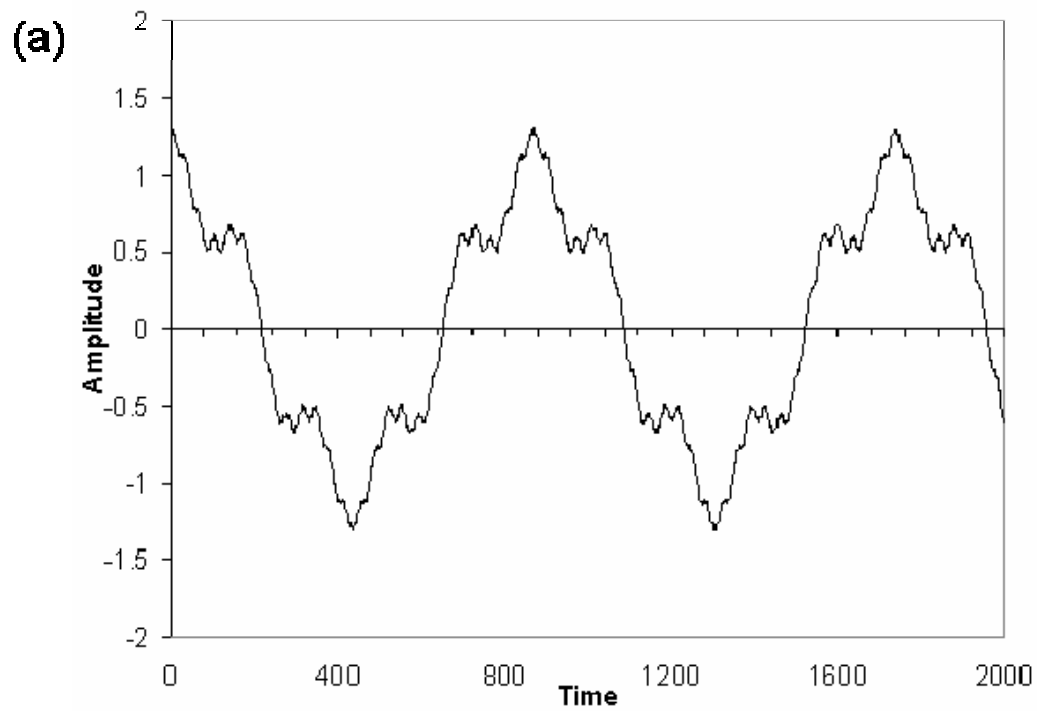


Figure 4.1: Weierstrass cosine function with a)  $H=0.9$  and b)  $H=0.5$

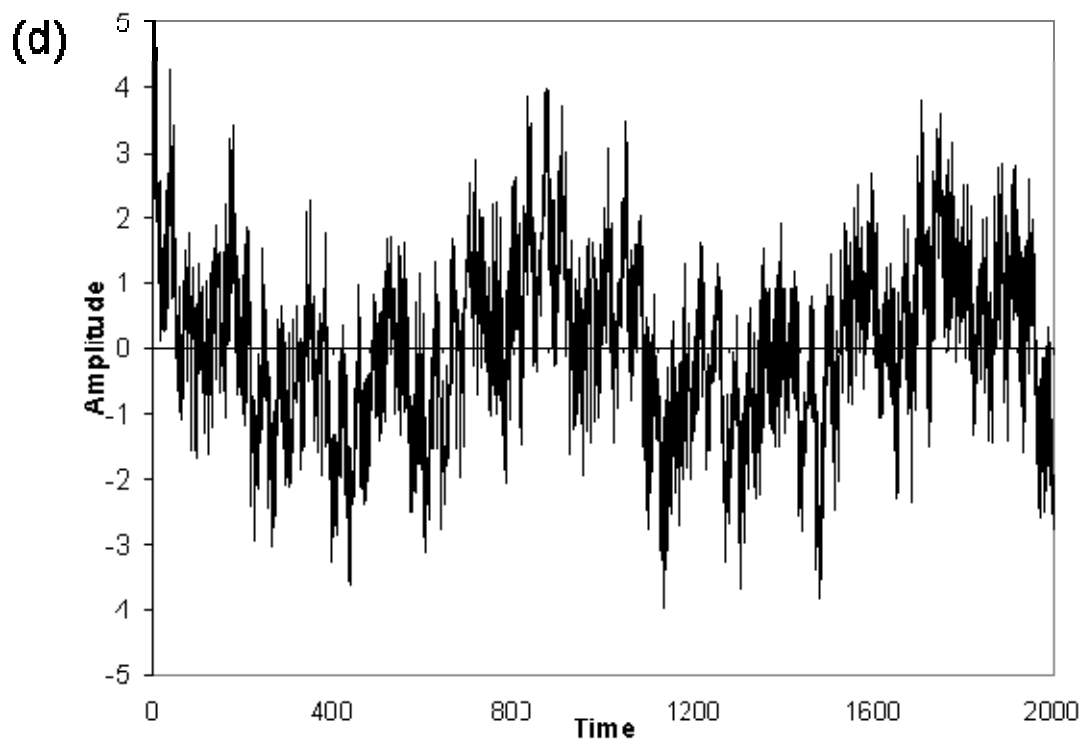
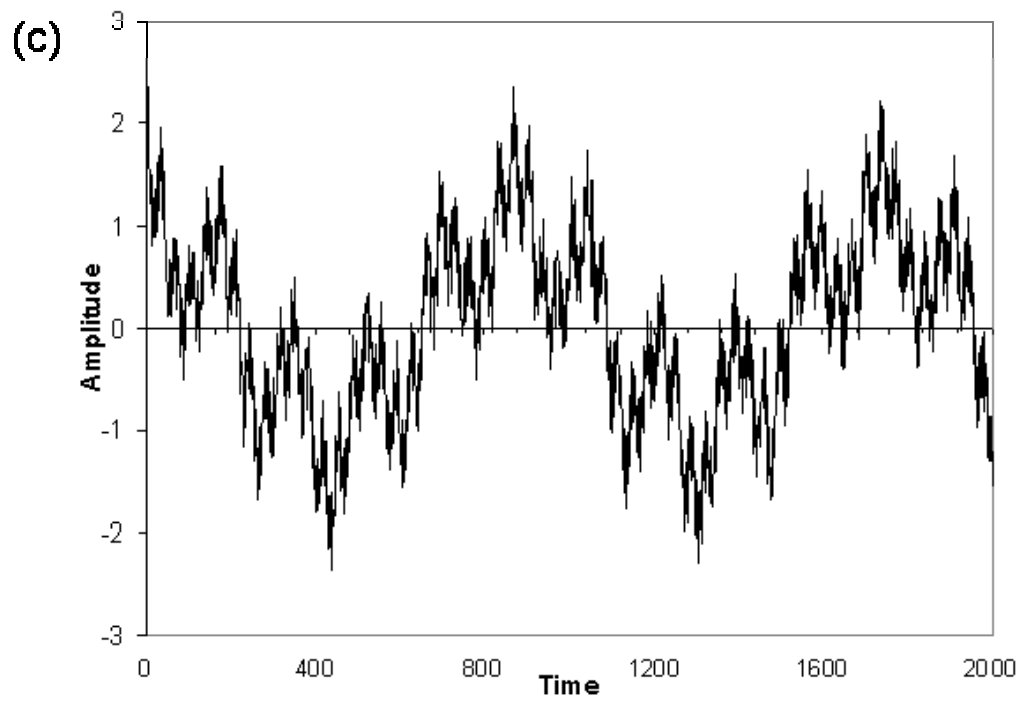


Figure 4.1: Weierstrass cosine function with c)  $H=0.3$  and d)  $H=0.1$

The two dimensional implementation of fBm function  $\{B_H(x, y)\}_{x, y \in \mathbb{R}}$  [2,4] has the similar proportionality given as

$$\langle B_H(x, y) - B_H(x + \Delta x, y + \Delta y) \rangle = c \sigma^2 \sqrt{|\Delta x^2 + \Delta y^2|}^{2H} \quad (4.7)$$

The power spectral density (PSD)  $\{P(f)\}_{f \in [-\pi, \pi]}$  of the fBm surface is given as

$$P(f) \propto \frac{1}{f^{2H+2}} \quad (4.8)$$

where  $f = \sqrt{u^2 + v^2}$  and  $u$  and  $v$  are the frequency components in two dimensions.

There are different algorithms for generating fBm surface represented by equation (4.7). Fourier Filtering (FF) method uses a uniform random variable  $rand() \in [0,1]$  to generate a complex function  $X(u, v)$  in the Fourier domain as

$$\left. \begin{aligned} X(u, v) &= r.e^{j\theta} \\ \text{where} \\ j &= \sqrt{-1} \\ r &= \frac{1}{(u^2 + v^2)^{\frac{H+1}{2}}} \cdot rand() \\ \theta &= \tan^{-1}\left(\frac{v}{u}\right). \end{aligned} \right\} \quad (4.9)$$

The PSD,  $P(f)$  is given as

$$P(f) \propto \frac{|X(u, v)|^2}{N^2} \quad (4.10)$$

where  $N^2$  is the total number of data points in a  $N \times N$  image..

The properties of fBm are

- $B_H(x, y)$  is non-stationary
- $B_H(x, y)$  is a Gaussian process
- $B_H(x, y)$  has stationary increments
- $\langle (B_H(x, y)) \rangle = 0$ , where  $\langle \rangle$  is the symbol for the expectant or mean
- $\langle (B_H^2) \rangle = \sigma^2 = 1$  is called standard fBm function
- $B(at) \cong a^H B(t)$  is the scaling property for  $a > 0$

- Power Spectral density

$$P(f) \propto \frac{1}{f^{2H+D_T}} \text{ where } D_T \text{ the topological dimension}=1 \text{ for 1D signal and } D_T=2$$

for 2D images

- Its covariance or auto correlation function is

$$\text{Cov}(B_H(s), B_H(t)) = \frac{\sigma^2}{2} \left( |t|^{2H} + |s|^{2H} - |t-s|^{2H} \right) \quad (4.11)$$

Figures 4.2 (a) and (b) show the fBm surfaces generated by using equations (4.7), (4.9) and (4.10) for  $H=0.9$  and  $H=0.1$  respectively. Initially a random number is generated and substituted in equation (4.9) for a point  $(u,v)$  in frequency domain to compute  $r$ ,  $\theta$  and  $X(u,v)$ . Inverse Fourier transform of  $X(u,v)$  is the desired fBm surface  $B_H(x,y)$ .

#### 4.1.3 Fractional Gaussian noise (fGn) (2D)

The increment of the fBm is the fGn process [3,4],  $\{V_H(t)\}_{t \in \mathbb{R}}$  is given as

$$V_H(t) = \lim_{\Delta x, \Delta y \rightarrow 0} \{B_H(t) - B_H(t + \Delta t)\} \quad (4.12)$$

The properties of fGn are

- $V_H(t)$  is stationary
- $\langle V_H(t) \rangle = 0$
- $\langle V_H^2 \rangle = \sigma^2 = \langle V(1)^2 \rangle$
- Power Spectral density

$$P_V(f) \propto \frac{1}{f^{2H-D_T}} \text{ where } D_T=1 \text{ for 1D signal and } D_T=2 \text{ for 2D images}$$

- Its covariance or auto correlation function is

$$\text{Cov}(V_H(t), V_H(t + \Delta t)) = \frac{\sigma^2}{2} \left( |\Delta t + 1|^{2H} - 2|\Delta t|^{2H} + |\Delta t - 1|^{2H} \right) = \frac{\sigma^2}{2} \delta^2(\Delta t^{2H}) \quad (4.13)$$

where  $\delta^2$  is the second difference operator. The  $H$  exponent measures the degree of self-similarity of the fGn type signal. When  $H=0.5$ , fGn is the Gaussian noise with  $\text{Cov}(V_{0.5}(s), V_{0.5}(t)) = 0$  for  $\Delta t > 1$ . By differentiation of synthetically generated fBm surface  $B_H(x,y)$ , fGn surface is generated which is shown in Figure 4.3 (a) and (b) for  $H=0.9$  and  $H=0.1$  respectively.

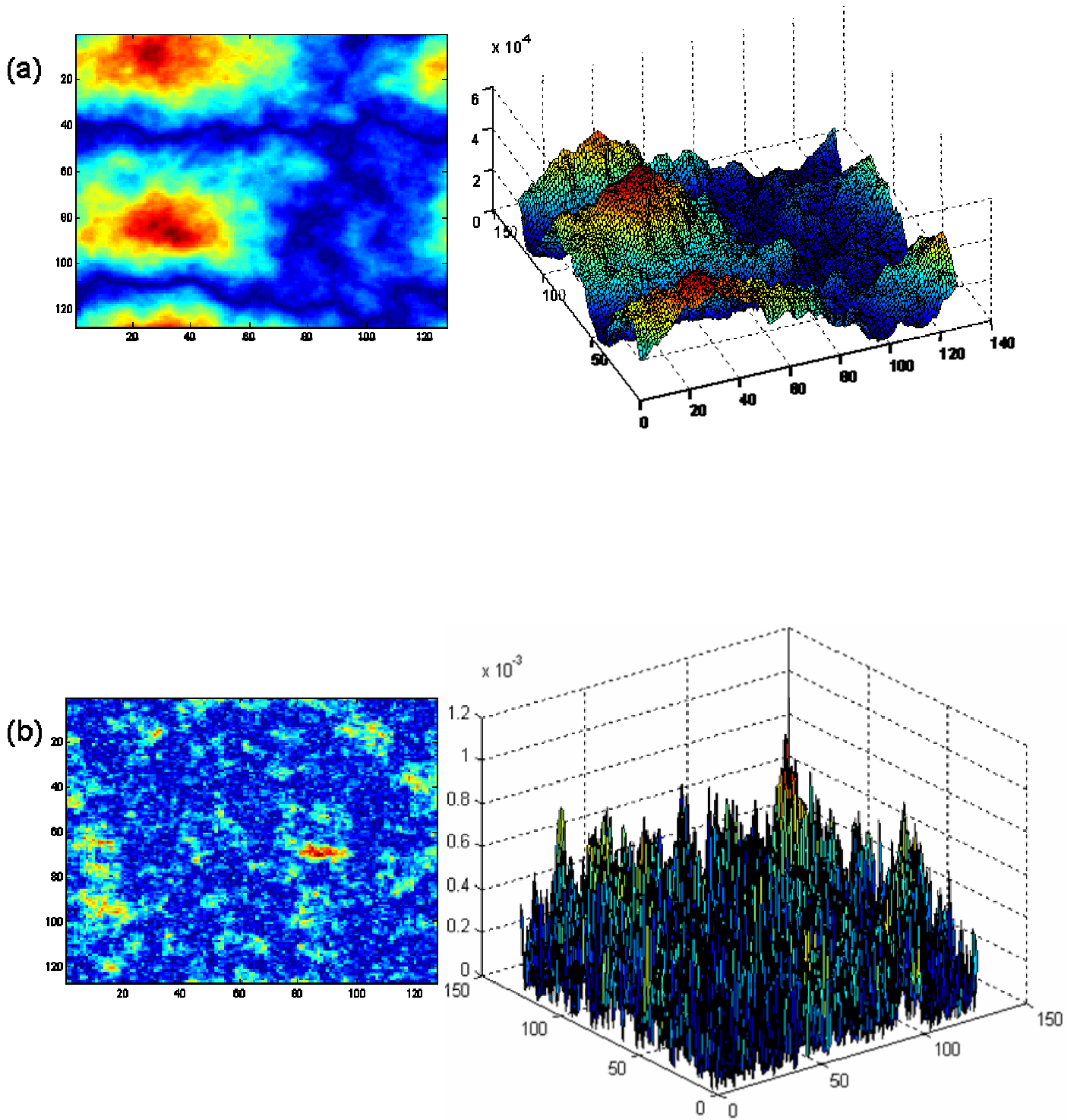


Figure 4.2: fBm images with 3D surfaces for a)  $H=0.9$  and b)  $H=0.1$

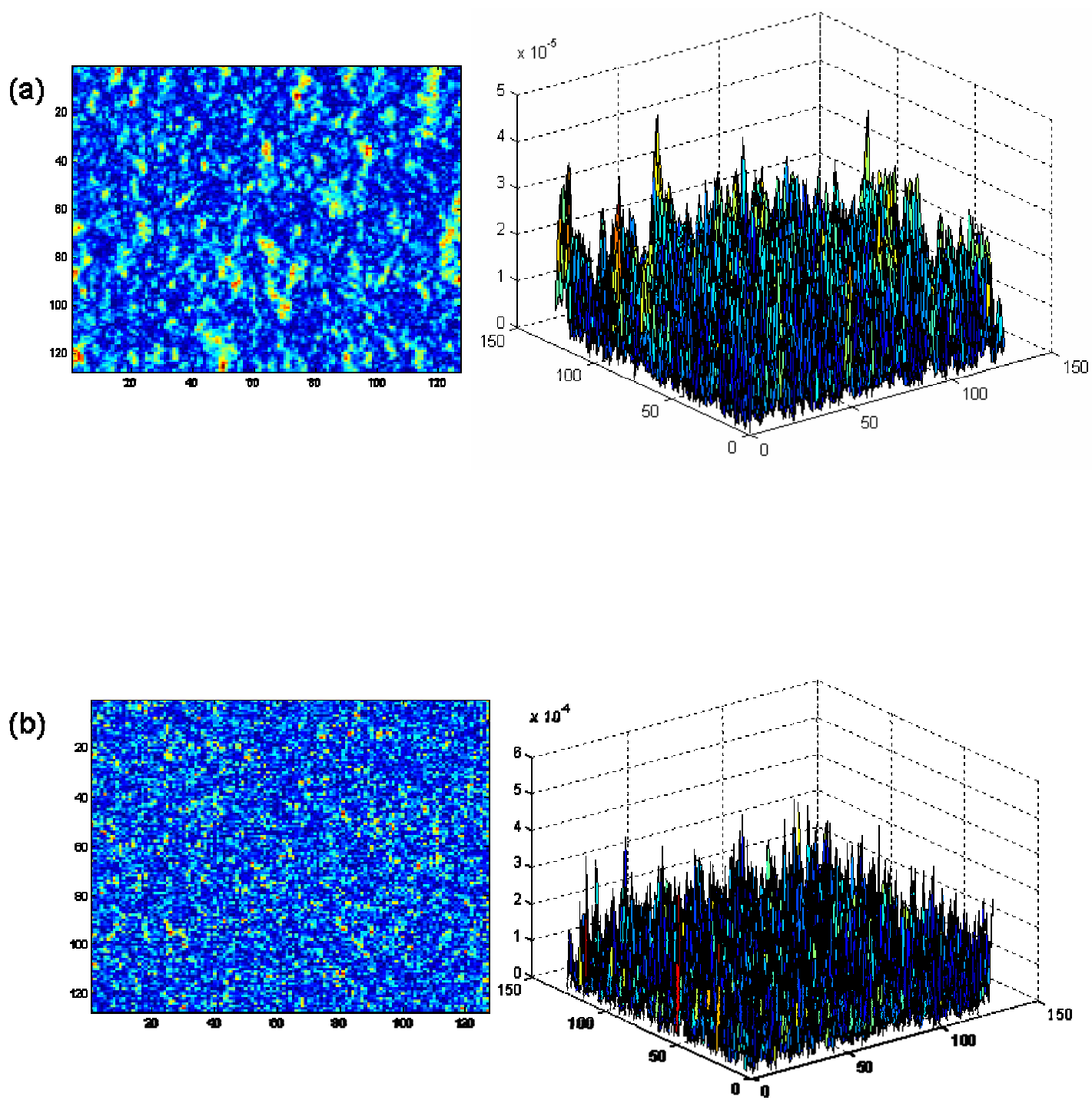


Figure 4.3: fGn images with 3D surfaces for c)  $H=0.9$  and d)  $H=0.1$

## 4.2 Results & discussion

For computing fractal dimensions from 1D signals and 2D images, three algorithms: R/S, PSD and Wavelet analyses have been implemented using MATLAB software package. The methods are presented in chapter 2 and detailed algorithms are given in Appendix-II. The fractal dimensions computed from the synthetic signals and images are verified with the same used for generating them.

For verifying the fractal analysis codes, synthetic 1D signals are generated by the WCF and synthetic images by the fBm algorithm. The  $H$  exponents computed by three methods are  $H_r$  for R/S method,  $H_p$  for PSD method and  $H_w$  for Wavelet method. To compute the  $H$  exponent, logarithmic correlations showing variations of the measured quantity with scale, known as Richardson plot or fractal plot, are presented in Table 4.1.

Table 4.1: Correlations and the Richardson plots by R/S, PSD and Wavelet analyses

Method	Correlations	Richardson plot	Hurst exponent
R/S	$\left\langle \frac{R(k)}{S(k)} \right\rangle = Ck^{H_r}$	$\log\left\langle \frac{R}{S}(k) \right\rangle = \log(C) + H_r \log(k)$	$H_r$
PSD	$P(f) \propto \frac{1}{f^{\beta_p}}$	$\log(P(f)) = \log(A) - \beta_p \log(f)$	$H_p = \frac{\beta_p - D_T}{2}$
Wavelet	$E(j) \propto \frac{1}{j^{\beta_w}}$	$\log(E(j)) = \log(B) - \beta_w \log(j)$	$H_w = \frac{\beta_w - D_T}{2}$

For natural images with fractal behaviour, the Richardson plot may not always remain linear. Nonlinearity in Richardson plot gives multi-fractal behaviour in fractal images or signals. Multi-linear behaviour, the ranges within which the multi-linearity prevails, and the corresponding slopes signify various physical phenomena responsible for the morphological or feature specific characteristic of the image. To obtain a uni-fractal quantification, standard practice is to omit few outliers particularly the initial and final data points (corresponding to too fine and too coarse scales) for fitting the straight line.

The robustness and applicability of the particular algorithm are ascertained by computing the percentage error which is the percentage difference between estimated  $H$  values and input  $H$  values used for generating the signal. The expression for the percentage error is given as

$$\%Error = \frac{100 * (Estimated - Input)}{Input} \quad (4.14)$$

For the synthetic fBm images, standard deviations of twenty images for  $H$  exponents varying from 0.1 to 1.0 with an increment of 0.05 are reported here.

#### 4.2.1 Verification of fractal analysis codes using Weierstrass Cosine Function (WCF)

The fractal 1D synthetic signals based on WCF are the input to the fractal analysis codes which estimate fractal dimensions or the  $H$  exponents. Table 4.2 presents the computed  $H$  exponents obtained by three methods. The table includes results for both the fBm and fGn type signals. Differences between the computed and exact values, presented in the form of percentage errors, are also given in the table.

Table 4.2:  $H_r$ ,  $H_p$  and  $H_w$  computed by R/S, PSD and Wavelet analyses for the Weierstrass cosine function.

H-input	RS				PSD				Wavelet			
	fBm $H_r$	fGn $H_r$	fBm %Error of $H_r$	fGn %Error of $H_r$	fBm $H_p$	fGn $H_p$	fBm %Error of $H_p$	fGn %Error of $H_p$	fBm $H_w$	fGn $H_w$	fBm %Error of $H_w$	fGn %Error of $H_w$
0.10	0.92	0.36	-819.49	-259.15	0.03	-0.63	72.94	734.37	0.04	-0.17	61.52	118.50
0.15	0.94	0.36	-523.91	-139.14	0.11	-0.56	26.28	473.65	0.09	-0.21	38.56	121.99
0.20	0.94	0.37	-371.81	-85.26	0.19	-0.49	4.91	346.24	0.15	-0.23	26.38	124.31
0.25	0.95	0.39	-278.79	-56.65	0.27	-0.43	-6.40	271.08	0.20	-0.24	19.24	125.13
0.30	0.95	0.42	-216.03	-39.48	0.34	-0.37	-13.44	222.47	0.26	-0.23	14.52	124.34
0.35	0.95	0.45	-170.96	-28.39	0.41	-0.31	-18.39	188.36	0.31	-0.21	11.15	122.08
0.40	0.95	0.48	-137.21	-20.58	0.49	-0.25	-22.08	162.01	0.37	-0.18	8.61	118.67
0.45	0.95	0.52	-110.71	-14.76	0.56	-0.19	-23.70	142.05	0.42	-0.14	6.64	114.56
0.50	0.95	0.55	-89.54	-10.09	0.62	-0.14	-23.19	127.36	0.47	-0.10	5.09	110.12
0.55	0.95	0.58	-72.32	-6.30	0.66	-0.09	-20.72	116.33	0.53	-0.05	3.85	105.66
0.60	0.95	0.62	-57.95	-3.10	0.71	-0.05	-17.87	107.60	0.58	-0.01	2.84	101.40
0.65	0.95	0.65	-45.77	-0.32	0.75	-0.01	-14.83	101.18	0.64	0.02	2.03	97.52
0.70	0.95	0.68	-35.20	2.25	0.80	0.02	-14.44	96.65	0.69	0.06	1.36	94.12
0.75	0.95	0.71	-26.10	4.72	0.85	0.05	-13.31	93.10	0.74	0.08	0.81	91.27
0.80	0.94	0.75	-18.08	6.87	0.89	0.06	-11.69	91.96	0.80	0.10	0.36	88.97
0.85	0.94	0.78	-11.05	8.73	0.94	0.09	-10.51	89.64	0.85	0.12	-0.01	87.21
0.90	0.94	0.80	-4.70	10.68	0.99	0.11	-9.47	88.13	0.90	0.13	-0.32	85.89
0.95	0.94	0.83	1.00	12.72	1.04	0.07	-9.42	92.22	0.96	0.14	-0.57	84.94
1.00	0.94	0.85	6.03	14.97	1.02	-0.01	-1.60	101.35	1.01	0.15	-0.78	84.29

Figures 4.4 (a) and (b) show the Richardson plots obtained by three methods for the WCF. For R/S and Wavelet methods the log-log plots are linear with correlation coefficients more than 0.9 (Figure 4.4 (a)). However for the PSD analysis, the correlation coefficient is very low (Figure 4.4 (b)). A change in data range could not improve the correlation coefficients. Nevertheless the  $H$  exponents calculated from the slopes are found to be close to the input  $H$ .

Figure 4.5 shows the correlation between the estimated and actual values for the fBm type signal. While PSD and Wavelet analyses show good correlations between estimated and the input  $H$  exponents, R/S analysis gives very high percentage errors particularly for low values of  $H$ . This demonstrates that R/S analysis can not be used as an estimator of fBm type signal. This observation is in agreement with the similar work reported by Li [7]. It was reported that for fBm type signal,  $H$  exponents estimated by the R/S and PSD analyses are not the same i.e.  $H_r(fBm) \neq H_p(fBm)$ . To be in agreement of  $H$  exponents, the fBm signal needs to be transformed to fGn for R/S analysis. It was demonstrated by Li that  $H_r(fGn) = H_p(fBm)$  which can be seen in Figure 4.5 as well.

For estimation of correct fractal dimensions, linear correlations between input and computed  $H$  exponent values are obtained. These linear correlations are the calibration equations. For R/S analysis to get comparable  $H$  values, fGn type signals are used. Table 4.3 presents the calibration equations, regression coefficients to show the goodness of fit, data range before and after calibration, for the three methods for the 1D signal. Improvement in the data range can be found after using the calibration equation for estimating the  $H$  exponents. Figure 4.6 shows percentage errors obtained before and after using the calibration equation for correction of the  $H$  exponents. Percentage errors for  $H$  are found to be less than 10% within the data range of 0.25 to 0.95 for the worst performing PSD analysis.

Table 4.3: Calibration equations for fractal analysis of 1D signal with the range of 0.1 to 1.0. Here  $x$  is the estimated Hurst exponent and  $y$  is the corrected Hurst exponent.

Method	Type	Calibration equations	Regression co-efficient	Range (before calibration)	Range (after calibration)
R/S analysis	fGn	$y = 1.6492x - 0.4183$	$R^2 = 0.9931$	0.49	0.81
PSD analysis	fBm	$y = 0.8772x + 0.0122$	$R^2 = 0.98$	1.01	0.88
Wavelet analysis	fBm	$y = 0.9285x + 0.0608$	$R^2 = 1$	0.97	0.90

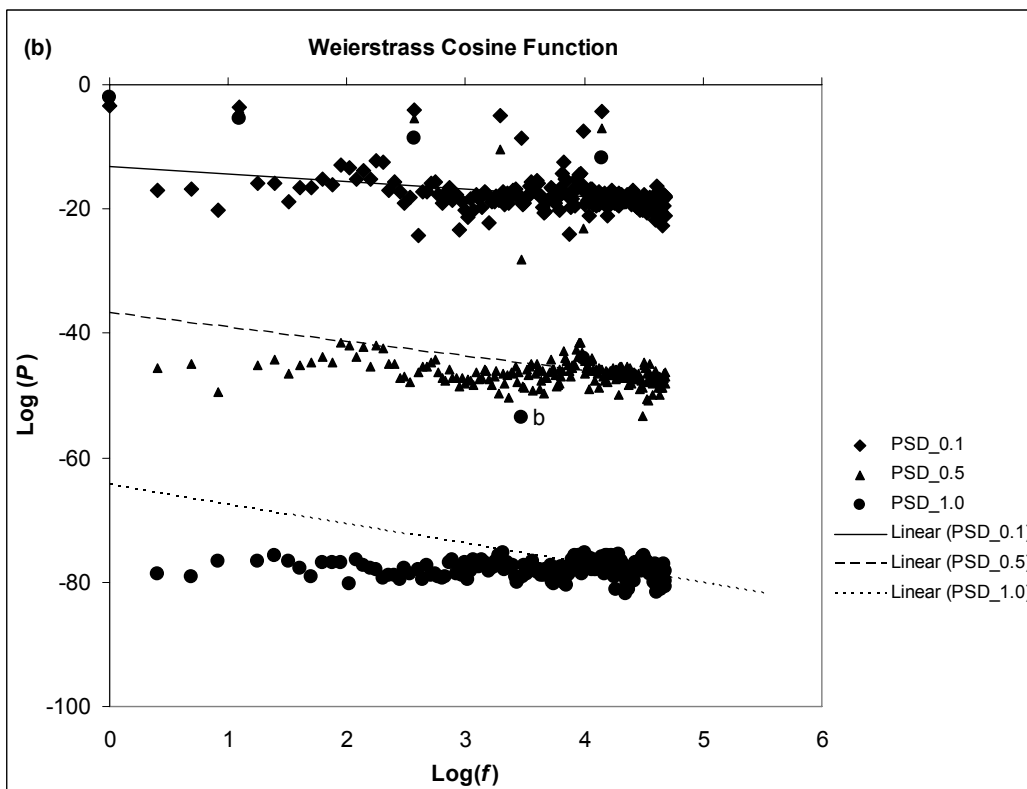
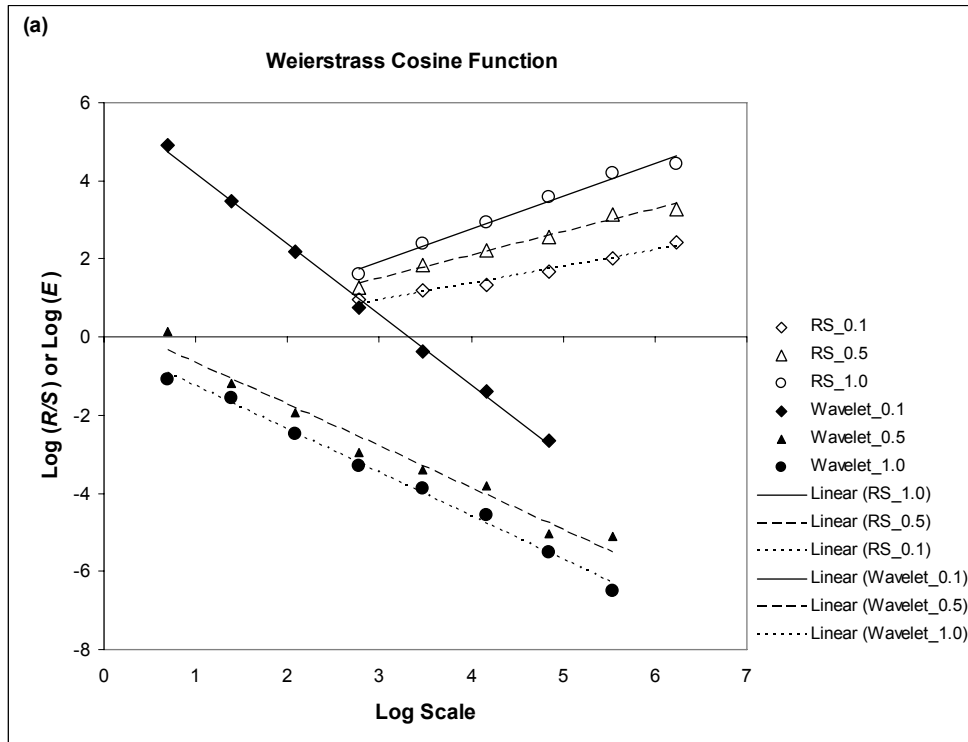


Figure 4.4: Richardson plots for Weierstrass cosine function by a) RS and Wavelet analyses  
b) PSD analysis

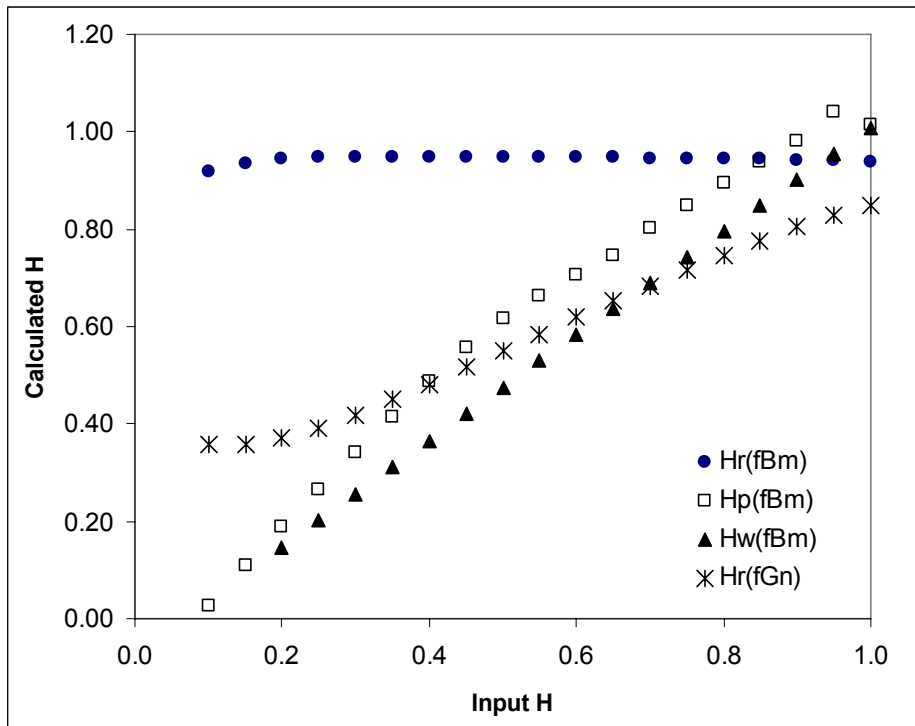


Figure 4.5: Correlation between calculated H and input H for the fBm type Weierstrass cosine function (WCF). Note that R/S`analysis generates the worst results for the fBm form of the`WCF. The results improve when fGn type was used.

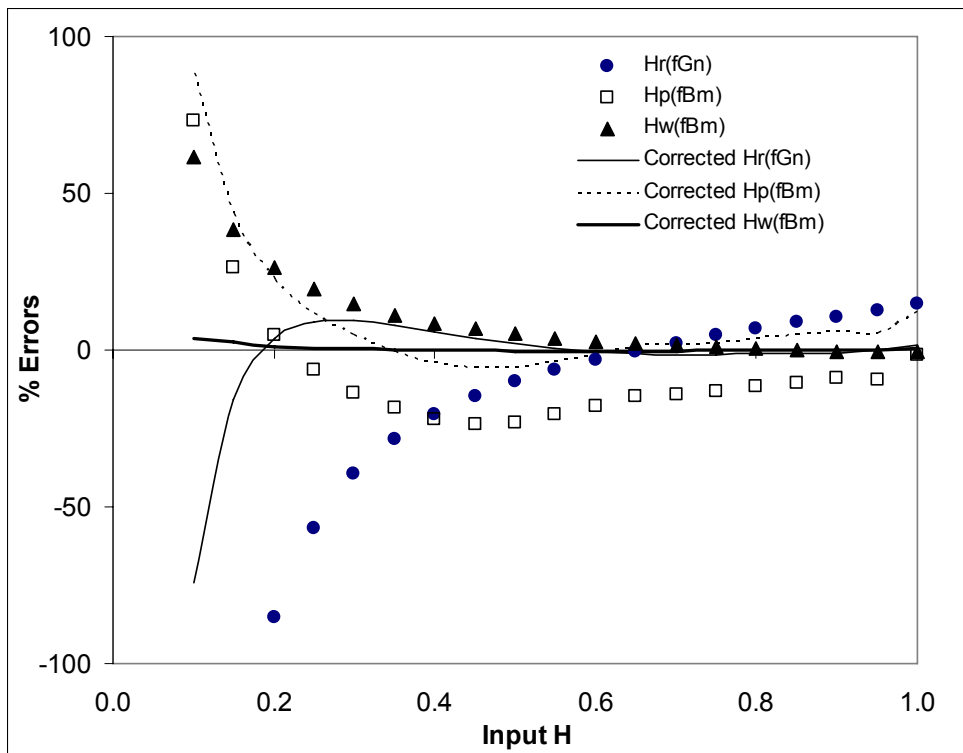


Figure 4.6: % Errors estimated using calibrated Hurst exponent values for WCF before and after using the calibration equation. Note that Wavelet analysis generates the best results.

#### 4.2.2 Verification of fractal analysis codes using fBm images

For verification of the developed fractal analysis codes, fBm type synthetic images have been generated using Fourier filtering algorithm as described in section 4.1. Variation of complexity is incorporated in the image by the  $H$  exponent. Complexity of the surface increases with decreasing  $H$  where  $0 \leq H \leq 1$ . Input  $H$  was varied from 0.1 to 1.00 with an interval of 0.05 for generating 19 sets of synthetic images. For each set 20 images were generated stochastically using random variables. The 3D representations of the fBm type synthetic images are shown in Figure 4.2. To obtain fGn type of image, shown in Figure 4.3, first derivatives or gradient of the fBm image is taken.

Tables 4.4 presents the estimated  $H_r$ ,  $H_p$  and  $H_w$  obtained respectively by the R/S, PSD and Wavelet analyses. Standard deviations of the  $H$  exponents for 20 images are included in the same table. Variations of the standard deviations show the randomness of the images generated for a specific  $H$  exponent and may not have effect on the robustness of the algorithm used. It may be understood from the listed results that Wavelet analysis is more sensitive to the randomness than the R/S analysis since the standard deviations for the Wavelet analysis has wider range. Richardson plots for the fBm images are given in Figures 4.7 (a) and (b). For the PSD analysis, unlike WCF implementation, the correlation between logarithmic power and frequency is linear and the correlation coefficient is found to be more than 0.9. The R/S and Wavelet analyses of the fBm images show linear correlations with correlation coefficients more than 0.95 as well.

Figure 4.8 presents variations of estimated  $H$  from fBm images with the input  $H$ . From the deviation between the input and estimated values, it is found that errors are approximately within  $\pm 20\%$  for the  $H$  computed by PSD and Wavelet analysis, however for R/S analysis the errors are found to be substantial. R/S analysis fails to generate correct  $H$  exponent for the fBm type signal, as discussed earlier, particularly for lower  $H$  exponent. The results are improved when fGn type images are used. This can be seen in Figure 4.8, where the correlation between estimated  $H$  and the input  $H$  is improved when fGn type images are used for the R/S analysis.

Using the input and estimated  $H$  parameter, the calibration equations are derived which are presented in Table 4.5. These calibration equations are used for correction of the  $H$  exponents when real images are analyzed. After calibration the data range improves remarkably from 0.25 to 0.86 for R/S analysis. Figure 4.9 shows the percentage errors for the calibrated  $H$  exponents, where the errors are within 10% for the PSD and Wavelet analysis and relatively higher for the R/S analysis.

Table 4.4 The Hurst exponents estimated R/S, PSD and Wavelet analyses of 380 images. For R/S analysis fGn type images were used.

<i>H-input</i>	R/S Analysis					PSD Analysis					Wavelet analysis				
	Average $H_r$	Corr. $H_r$	SD	% Error for $H_r$	% Error corr. $H_r$	Average $H_p$	Corr. $H_p$	SD	% Error for $H_p$	% Error corr. $H_p$	Average $H_w$	Corr. $H_w$	SD	% Error for $H_w$	% Error corr. $H_w$
0.10	0.48	0.06	0.04	377.77	-37.00	0.04	0.09	0.07	-63.45	-10.52	0.02	0.07	0.07	-75.33	-29.62
0.15	0.51	0.16	0.05	238.23	8.56	0.15	0.20	0.07	-3.17	31.98	0.08	0.13	0.09	-45.21	-16.12
0.20	0.55	0.29	0.06	172.98	46.58	0.17	0.22	0.07	-17.34	9.00	0.20	0.24	0.08	-0.48	19.22
0.25	0.52	0.21	0.05	108.79	-15.12	0.19	0.24	0.07	-25.39	-4.33	0.23	0.27	0.08	-6.96	8.32
0.30	0.56	0.35	0.06	87.55	16.52	0.26	0.31	0.07	-14.62	2.89	0.27	0.31	0.09	-10.17	2.12
0.35	0.58	0.40	0.07	65.19	14.82	0.27	0.32	0.09	-24.00	-9.00	0.37	0.41	0.12	6.33	15.81
0.40	0.56	0.35	0.05	40.91	-11.78	0.34	0.39	0.07	-14.75	-1.66	0.42	0.45	0.07	3.97	11.87
0.45	0.60	0.47	0.06	33.11	4.92	0.38	0.44	0.06	-14.69	-3.07	0.48	0.50	0.10	5.56	12.11
0.50	0.60	0.46	0.06	19.35	-7.08	0.46	0.51	0.07	-8.99	1.44	0.53	0.55	0.10	5.09	10.62
0.55	0.61	0.50	0.05	10.28	-9.51	0.51	0.56	0.07	-7.55	1.91	0.61	0.63	0.10	10.22	14.72
0.60	0.62	0.55	0.06	3.47	-9.01	0.58	0.63	0.06	-3.32	5.33	0.65	0.68	0.11	8.99	12.82
0.65	0.65	0.63	0.08	-0.56	-2.75	0.60	0.65	0.07	-8.09	-0.12	0.74	0.76	0.10	13.57	16.64
0.70	0.70	0.80	0.07	-0.47	14.58	0.63	0.69	0.09	-9.44	-2.04	0.81	0.83	0.10	16.21	18.67
0.75	0.69	0.78	0.07	-8.06	3.73	0.70	0.75	0.08	-6.75	0.14	0.87	0.89	0.12	16.02	18.05
0.80	0.70	0.80	0.09	-12.80	0.62	0.75	0.81	0.08	-5.78	0.67	0.89	0.91	0.11	11.46	13.26
0.85	0.73	0.91	0.08	-14.28	7.04	0.80	0.86	0.07	-5.31	0.74	0.92	0.94	0.09	8.56	10.12
0.90	0.72	0.90	0.07	-19.47	-0.36	0.86	0.91	0.09	-4.43	1.28	1.00	1.01	0.09	11.58	12.73
0.95	0.72	0.89	0.05	-24.00	-6.59	0.91	0.96	0.08	-4.29	1.11	1.03	1.04	0.13	8.33	9.33
1.00	0.73	0.92	0.10	-26.77	-7.79	0.95	1.00	0.06	-4.77	0.35	1.15	1.16	0.10	15.23	15.73

SD: Standard Deviation

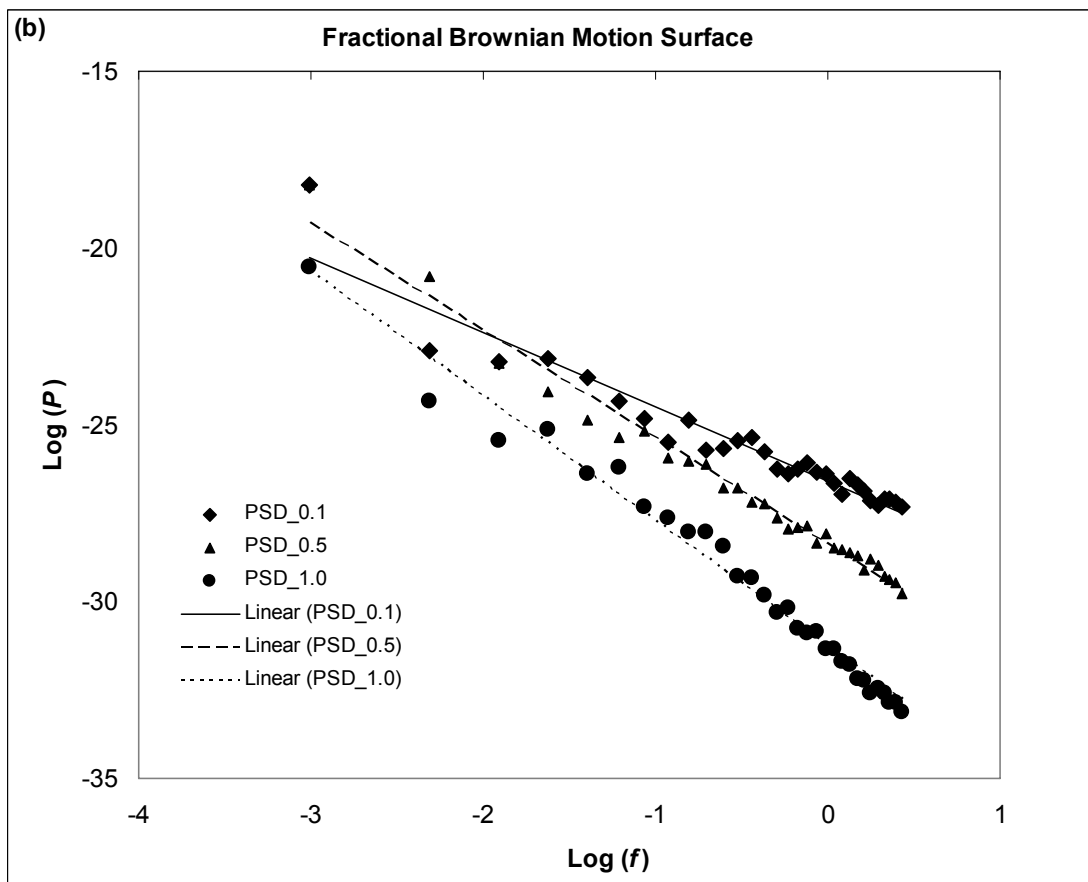
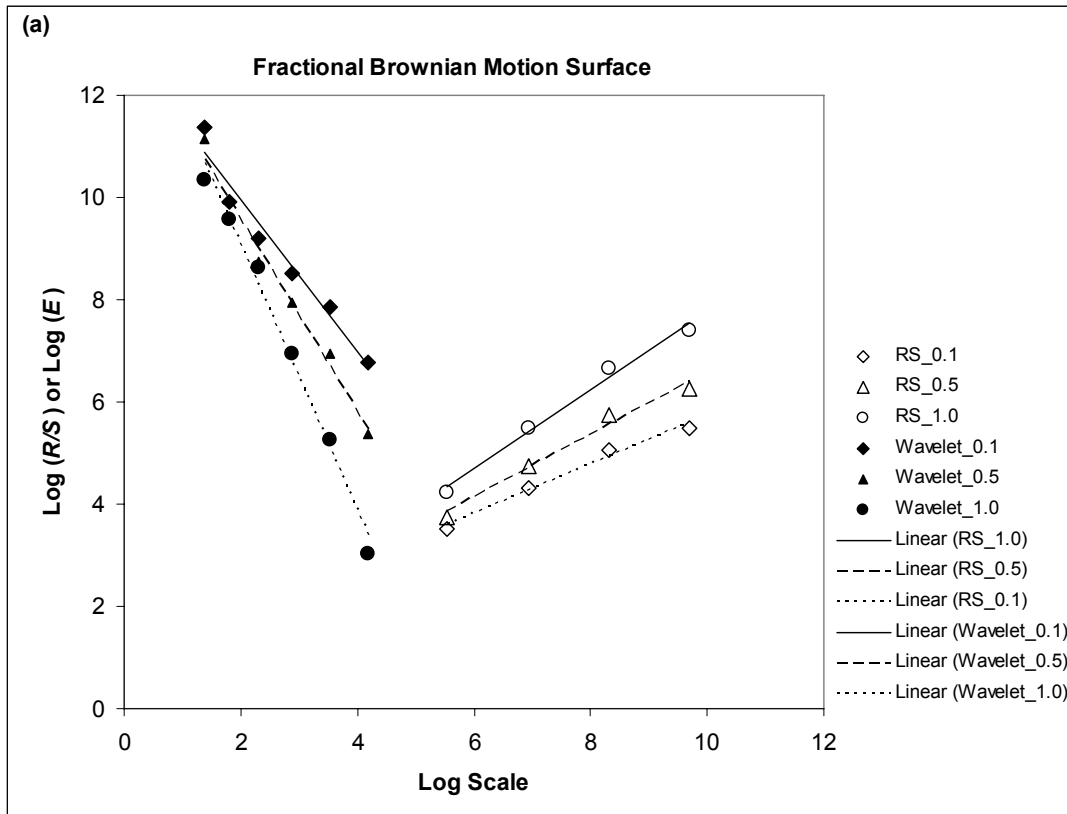


Figure 4.7: Richardson plots for fBm images by a) RS and Wavelet analyses b) PSD analysis

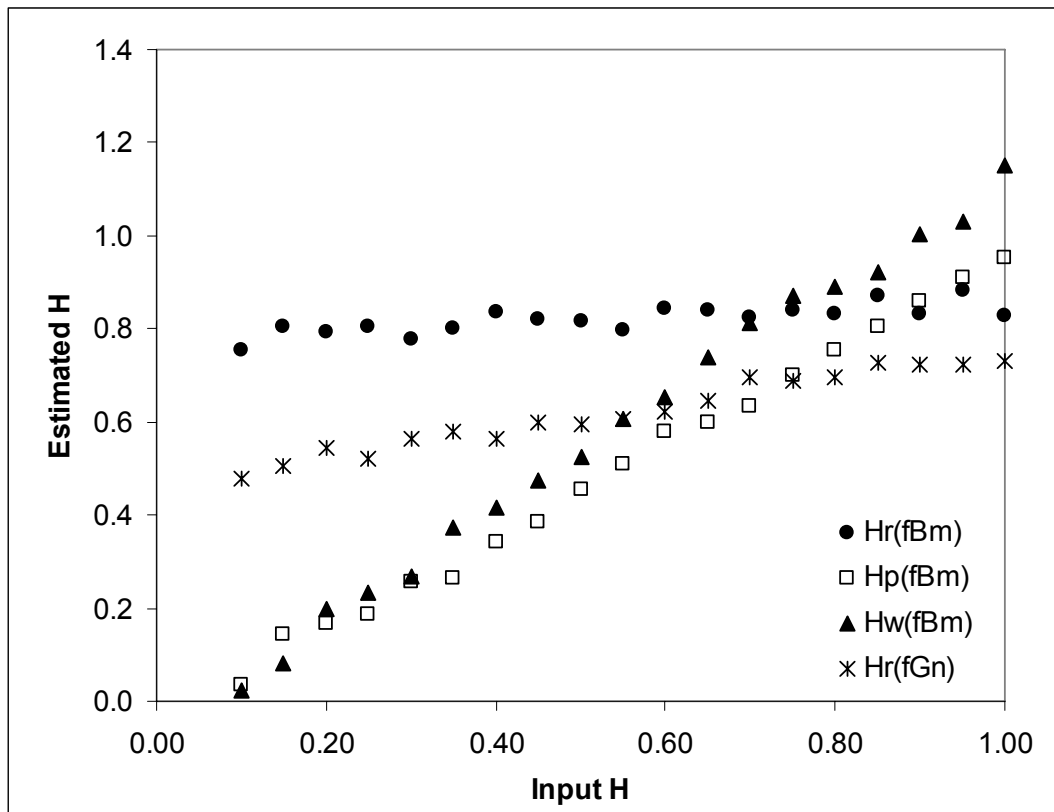


Figure 4.8: Correlation between calculated  $H$  and input  $H$  for synthetic images. Note that R/S analysis generates better results for fGn type image.

Table 4.5: Calibration equations for fractal analysis of image. Here  $x$  is the estimated Hurst exponent and  $y$  is the corrected Hurst exponent.

Method	Type	Calibration equations	Regression co-efficient	Range (before calibration)	Range (after calibration)
R/S analysis	fGn	$y = 3.3755x - 1.5497$	$R^2 = 0.9638$	0.25	0.86
PSD analysis	fBm	$y = 0.9933x + 0.0515$	$R^2 = 0.9961$	0.92	0.91
Wavelet analysis	fBm	$y = 0.8231x + 0.0614$	$R^2 = 0.995$	1.13	0.93

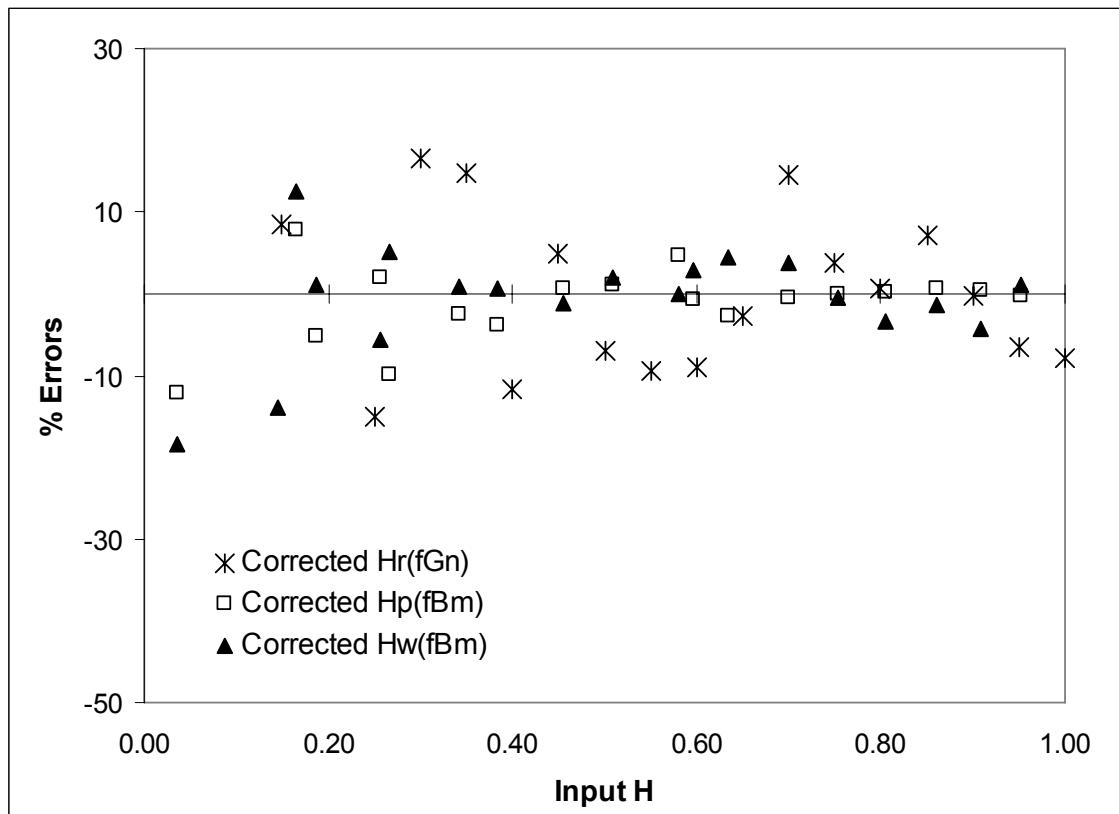


Figure 4.9: % Errors estimated using the Hurst exponent values for the fBm type images

### 4.3 Conclusions

In this chapter validation report of the fractal analysis codes based on R/S, PSD and Wavelet methods, which have been used for computing fractal dimensions for microstructural and fractographic images in this work, has been presented. Synthetic 1D signals based on Weierstrass Cosine Function (WCF) and images based on fractional Brownian motion (fBm) were generated for the  $H$  exponent varying between 0.1 and 1.0 with an increment of 0.05. Analysing 19 WCF signals and 380 fBm images by three fractal analysis algorithms, the following conclusions can be made:

- While PSD and Wavelet analysis for estimating  $H$  show good correlations, R/S analysis generates very high percentage errors particularly for low values of  $H$ . Usage of fGn type signal and images instead of fBm type for the R/S analysis reduces the errors.
- Percentage errors are found to be very high for low values of  $H$  exponent for all three methods. Amongst those, Wavelet appears to be the best method and R/S analysis is the worst estimator of 1D signals.

- Percentage errors are minimized by using calibration equations which essentially the straight lines correlating input  $H$  with the estimated  $H$  values when the fBm type signals are taken as standard. The correlation coefficient is found to be excellent for all the methods.
- Analysis of 380 fBm type images show standard deviations varying between 0.04 and 0.13. Variations of the standard deviations show the randomness of the images generated since they are generated using random functions. Wavelet analysis is more sensitive to the randomness than the R/S analysis since Wavelet analysis generates greater range of standard deviations.

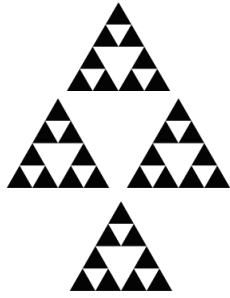
#### 4.4 References

1. Heinz-Otto Peitgen and Dietmar Saupe, ed.: The Science of Fractal Images, 1988, Springer Verlag, Berlin, Germany.
2. Stefan Jansson: Evaluation of methods for estimating fractal properties of intensity images, Master's Thesis in Computer Science, 2006, Umea University, Umea, Sweden.
3. B. B. Mandelbrot: The Fractal Geometry of Nature, 1983, W. H. Freeman, New York.
4. K. Falconer: 'Fractal geometry- Mathematical Foundations and Applications', 1990, John Wiley & Sons Ltd., Baffins Lane, Chichester, West Sussex PO19 1UD, England.
5. Xinxia Jiang: Fractal analysis of topography and reflectance surfaces, PhD thesis, 1998, University of Southampton, UK.
6. Weierstrass function. (2008, June 14). In *Wikipedia, The Free Encyclopedia*. Retrieved 11:35, August 8, 2008, from [http://en.wikipedia.org/w/index.php?title=Weierstrass\\_function&oldid=219364729](http://en.wikipedia.org/w/index.php?title=Weierstrass_function&oldid=219364729)
7. Chun-Feng Li: Rescaled  $\gamma$ -range and power spectrum analyses on well-logging data, *Int. Journal of Geophysics*, 153, 201-212(2003).

# CHAPTER 5

<b>5.0 Fractal analysis of microstructural images</b>	
5.1 Preparation of metallographic samples	110
5.2 Results and discussion	111
5.2.1 Effect of magnification, spatiality and image preprocessing	112
5.2.2 Self-similar & self-affine characteristics of microstructural images	115
5.2.3 Fractal analysis of microstructural images	121
5.2.4 Correlations between fractal dimensions and material properties	126
5.3 Conclusions	129
5.4 References	130





# 5

## FRACTAL ANALYSIS OF MICROSTRUCTURAL IMAGES

Investigation of materials invariably requires usages of high resolution images of material structures captured by Scanning Electron Microscopes (SEM), Transmission Electron Microscopes (TEM) and/or Atomic Force microscopes (AFM) for microstructural characterization and quantification of microstructural features, and subsequent establishment of correlation of the quantitative parameters with the material properties. Often microstructural images of materials exhibit self similar structures or patterns. These patterns are formed due to network of grain boundaries, presences of precipitates, uneven surface elevations, *etc.* Microstructural images containing self similar patterns at different scales or resolutions are said to have fractal property. It is unaffected by translations, rotations, projections and many other operations with regard to images. This makes the fractal analysis a useful technique for quantifying microstructural images by fractal dimensions.

This chapter presents fractal analysis of a set of microstructural images of high strength low alloy (HSLA) steel. Preparation of samples of metallic materials in order to acquire SEM images with prominent morphological characteristics is an involved task. Detailed discussion on the procedure is given in the first section followed by results and discussion and conclusions.

## **5.1 Preparation of metallographic samples**

The SEM microstructure is obtained by etching the specimen surface by an appropriate chemical reagent which is selected according to the material used. Typically micrographs are analysed for measuring grain size, identifying various microstructural phases along with their distributions, and to ascertain chemical homogeneity. In addition, formation of sub structures due to precipitation and plastic deformation is identified and measured from micrographs. Since the grain boundaries and some precipitates like carbides, nitrides, *etc* are chemically more active, they are etched more forming grooves or pits. The differential scattering of secondary and back scattered electrons by constituent parts of microstructure aids identification of various sub structures in the SEM images. Features observed under the microscope therefore depend upon the surface preparation procedure. This would subsequently affect the intensity or brightness of an image.

For the preparation of metallographic samples, specimens of HSLA steel at various aging conditions have been used. The heat treatment scheme and the corresponding mechanical properties are given in Appendix-I. Various steps followed for the preparation of metallographic samples are described below:

*Cutting:* Slow speed diamond cutter (ISOMET 4000) was used for cutting out samples of approximately 1cm x 1cm x 1cm dimension.

*Mounting:* The samples were mounted using the conductive copper powder in a molding machine. The sample surface is exposed when it is fixed inside the solidified copper mold.

*Grinding:* This process eliminates uneven surface elevation due to the mounting of the sample in the copper mold. The exposed surface becomes flat since the surface inclination is eliminated.

*Paper polishing:* To generate a polished surface, emery papers of various grid sizes were used. The coarsest paper was used first and finally ended with the finest one. The grid sizes

used here were 80, 120, 200, 400, 500, 800, 1000 and 1200 particles per square inch. This differential grinding helps to remove scratches.

*Cloth polishing:* This is the finest polishing for getting mirror finished surface. Alumina powder ( $\text{Al}_2\text{O}_3$ ) is used as abrasive. The  $\text{Al}_2\text{O}_3$  particles are of different sizes: 3 micron, 1 micron and 0.05 micron. In addition to Alumina polishing, to get a completely strain free mirror finished sample, Colloidal Silica (OPSOT) of 0.04 micron was used.

*Etching:* For etching the smooth sample, 4% nital (96%  $\text{C}_2\text{H}_5\text{OH}$ + 4%  $\text{HNO}_3$ ) is used. The sample is submerged for 40-50 seconds in the solution. The surface becomes dull which is cleaned in distilled water followed by acetone.

To examine the metallographic samples, JEOL JSM 840A SEM equipped with Noran Quest energy dispersive X-ray microanalysis (EDS) system was used. Digital images were stored in “jpg” format for fractal analysis.

## 5.2 Results and Discussion

Fractal dimensions were computed using the correlations between the frequencies/scales and the measured quantities like energy, power or R/S data, presented in Table 4.1. Higher the fractal dimension, higher the energy or power content in an image. Higher energy signifies more information in the image for which complexity in image increases.

Two types of images have been analysed for microstructural quantification. They are back-scattered electron (BE) and secondary electron (SE) images. Difference between these two image types and the electron imaging principles were discussed in chapter 2. Sensitivity of the fractal parameters with respect to magnifications, spatial locations and pre-processing of images are assessed and presented here. Three methods, namely, R/S analysis, PSD analysis and Wavelet analysis have been employed. Theoretical background and algorithms of these methods have been discussed in previous chapters. For denoting fractal analysis of microstructural images subscript “ $m$ ” is used, and for distinguishing methods, “ $r$ ”, “ $p$ ” and “ $w$ ” are used for R/S, PSD and Wavelet analyses respectively.

Selection of appropriate magnification for fractal quantification is imperative since natural images have multi fractal characteristics and fractal behaviour becomes prominent in certain length scales. To identify self-similar or self-affine characteristics of microstructural images, PSD analysis has been employed to ascertain the acceptable

magnification for image acquisition by the SEM. Fractal dimensions of microstructural images of the identified magnification are obtained and reported with appropriate error estimation for both the SE and BE images. Finally correlations between fractal dimensions and mechanical properties have been discussed.

### **5.2.1 Effect of magnification, spatiality and image preprocessing on fractal dimensions**

Invariance property of fractal dimensions has been investigated since it is important to check how sensitive the fractal parameter is if the operating conditions are changed. It is essential that the fractal dimension should be reproducible as well as that it remains invariant to various external operating conditions. In addition, the effects of spatiality *i.e.* image taken at various locations on the same specimen surface, and pre processing on fractal dimensions have also been investigated.

#### **a) Effect of magnification and spatiality**

The effect of magnification and spatiality on fractal dimension computed using BE and SE type images can be seen in Figure 5.1. The error bars shown in Figure 5.1 (a) were obtained by analysing 10 images captured from different locations of the same metallographic samples.

It can be pointed out that fractal dimensions vary with magnification. Generally negative correlation exists between fractal dimension and magnification. As the magnification increases, field of view decreases with increased details. Smaller field of view reduces the information content of the image and therefore fractal dimension reduces. Although at lower range of magnification, a positive correlation may exist. Since at very low magnification, micro details are not captured making the image featureless. The SE images have the similar inverse correlation with the magnification. However the fractal dimensions computed from the SE images are less than the same computed from the BE images which indicates that information or signal content in BE images are more than the SE images. There is a similarity trend found between fractal dimensions obtained by Wavelet method and RS method. Fractal dimensions estimated by the PSD method are found to be the lowest for magnification 2000x.

Effect of spatiality is presented for 1000 magnification in Figure 5.1 (b & d). It can be seen that, for the SE images, the effect is minimum for the Wavelet analysis, whereas for the

PSD analysis the variation of fractal dimension is  $\sim 12\%$ . Similar trend is found for the BE images. Fractal dimensions are found to be approximately invariant to the spatiality in all the cases.

### c) Effect of pre-processing

Two image pre-processing techniques such as histogram equalization and binarisation have been used for enhancing image quality as well as to distinguish prominent features prior to applying fractal analysis routines for both the BE and SE images. It has been specified in the previous sections that fractal dimensions of BE images are more than SE images. The trend remains the same for both the cases. Only results obtained from the BE images are presented here for better appreciation of results.

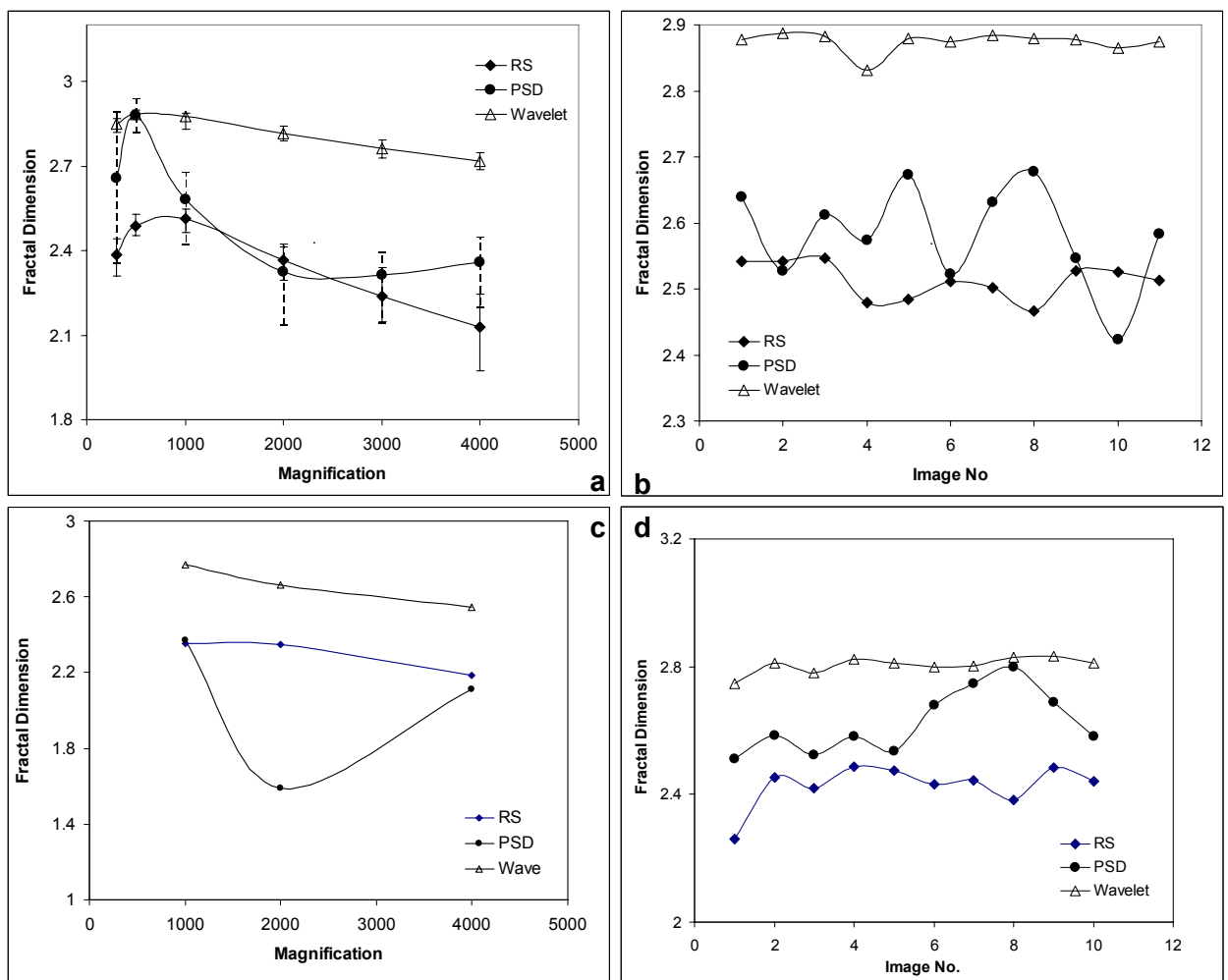
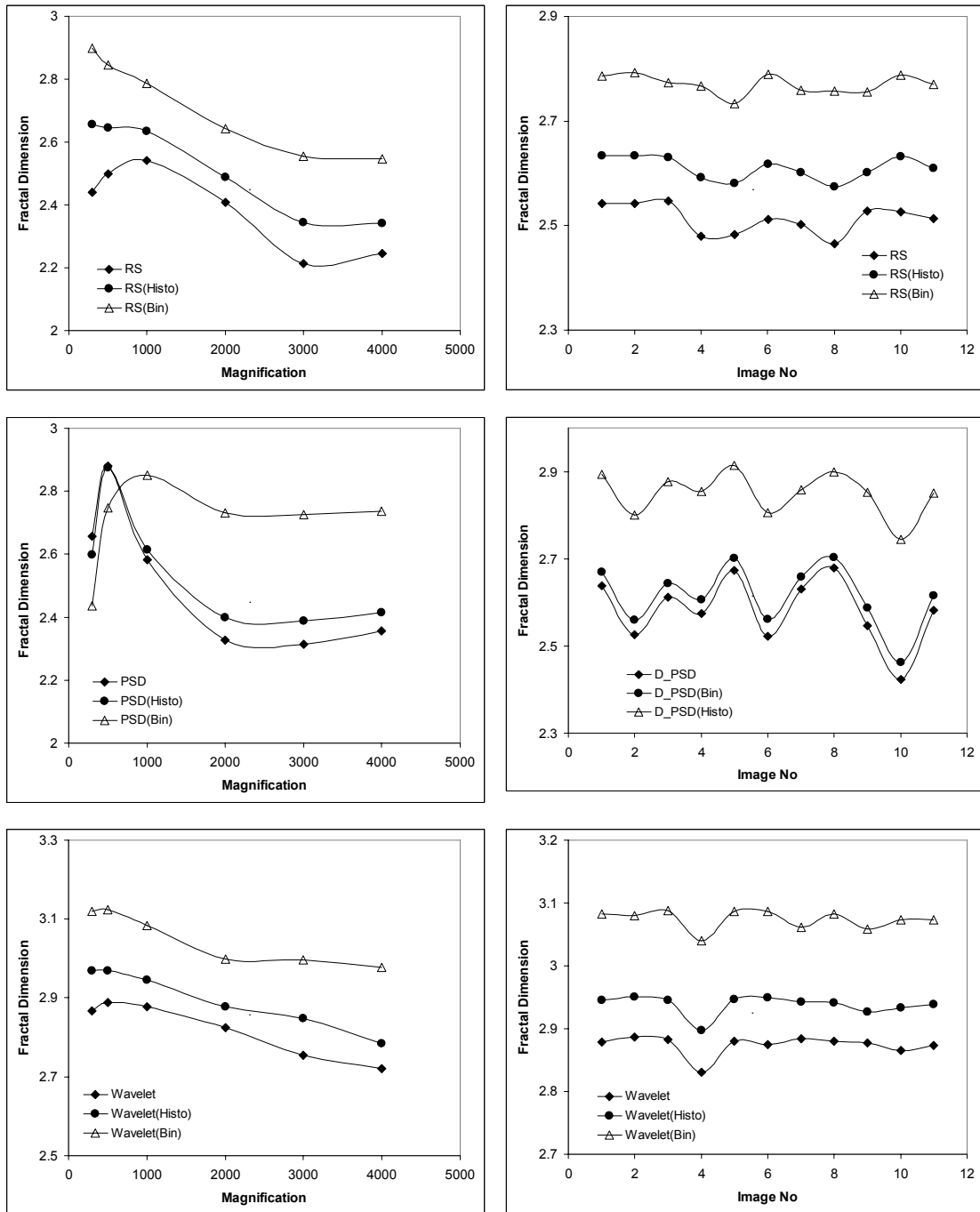


Figure 5.1: Variations of fractal dimensions with magnifications and spatiality a) magnification (BE) b) spatiality (BE) c) magnification (SE) and d) spatiality (SE).

Figure 5.2 show the effect of preprocessing on fractal dimensions estimated by three methods for the BE images captured at different magnifications and from different

locations of the same specimen. Each of the plots shows variations of average fractal dimensions estimated from un-processed imaged and the processed images as well. It can be seen that preprocessing changes fractal dimensions. For the binarised image, the computed fractal dimensions are the largest followed by the histogram equalization. The unprocessed image generates the lowest fractal dimensions. Similar trend is observed for the PSD and Wavelet analyses shown in the same figure.



a	b
c	d
e	f

Figure 5.2: Effect of preprocessing on fractal dimensions for BE type microstructural images captured at a) different magnification (RS), b) different spatiality (RS), c) different magnification (PSD), d) different spatiality (PSD), e) different magnification (Wavelet) and f) different spatiality (Wavelet).

### 5.2.2 Self-similar & self-affine characteristics of microstructural images

For the characterisation of materials, surfaces of materials are observed under high resolution microscopes with different resolving capabilities. The SEM is used for viewing objects by magnifying it 15 to 100,000 times or more. Magnification is controlled by varying the size of the probe by which an object is scanned. Low magnification micrographs can not be photographically enlarged or zoomed to obtain detailed information. This is because the magnification is controlled by changing the beam diameter or the probe size. For lower magnification, beam diameter is enlarged so that more area can be scanned with fewer details. Hence the resolution of the image formed on the display unit decreases, increasing the total field of view. Increasing resolutions aid in acquiring detailed and new features in microstructures which is not discernable in lower magnification. The new features may or may not have fractal characteristics. Since microstructure has multifractal characteristics, it is important to understand the appropriate length scales within which they remain self-affine and/or self-similar.

This section reports PSD method, based on fast Fourier Transformation (FFT) algorithm, adopted for verifying the statistical self similarity and self-affinity in microstructural images of HSLA steel. The procedure was first applied on synthetic images to show the degree of self similarity or self-affinity in them and finally it has been extended to microstructural images of HSLA steel. The technique proposed in this section needs to be used as a precursor to identify appropriate characteristic length (minimum length scale for measuring a complex or fractal object) and resolution for implementing fractal based quantification of microstructural images. As mentioned in earlier chapters, fractal based quantification is useful for understanding multi-dimensional or multifractal characteristic in microstructure and how these dimensions contribute to the evolution of different sub-structures and statistically self-affine geometric patterns in microstructural images of materials.

Images of microstructures were obtained for three different magnifications of 1000, 2000 and 4000 as shown in Figure 5.3. The area viewed under the maximum resolution (4000) was  $37.5 \times 37.5 \mu\text{m}^2$ , which approximately relates to a single grain size. Other resolutions would correspond to proportionately larger areas.

Figure 5.4 presents the radially averaged PSD characteristics with respect to the length scale in micron for images with 1000, 2000 and 4000 magnifications. In the same Figure, images of 2D power spectra are shown in insets.

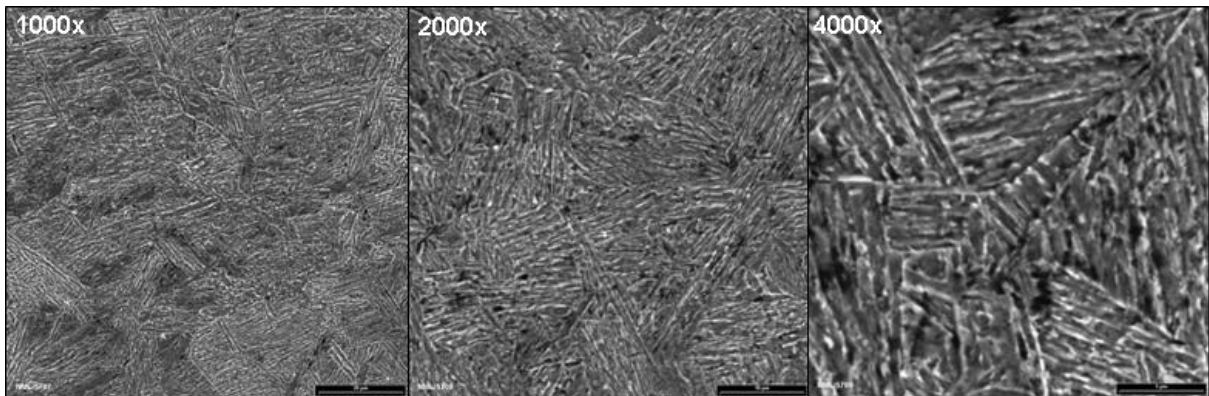


Figure 5.3: SEM images of microstructure for three different magnifications of 1000, 2000 and 4000

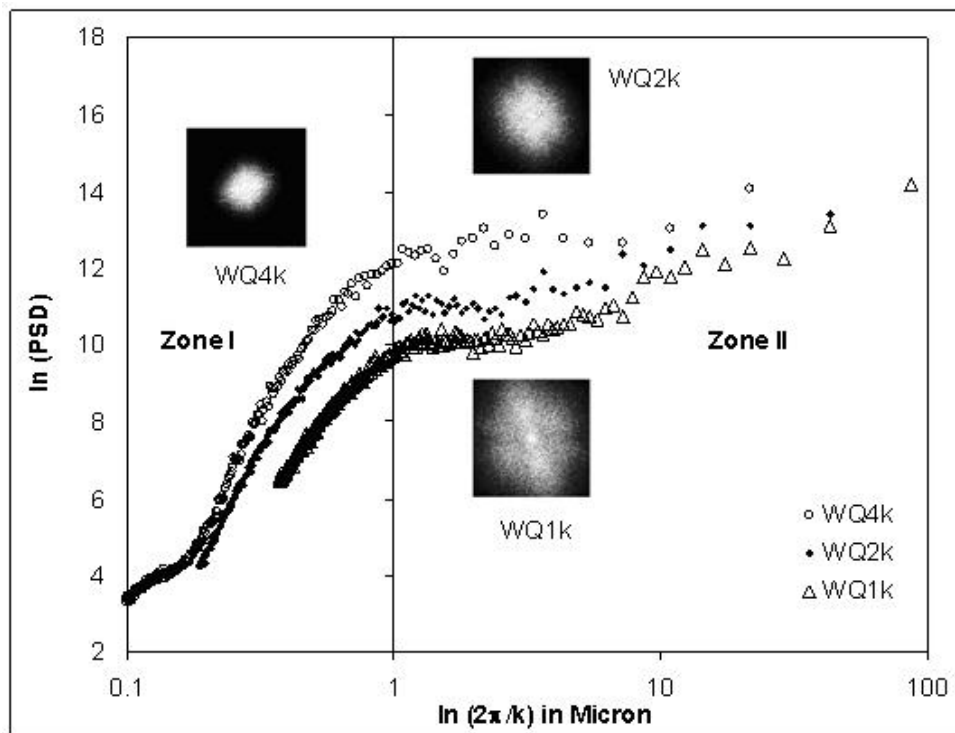


Figure 5.4: Radially averaged PSD characteristics with respect to the length scale in micron for images with 1000, 2000 and 4000 magnifications.

Following points are observed in the PSD characteristics of the HSLA microstructures:

- A bilinear trend in the log-log plots of the PSD vs. length scale with a unique cross over point at  $\sim 1\mu\text{m}$  for all the magnifications is observed.
- The estimated PSD value increases as the length scale increases.
- Data scatter is more at higher length scales.

Evidence of non-linear log-log plot of the PSD vs. scale is found in the literature [1-4]. The bilinear feature signifies two characteristics length scales and a crossover point [3,4]. Initial length scales when  $\lambda < 1\mu\text{m}$ , is referred to as zone I, where Hurst exponents obtained for the images were found to be more than 1 for 2000 and 4000 magnifications.

For length scale  $> 1\mu\text{m}$ , in zone II, negative Hurst exponent was obtained. The negative Hurst exponent signifies “monoscale” [5,6], where the effect of short length scale (high frequency component) is highly significant compared to the low frequency component as shown in Figure 5.5.

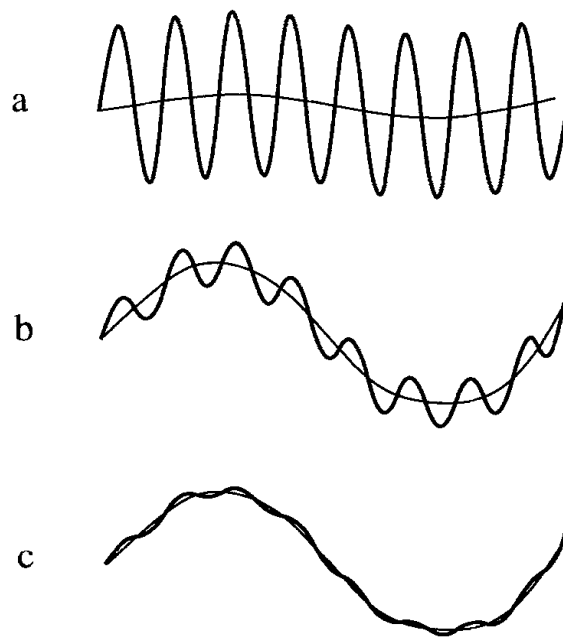


Figure 5.5: Scaling behaviour represented by the Hurst exponent a)  $H < 0$ , b)  $0 < H < 1$  and c)  $H > 1$

Reverse fractal characteristics between zone I and zone II can be appreciated from the classification of surfaces based on the Hurst exponent. Three types of surfaces according to  $H$  are reported as

(i)  $H < 0$ : “monoscale”, surface looks like a landscape with hills of approximately same size, the surface height is bounded; The results show that the slope  $\beta$  approaches 0 as the magnification increases when the length scale is more than  $1\mu\text{m}$ , indicating uncorrelated white noise ( $P(k)=\text{const}$ ). Fractal quantification is not recommended within this length scale.

(ii)  $0 \leq H < 1$ : “rough”, looks like rocky mountains with smaller and higher peaks and unbounded height; Microstructures represented by  $H$  within this range is classified as self-

affine fractal microstructures. Here microstructure at 1000 magnification is found to be self affine when the length scale is less than  $1\mu\text{m}$ .

(iii)  $H \geq 1$ : “smooth”, the largest scale defines the surface roughness. Within a single grain for 4000 resolution and proportionately larger area for 2000 resolution, self-similar characteristic is observed in the microstructure. Microstructural objects measuring less than  $1\mu\text{m}$  such as width of a single lath, interfaces between  $\alpha$ - $\alpha$  phases and  $\alpha$ - $\gamma$  phases, identifiable through intensity gradients in images, are found to be self-similar. The microstructure corresponding to large wave number or high frequency is thus self similar for high magnification observations.

Bilinear characteristic of the radially averaged power spectrum for the image of 1000 resolution is shown in Figure 5.6. For all resolutions, Table 8.2 gives the values of  $H$ ,  $D$ , the standard deviation (STD), standard error ( $\Delta\beta$ ), and corrected  $H$  and % error for computing  $D$  from the exponent  $\beta$ .

Table 5.2: Bilinear characteristic of the radially averaged FFT power spectrum of microstructural image for small and large length scales with corresponding  $D$  and  $H$  values.

ZONE I: Short length scale ( $\lambda < 1\mu\text{m}$ )									
Magnification	Slope, $\beta$	Offset	$R^2$	STD	SE, $\Delta\beta$	$H_{psd}$	$H_{corr}$	D	%Error (D)
1000	3.4317	16.4000	0.9789	0.4522	0.2778	0.72	0.77	2.23	6.23
2000	4.1921	19.5120	0.9679	0.1812	0.2690	1.10	1.16	1.84	7.30
4000	4.9000	22.3840	0.9764	0.2957	0.4140	1.45	1.52	1.48	13.94
ZONE II: Large length scale ( $\lambda > 1\mu\text{m}$ )									
1000	0.8129	11.1720	0.8755	0.1285	0.0605	-0.59	-0.56	3.56	0.85
2000	0.6889	11.9380	0.8210	0.1464	0.1638	-0.66	-0.62	3.62	2.26
4000	0.4354	13.0720	0.6041	0.1247	0.1397	-0.78	-0.75	3.75	1.86

Bilinear characteristics of the radially averaged power has been reported by previous investigators [3,4] for microstructures containing various forms of martensitic morphologies such as lenticular, thin plate, butterfly and lath. The results show that while the microstructure has self-affine ( $\beta=3.4317$  and  $H=0.7713$ ) behaviour for short length scale for 1000 magnification, it has negative  $H$  exponent i.e. it is monoscale at large length scales. Monoscale object has the spatial behavior which is dominated by a single characteristic length indicated by the cross over point in the bilinear radially averaged FFT power spectrum shown in Figures 5.4 and 5.6. For instance, the martensitic microstructure

can have characteristic lengths like width of the lath martensite, self-accommodating packets, a single grain, etc. Microstructure above the characteristic length scale more than  $1\ \mu\text{m}$  is classified as non-fractal or ‘monoscale’. The characteristic length scale of  $\sim 1\ \mu\text{m}$  indicates width of lath martensites which are diagonally oriented feature as explained using the power spectrum image. It is possible to specify the dimensionality of the self-accommodating packets (above  $1\ \mu\text{m}$ ) by analysing microstructures of lower magnifications as reported in reference [3]. The multi-scaling or multi-fractal behaviour of microstructure may limit the universality of fractal behaviour within wider length scales, however it elicits the morphological self-similarity or self-affinity which would have an intrinsic effect on the deformation behaviour of materials especially when the progressive evolution of microstructure creates random behaviour from the ordered structure. The lath martensite feature visible under the Transmission Electron Microscope (TEM) is shown in Figure 5.7 which shows diagonally oriented structure with width less than 1 micron.

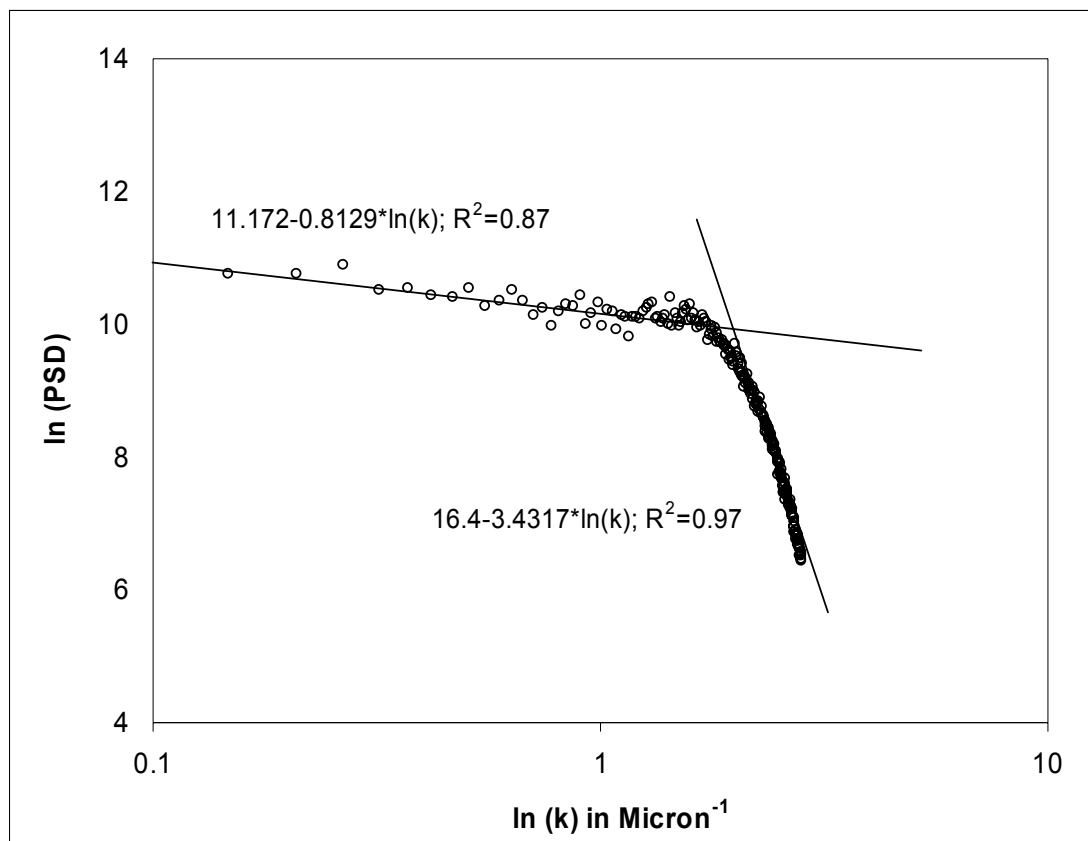


Figure 5.6: Radially averaged FFT power spectrum which has bilinear characteristic with a crossover point at  $\ln(k) \sim 2\ \mu\text{m}^{-1}$ .

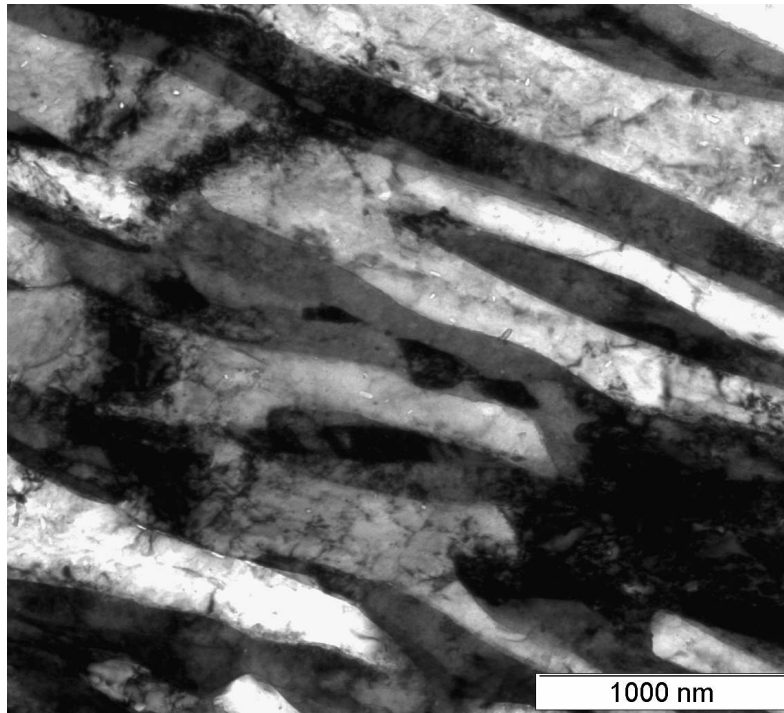


Figure 5.7: TEM image of microstructure at WQ condition showing diagonally oriented lath martensite

True fractal behaviour ( $2 < D < 3$ ) is only observed for the image with 1000 magnification having length scale less than  $1 \mu\text{m}$ . This result agrees with the same reported in [3] where light microscopic images were analysed. Additionally it can be seen that higher magnifications generate  $D < 2$  *i.e.*  $H > 1$ .

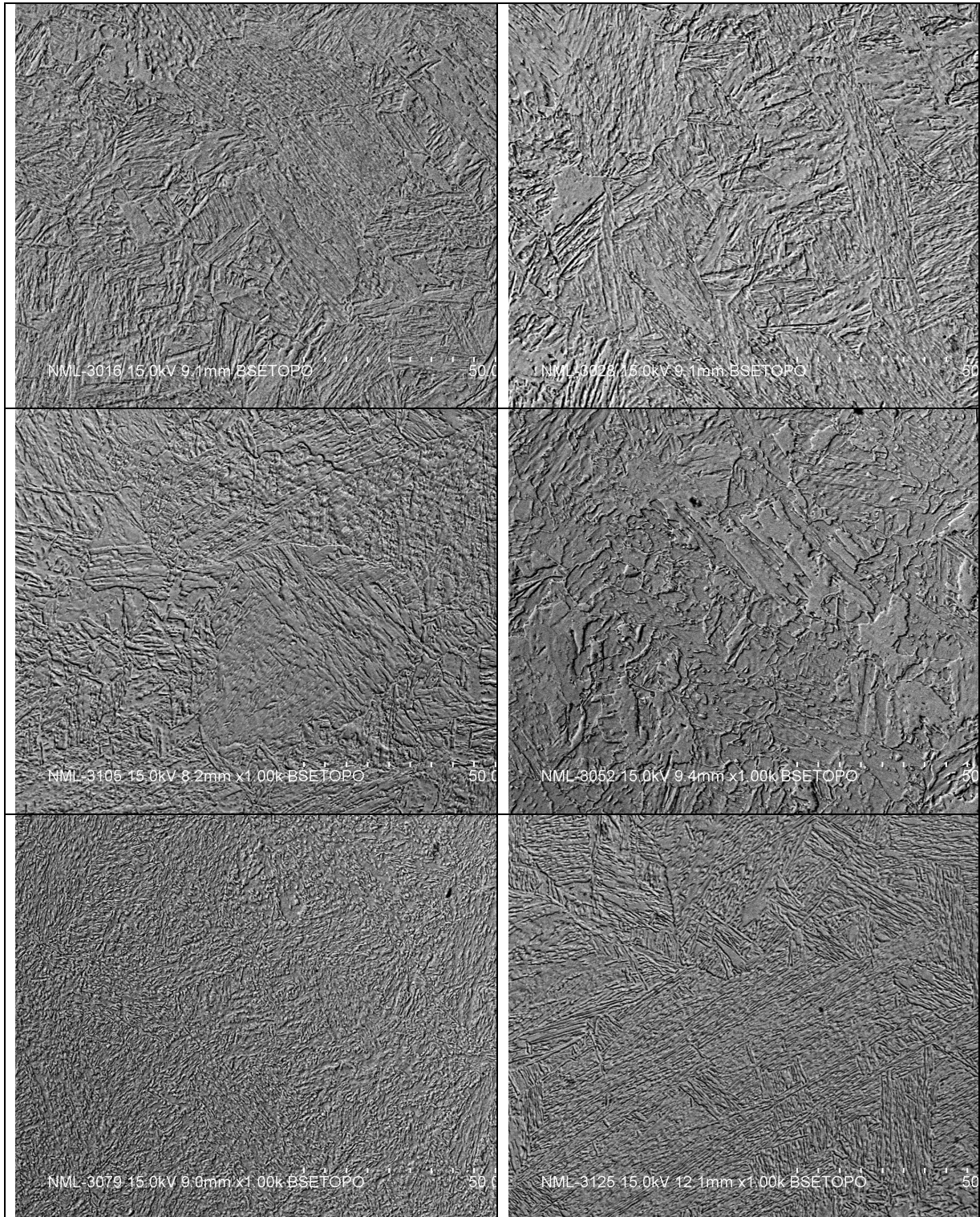
For estimating fractal dimensions from microstructural images, it is therefore important to recognize the length scales which can identify the true fractal behaviour. Too small characteristic length will always generate self-similar behaviour  $H \geq 1$  while larger length scales will result in “monoscale” random surface. In addition to the length scale, selection of magnification of the image is vital, if true fractal characteristics need to be evaluated. Additionally it may be pointed out that at high magnification electron-specimen interaction generates high level of noise in SEM images which impairs the Lambertian relationship between image intensity and fractal dimension representing surface roughness. This investigation concludes that images of 1000 magnification show true fractal behaviour for the length scale less than  $1 \mu\text{m}$  and “monoscale” fractal behaviour for length scale above 1 micron for images at all three magnifications.

### 5.2.3 Fractal analysis of microstructural images

The preceding section emphasizes that the magnification of 1000 be taken for acquiring microstructural images. Microstructural images for samples of WQ condition and tempering temperatures of 350°C, 450 °C, 550 °C, 650 °C and 675 °C were captured in BE and SE modes. Microstructural images in the intermediate temperatures (400°C, 500 °C, 600 °C and 700 °C) could not be made available for fractal analysis. Figures 5.8 and 5.9 show representative microstructural images of BE and SE types respectively. For each case, 10 images were taken from various regions of the metallographic sample to ascertain statistical relevance. Total 120 images were analysed and fractal dimensions are presented in this section. The logarithmic variations of R/S, power and energy with the scale or frequency of measurement for the R/S, PSD and Wavelet methods respectively are plotted in Figure 5.10. Each log-log plot presents data for both the BE and SE type images. The variations of measured quantity are found to be nominal for the images corresponding to two aging temperatures. The goodness of fitting of straight lines through the data points is excellent for the R/S analysis and found worst for the PSD analysis, although the regression coefficients are more than 0.9. It needs to be pointed out that for the R/S and Wavelet analysis methods, fractal dimensions remain scale invariant for three decades whereas for the PSD analysis they remain scale invariant in one decade.

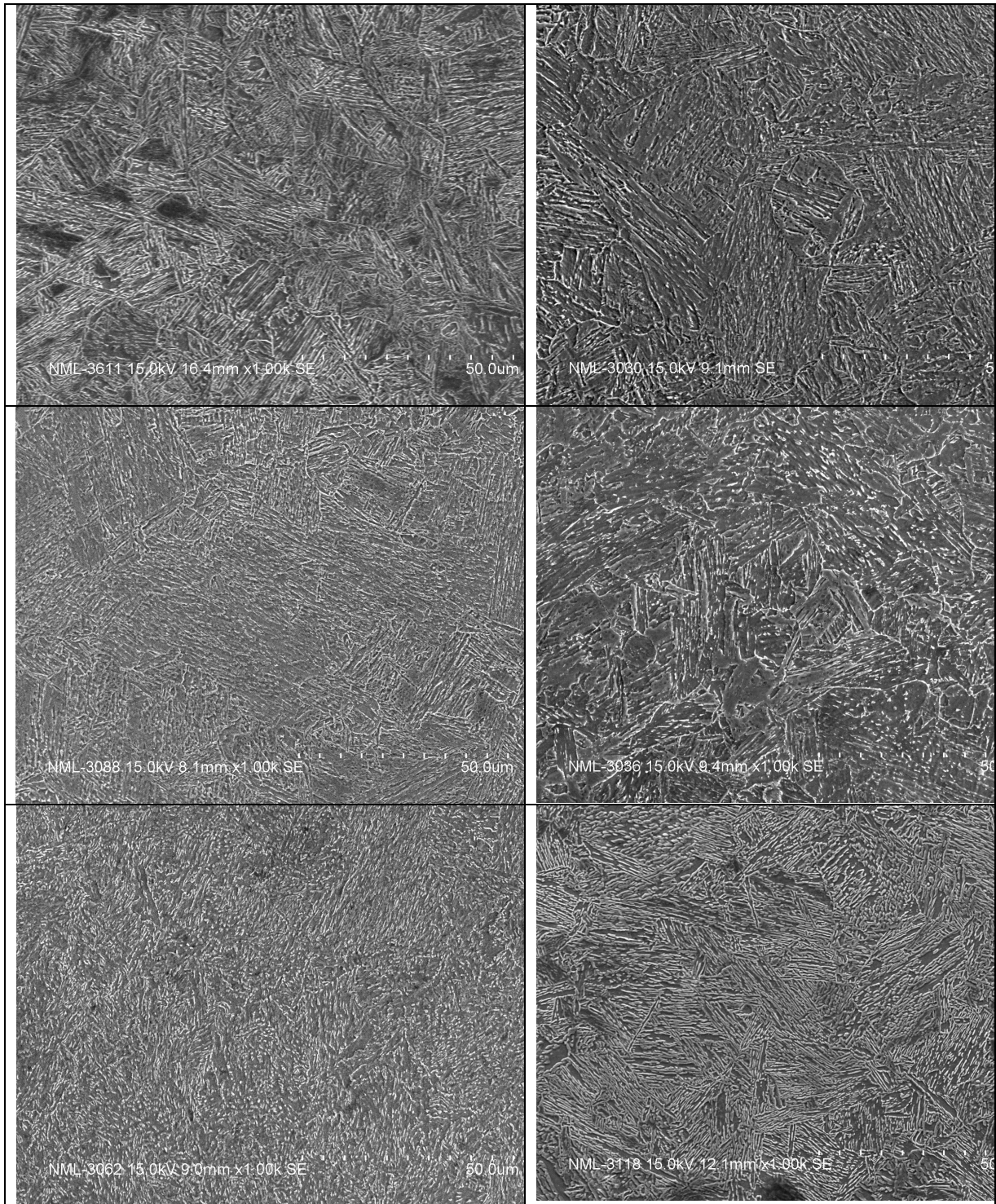
Fractal dimensions were computed from the slope of the log-log plots using the correlations presented in Table 4.1. Figures 5.11 and 5.12 show the variations of fractal dimensions with the aging temperatures for the BE and SE images respectively and the corresponding data is presented in Tables 5.3 and 5.4 respectively. The tables show standard deviations (stdev), maximum and minimum values of the Hurst exponent,  $H$ , coefficient of variance (ratio of standard deviation and average) and the fractal dimensions.

From Tables 5.3 and 5.4 and the plots (Figures 5.11 and 5.12), it can be seen that maximum data scatter is found for the PSD analysis. SE images show more data scatter than the BE images. This indicates that noise level is higher in the SE images than the BE images which agree with the general principle of electron imaging, discussed in chapter 2. PSD and R/S methods generate fractal dimensions which can clearly distinguish the morphological changes at various aging temperatures. However Wavelet analysis has the poorest discrimination capability since the fractal dimension is found to be nearly invariant throughout the aging process. Minimum fractal dimension is obtained at 450°C temperature by all the three analyses.



a	b
c	d
e	f

Figure 5.8: Representative microstructural images (1000x BE type) of HSLA steel for various tempered temperatures a) WQ, b)350°C, c)450 °C, d)550 °C, e)650 °C and f) 675 °C .



a	b
c	d
e	f

Figure 5.9: Representative microstructural images (1000x SE type) of HSLA steel for various tempered temperatures a) WQ, b)350°C, c)450 °C, d)550 °C, e)650 °C and f) 675 °C .

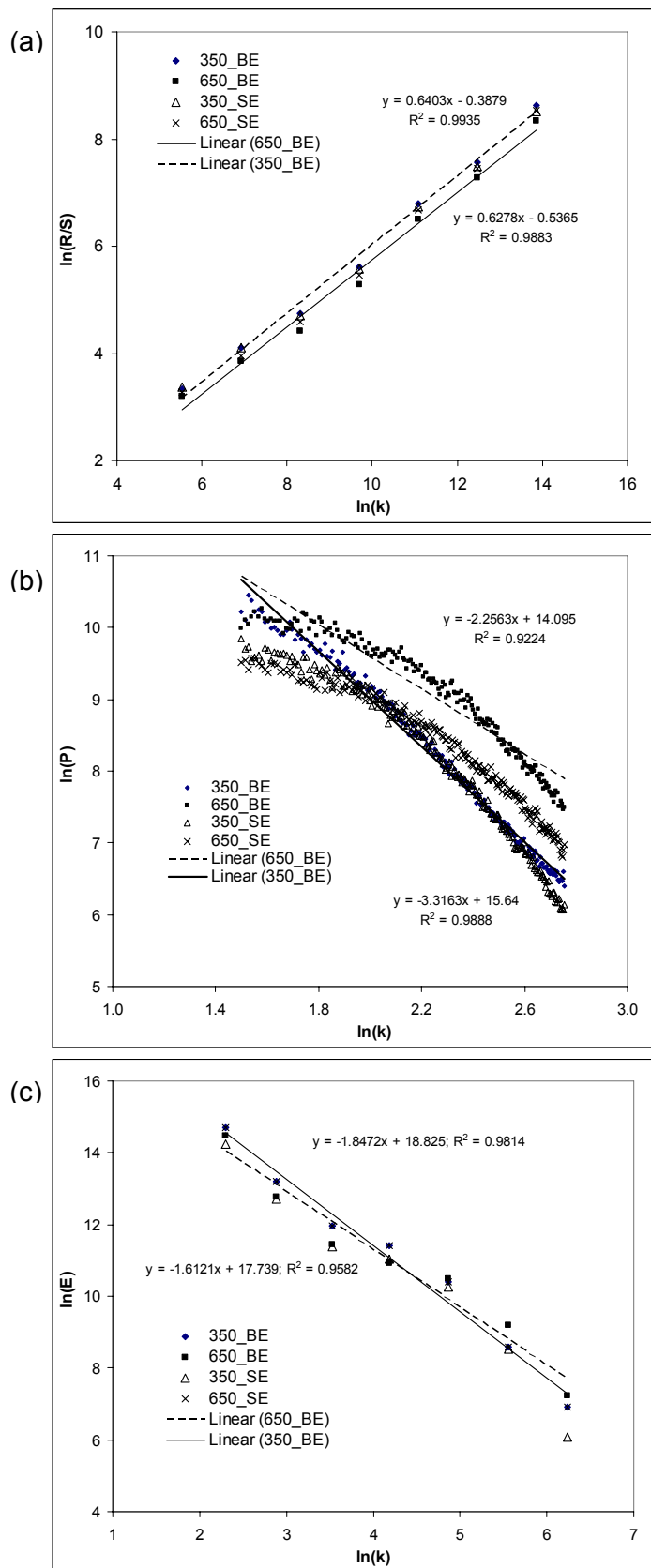


Figure 5.10: Logarithmic variations of R/S value, power and energy with the scale of measurement by a) R/S analysis, b) PSD analysis and c) Wavelet analysis respectively.

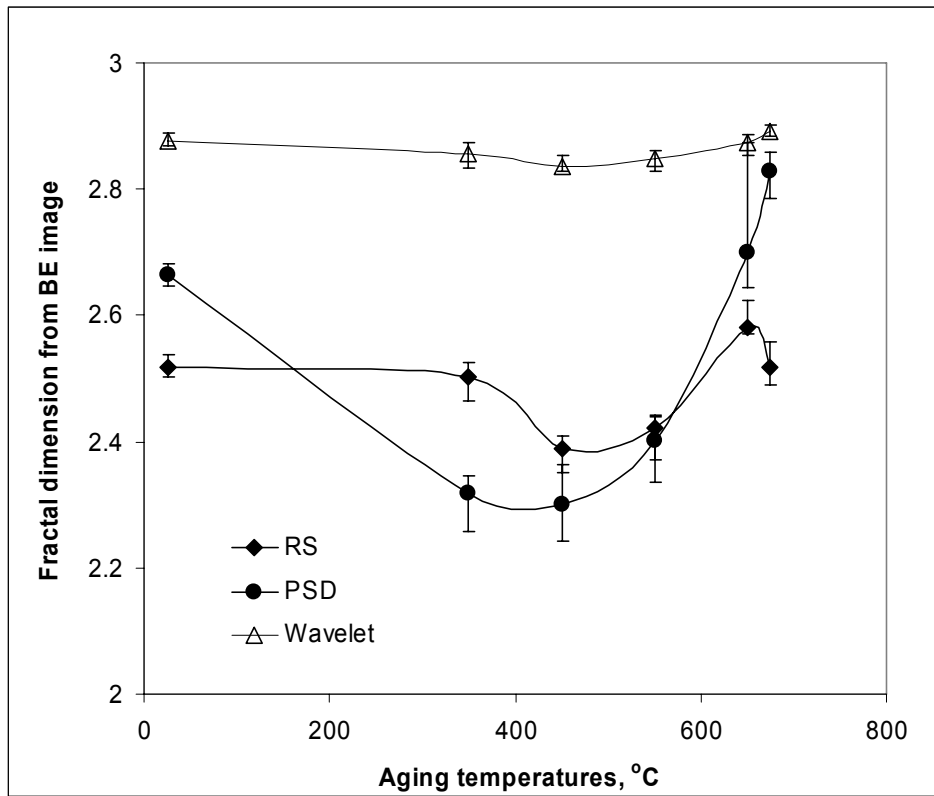


Figure 5.11: Variations of fractal dimensions with the aging temperatures for the BE images

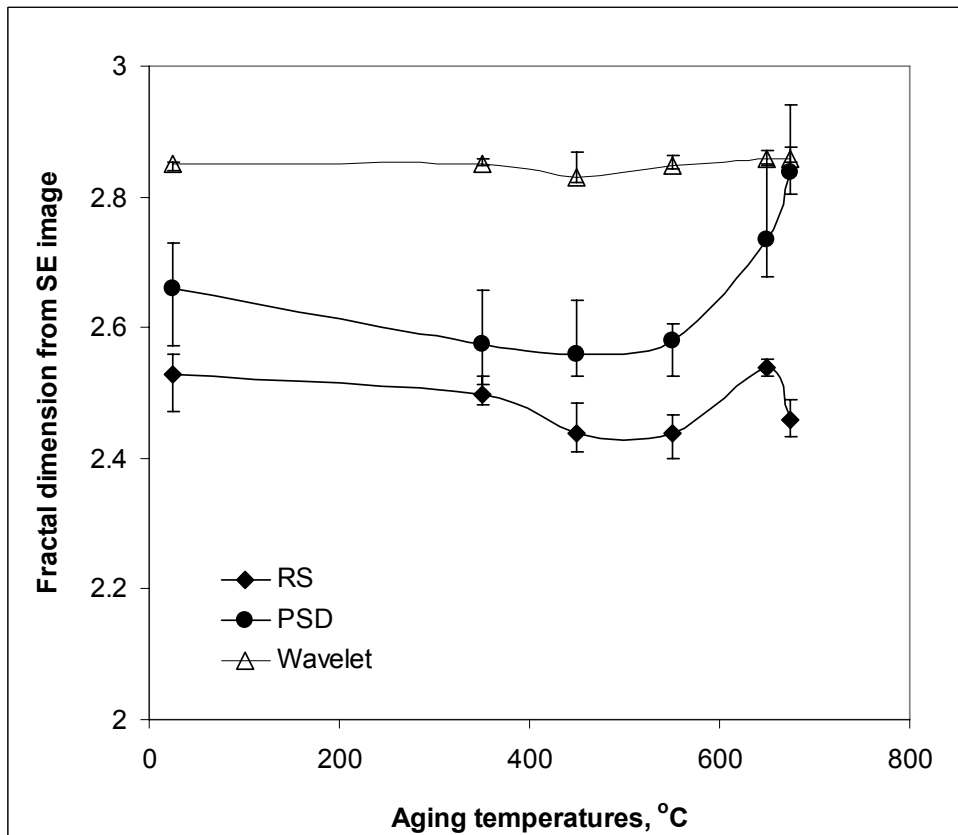


Figure 5.12: Variations of fractal dimensions with the aging temperatures for the SE images

Table 5.3: Data obtained by fractal analysis of microstructural images of BE type

	BE image						
	Temperature	WQ	350	450	550	650	675
R/S	Stdev	0.027	0.049	0.049	0.056	0.042	0.055
	Max of $H_{mr}$	0.504	0.521	0.632	0.597	0.460	0.521
	Min of $H_{mr}$	0.470	0.460	0.572	0.528	0.408	0.453
	Coeff-of var (%)	5.629	10.019	8.076	9.950	9.602	11.194
	$D_{mr}$	2.516	2.502	2.389	2.422	2.582	2.518
PSD	Stdev	0.028	0.072	0.097	0.084	0.185	0.060
	Max of $H_{mp}$	0.353	0.709	0.760	0.636	0.472	0.203
	Min of $H_{mp}$	0.318	0.620	0.640	0.532	0.243	0.129
	Coeff-of var (%)	8.342	10.773	13.914	14.327	51.765	36.207
	$D_{mp}$	2.664	2.319	2.302	2.402	2.700	2.828
Wavelet	Stdev	0.015	0.033	0.021	0.027	0.020	0.016
	Max of $H_{mw}$	0.136	0.163	0.182	0.162	0.139	0.122
	Min of $H_{mw}$	0.127	0.147	0.159	0.145	0.128	0.140
	Coeff-of var (%)	5.457	5.457	20.974	10.530	14.243	12.093
	$D_{mw}$	2.877	2.855	2.836	2.850	2.874	2.890

Table 5.4: Data obtained by fractal analysis of microstructural images of SE type

	SE image						
	Temperature	WQ	350	450	550	650	675
R/S	Stdev	0.071	0.034	0.060	0.054	0.022	0.046
	Max of $H_{mr}$	0.504	0.529	0.606	0.589	0.475	0.572
	Min of $H_{mr}$	0.416	0.487	0.531	0.522	0.448	0.515
	Coeff-of var (%)	15.500	6.631	10.609	9.760	4.674	8.425
	$D_{mr}$	2.527	2.498	2.439	2.438	2.539	2.459
PSD	Stdev	0.128	0.117	0.094	0.066	0.139	0.110
	Max of $H_{mp}$	0.410	0.509	0.523	0.444	0.379	0.266
	Min of $H_{mp}$	0.251	0.364	0.406	0.363	0.207	0.129
	Coeff-of var (%)	38.692	26.926	20.193	16.309	47.489	55.757
	$D_{mp}$	2.660	2.574	2.560	2.581	2.735	2.837
Wavelet	Stdev	0.011	0.008	0.038	0.016	0.020	0.018
	Max of $H_{mw}$	0.154	0.158	0.206	0.165	0.153	0.162
	Min of $H_{mw}$	0.141	0.147	0.159	0.145	0.128	0.140
	Coeff-of var (%)	7.561	5.457	20.974	10.530	14.243	12.093
	$D_{mw}$	2.850	2.850	2.831	2.849	2.859	2.857

#### 5.2.4 Correlations between fractal dimensions and material properties

For mechanical characterisation of the HSLA steel [7], properties like hardness, yield strength, ultimate tensile strength, percentage elongation, percentage reduction of area, etc. are evaluated by tensile test. Mechanical properties are listed in Appendix-I which have been used here to obtain their correlations with fractal dimensions. The correlation coefficients (CoR) are given in Table 5.5 for fractal dimensions computed by three

methods and for both the BE and SE type images. While the correlations are found to be negative for the hardness and strength properties, they are positive for the percentage elongation and reduction of area. The correlations (minimum  $R_{el}=0.53$  for BE image and 0.07 for SE image) are found to be worst for the R/S method and excellent for the PSD method. Figures 5.13 and 5.14 show the correlations between fractal dimensions and hardness for BE and SE images respectively.

Table 5.5: Correlation coefficients ( $CoR$ ) obtained between fractal dimension and material properties. The subscript  $Hv$  is for hardness,  $YS$  is for yield strength,  $UTS$  is for ultimate tensile strength,  $el$  is for percentage elongation and  $ra$  is for percentage area reduction.

Image	Method	$CoR_{Hv}$	$CoR_{YS}$	$CoR_{UTS}$	$CoR_{el}$	$CoR_{ra}$
BE	RS	-0.84	-0.85	-0.75	0.53	0.85
	PSD	-0.89	-0.92	-0.92	0.76	0.87
	Wavelet	-0.91	-0.90	-0.88	0.69	0.97
SE	RS	-0.45	-0.51	-0.37	0.07	0.52
	PSD	-0.94	-0.95	-0.91	0.83	0.87
	Wavelet	-0.89	-0.83	-0.89	0.80	0.90

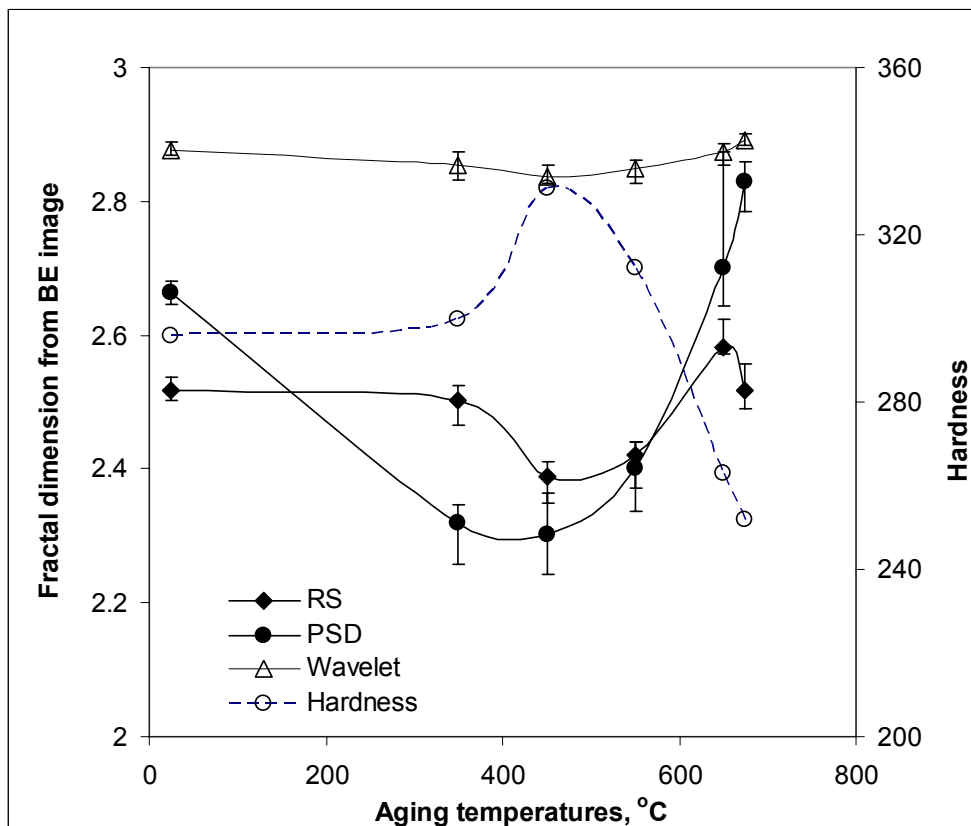


Figure 5.13: Correlations between fractal dimensions estimated from BE images and hardness.

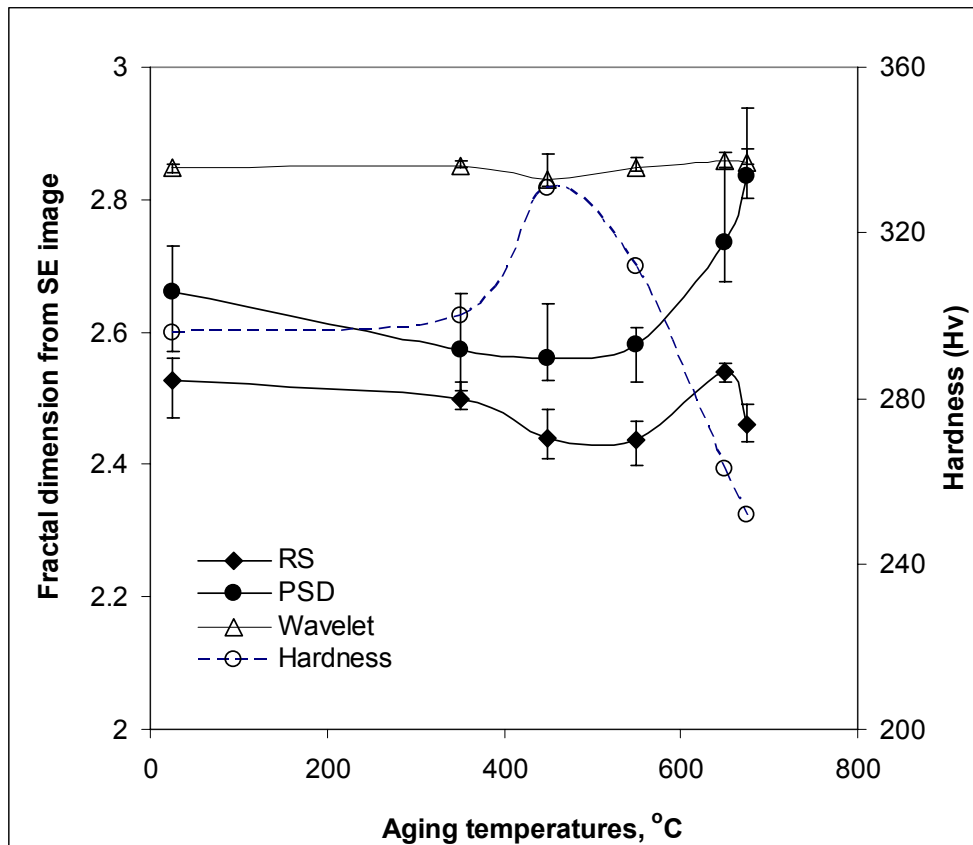


Figure 5.14: Correlations between fractal dimensions estimated from SE images and hardness.

Previous investigators [7,8] have reported variations of microstructural constituents with the tempering temperatures. Four phases of steel can be identified in the microstructures: acicular ferrite, bainite, lath martensite and retained austenite. Second phase particles like carbide and carbo-nitrides are present in the form of precipitates. Progressive tempering produces copper precipitates which increase in volume fractions and play a crucial role in altering the mechanical properties. Below 550°C, there is decreasing trend of fractal dimensions, which signifies the gradual improvement of persistent behaviour in images. Persistent behaviour in the structural sense is smoothing or ordering. It was highlighted by previous investigators that up to 500°C temperature there is no change in microstructural morphology in micro level, however in nano scale, changes were identified from the TEM images. It was found out that copper was present as solid solution in the WQ state which started precipitating and form nano size copper particles. These particles grow in size, remain coherent up to 500°C temperature and then form large clusters of incoherent copper precipitates beyond 500°C tempering temperature. Mechanical properties like hardness, yield strength and UTS are maximum around 500°C, where the fractal dimensions are found to be minimum by all the three methods.

Beyond 450°C, fractal dimensions, computed by R/S and Wavelet analyses, increase upto 650°C and then decrease nominally. However for the PSD analysis, fractal dimensions increase upto 675°C. This is due to break-up of martensitic lath, formation of tempered martensite, polygonisation of acicular ferrite as well as loss of coherency of copper precipitates. Morphological ordering is progressively broken between 450°C to 675°C temperatures, and higher fractal dimensions are obtained. Above 675°C, recovery of lath martensite and formation of new composite phase of martensitic island and retained austenite were identified during microstructural characterization which again generates ordered or persistent image characteristics. Reverse trend in fractal dimension could be found for the R/S analysis of samples aged at 650°C and it is expected that the similar trend reversal could be obtained for other methods if images of samples aged at 700°C temperature were analysed. The correlations between fractal dimensions and mechanical properties are found to be good and it is interesting to note that the morphological changes occurring in the nano scale could be identified by fractal analysis of images captured in the micro scale

### **5.3 Conclusions**

The fractal analysis of microstructural images of HSLA steel reveals interesting findings in this chapter which are given below:

- Sensitivity analysis to ascertain effect of magnification, spatiality and images preprocessing clearly brings out that fractal dimensions vary with magnifications inversely for both the BE and SE images. Fractal dimensions computed from the SE images are less than the same computed from the BE images which indicates that information or signal content in BE images are more than the SE images. Spatial effect on fractal dimensions is found to be minimum for the Wavelet analysis whereas for the PSD analysis the variation is maximum ~12%. Similar trend is found for the BE images. Image preprocessing changes fractal dimensions. For the binarised image, the computed fractal dimensions are the largest followed by the histogramme equalization. The unprocessed image generates the lowest fractal dimensions. Similar trend is observed for the PSD and Wavelet analyses as well for both image types.
- By PSD analysis, self-similar and self-affine fractal behaviour of microstructural images for three magnifications has been determined. In addition to magnification, it is important to recognize the length scales which can identify the true fractal behaviour. Too small characteristic length will always generate self-similar behaviour ( $H \geq 1$ )

while larger length scales will result in “monoscale” random surface. This investigation concludes that images of 1000 magnification show true fractal behaviour for the length scale less than 1µm and “monoscale” fractal behaviour for length scale above 1 micron for images at all three magnifications

- Fractal analyses of the HSLA steel at various tempering temperatures generate maximum data scatter for the PSD analysis. SE images show more data scatter than the BE images. This indicates that noise level is higher in the SE images than the BE images which agree with the general principle of electron imaging PSD and R/S methods generate fractal dimensions which can clearly distinguish the morphological changes at various aging temperatures. However Wavelet analysis has the poorest discrimination capability since the fractal dimension is found to be nearly invariant throughout the aging process. Minimum fractal dimension is obtained at 450°C temperatures by all the three analyses.
- Good correlations between fractal dimensions and mechanical properties have been obtained. While the correlations are found to be negative for the hardness and strength properties, they are positive for the percentage elongation and reduction of area. The correlations (minimum  $R_e=0.53$  for BE image and 0.07 for SE image) are found to be worst for the R/S method and excellent for the PSD method. Below 550°C, there is decreasing trend of fractal dimensions, which signifies the gradual improvement of persistent behaviour in images. Persistent behaviour in structural sense is smoothing or ordering which could be due to the nano size copper precipitations, observed by the TEM, occurring between 350°C-550°C. The interesting finding of the fractal analysis is that the morphological changes occurring in the nano scale could be identified by fractal analysis of images captured in the micro scale.

### 5.3 References

1. C.K. Bora, E.E. Flater, M.D. Street, J.M. Redmond, M.J. Starr, R.W. Carpick and M.E. Plesha: Tribology Letters, 19(1), 37-48 (2005)
2. J. O. Fossum, H. H. Bergene, Alex Hansen, B. O'Rourke, and G. Manificat: Self-affine crossover length in a layered silicate deposit, Physical Review E , 69, 036108, 1-4 (2004).
3. A.A. Likhachev, J. Pons, E. Cesari, A.Yu. Pasko, V.I. Kolomytsev: Observation and analysis of scaling behavior in surface martensite-austenite relief during the reverse

martensitic transformation in Cu-Al-Ni single crystal by using 2D Fourier processing method, *Scripta Mater.*, 43, 765-769(2000).

4. E. Hornbogen, Fractals in microstructure of metals, *Int. Materials Reviews*, 34, 277-296(1989).
5. M. B. Isichenko and J. L. Kalda: Statistical Topography. I. Fractal Dimension of Coastlines and Number-Area Rule for Islands, *J. Nonlinear Science*, 1(3), 255-277 (1991).
6. J. Kalda: <http://www.citebase.org/abstract?id=oai:arXiv.org:cond-mat/0210650>, 2002.
7. S. K. Das, S. Sivaprasad, S. Das, S. Chatterjee and S. Tarafder: The effect of variation of microstructure on fracture mechanics parameters of HSLA-100 steel, *Material Science and Engineering A*, 431, 68 – 79 (2006).
8. S. K. Das, N. Narasaiah, S. Sivaprasad, S. Chatterjee and S. Tarafder, *Mat. Sci. and Tech.*, 23, 177-182 (2007).

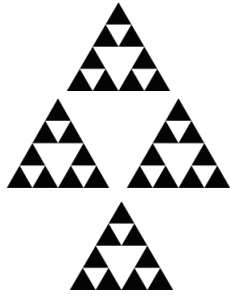


# CHAPTER 6

## **6.0 Fractal analysis of fractographic images**

6.1	Materials and fractographs	134
6.2	Results and discussion	134
6.2.1	Effect of magnification, spatiality and image pre-processing on fractal dimensions	135
6.2.2	Fractal analysis of fractographic images	139
6.2.3	Correlations between fractal dimensions and mechanical properties	145
6.3	Conclusions	154
6.4	References	156





6

## FRACTAL ANALYSIS OF FRACTOGRAPHIC IMAGES

Topographic variations on material surfaces are created by various damaging mechanisms like fracture, fatigue, creep, wear, corrosion, machining etc. These variations are caused due to the presence of voids, micro cracks, striation marks, cleavage planes, corrosion pits, *etc.* on the surfaces. Some of these characteristic features are the indelible signatures left behind on the material surface during the progression of damage. These characteristic features, identifiable in high resolution fractographic images, give meaningful information to material scientists studying the influence of micro-, meso- and macro-structural parameters on material behaviour for the assessment of structural integrity and lives of engineering components. The quantitative estimation of these characteristic features is necessary in order to establish correlations between material processing parameters, morphological characteristics of microstructures, test or service parameters and materials properties. For example, the size of dimples formed on fracture surfaces by coalescence of voids during ductile fracture can be correlated to the tensile properties

of materials. Similarly the blunted crack tip profile can explain the high fracture toughness property of materials. The interaction of voids with the crack tip can also be understood from the morphological characteristics of local fractographic features. In fatigue applications, from the striation spacing on fracture surfaces, the rate of crack growth can be assessed. All these fractographic features may create self-similar patterns in the statistical sense which essentially alter the roughness of the fracture surface. Fractal dimension computed from the fractographic image quantify the fracture surface roughness which may be found to be correlated to the damage resistance property of the material.

This chapter presents fractal analysis of a set of fractographic images of the HSLA steels. Sensitivity of the fractal parameters with respect to magnifications, spatial locations and pre-processing of images are assessed and presented as results. Later fractal dimensions obtained by three methods (R/S, PSD and Wavelet) have been reported with error estimates. Finally correlations between material properties and fractal dimensions computed from fractographic images have been discussed. Attempt has been made to develop models to predict mechanical properties based on fractal characteristics.

## **6.1 Materials and fractographs**

Specimens of HSLA steel quenched and aged to produce ten variations of microstructural condition, described in Appendix-I, were fractured by pulling them under tensile loading and fracture surfaces were generated. These surfaces were examined in the SEM and digital images were captured and stored. For each aging temperature, multiple images were taken from different locations of the same specimen. Mechanical and fracture properties, given in Appendix-I, have been used for presenting verification of the proposed fractal based correlations discussed later.

## **6.2 Results and discussion**

Results of fractal analysis of fractographic images are presented in three subsections. Initially invariance property of fractal dimensions with respect to magnifications, spatial locations and pre-processing has been investigated. Fractal analysis of fractographic images has been carried out next using three methods of determination of fractal dimensions. For referencing, subscript “*f*” is used to denote fractographic source of images, and for distinguishing methods, “*r*”, “*p*” and “*w*” are used as subscripts for R/S analysis, PSD analysis and Wavelet analysis respectively. Finally, correlations between fractal dimensions and material properties have been discussed and development of models for predictions has been presented.

## 6.2.1 Effect of magnification, spatiality and image pre-processing on fractal dimensions

### a) Effect of magnification

Using SEM, images of fracture surfaces were captured centred on the same location at magnifications varying from 200 to 4000. Below 200 magnification, the information in images is inadequate from the detail point of view, and above magnification of 2000, the information is too localized. It may be mentioned that as the magnification increases, less area is viewed with more details of features. This would invariably affect the fractal dimension, if the image is not fractal in the strict mathematical sense. A true fractal object shows self-similarity or self-affinity between the object parts and the overall features of the object. A natural image can have fractal behaviour within certain range of magnifications, as reported by previous investigators [1, 2]. Robustness of a particular method depends upon how insensitive the computed fractal dimensions are with change of magnification or any other operations on the image. Figure 6.1 shows representative fractographic images at various magnifications.

Figure 6.2(a) shows variations of fractal dimensions with magnifications obtained by the three methods employed. Generally, an inverse correlation is found between fractal dimension and magnification. Beyond 2000 magnification, the decreasing trend is persistent ( $D < 2.5$ ). Below a magnification of 2000, anti-persistent behaviour ( $D > 2.5$ ) is displayed. The Wavelet method always gives a anti-persistent behaviour. Table 6.1 presents various statistical parameters obtained from images. It can be seen that for unaltered images (i.e. with no pre-processing), the standard deviation is the largest for PSD analysis, which is less than 0.194, and the coefficient of variance (ratio between standard deviation and average) is less than 8%. The least standard deviation is obtained for the wavelet analysis, which is 0.123.

### b) Effect of spatiality

Images from 21 different locations of the specimen at 1000 magnification were captured. Fractal dimension for each of these 21 images was computed by the three methods. Figure 6.2(b) shows the plot of the fractal dimensions for these images. Fractal dimensions estimated by PSD analysis method is more than the same estimated by the other two methods. The standard deviation is found to be the largest for the PSD technique, which is less than 0.04, and coefficient of variance is less than 1.3% as given in Table 6.1. The effect of spatiality on fractal dimensions is less in comparison to that of magnification since the standard deviation is lower for former than the later. With changes in magnification, changes of fractal dimension

demonstrate certain trends, whereas complete random digression is noticed with spatial variations. Similar variations of fractal dimensions estimated from the fracture surface ahead of a crack tip have been reported by previous investigators [3].

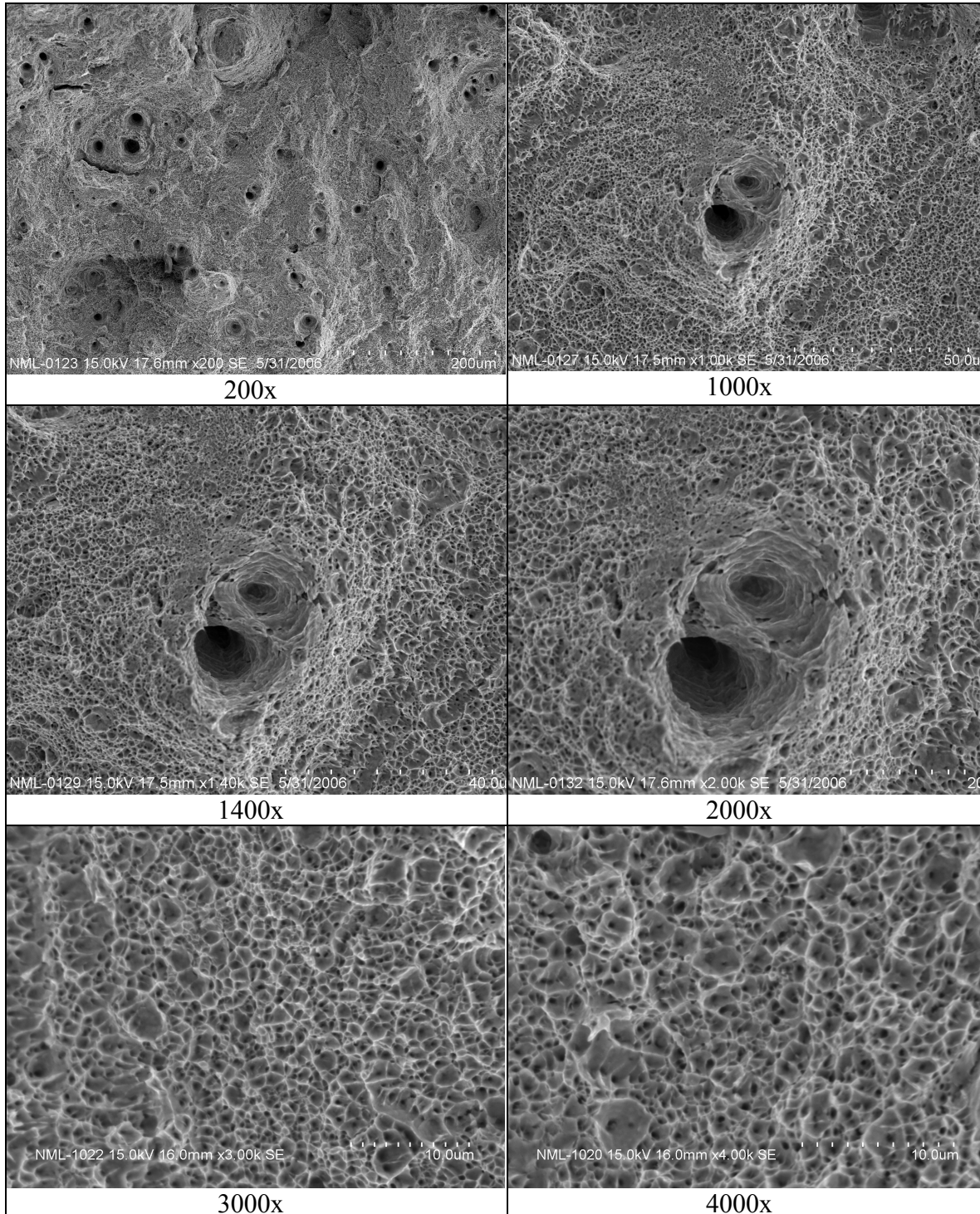


Figure 6.1: Fractographs of HSLA steel of WQ condition at various magnifications, as noted.

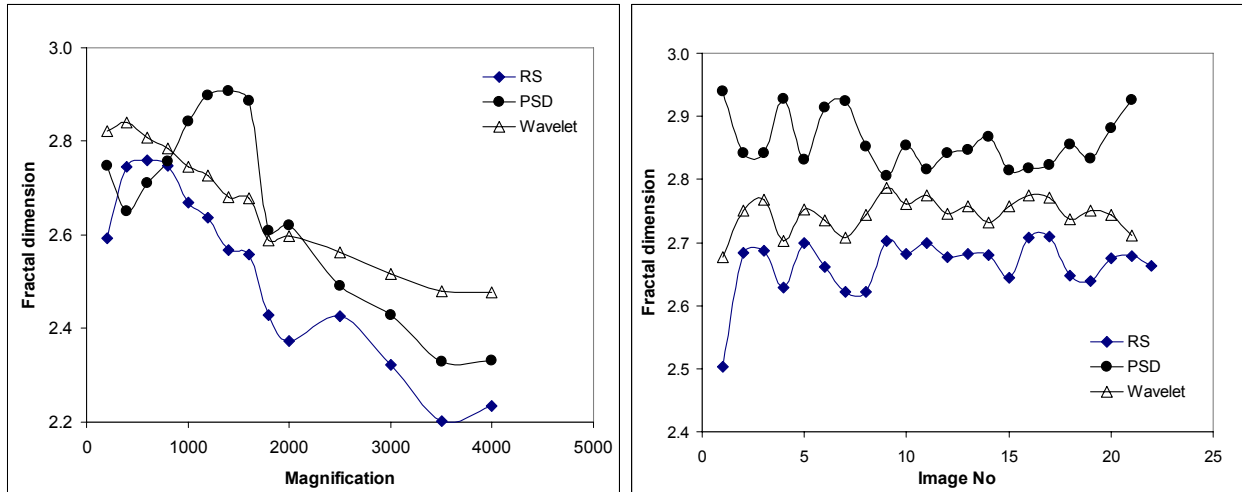


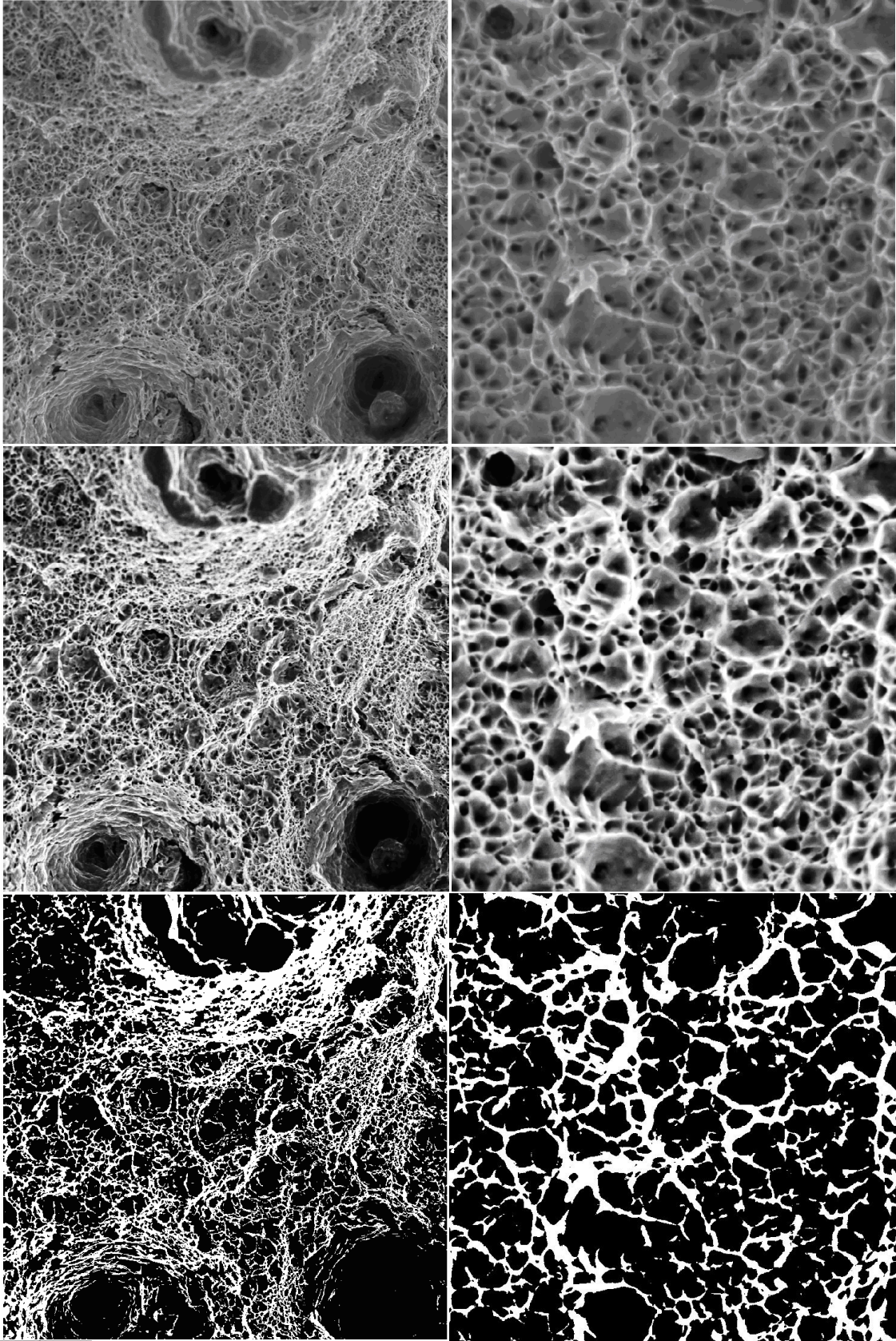
Figure 6.2: Variations of fractal dimensions with a) magnifications and b) spatiality for unprocessed fractographic images

Table 6.1: Average fractal dimensions and statistical parameters obtained for images taken at different magnifications and locations (spatial variations). Data corresponding to pre-processed images are also included.

Image state	Method	Magnifications				Spatial Variations			
		Average	STD	Range	Coeff of var (%)	Average	STD	Range	Coeff of var (%)
No Pre-processing	RS	2.519	0.182	0.557	7.226	2.664	0.027	0.206	0.010
	PSD	2.658	0.194	0.577	7.288	2.860	0.037	0.133	0.013
	Wavelet	2.665	0.123	0.363	4.633	2.745	0.022	0.110	0.008
Histogram Equalization	RS	2.589	0.191	0.590	7.390	2.759	0.029	0.187	0.011
	PSD	2.657	0.193	0.629	7.273	2.835	0.043	0.153	0.015
	Wavelet	2.733	0.126	0.376	4.609	2.817	0.018	0.088	0.006
Binarization	RS	2.662	0.216	0.664	8.116	2.850	0.032	0.179	0.011
	PSD	2.752	0.130	0.410	4.712	2.669	0.033	0.133	0.012
	Wavelet	2.944	0.079	0.257	2.668	2.993	0.026	0.113	0.009

### c) Effect of pre-processing of images

The digital images captured by SEM often require pre-processing depending upon the quality of images, especially for feature-based quantification. Since quantification of images by fractal dimension is a global quantification procedure, pre-processing may not be necessary. Nevertheless, it is important to ascertain whether pre-processing has any effect on fractal dimensions. For pre-processing two popularly used methods, *i.e.* histogram equalization and binarization, have been used for images at different magnifications and spatiality. In chapter 2, these two pre processing methods have been described. Figure 6.3 shows the effect of pre-processing on images of low and high magnifications.



a	b
c	d
e	f

Figure 6.3: Unprocessed and pre-processed fractographs of HSLA steel of WQ condition at two magnifications: a) 1000x unprocessed, b)4000x unprocessed, c) 1000x histogram equalized, d) 4000x histogram equalized, e) 1000x binarized and f) 4000x binarized.

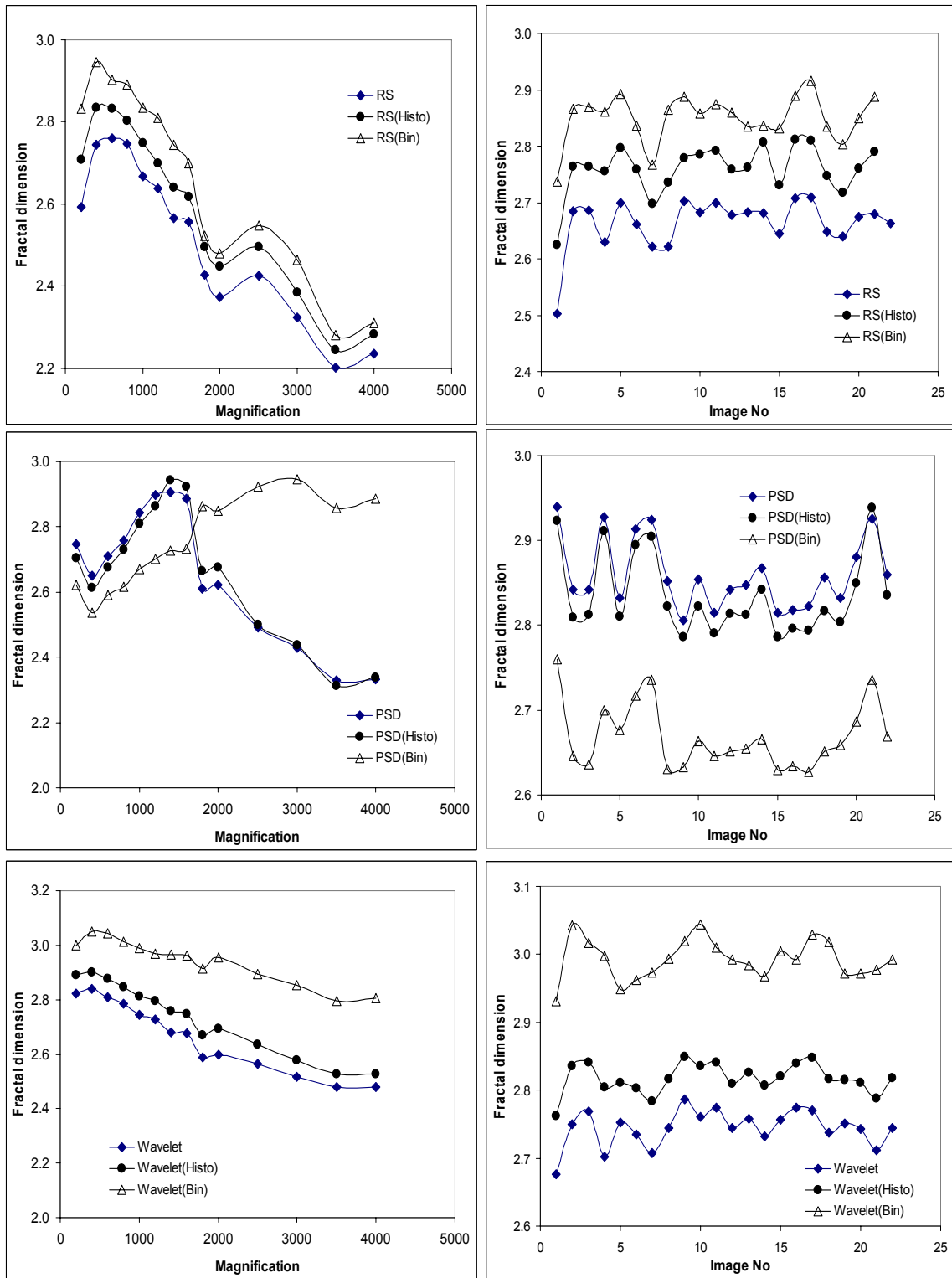
Figure 6.4 shows a set of plots which present the variations of fractal dimensions due to pre-processing of images by histogram equalization and binarization for the three fractal analysis methods. The effects of magnification and spatiality can be noted in the plots. Results obtained from unaltered images are included in the same figure to highlight the effect of pre-processing on fractal dimensions. It can be observed that binarized images consistently generate higher fractal dimensions for R/S and Wavelet analyses.

For PSD analysis, 'no pre-processing' and histogram equalization show similar trend for spatial varied images and generates larger values than the same computed from binarized images, as shown in Figure 6.4(d). However on variations of magnifications beyond 1800x, the effect of binarization is markedly different from the other two cases. In Figure 6.4 (c), it can be seen that unaltered and histogram equalized images generate similar fractal trend while for the binarized images, the variations of fractal dimensions with magnifications show reverse trend beyond 1600x magnification, *i.e.* fractal dimension increases with magnification and approaches the limiting value of 3. At higher magnification, characteristic features identifiable in fractographs are found to be markedly different from that observed at lower magnification, as can be seen in Figure 6.3. This distinction is prominent in binarized images when the high frequency component is eliminated resulting in lowering of the slope of the fractal plot. This phenomena leads to the reversal of trend for the PSD analysis.

Wavelet and R/S analyses show similar trends when the variations of fractal dimensions with respect to magnifications and spatiality are plotted, as in Figure 6.2. The range and standard deviation of fractal dimensions computed by the Wavelet method are found to be the least. This makes the Wavelet method least insensitive to magnification, spatiality and pre-processing of images.

### **6.2.2 Fractal analysis of fractographic images**

Figure 6.5 shows representative fractographic images of fracture surfaces from specimens aged at various temperatures. In the fractographs, micro-voids or dimples with various sizes and shapes can be identified. Small, shallow, equiaxed micro-voids are pre-dominant in the WQ condition. However, specimens aged at temperatures between 400-500°C, exhibit mixed fractures, having flat quasi-cleavage features with small micro-voids. Increase in size of micro-voids and disappearance of quasi-cleavage are observed in specimens aged above 550°C.



a	b
c	d
e	f

Figure 6.4: Effect of pre-processing on fractal dimensions for fractographic images captured at a) different magnification (R/S), b) different spatiality (R/S), c) different magnification (PSD), d) different spatiality (PSD), e) different magnification (Wavelet) and f) different spatiality (Wavelet)

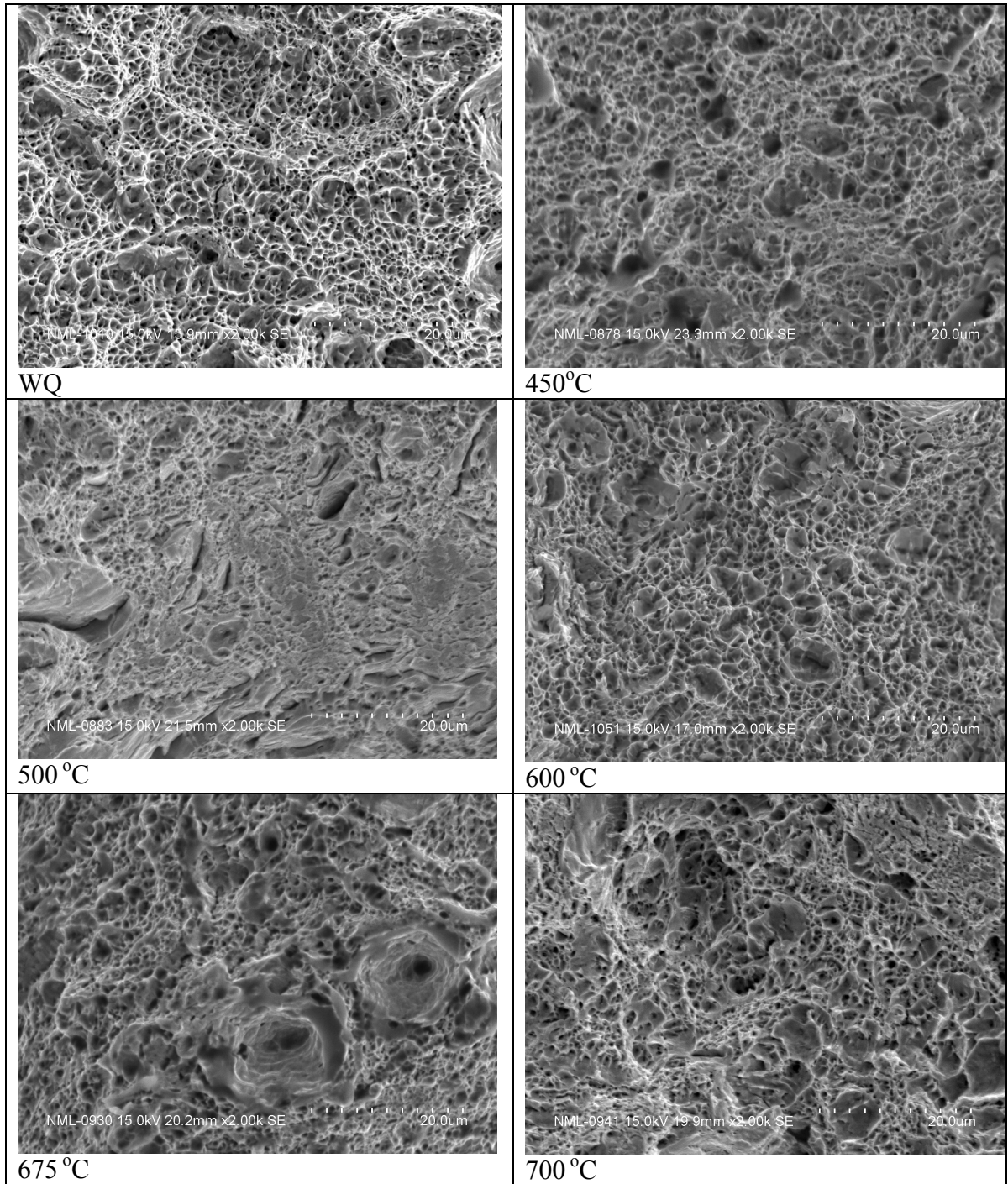


Figure 6.5: Fractographs of HSLA steel aged at various temperatures: (a) Water quenched WQ, (b) 450°C, (c) 500°C, (d) 600°C, (e) 675°C, and (d) 700°C.

For implementing fractal quantification procedures, fractographic images of HSLA steel at ten different aging conditions have been captured by the SEM in SE mode. For each aging condition, 10 images at 2000 magnification were taken to ascertain statistical relevance of the results.

From the sensitivity analysis, it was revealed that fractal dimension changes with magnification for the fractographic images. The average fractal dimension for images between 200 to 4000

magnifications is found to be occurring approximately at 2000 magnification. Moreover each pixel of the image of 2000x measures 0.05 micron, which seems to be quite relevant to the length scale being investigated in this work. For computing fractal dimension, it is necessary to find out slope of the Richardson plot which is given by

$$(slope) = \frac{\log(Measured\_quantity)}{\log(Scale\_of\_measurement)} \quad (6.1)$$

Figures 6.6 (a), (b) and (c) show the Richardson plots obtained by R/S, PSD and Wavelet methods respectively. The plots corresponds to the WQ state and two different aging temperatures, i.e. 400°C and 700°C.

For the R/S and Wavelet analyses, the logarithmic power is found to be a linear function of the logarithmic scale, and has regression coefficient of more than 0.95, whereas for the PSD analysis, the coefficient is found to be 0.89. Fitting error can be minimised by reducing the data range which subsequently reduces the length scale; however to maintain consistency throughout the investigation,  $N/2$  data are used for fitting the line, where  $N$  is the number of pixels along the image width. Table 6.2 presents fractal dimensions estimated from fractographs obtained for 10 aging temperatures. For each aging temperature, 10 images are used to compute the Hurst exponents ( $H$ ). Statistical parameters such as average, standard deviations, maximum, minimum and coefficient of variance for the  $H$  are computed. To eliminate outliers, student's t-test was performed and the average values were calculated. Figure 6.7 shows variations of fractal dimensions with aging temperatures. Consistent trend in variations of fractal dimensions with aging temperatures is observed, although the values are different for different methods.

Consistent variations of fractal dimensions with aging temperatures, estimated from the fractographic images directly, can therefore be used for evaluation of materials. This finding is significant to materials research, especially with regard to directly using fractographic images, since the SEM imaging does not require extra effort in sample preparations [4] or implementation of advanced stereo photogrammetry [5] to get the digital elevation model of the fracture surface.

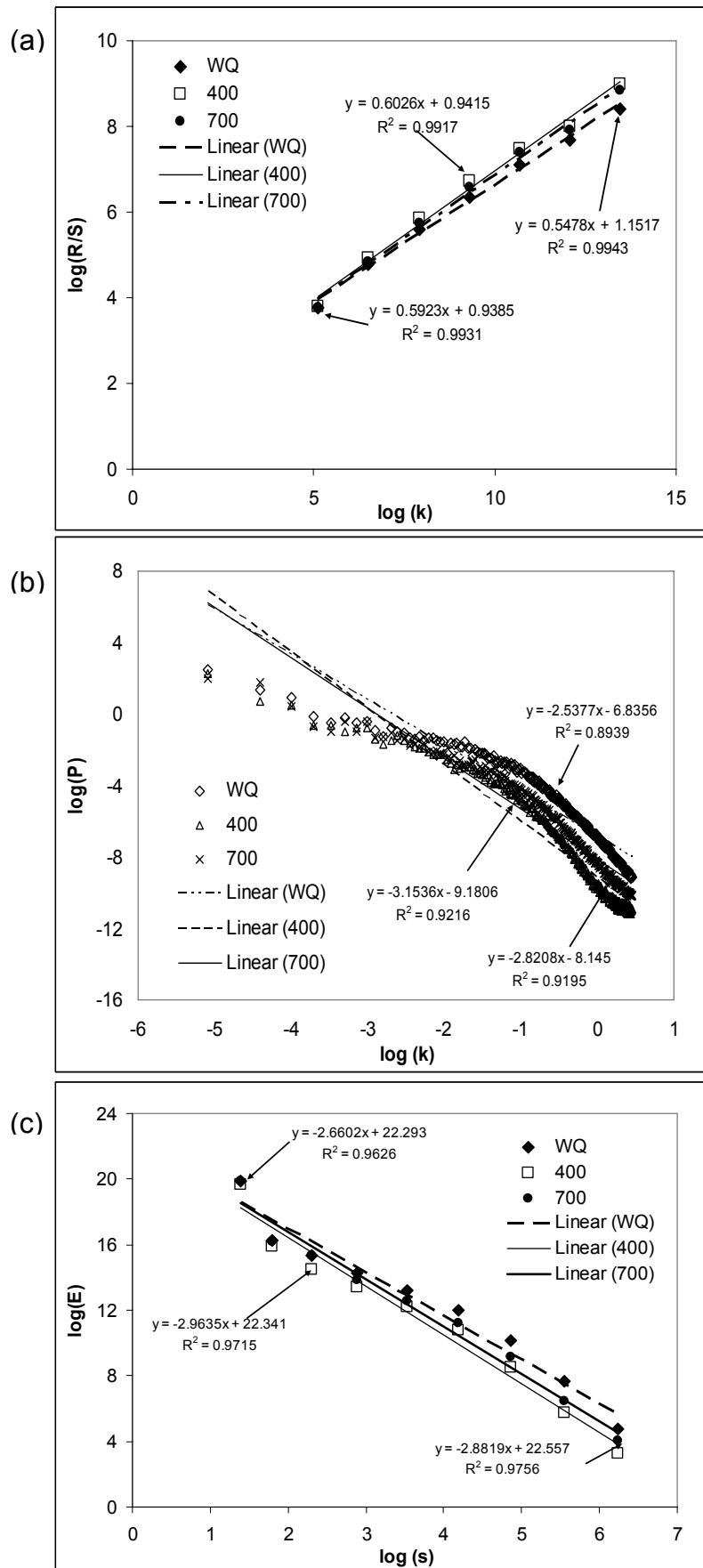


Figure 6.6: Logarithmic variations of R/S value, power and energy with the scale of measurement by a) R/S analysis, b) PSD analysis and c) Wavelet analysis respectively for fractographic images

Table 6.2: Average fractal dimensions ( $D$ ) and statistical parameters obtained for fractographic images for various aging temperatures. For each aging temperature 10 images are analysed to obtain the statistical parameters.

	Temperature	25	350	400	450	500	550	600	650	675	700
RS	Stdev	0.038	0.069	0.067	0.028	0.059	0.073	0.046	0.087	0.060	0.045
	Max of $H_{fr}$	0.543	0.864	0.837	0.747	0.648	0.642	0.687	0.876	0.755	0.685
	Min of $H_{fr}$	0.434	0.611	0.617	0.645	0.449	0.412	0.534	0.577	0.549	0.538
	Coeff-of-var	7.700	9.668	9.334	4.026	11.291	14.152	7.778	13.050	9.037	7.353
	$D_{fr}$	2.503	2.276	2.281	2.306	2.480	2.484	2.406	2.349	2.348	2.374
PSD	Stdev	0.031	0.049	0.031	0.026	0.049	0.042	0.040	0.042	0.037	0.026
	Max of $H_{fp}$	0.413	0.646	0.624	0.636	0.447	0.453	0.521	0.584	0.623	0.521
	Min of $H_{fp}$	0.309	0.477	0.541	0.535	0.294	0.305	0.388	0.436	0.515	0.428
	Coeff-of-var	8.941	8.653	5.225	4.410	13.574	11.460	9.207	8.254	6.666	5.519
	$D_{fp}$	2.661	2.429	2.416	2.403	2.641	2.639	2.568	2.487	2.444	2.531
Wave-let	Stdev	0.024	0.015	0.014	0.015	0.024	0.024	0.024	0.018	0.015	0.014
	Max of $H_{fw}$	0.410	0.496	0.491	0.487	0.425	0.436	0.466	0.478	0.492	0.431
	Min of of $H_{fw}$	0.333	0.446	0.446	0.442	0.358	0.361	0.394	0.431	0.444	0.390
	Coeff-of-var	6.210	3.204	2.869	3.296	6.173	6.125	5.615	4.070	3.209	3.399
	$D_{fw}$	2.621	2.533	2.527	2.544	2.611	2.602	2.574	2.554	2.542	2.584

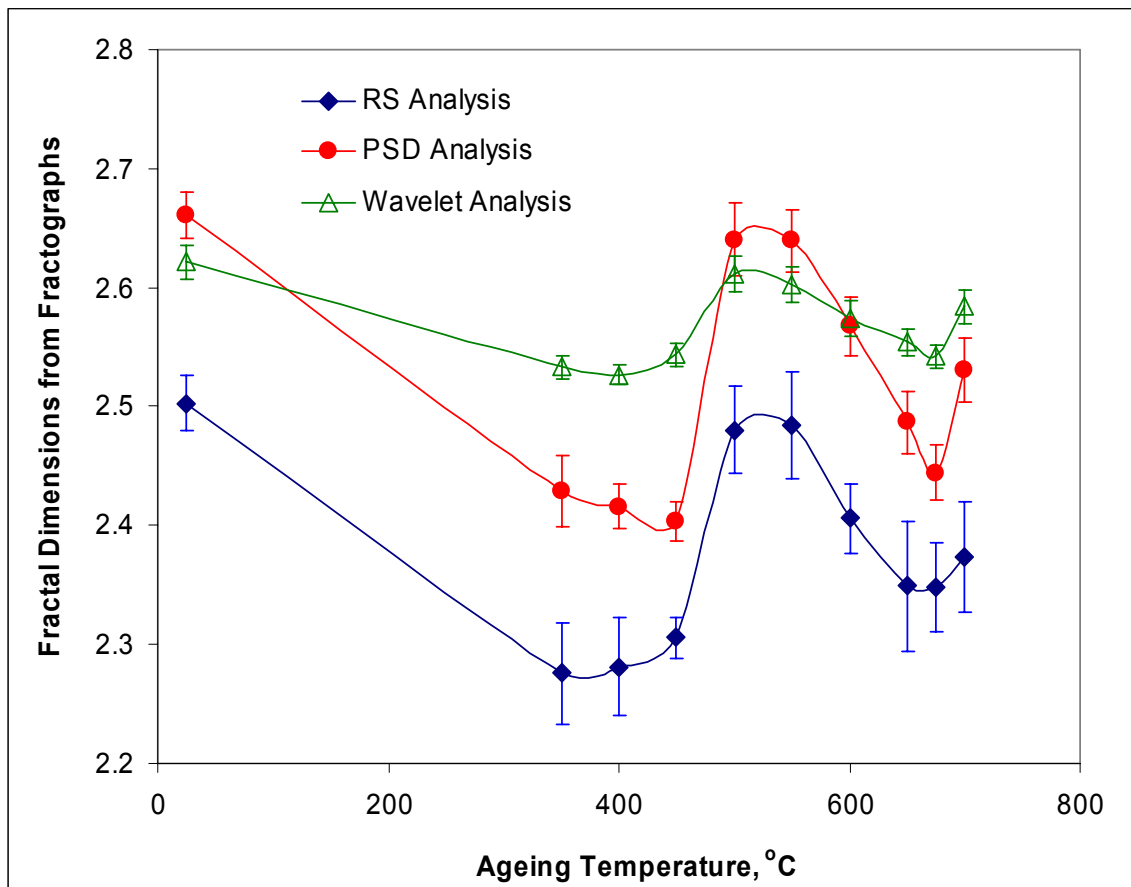


Figure 6.7: Fractal dimensions with respect to the aging temperatures by three methods. Error bars show the variability of fractal dimensions

From the error bars shown in Figure 6.7, it can be seen that R/S method generates larger errors than other methods. However the estimated fractal dimensions by R/S method have greater range which indicates that this method has better discrimination capability. Similar is the observation for the PSD analysis. However Wavelet analysis generates narrow data range, hence the discrimination capability is limited. Nevertheless the error bars show minimum variations by this method.

### **6.2.3 Correlations between fractal dimensions and material properties**

Fractal dimension is used as the morphological characterizing parameter which quantifies surface roughness. Since surface roughness is one of the material characterising parameters which have correlation with the mechanical properties, a similar correlation may exist between fractal dimensions and material properties. Correlations between material properties and fractal dimensions computed from fractographic images of HSLA steel are presented in this section and mathematical models to determine particle spacing (average distance between two particles like precipitates, inclusions, *etc.* which are void initiating sites) and to estimate fractal fracture toughness have been developed and presented

#### **a) Particle spacing and ductile fracture toughness**

To implement fractal concept for characterizing fracture surface roughness, it is important to consider a characteristic length scale. For an object, it can be assumed that the characteristic length scale is the minimum ruler size or scale. Particle spacing is considered as the characteristic length scale of ductile fracture surfaces. During ductile fracture through void nucleation, coalescence and growth in high toughness materials like HSLA steel, microstructural constituents like inclusions, precipitates and other second phase particles play a critical role. They act as void nucleating sites, their shape and size control the initial void size, and their distribution determines the inter-void distance. The ductile fracture toughness model proposed by Thomson *et al.* [6] included a characteristic fracture distance which is a function of inter-particle distance and the local fracture strain. Similarly, a ductile fracture model proposed by Garrison *et al.* [7] incorporated inter-particle distance as the scaling parameter for expressing crack tip opening displacement. The inter-particle distance is denoted as the particle spacing, where particles are the void initiating fine-scale microstructural constituents present in materials.

The generalised microstructural model of ductile fracture toughness [8] expresses that the fracture toughness parameter ( $J_{Ic}$ ) is a function of the characteristic fracture distance ( $l_0$ ), local fracture strain ( $\varepsilon_f^*$ ) and the yield stress ( $\sigma_y$ ) as

$$J_{Ic} = \sigma_y \varepsilon_f^* l_0 \quad (6.2)$$

While  $\sigma_y$  may be evaluated through a standard tensile tests, estimation of  $\varepsilon_f^*$  and  $l_0$ , being local parameters, is somewhat difficult. Ritchie and Thompson [9] had shown that, for the stress modified strain control model for micro void coalescence, the characteristics distance ( $l_0$ ) can be approximated as the average spacing between two micro voids or more precisely the particle spacing,  $\lambda$ . Garrison [10] further refined the model by incorporating the micro mechanism of ductile fracture operative on the scale of material microstructure and proposed that  $l_0$  is the function of local fracture strain  $\varepsilon_f^*$  and the particle spacing,  $\lambda$ , and may be written as

$$l_0 = c\lambda \left( \frac{\varepsilon_f^*}{b} \right)^2 \quad (6.3)$$

where  $c$  and  $b$  are constants. On substitution of  $l_0$  into equation (6.2), it becomes

$$J_{Ic} \approx \frac{c}{b^2} \sigma_y \lambda (\varepsilon_f^*)^3 \quad (6.4)$$

It is often found that the determination of  $\lambda$  through quantitative metallography is difficult especially for HSLA steel or ultra high strength steel, as particles in their microstructures are of nano-size and widely dispersed [11,12]. In the following section, a model based on fractal mathematics has been developed for estimating  $\lambda$ .

### **b) Development of an expression for $\lambda$ based on the fractal concept**

During tensile deformation of a standard specimen, volume consistency of material is preserved till the onset of necking (progressive thinning of specimen on application of tensile load), after which it will be compromised through a reduction of density. In ductile materials, in which fracture takes place predominantly due to initiation, growth and coalescence of voids, volume is enhanced locally as the void volume fraction increases during the process of localized deformation or necking. To conserve mass, density is reduced to compensate for the post-necking local volume enhancement. The constancy of mass throughout the tensile deformation, up to the onset of fracture, of a specimen can be written as

$$V_0 \rho_0 = V_f \rho_f \quad (6.5)$$

where  $\rho_0$  is the average density that is constant till the point of initiation of necking (elastic changes are neglected),  $\rho_f$  is the average density at fracture,  $V_0$  is the initial volume and  $V_f$  is the volume at fracture, with all parameters being referred to localised occurrences.

It is a contention here that the localised and globally non-conservative behaviour taking place through necking up to fracture cannot be adequately quantified in terms of dimensional sizing of physical entities using classical concept of Euclidean geometry. The use of fractal science and its geometrical interpretations are more suitable for representing the stochastic phenomena responsible for the processes of void initiation, growth and coalescence that lead to a chaotic fracture surface.

On a ductile fracture surface, the uneven surface area ( $A_f$ ) is substantially larger than the projected surface area ( $A_{f0}$ ), and similarly it can be upheld that any true local length ( $L_f$ ) at fracture is considerably larger than the projected length ( $L_{f0}$ ). Using fractal concepts [13, 14], and assuming that the material has longitudinal and transverse homogeneity, an uneven fracture surface area can be defined by

$$A_f = A_{f0}(\eta_1)^{D^*} = A_{f0}(k_1 \cdot \lambda)^{D^*} \quad (6.6)$$

where  $\eta_1$ , a dimensionless parameter greater than 1, is the measurement yardstick in microscale and  $D^*$  is the fractional part of the fractal dimension  $D$ . The parameter  $\eta_1$  can further be expressed as a function of  $\lambda$ , the particle spacing described earlier, as given in the second part of the equation. A similar definition is valid for linear dimensions when profile roughness or waviness is to be measured, and can be written as

$$L_f = L_{f0}(\eta_2)^{D^*} = L_{f0}(k_2 \cdot \lambda)^{D^*} \quad (6.7)$$

It may be noted that the scaling parameters  $k_1$  and  $k_2$  have units of per metre.

Equation (6.5) can be rewritten as

$$\frac{\rho_0}{\rho_f} = \frac{V_f}{V_0} = \frac{L_f}{L_0} \times \frac{A_f}{A_0} = \left( \frac{L_f}{L_{f0}} \times \frac{L_{f0}}{L_0} \right) \left( \frac{A_f}{A_{f0}} \times \frac{A_{f0}}{A_0} \right) \quad (6.8)$$

Replacing  $\frac{L_{f0}}{L_0}$  by  $(e_f+1)$  and  $\frac{A_{f0}}{A_0}$  by  $(1-q)$  in equation (6.8), where  $e_f$  is the elongation and  $q$

is the reduction of area at fracture, and using the fractal scaling for fracture surface given in equation (6.6) and equation (6.7), the expression for  $\lambda$  can be obtained by rearranging as

$$\lambda = \frac{1}{\sqrt{k_1 k_2}} \left( \frac{\rho_0}{\rho_f} \frac{1}{(e_f + 1)(1 - q)} \right)^{\frac{1}{2D^*}} \quad (6.9)$$

Assuming that the decrease in density is a linear function of percent reduction [15], equation (6.9) can be rewritten as

$$\lambda = \frac{1}{k} \left( \frac{k_3 q}{(e_f + 1)(1 - q)} \right)^{\frac{1}{2D^*}} \quad (6.10)$$

In equation (6.10),  $k$  is a calibration constant with unit per meter which is of the order of the circular diameter of voids on the fracture surface. For isotropic materials, voids would normally be prolate spheroid in shape so that  $k_1$  and  $k_2$  are equal; in case of highly oriented microstructures, voids may take the shape of oblate spheroids, and  $k_1$  and  $k_2$  will correspond to the major and minor axes of the elliptical cross-section. The proportionality constant  $k_3$  is taken as 0.4 to achieve better fitting with the experimental results. It may be pointed out that these constants need to be calibrated for accurate predictions.

### c) Micro roughness, local strain and the fractal fracture toughness

In equation (6.4), for the estimation of fracture toughness, the local fracture strain  $\varepsilon_f^*$  is required in addition to the material parameters  $\sigma_y$  and  $\lambda$ . A number of strategies have been developed for evaluating  $\varepsilon_f^*$ , including employing a value proportional to the strain at fracture under uniaxial tension [16], using finite element modelling to capture the strain at critical locations ahead of a crack [17] *etc.* Thompson and Ashby [18] have used the concept of micro roughness ( $M$ ) of the fracture surface to derive an expression for estimating  $\varepsilon_f^*$  as

$$\varepsilon_f^* = \frac{1}{3} \ln \left( \frac{M^2}{3V_f} \right) \quad (6.11)$$

where

$$M = \frac{h}{w} \quad (6.12)$$

in which  $h$  is the depth and  $w$  is the width of voids on the fracture surface.  $V_f$  is the volume fraction of the void nuclei and may be given by

$$V_f \propto \frac{K_v^6 x_0^3}{D_0^3} \quad (6.13)$$

where  $D_0$  is the initial diameter of the round tensile specimen,  $K_v$  is the number of voids covering the final diametric space of the specimen,  $x_0$  is the average initial diameter of the spherical void

nuclei. The value of  $x_0$  is assumed as 30nm. A detailed appraisal of the derivation of  $V_f$  is given in Appendix III.

The roughness ( $R_s$ ) of a fracture surface can be expressed using fractal geometry using [13, 14]

$$R_s = \eta_1^{D^*} \quad (6.14)$$

where  $\eta_1$  is a non dimensional parameter greater than unity. It may be noted that such a definition of roughness is related to the size of the measurement yardstick,  $\eta$ . In this work, particle spacing  $\lambda$  has been used as the measurement yardstick or characteristic length in microscale in order to evolve the local fracture strain that is scale-consistent for calculation of fracture toughness.

It may be noted that  $M$  in equation (6.11) is a linear or profile parameter, whereas  $R_s$  is a parameter related to surface. Using the correlation between the linear roughness parameter with the surface roughness parameter given by Underwood and Banerji [14],  $M$  can be rewritten as

$$M = 1 + \frac{\pi}{4} (\eta_1^{D^*} - 1) \quad (6.15)$$

Substituting  $M$  in equation (6.11) and using it in equation (6.4), a parameter proportional to the fracture toughness of the material is obtained. This parameter defined as the *fractal fracture toughness*,  $J_f$ , that can be expressed as

$$J_f = \sigma_y \lambda \left( \ln \left( \frac{M^2}{3V_f} \right) \right)^3 \quad (6.16)$$

In order to use the above equations, the yield stress  $\sigma_y$  is required to be evaluated through a tensile test, the fractal dimension of the fracture surface of the tensile specimen has to be obtained from fractographs, the particle spacing  $\lambda$  has to be estimated through equation (6.10) employing essentially tensile test parameters and the fractal dimension  $D$ , the surface micro roughness  $M$  has to be calculated using equation (6.15) where again  $D$  and  $\lambda$  has are the primary inputs, and  $V_f$  has to be computed from equation (6.13) using void size measurements carried out on fractographs. It may be pointed out, though, that a number of constants are involved in the process that may have to be assumed or calibrated.

#### d) Computation of $\lambda$

For estimating  $\lambda$ , equation (6.10) has been used in which the tensile properties  $q$ ,  $e_f$  and  $D$  were substituted for the various aging temperatures. Variations of  $\lambda$  with the temperature of aging are shown in Figure 6.8 for the various methods of fractal determination used. The  $\lambda$  values are normalised using its value at the WQ condition. In the same plot, variations of the circular diameter of voids (similarly normalised), estimated from the tensile fracture surfaces by image analysis, are shown. It can be seen that the predicted particle spacing has good correlation with the circular diameter of voids, as may be expected.

A minimum in  $\lambda$  at 450°C suggests the shortest inter-particle distance and signifies maximum number of void nuclei and smallest circular diameter of voids. TEM study [19-22] of the same material indicates formation of coherent precipitation of nano-scale copper in the neighbourhood of 500°C. These nano-size copper precipitates act as dislocation pinning sites as well as void nucleation sites and decrease the effective particle spacing. The positive correlation between particle spacing and the void size, as seen in Figure 6.8, can thus be rationalized.

It is reported by previous investigators [23] that copper precipitates act as geometrical obstacles to dislocation motion. These precipitates are not the dislocation blockers but slow down the flow of dislocations. Impediment of dislocation motion strengthens the material by increasing the yield stress, keeping the elastic modulus unaffected. The increase of yield stress,  $\Delta\sigma_y = \sigma_y - \sigma_0$ , based on the theory of Russell and Brown [24] is given as  $\Delta\sigma = 2.5\Delta\tau$ , where  $\Delta\tau$  depends inversely upon the distance between the precipitates, which is  $\lambda$ , the fractal based measurement yardstick, *i.e.* particle spacing. Decrease in  $\lambda$  leads to increasing of  $\Delta\tau$  for which  $\Delta\sigma_y$  increases. Here  $\sigma_0$  is the yield stress of the unstrengthened state and  $\sigma_y$  is the yield strength after the strengthening by  $\Delta\sigma_y$ . Figure 6.9 shows the correlation between  $\sigma_y$  and the particle spacing, where  $\sigma_0$  is considered as the yield stress in the WQ state, when the copper is largely present in solid solution in a super saturated state. Within the aging temperature range of 350-500°C, the copper precipitates are in a coherent state, increasing in amount with increasing aging temperature.

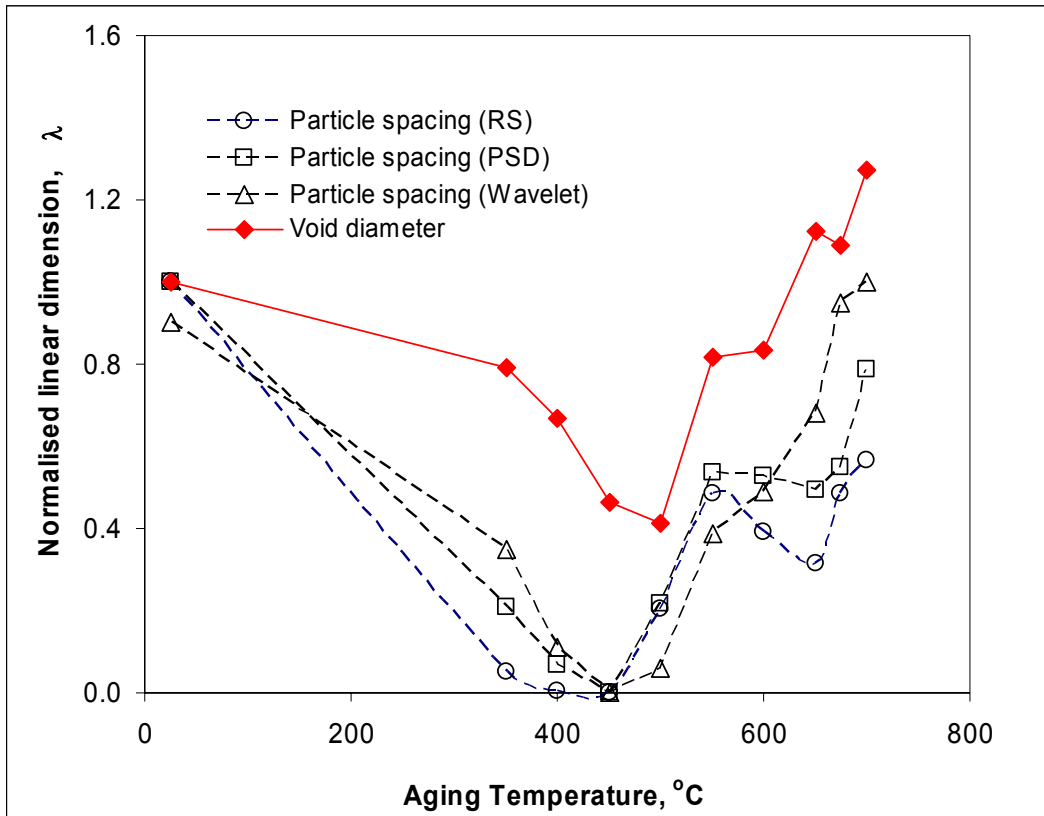


Figure 6.8: Variations of normalised  $\lambda$  with variation of aging temperatures. Correlation with the void diameter can be seen.

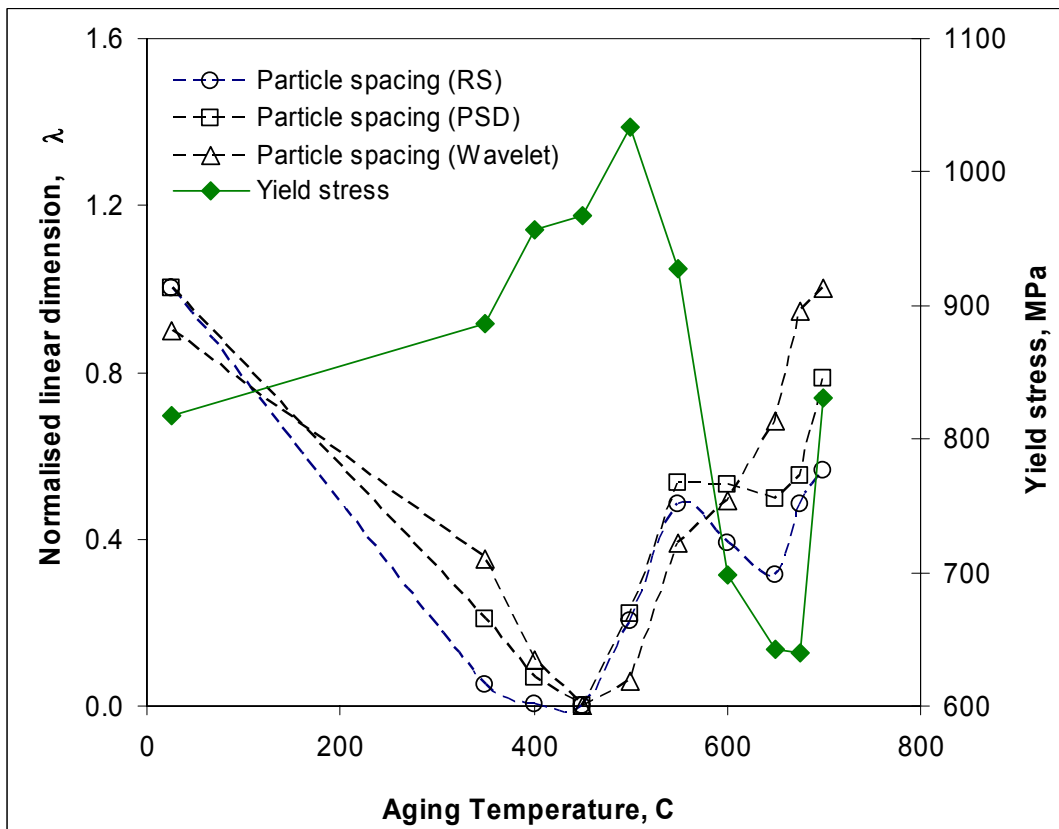


Figure 6.9: Correlation between normalised  $\lambda$  and yield stress (secondary y-axis).

Loss of coherency and the progressive coarsening of precipitations between 500-675°C increase the inter-particle distance, which allow greater dislocation mobility, and reduce the yield stress. It may be pointed out that in addition to the growth of incoherent copper precipitates, tempering of lath martensite is also responsible for the gradual decrease of yield stress on ageing at 500°C to around 675°C. Inverse correlation between  $\lambda$  and yield stress is maintained up to the aging temperature of 675°C. Above 675°C, although growth of incoherent copper precipitates continues, the increase of yield stress is due to the generation of new microstructural phase [22]. Since the aging temperature 675°C exceeds the  $A_1$  transformation temperature in localized regions depleted of austenite stabilizers, some of the ferrite is converted to reverted austenite, a part of which converts to martensite on cooling, resulting in the formation of new small martensite islands. These hard localized entities are responsible for increase of yield stress. Thus the inverse correlation between the increased yield stress and the particle spacing as proposed by Russell and Brown can not be maintained beyond an aging temperature of  $\sim 675^\circ\text{C}$ .

Table 6.3 presents the correlation coefficient (*CoR*) matrix, where the correlation coefficients between material properties and computed particle spacing are given in the first six columns. With particle spacing, there is a positive correlation with void size, percentage elongation (*el*) and percentage reduction of area (*RA*), whereas inverse correlation was found for hardness, yield strength and tensile strength (UTS). While void size and RA show good correlations, others show weak correlation except for the Wavelet analysis where the absolute correlation coefficients are above 0.7. It can be seen that the correlation coefficient between yield stress and particle spacing computed by fractal dimension determined by the R/S analysis is minimum (-0.40); however plotting both of them with the aging temperatures, a correlation can be easily identified. Minimum particle spacing found at 450°C aging temperature correlates well with maximum yield stress at 500°C. Since for the HSLA steel, the maximum hardness can occur between 450-500 °C, the correlation between the particle spacing and yield stress can be accepted.

#### **e) Estimation of fractal fracture toughness**

To compute fractal fracture toughness using  $\lambda$ , equation (6.16) has been used, where the local fracture strain ( $\epsilon_f^*$ ) is calculated from the micro-roughness of the fracture surfaces as suggested by Garrison [14]. Figure 6.10 shows the comparison between normalized experimental fracture toughness with the same computed using equation (6.16). The correlation coefficients between these two parameters, listed in the last column in Table 6.3, are found to be good for all the

methods. The correlation would improve further if the proportionality constants,  $k$  and  $k_3$  in equation (6.10) are obtained rigorously through careful experimentation.

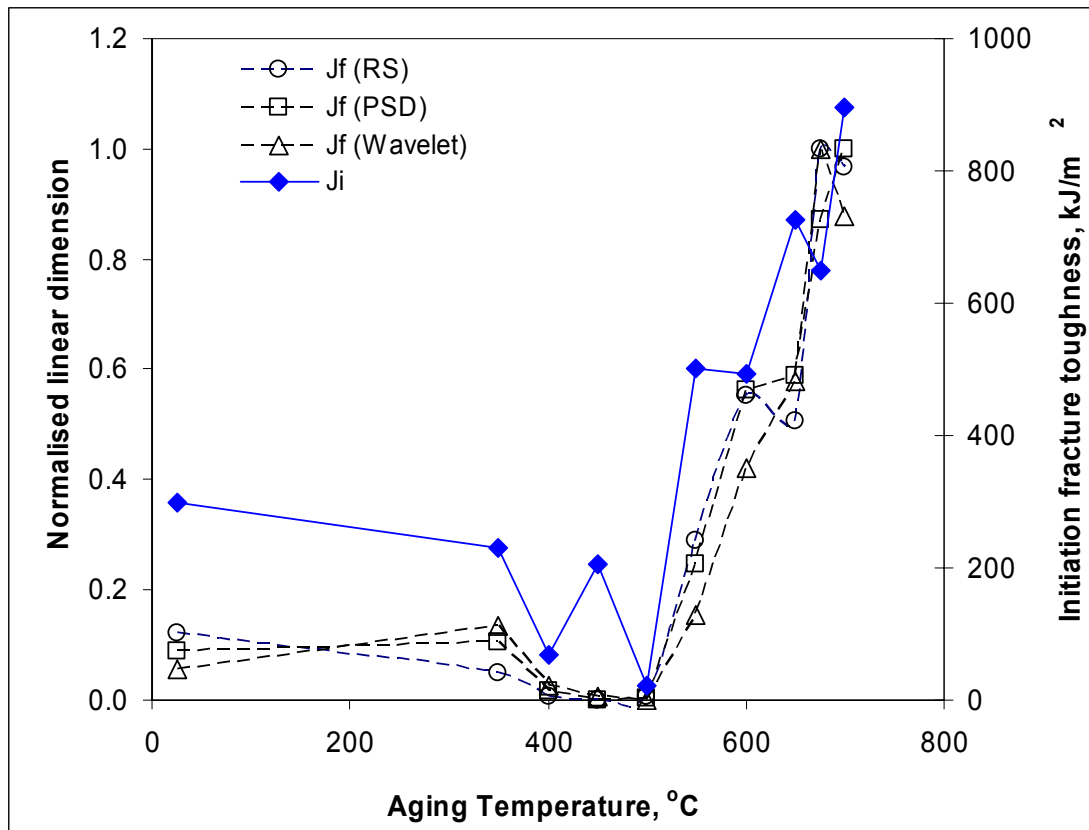


Figure 6.10: Correlation between fractal fracture toughness and experimental fracture toughness

It was observed that the correlation coefficients ( $CoR$ ) given in Table 6.3 are sensitive to the coefficient  $k_3$  in equation (6.10). Sensitivity analysis has been performed to assess the effect of  $k_3$  on the correlation coefficients between the particle spacing and the void diameter,  $CoR_{v\lambda}$ , and the same between the fractal fracture toughness and experimental fracture toughness,  $CoR_{JfJ}$ . Figure 6.11 gives the variations of the correlation coefficients with the constant  $k_3$ . To obtain an optimum value, the intersection of the two correlation curves has been considered. It may be noted that the points of intersection are 0.075, 0.13 and 0.175 for the Wavelet, PSD and RS methods respectively. Since the variation is not substantially large, an average value of 0.13 is accepted for all the three methods. All figures presented in this section have been generated using  $k_3=0.13$ .

Table 6.3: Cross correlation matrix showing correlation coefficient ( $CoR$ ) between particle spacing,  $\lambda$ , and material properties like hardness ( $Hv$ ), yield strength ( $YS$ ), ultimate tensile strength ( $UTS$ ), percentage elongation ( $e_l$ ), percentage reduction of area ( $RA$ ), void diameter ( $V$ ).  $CoR_{JFJ}$  stands for correlation coefficient between experimental fracture toughness and fractal fracture toughness.

Method	$CoR_{Hv\lambda}$	$CoR_{YS\lambda}$	$CoR_{UTS\lambda}$	$CoR_{e_l\lambda}$	$CoR_{RA\lambda}$	$CoR_{v\lambda}$	$CoR_{JFJ}$
RS	-0.427	-0.403	-0.539	0.430	0.603	0.619	0.898
PSD	-0.568	-0.516	-0.656	0.576	0.749	0.768	0.925
Wavelet	-0.817	-0.735	-0.823	0.776	0.949	0.943	0.875

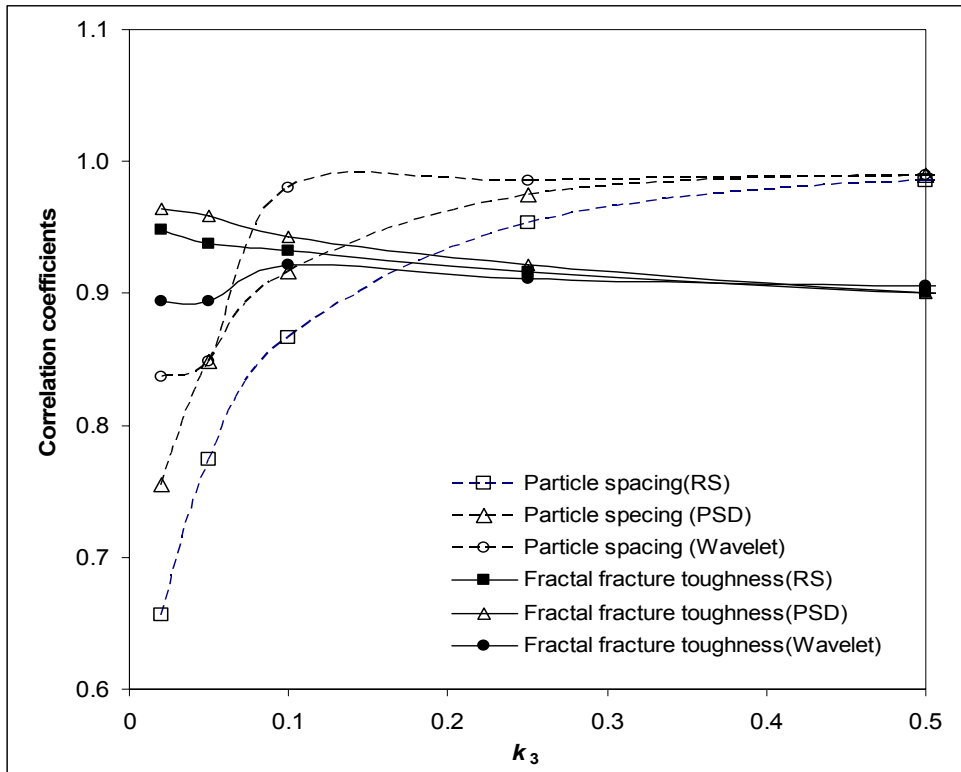


Figure 6.11: Variations of correlation coefficients with the constant  $k_3$ .

### 6.3 Conclusions

The fractal dimensions for fractographic images of HSLA steel aged at various temperatures after water quenching are reported in this chapter. R/S, PSD and Wavelet analyses are employed to compute fractal dimensions using high resolution SEM images. Following are the conclusions made:

- An inverse correlation is found between fractal dimension and magnification. Beyond 2000 magnification, the decreasing trend is persistent ( $D < 2.5$ ). Below 2000, except Wavelet method, others show anti-persistent behaviour ( $D > 2.5$ ). For unaltered images, the standard

deviation is the largest for PSD analysis, which is less than 0.194 and the coefficient of variance is less than 8%. The least standard deviation is obtained for the wavelet analysis which is 0.123.

- Variation of locations (spatiality) has insignificant effect on fractal dimensions since the standard deviation is less than 0.04 and the co-efficient of variance about 1.3%.
- Wavelet analysis is found to be the most robust method and efficient in terms of time and memory. The least efficient method is found to be the PSD method in terms of time.
- Consistent trend in variations of fractal dimensions with aging temperatures is observed for the three methods, although the values are different for different methods. Systematic variations of fractal dimensions with aging temperatures, estimated from the fractographic images directly, can therefore be used for evaluation of materials. This finding is significant to material research, especially with regard to directly using fractographic images by SEM in preference to more cumbersome procedures.
- While the R/S method is found to be the worst performing method in terms of variability, the estimated fractal dimensions with aging temperatures show better discrimination capability because of the wider range of variations. Similar is the observation for the PSD analysis. Wavelet analysis generates narrow data range; hence the discrimination capability is limited. Nevertheless the error bars shows minimum variations for the Wavelet analysis.
- Using the concept of fractal mathematics, an expression for the particle spacing have been developed where tensile properties like percentage area reduction ( $q$ ), elongation ( $e_f$ ) and the fractional part of the fractal dimension ( $D^*$ ) computed from the tensile fracture surface are used. The developed expression is given by

$$\lambda = \frac{1}{k} \left( \frac{k_3 q}{(e_f + 1)(1 - q)} \right)^{\frac{1}{2D^*}}$$

- The particle spacing  $\lambda$  has been shown to have good correlation with the circular diameter of voids estimated from the tensile fracture surface of HSLA steel aged at different temperatures. Inverse correlation between the particle spacing in the copper containing HSLA steel on aging and the increment in yield stress due to copper precipitation kinetics has been demonstrated.

- For computing fractal fracture toughness, a mathematical model is devised where the local fracture strain  $\varepsilon_f^*$  is calculated from the micro-roughness of the fracture surface and the characteristic length,  $l_0$  scaled by the particle spacing. The agreement between experimentally determined fracture toughness and the same predicted using the proposed model is found to be good.

## 6.4 References

1. Zhi-bin Liu, Bin Shib, Hilary I. Inyang and Yi Cai: Magnification effects on the interpretation of SEM images of expansive soils, *Engineering Geology*, 78, 89-94 (2005).
2. XiaoWu Li, JiFeng Tian, Yan Kang and ZhongGuang Wang: Quantitative analysis of fracture surface by roughness and fractal method, *Scripta Metallurgica et Materialia*, 33, 5, 803-809(1995).
3. I. Dlouhy´ and B. Strnadel: The effect of crack propagation mechanism on the fractal dimension of fracture surfaces in steels, *Engineering Fracture Mechanics* 75, 726–738 (2008).
4. References [30-41] of chapter-2 of this thesis.
5. J. Stampfl, S. Scherer, M. Berchthaler, M. Gruber and O. Kolednik: Determination of the fracture toughness by automatic image processing, *International Journal of Fracture*, 78,1,35-44(1996).
6. A.W. Thompson: Modeling of local strains in ductile fracture, *Metall Trans A*, 18A, 1877–1886(1987).
7. W.M. Garrison and N. R. Moody: The influence of inclusion spacing and microstructure on the fracture toughness of the secondary hardening steel AF1410, *Metall. Trans A*, 18,7,1257-1263(1987).
8. R.O. Ritchie, W.L. Server, R A.Wullaert: Critical fracture stress and fracture strain models for the prediction of lower and upper shelf toughness in nuclear pressure vessel steels, *Metall Trans A*, 10A, 1557–1570(1979).
9. R. O. Ritchie, A. W. Thompson: On macroscopic and microscopic analyses for crack initiation and crack growth toughness in ductile alloys, *Metall Trans A*, 16A:233–248(1985).
10. W. M. Garrison : A microstructurl interpretation of the fracture strain and characteristic fracture distance, *Scripta Matall.*, 18, 583-586(1984).
11. J. R. Rice and M.A. Johnson: Inelastic behavior of solids, edited by Kannien MF, Adler WG, Rosenfield AR, Jaffe RJ, 1970, McGraw-Hill, NY.

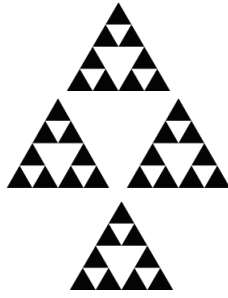
12. S.K. Das: Fracture behaviour of Copper strengthened HSLA steel, PhD Thesis, 2007, BESU, India.
13. B. Mandelbrot: The fractal geometry of nature, 3<sup>rd</sup> Edition, 1983, W. H. Freeman and Company, New York.
14. E. E. Underwood and K. Banerji: Fractal analysis of fracture surfaces. In: Fractography, 1992, 12, ASM Handbook, ASM International, USA.
15. G. Guiglionda and W.J. Poole: The role of damage on the deformation and fracture of Al-Si eutectic alloys, Materials Science & Engineering A, 336, 159-169(2002).
16. Sivaprasad S, Tarafder S, Ranganath VR, Ray KK. Materials Science and Engineering A 2000; 284:195
17. Kiran Solanki, S. R. Daniewicz and J. C. Newman: Finite element analysis of plasticity-induced fatigue crack closure: an overview, Engineering Fracture Mechanics, 71, 2, 149-171(2004).
18. A.W. Thompson and M.F. Ashby: Fracture surface micro-roughness, Scripta Metal., 18, 127-130(1984).
19. S. K. Das, S. Sivaprasad, S. Das, S. Chatterjee and S. Tarafder: The effect of variation of microstructure on fracture mechanics parameters of HSLA-100 steel, Material Science and Engineering A, 431, 68 – 79 (2006).
20. S. K. Das, N. Narasaiah, S. Sivaprasad, S. Chatterjee and S. Tarafder: Effect of aging on fatigue crack growth behaviour of Copper bearing HSLA-100 steel, Mat. Sci. and Tech., 23, 177-182 (2007).
21. A. Ghosh and S. Chatterjee: Characterization of precipitates in an ultra low carbon Cu bearing high strength steel: A TEM study, Material Characterization, 55, 298–306(2005).
22. S. K. Dhua, D. Mukerjee, D. S. Sarma: Influence of Tempering on the Microstructure and Mechanical Properties of HSLA-100 Steel Plates, Met. Trans. 32A:2259-2269(2001).
23. P. Kizler, D. Uhlmann, S. Schmauder: Linking nanoscale and macroscale: calculation of the change in crack growth resistance of steels with different states of Cu precipitation using a modification of stress-strain curves owing to dislocation theory, Nuclear Engineering and Design, 196, 175-183(2000).
24. K.C. Russell and L.M. Brown: A dispersion strengthening model based on differing elastic moduli applied to the iron-copper system, Acta Met., 20, 969-974(1972).



# CHAPTER 7

<b>7.0</b>	<b>Fractal analysis of magnetic Barkhausen emission signals</b>	
7.1	MBE signal acquisition	160
7.2	Standard magnetic properties from MBE signal	164
7.3	Results and discussion	165
7.3.1	Probability density function for the MBE signals	165
7.3.2	Fractal analysis of MBE signals	169
7.3	Conclusions	176
7.4	References	177





# 7

## **FRACTAL ANALYSIS OF MAGNETIC BARKHAUSEN EMISSION SIGNALS**

This chapter presents results obtained by fractal analysis of Magnetic Barkhausen Emission (MBE) signals. The MBE signals are said to have fractal properties. The stochastic nature of the MBE signals is responsible for the fractal behaviour. Variations of magnetic properties take place when materials are exposed to operating environment or loading, causing micro or macro damages in materials which may or may not be visibly identifiable in their microstructures. However the MBE signals, acquired through non-destructive means, can identify these damages since the coercivity and magnetic permeability are altered owing to the magnetic domain wall (DW) movement. Similarly various microstructural constituents (non-magnetic or magnetic) have differential effect on the magnetic properties of the materials; MBE signals can determine these microstructural constituent parts. This chapter reports magnetic properties of the HSLA materials by MBE and Magnetic Hysteresis Loop (MHL) methods. Correlation between magnetic properties and the fractal dimensions computed from the MBE signal has been

investigated. In addition to the magnetic properties, attempt has been made to find out correlations between fractal dimensions of MBE signal with the mechanical properties of the same material.

## 7.1 MBE signal acquisition

Figure 7.1 shows the schematic diagram of the MBE setup. Samples are magnetized by a C-core magnet. The induced signal, acquired in millivolts, was picked up by the secondary coil. The induced pick up voltage which is proportional to the rate of change of flux,  $\dot{\Phi}$ , depends on the applied field ( $H$ ), magnetization of the sample ( $M$ ) and the effective cross sectional area of the coil. The expression for  $\dot{\Phi}$  [1] is thus

$$\dot{\Phi} = N\mu_0(A_{pickup}\dot{H} + A_s\dot{M}) \quad (7.1)$$

where  $N$  is the number of turns at the secondary coil,  $A_{pickup}$  is the cross sectional area of the pick up coil,  $A_s$  is the cross sectional area of the specimen,  $\mu_0$  is the permeability of medium. In low alloy steel which is considered to be soft ferromagnetic material generating higher level of magnetization of the sample ( $M$ ), and as the interest of the present study is the variation of microstructural changes, the first term in equation (7.1) should be insignificant compared to the rate of change of magnetization due to applied field *i.e.*,  $A_{pickup}\mu_0\dot{H} \ll A_s\dot{M}$ . To ensure that the value of  $A_{pickup}\mu_0\dot{H}$  is insignificant, the pickup coil area is usually chosen very small compared to the total sample area and low frequency magnetic field is used to minimize applied magnetic field intensity. In addition, the sensitive orientation of the pick-up coil is chosen perpendicular to the applied field, *i.e.* a tangential magnetization in the sensed inspection region is ensured. Applied magnetizing field produces an opposite demagnetizing field having differential effect on the MBE signal, therefore, to keep the demagnetizing field constant, it is recommended that the signal be acquired at high coercivity point where the  $B$ - $H$  curve is linear; here  $B$  is the flux density. As the change of magnetization is maximum at coercive point, majority of MBE activity is found close to coercive field of the material.

In a metallic system, the correlation between the rate of change of induced flux,  $\dot{\Phi}$ , can also be written in terms of DW velocity [3],  $v$  as:

$$\langle \dot{\Phi} \rangle = \left( \frac{AA_s\mu_0}{\sigma.G} \right) \langle v \rangle. \quad (7.2)$$

In equation (7.2),  $\sigma$  is the electrical conductivity,  $G$  is a constant value equal to 0.1357 [3], and  $A$  is the parameter measuring the strength of the local pinning interactions.

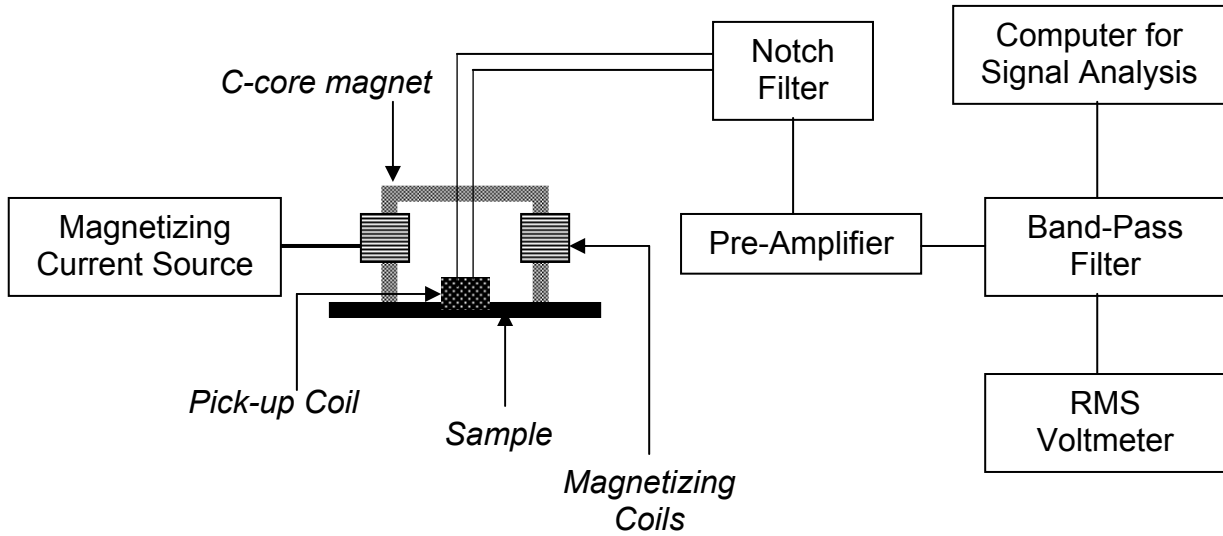


Figure 7.1: Schematic diagram of MBE setup [2]

The MBE signal amplitude *i.e.* the induced Barkhausen voltage,  $V$ , in the pick-up coil wound around a sample can be represented as

$$V = -\mu_0 N A_s \frac{dM_{js}}{dt} \propto \langle v \rangle \quad (7.3)$$

where  $M_{js}$  is the total Barkhausen activity in terms of the 'jump sum' which represents the discontinuous change of magnetization [4] and is a direct function of DW velocity,  $v$ . It is clear from equations (7.2) and (7.3) that as the strength of the local pinning interactions ( $A$ ) increases, the DW velocity decreases and so does the RMS value of induced voltage for constant  $\langle \dot{\Phi} \rangle$ .

To acquire MBE signal, the same specimens of water quenched HSLA steel aged at aging temperatures of 350°C, 400°C, 450°C, 500°C, 550°C, 600°C, 650°C, 675°C, 700°C were magnetized. The sinusoidal magnetizing field was of strength 4kA/m with frequency 40Hz. Notch filter was used to eliminate the magnetizing frequency and bandpass filter of 30-300 kHz was used to capture the MBE signal. The coercivity of the material was measured by magnetic hysteresis loop (MHL) technique using surface probe. Details of the hysteresis measurement have been reported elsewhere [5].

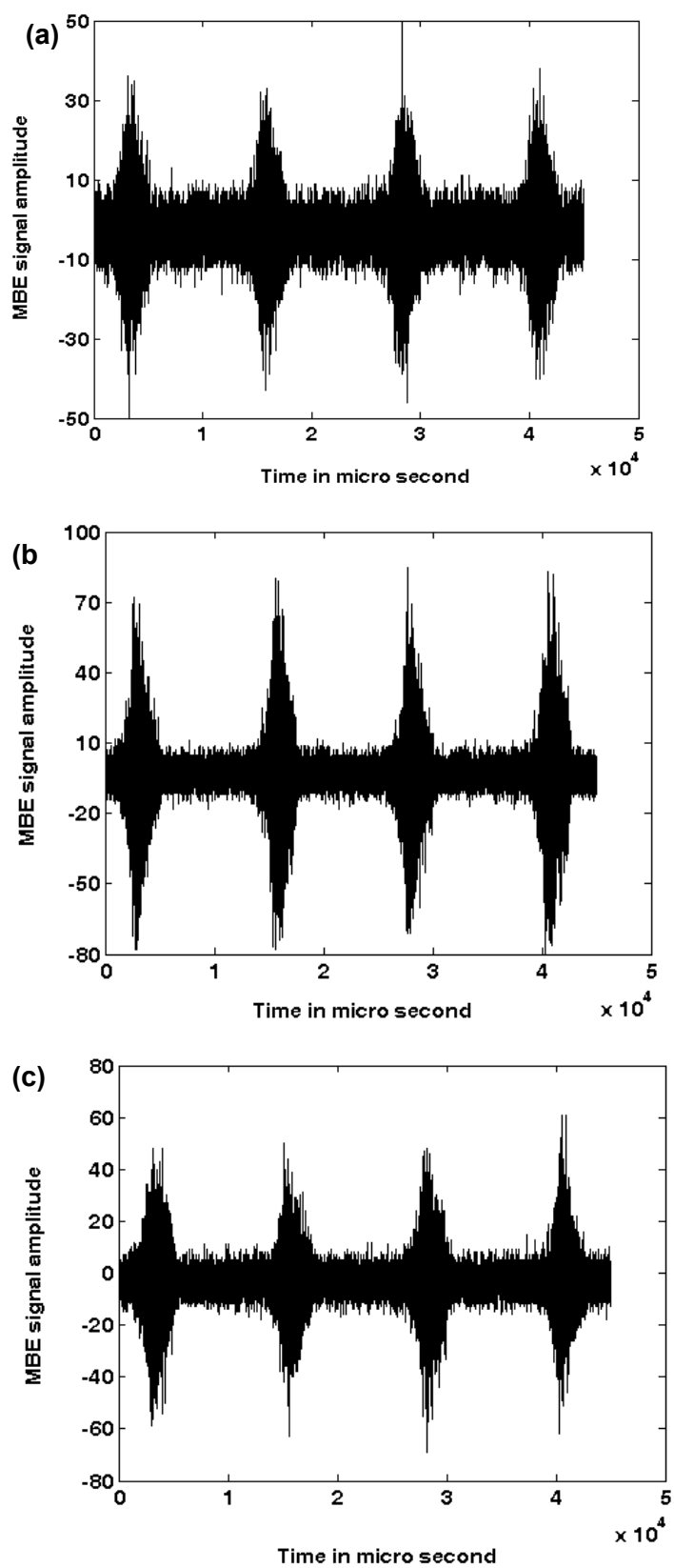


Figure 7.2: MBE signals for (a) WQ sample and after heat-treatment at temperature (b) 500°C and (c) 700°C.

The time domain MBE signal is of burst type. Each signal contains 62500 data samples, 4 bursts and 12500 samples in each burst. Each hysteresis loop gives two bursts therefore each sample of the signals is acquired from two hysteresis loops. The sampling frequency was 1 MHz. For each specimen, three sets of MBE signals were acquired. Figure 7.2 presents the MBE signals for three aging temperatures. A driving sinusoidal signal acts as a carrier wave for the high frequency MBN packets coming out from the sample. The following is the correlation between sampling frequency, total signal acquiring time, number of magnetic Barkhausen noise (MBN) packets and the frequency of the driving field

$$f = \frac{N_b}{2t} = \frac{N_b f_s}{2N} \quad (7.4)$$

where the total number of data acquired is  $N$ , the sampling frequency is  $f_s$ , the total signal acquiring time,  $t = \frac{N}{f_s}$ , the number of MBN packets is  $N_b$  and the frequency of the driving field is  $f$ .

A careful examination of a MBN packet reveals that  $DW$  motion has three states in each of the positive and negative half cycles of the driving field-

- Creation of DW, showing increasing MBN signal strength
- Positive or negative saturation at peak
- Annihilation of DW, showing decreasing MBN signal strength

In between two packets, there is a saturated state of the material when no MBN are acquired. The MBN characteristics can be changed by altering the nature, frequency and amplitude of the driving magnetic field. For a Fe-Si-B amorphous alloy, it was found that steady state was reached when the magnitude of the driving magnetic field was more than  $60\text{Am}^{-1}$ . No appreciable difference in MBE signals can be observed if the magnitude is increased further. Frequency of the driving field has inverse correlation with the MBE events and a direct correlation with the root mean square value of the induced voltage ( $V_{RMS}$ ). One can decrease the frequency of the driving field to acquire more MBN signals; however the amplitude of the signal will be low which may require higher amplification. Elimination of noise would be an important issue when low frequency driving field is used.

## 7.2 Standard magnetic properties from MBE signal

Standard magnetic properties of a ferromagnetic material, considered in the present work, are the  $V_{RMS}$ , pulse height distribution (PHD) and coercivity. While the  $V_{RMS}$  and PHD are obtained from the MBE signal, coercivity is estimated from the hysteresis loop by the MHL method. For the HSLA materials, these properties are reported in the literature [5, 6], which are used for verification and validation of the fractal dimensions computed from the MBE signals. The magnetic properties like coercivity and  $V_{RMS}$  are given in Table A.2 of Appendix I. The PHD has been computed and is reported in section 7.3 of this chapter.

It was reported that the material became magnetically softer as the coercivity decreases since coercivity is the amount of resistance a material presents against magnetization. Figure 7.3 shows the plot for the variations of coercivity and RMS voltage amplitude with the aging temperatures.

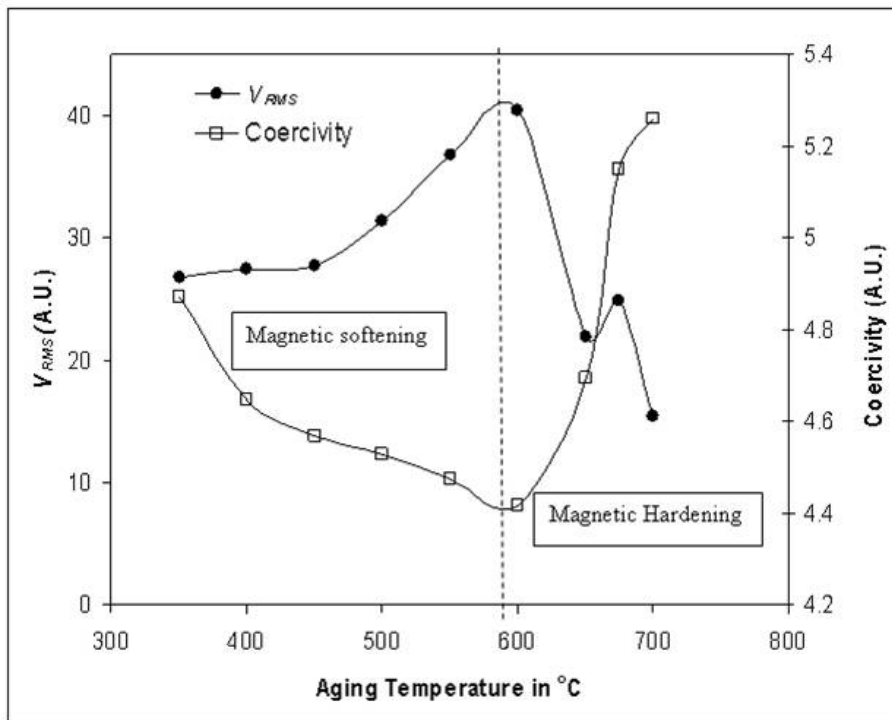


Figure 7.3: Variations of coercivity and  $V_{RMS}$  with the aging temperatures.

During the initial stage of aging, coercivity decreases up to the aging temperature of 600°C when the material was magnetically soft. However, when the aging temperature was above 600°C, a rapid increase in coercivity with aging temperature was observed leading to magnetically harder material. The peak  $V_{RMS}$  found to be at 600°C as well, showing the maximum domain wall (DW) motion at this temperature. DW motion decreases as the material becomes magnetically hard.

## 7.3 Results and Discussion

### 7.3.1 Probability density function for the MBE signal

At time,  $t$ , the probability density function of the MBE signal,  $P_t(V)$ , which is directly related to the domain wall velocity ( $v$ ), and decays as power law [3,7,8] can be given as

$$P_t(V) \approx V^{-\gamma} \exp\left(\frac{V}{V_0}\right) \quad (7.5)$$

where  $V_0$  is the cut-off voltage. To compute the probability density, histogram of the  $V_{RMS}$  signal within the minimum and maximum values was obtained for different bin sizes. In statistics a bin is the disjoint category of features of which the frequency of occurrence is discussed. To obtain PHD for the  $V_{RMS}$ , five voltage categories have been considered as shown in Figure 7.4, which presents the probability density function of the MBE signal for aging temperature 350°C.

It may be seen that depending upon the bin size, the peak value of the probability density function changes. However the  $\gamma$  exponent, which signifies the extent of decay of the power law and obtained from the slope of the logarithmic plot of the  $P_t(V)$  vs  $V$  data, was found to be weakly dependent on the bin size. To eliminate this weak dependence, the  $\gamma$  exponent was computed by taking average from five bin sizes. Each MBE signal has four bursts; the  $\gamma$  exponent was computed from (i) each of these bursts and (ii) the average of these four bursts and (iii) full signal. . For cases (i) and (ii), signals acquired during magnetic saturations were disregarded. Variation of  $\gamma$  exponent with aging temperatures is given in Figure 7.5. In the full signal, noise acquired during the magnetic saturation reduces the variation of the exponents with aging temperatures which can be seen in figure 7.5. However, ignoring values for the WQ state and rescaling the  $\gamma$  exponent range, the variation of the  $\gamma$  exponent for the total signal is found to be highly correlated when it was plotted against the hardness of the material, shown in Figure7.6.

For reporting correlations between the  $\gamma$  exponent and material properties, above mentioned two cases, (ii) and (iii), have been considered. The correlation coefficients ( $R$ ) are given in Table 7.1 where subscripts correspond to material properties like  $YS$  for yield strength,  $H$  for hardness,  $el$  for percentage elongation,  $J_i$  for the initiation fracture toughness,  $UTS$  for the ultimate tensile strength,  $c$  for the coercivity and  $V$  for the RMS voltage. Detailed experimental methods for evaluating the mechanical properties can be found elsewhere [9-11].

Table 7.1: Correlation coefficients(*CoR*) showing cross-correlation between  $\gamma$  exponents and material properties\*.

	$CoR_{YS}$	$CoR_{Hv}$	$CoR_{el}$	$CoR_{J_i}$	$CoR_{UTS}$	$CoR_c$	$CoR_V$
Average	0.30	0.29	-0.12	-0.01	0.10	0.08	-0.46
Full signal	0.83	0.81	-0.91	-0.88	0.92	-0.72	0.51

\* the subscripts are the *YS* for yield strength, *Hv* for hardness, *el* for percentage elongation, *J<sub>i</sub>* for the initiation fracture toughness, *UTS* for the ultimate tensile strength, *c* for the coercivity and *V* for the  $V_{RMS}$ .

While the correlation coefficients for  $\gamma$  exponents computed from the full signal are found to be excellent, the same is not true for the average  $\gamma$  exponents. Nevertheless the average  $\gamma$  exponent has significance in terms of microstructural evolution due to the progressive aging of the HSLA steel. Lack of a unique trend (positive or negative) throughout the aging process can therefore be explained in the light of the microstructural evolution.

For ferritic steel, mechanical hardness has a positive correlation with the magnetic hardness. However for the HSLA steel this correlation could not be explained using standard magnetic parameters like  $V_{RMS}$  and coercivity. However, a direct correlation with the hardness was observed when  $\gamma$  exponent from the full signal is used as the magnetic characterizing parameter as shown in Figure 7.6.

Higher the value of the  $\gamma$  exponent, faster is the decay of the probability distribution of the MBE voltage. This may take place when the distribution curve is skewed towards the right signifying maximum probability of the higher voltage amplitude. Higher voltage amplitude is due to increased DW velocity. This can happen when the strength of the local pinning interactions is reduced for constant rate of change of flux density (equation 7.2). Thus, an inverse correlation between  $\gamma$  exponent and the strength of local pinning interactions is observed. From the WQ condition to aging upto 350°C, the  $\gamma$  exponent reduces which indicates slow decay of the probability distribution curve and increased pinning interaction. . The DW motion is obstructed due to the mismatch strain fields between the coherent Cu-precipitates[12] formed due to aging and the Fe bcc lattice. However from 350°C to 500°C the pinning interaction reduces and the DW motion was increased gradually. It is usual that with aging, the material will have second phase microstructural constituents acting as barriers to the DW motion. However for HSLA steel, the DW motion was not impeded as there were coherent Cu precipitations in the matrix. The coherent Cu precipitates is of nanosize (~5nm-20nm)[13] which is less than the typical magnetic domain size of 30-50nm for which the DW motion could not be resisted. While the

DW motion was not impeded, dislocations were arrested or pinned by the nanosize Cu-precipitations. Impediment of dislocations enhances the hardness and strength of the HSLA steel upto 500°C aging temperature. Beyond 500°C aging temperature, the Cu precipitations increase in size. Due to the coarsening of the Cu precipitates, strength of the DW pinning interactions increases, for which DW motion is reduced and the material becomes magnetically hard. Coarsening of Cu precipitations allows dislocations to glide pass the obstacles due to which mechanical hardness and strength reduce. A new microstructural phase (martensite islands inside retained austenite) [6,9,10,11] is formed around 650°C for which the  $V_{RMS}$  as well as the  $\gamma$  exponent show variations at higher aging temperatures. Thus, inverse correlation between magnetic hardness and mechanical hardness was found up to 600°C in HSLA steel. While the error bar remains reasonable at all aging temperature except at 675°C, the data scatter is possibly due to the formation of the martensitic island inside retained austenite. The microstructural homogeneity is not maintained due to formation of the composite microstructure, which is responsible for generating highly scattered signal. The variation of microstructural constituents due to aging of the HSLA steel is a dynamic process which could not be identified by the standard magnetic parameters like RMS voltage and coercivity parameters; however the power law decaying exponent did identify these changes and shows a positive correlation with the hardness variations.

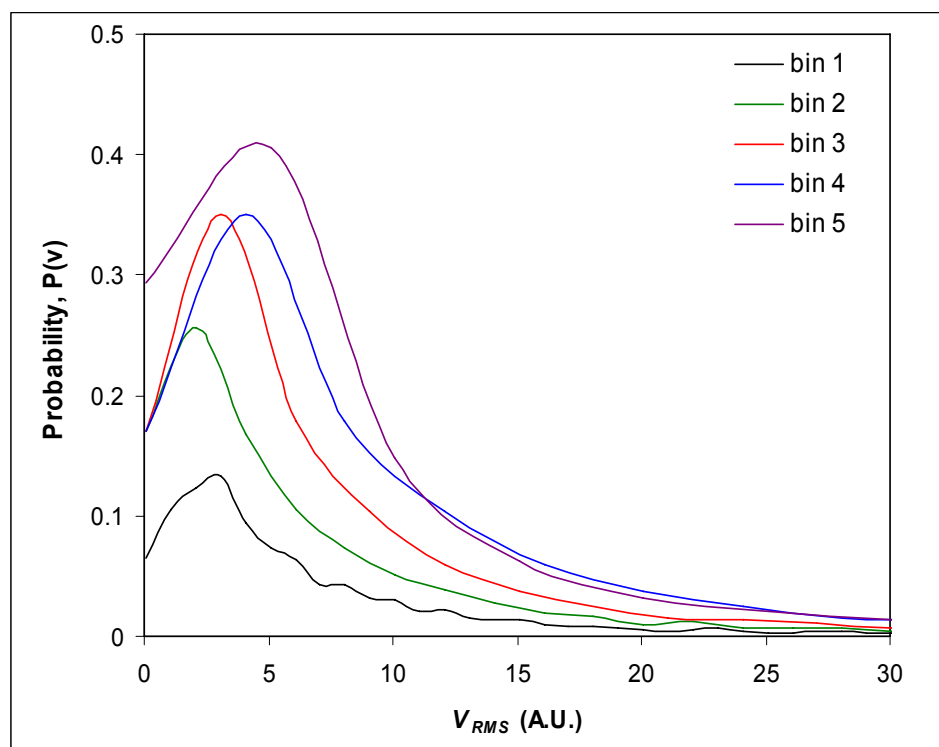


Figure 7.4: The probability density function for the MBE signal for samples aged at 350°C for different bin sizes (bin1=1 mV, bin 2=2 mV, bin 3 =3 mV, bin 4=4 mV and bin 5=5 mV).

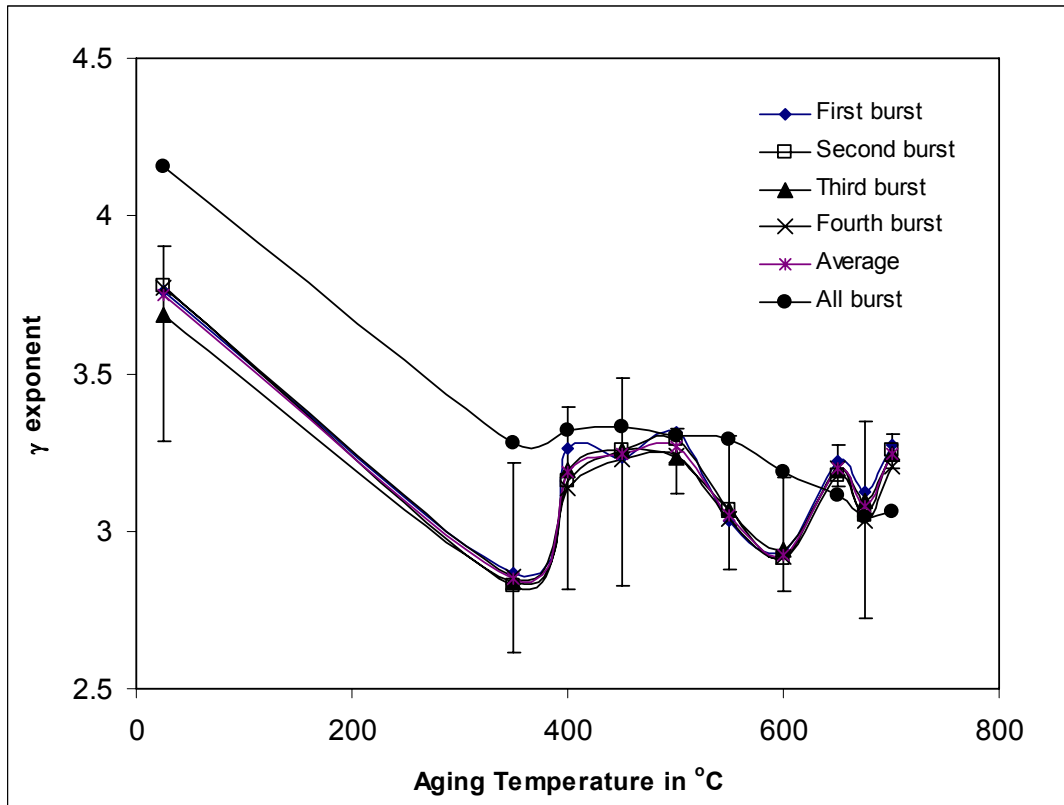


Figure 7.5: Variations of  $\gamma$  exponent with aging temperatures

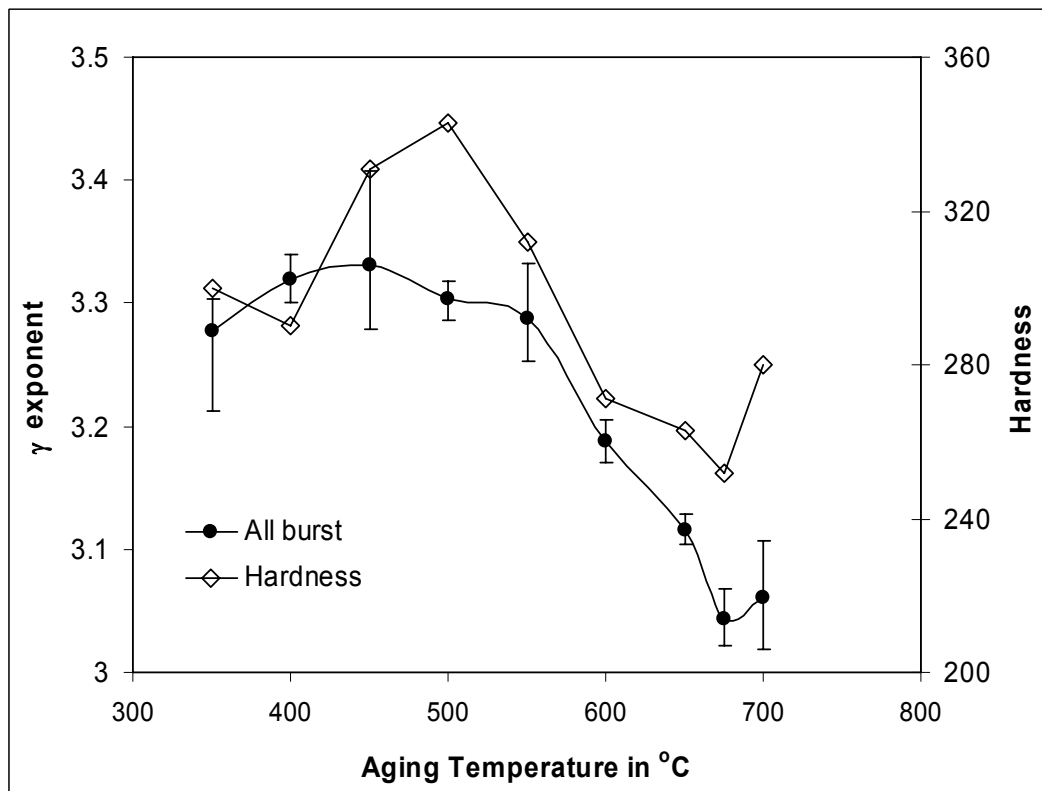


Figure 7.6: Correlation of  $\gamma$  exponent with the hardness of the HSLA steel. Full signal has been considered to estimate the  $\gamma$  exponent.

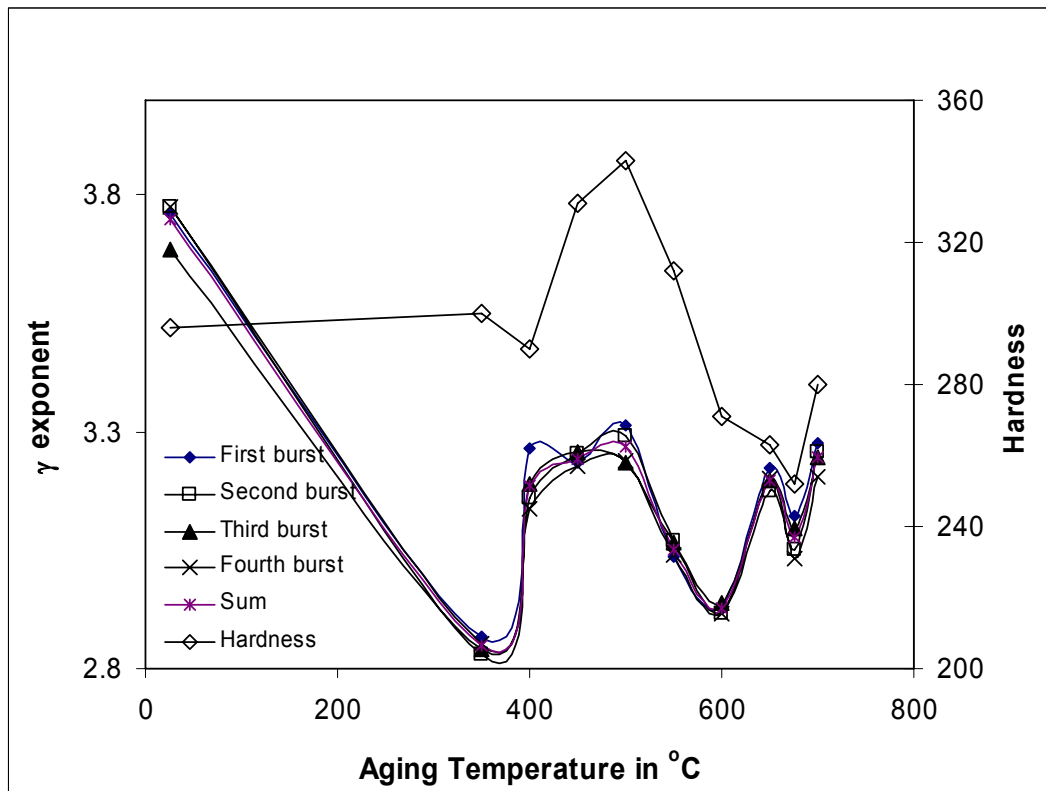


Figure 7.7: Correlation of  $\gamma$  exponent with the hardness of the HSLA steel. The four burst either separately or in all have been considered to estimate the  $\gamma$  exponent.

### 7.3.2 Fractal analysis of MBE signals

It has been discussed in Chapter 3 that fractal dimension is correlated ( $D=\gamma$  when Cantor fractal set was used to model Barkhausen Jump in Ref [3]) with the power law decaying exponent,  $\gamma$ ). In order to use the Cantor set the authors have normalized the DW velocity and the duration of a single burst (shown in equation 3.17), and assumed that the exponent will always remain within  $0 < \gamma < 1$ . The normalization of the DW velocity could not be implemented here, since the strength of pinning interactions ( $A$  in equation 7.2) was not available a priori. Nevertheless, it is expected that fractal dimensions computed from the MBE signals might have correlation with the  $\gamma$  exponent as well as with the mechanical and magnetic properties of materials.

Tadic [14] explored the scaling behaviour of Barkhausen noise (BN) and found it to be non-universal. When the degree of disorder is varied through non-equilibrium phase transition, the scaling exponent also varies. Based on extensive review of experimental and theoretical investigations on BN, it was concluded that the power spectrum decays with frequency ( $f$ ) as  $\sim f^{-\phi}$ , where  $5 \leq \phi \leq 2$ . The distribution of size, duration and energy associated with BN exhibit power law behaviour over a few decades with a cut-off.

The characteristics of BN signals and their power spectrums elucidated by previous researchers were classified into three groups by Plewka et al. [15]. They are

- Group I: Noise in BN, treated as a stochastic element [15], can be modeled using desired parameters to get a known shape of the power spectra.
- Group II: The evidence of  $1/f$  power spectrum signifies self-organised criticality [16] in which BN was considered as a collective phenomenon of several degrees of freedom. An avalanche like propagation of domain wall takes place for a small perturbation due to a single Barkhausen jump. The effect of Barkhausen jump may decay gradually generating a point of self organized criticality in spatial as well as time domains.
- Group III: Chaos in the BN pulses can be treated as deterministic rather than stochastic [17-19]. A single domain may show random disorder, however the presence of long range magnetostatic interactions orchestrated the random disorder in synchronized deterministic forms.

Using correlation dimension, a method to represent self-similar fractal behaviour in signals, Plewka et al. [15] demonstrated that Barkhausen effect exhibits low dimensionality below 1.5 and, therefore can be treated as a deterministic chaotic phenomenon. The authors used ferromagnetic amorphous ribbon to investigate the dimensionality.

The Hurst exponent,  $H$  can express the power spectrum of the MBE signal as an exponent of the decaying function of frequency as

$$P(f) \propto \frac{1}{f^\beta} \quad (7.6)$$

where  $\beta=2H+1$  for fractional Brownian motion (fBm) and  $\beta =2H-1$  for fractional Gaussian noise (fGn) type signal [20-22] and  $P(f)$  is the power estimated by taking fast Fourier transformation (FFT) of the MBE signal. The fBm is a non-stationary, zero mean Gaussian function and fGn is the first derivative of the fBm function. Detail discussion on these fBm and fGn functions is given in Chapter 4. Considering MBE signal as of fBm type, the classification by Plewka et al. [15] in terms of fractal dimensions and Hurst exponents is given in Table 7.2. When the value of  $H$  is confined within 0 and 0.5, the signal is treated as stochastic and anti-persistent. A change of behaviour is noticed when  $H$  becomes 0 and the power spectrum shows  $1/f$  noise characteristics which is termed as pink noise or a condition of self-organised criticality (SOC) [16]. Plewka elaborated that MBN signal is the effect of the DW motion owing to a small

perturbation to a single domain which creates an avalanche like propagation without any characteristic time or range constant. The local instability of the domain structure and size determine the size of the avalanche and the relaxation time of the system determines the lifetime of the avalanches. When  $H$  is within 0.5 and 1, the signal can be treated as deterministic chaotic. It has low dimensionality and the behaviour is persistent. It can be pointed out that MBE signal is the response of a dynamical system which is excited by a given magnetizing force. The frequency of magnetization as well as sensitivity of the measurement device will have profound effect on the acquired MBE signal and thus to determine the signal characteristics it is imperative to mention the operating parameters and appropriate calibration mechanisms.

Since MBE signal is the 1D time domain signal, rescaled range (R/S) analysis, power spectral density (PSD) and Wavelet methods suitable for 1D signal analysis have been employed. The algorithms for the implementation of these methods are given in Appendix-II. For each burst of the MBE signal, fractal dimensions were computed for various aging temperatures. Three sets of MBE signals for each aging temperature were captured from different locations of the specimen to ensure reliability of the results. To investigate the variations of fractal dimensions when the signal was fGn type, the signal was differentiated. The implementation of R/S method requires removal of average trend which essentially eliminates the low frequency components. Differentiation of the fBm type MBE signal keeps the high frequency components again and leaves the very high frequency fractional Gaussian noise. Figures 7.8 (a) and (b) show the variations of fractal dimensions with aging temperatures before and after differentiation of the MBE signals. It may be noted that there is a low dimensionality in the MBE signal signifying persistent behaviour. However for the differentiated MBE signal (fGn type), high dimensionality is noted in fractal dimensions. Since the differentiated MBE signal contains high frequency components, the signal is expected to have stochastic nature which conforms to the high dimensionality characteristic of the signal.

Table 7.2: Classification of MBE signal by fractal dimensions

Group	$\beta$	$H$	$D$	BN type
I	$1 < \beta < 2$	$0 < H < 0.5$	$2 > D > 1.5$	Stochastic <i>i.e.</i> high dimensionality
II	1	0	2	Pink noise signifying self-organised criticality (SOC)
III	$2 < \beta < 3$	$0.5 < H < 1$	$1.5 > D > 1$	Deterministic chaotic <i>i.e.</i> low dimensionality

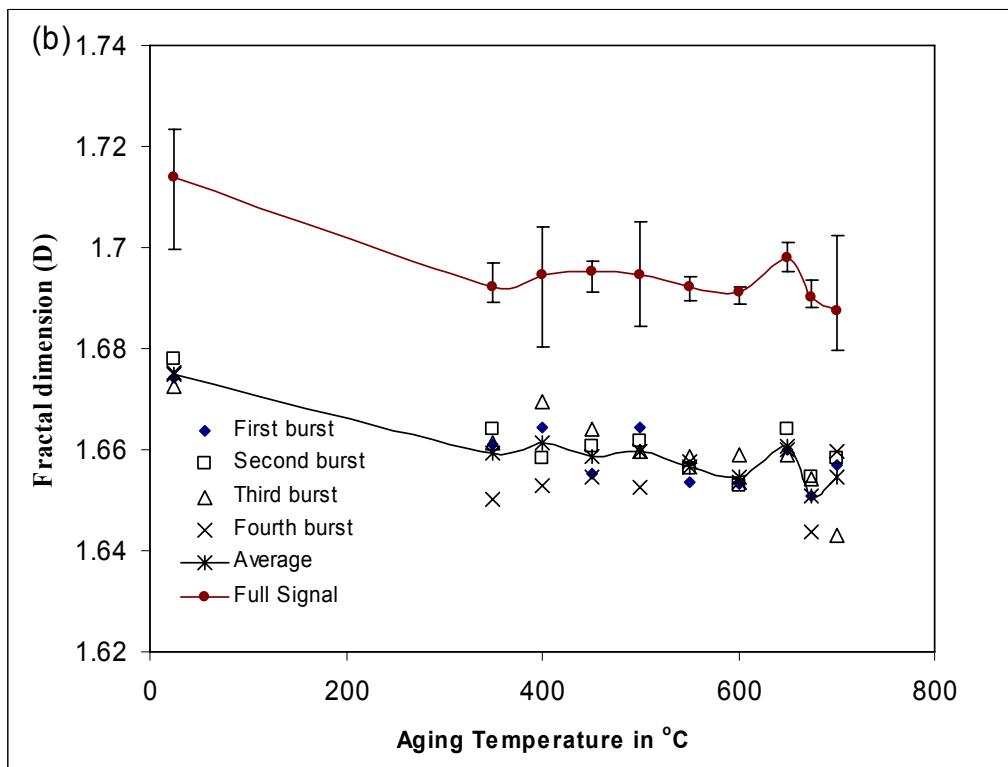
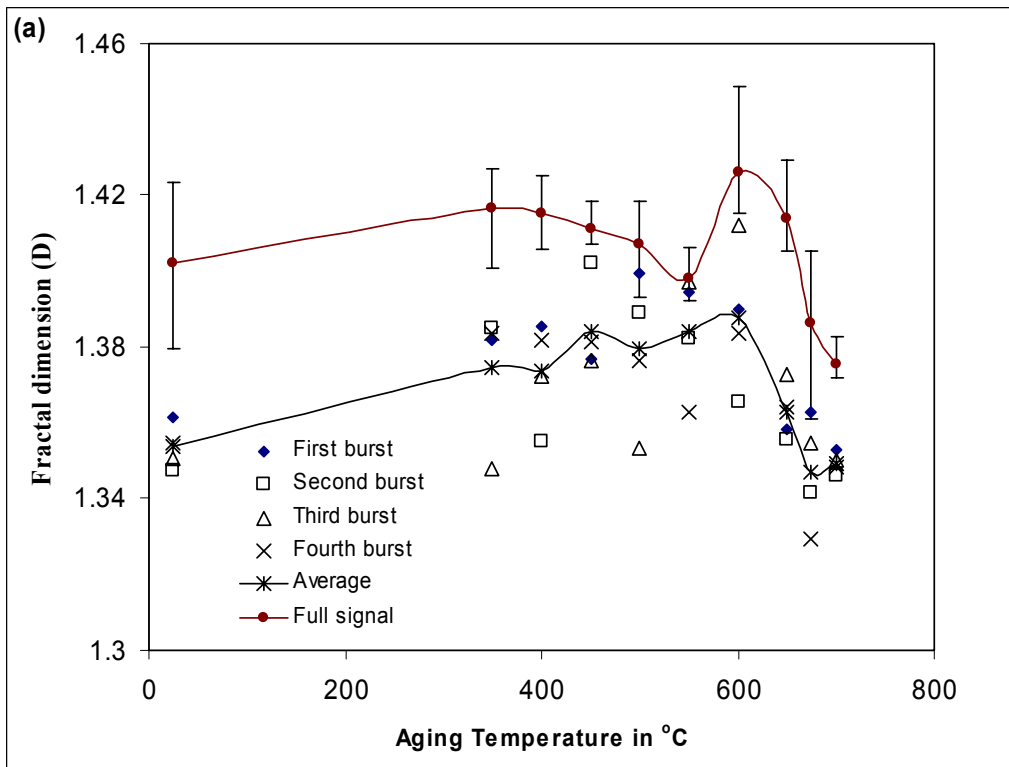


Figure 7.8: Fractal dimensions by RS method using (a) Raw MBE signal i.e. fBm type and (b) Differentiated to keep high frequency components i.e. fGn type.

Table 7.3 presents the correlation coefficients between the fractal dimensions and various magnetic and mechanical properties of the HSLA steels. The correlations are found to be good between the average fBm type signal and the magnetic properties of the materials. However with mechanical properties, the correlation is found to be weak above 0.5 for the average fBm type signal for mechanical properties. For the  $\gamma$  exponent, the correlation is found to be less than 0.5. While the fractal dimension has positive correlation with the hardness, UTS, YS and  $V_{RMS}$ , it has negative correlations with the percentage elongation ( $el$ ) and fracture toughness ( $J_i$ ). The correlations found here is logical since typically hardness of a material is positively correlated with the UTS, YS and negatively correlated with  $el$  and  $J_i$ . Fractal dimensions having opposite correlation with the two magnetic properties reported here indicate that these properties have negative correlation with each other. This agrees with the general trend of negative correlation between coercivity and  $V_{RMS}$ . Fractal dimensions obtained from the fGn type signal show poor correlations with the magnetic and mechanical properties. However they show good correlation with the  $\gamma$  exponent.

Table 7.3: Correlation coefficients( $CoR$ ) showing cross-correlation between fractal dimensions and material properties\*.

			$CoR_{YS}$	$CoR_{Hv}$	$CoR_{el}$	$CoR_{J_i}$	$CoR_{UTS}$	$CoR_c$	$CoR_V$	$CoR_g$
Average	fBm	RS	0.50	0.57	-0.51	-0.55	0.65	-0.92	0.82	-0.43
	fGn	RS-D	0.21	0.27	-0.52	-0.41	0.59	-0.49	-0.01	0.77
Full	fBm	RS	0.08	0.17	-0.51	-0.57	0.47	-0.76	0.58	-0.27
	fGn	RS-D	0.17	0.29	-0.49	-0.48	0.49	-0.60	0.12	0.81

\* the subscripts are the YS for yield strength,  $Hv$  for hardness,  $el$  for percentage elongation,  $J_i$  for the initiation fracture toughness,  $UTS$  for the ultimate tensile strength,  $c$  for the Coercivity,  $V$  for the  $V_{RMS}$  and  $g$  for gamma exponent.

Figures 7.9 (a) and (b) show the plots for the variations of fractal dimensions by PSD method in two frequency ranges: 30 kHz to 500kHz and 30kHz-300kHz respectively. The usual range of MBE signal is 30kHz-300kHz which generates fractal dimensions more than the mathematical limit of Euclidean dimension 2 for 1D signal. Since the aim is to investigate the variations of the fractal dimensions with the aging temperatures and to find out the suitability of this parameter to trace the microstructural evolution in materials, the mathematical limitation has been ignored and the results have been presented for completeness. The range of computed fractal dimensions (difference between maximum at 550°C and minimum at 450°C in Figure 7.9 (b) ) corresponding to the 30kHz-300kHz frequency is found to be greater than the same for the 30kHz-500kHz frequency. The reduction of data range is the effect of the high frequency noise. Variations of fractal dimensions by Wavelet method with the aging temperatures are shown in Figures 7.9 (c)

and (d). Raw MBE signal was used for carrying out Wavelet analysis and the results are shown in Figure 7.9(c), the same signal was filtered to remove the average trend in order to retain the high frequency components and the results are presented in Figure 7.9 (d). High frequency components increase fractal dimensions and insert noise in the system. Removal of average trend (low frequency part), enhances effect of high frequency noise; thus higher fractal dimension is obtained for the case presented in Figure 7.9 (d). Like PSD method, inflection at 450°C is found to be interesting.

It can be seen that the error is significantly high in the results in addition to the fact that the range of the estimated fractal dimensions is very small. All the three methods estimated fractal dimensions more than 1.5. This signifies that the signals are anti-persistent as the Hurst exponent is less than 0.5. The anti-persistent fractal behaviour is expected since Barkhausen Jumps have high frequency harmonic characteristics. To verify the correlations between fractal dimensions obtained by the PSD and Wavelet methods and the material properties, the correlation coefficients are presented in table 7.4.

In Table 7.4, 'Av' and 'Full' postfixed are used to indicate average value of four bursts individually and the full signal respectively. The correlation coefficients show no correlation between the fractal dimensions by PSD and Wavelet methods and the material properties. Nevertheless the data shows certain trend especially the inflection around the aging temperature of 450°C-500°C indicate embrittlement behaviour of the material due to high hardness and strength properties. The investigation clearly shows that fractal dimensions computed from the MBE signals can not correlate microstructural variations leading to the variations of mechanical and magnetic properties of the HSLA steel. The limitation is due to the fact that the MBE signals were acquired at high magnetizing frequency (40Hz). To carry out fractal dimensional analysis the magnetizing frequency should be about 10Hz. The slow response of the DW motion due to low magnetizing fields can show fractal nature which may correlate the material properties. In addition, HSLA steel is a multiphase polycrystalline material and the magnetic response is highly complicated. The sinusoidal nature of the fractal dimensions for different aging shown in Figures 7.9 (a) to (d) show the extent of complexity in the signals.

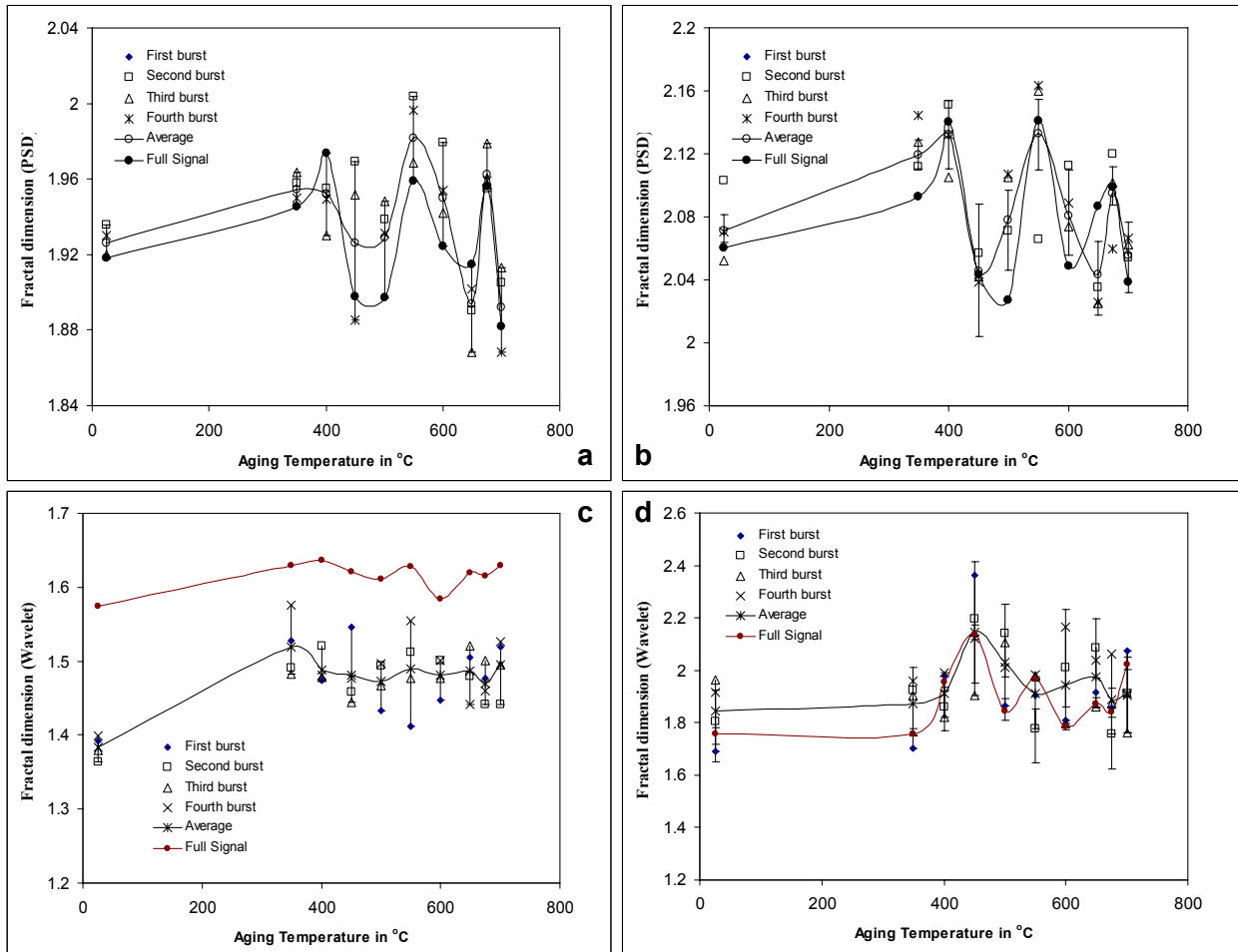


Figure 7.9: Variations of fractal dimensions with aging temperatures by a) PSD method with frequency range was 30 kHz to 500 kHz b). PSD method with frequency range was 30 kHz to 300 kHz, c) Wavelet method and d) Wavelet method removing the average trend.

Table 7.4: Correlation coefficients ( $CoR$ ) for the cross-correlation between fractal dimensions and material properties for the PSD and Wavelet methods.

	$CoR_{YS}$	$CoR_{Hv}$	$CoR_{el}$	$CoR_{J_i}$	$CoR_{UTS}$	$CoR_c$	$CoR_V$	$CoR_g$
PSD-Av	0.16	0.08	-0.13	-0.34	0.33	-0.31	0.69	-0.45
PSD-Full	-0.07	-0.28	0.01	-0.21	0.13	-0.12	0.34	-0.37
Wave-Av	0.11	-0.02	0.13	0.12	0.01	0.19	-0.22	-0.86
Wave-Full	0.32	0.09	0.01	0.04	0.12	0.38	-0.57	-0.46

\* the subscripts are the  $YS$  for yield strength,  $Hv$  for hardness,  $el$  for percentage elongation,  $J_i$  for the initiation fracture toughness,  $UTS$  for the ultimate tensile strength,  $c$  for the Coercivity,  $V$  for the  $V_{RMS}$  and  $g$  for gamma exponent.

## 7.4 Conclusions

- MBE signal is a burst type stochastic signal. Each burst contains magnetic noise which corresponds to the microstructural resistance against the DW motion.
- Probability density function of the MBE signal indicates an exponentially varying power law function. The power law exponent is found to be a suitable parameter to characterize microstructural evolution of the HSLA steel. The correlation coefficients between the  $\gamma$  exponents computed using the full signal and the mechanical and magnetic properties are found to be excellent.
- The  $\gamma$  exponents give the information on the strength of the local pinning field due to the microstructural evolution during the progressive aging of the HSLA steel. An inverse correlation between  $\gamma$  exponent and the strength of local pinning interactions is observed for this steel. The reduced strength of local DW pinning interactions increases the  $V_{RMS}$  which also increases the DW velocity. The DW motion is later obstructed due to the tensile residual stresses created by the mismatch strain fields between the incoherent Cu-precipitates formed due to aging effect and the Fe bcc lattice. Microstructural constituent like coherent Cu-precipitations allow DW motion but impede dislocation motion up to the aging temperature around 500°C for which  $\gamma$  exponent increases. Coarsening of Cu-precipitations is responsible for magnetic hardening as well as mechanical softening beyond 500°C and explains the anomalous behaviour of the HSLA steel throughout the aging process.
- The  $\gamma$  exponent can identify the new microstructural phase (martensite islands inside retained austenite) created around 650°C producing a composite microstructure which conforms to the high strength behaviour of the material.
- Fractal dimensional analysis of MBE signals generates fractal dimensions more than 1.5. This signifies that the MBE signal is anti-persistent as the Hurst exponent is less than 0.5. The anti-persistent fractal behaviour is expected since Barkhausen Jumps (BJ) have high frequency harmonic characteristics. Thus BJ activity at high magnetizing field rate for the HSLA material is found to be stochastic.
- Amongst the RS, PSD and Wavelet analysis methods, RS is found to be the most suitable method for computing fractal dimensions of the MBE signal. The cross-correlation between the fractal dimensions computed by the RS method and magnetic properties of HSLA steel is

found to be good and mechanical properties have weak correlation with the fractal dimension.

- The correlation coefficients show no correlation between the fractal dimensions by PSD and Wavelet methods and the material properties. Nevertheless the data shows certain trend especially the inflection around the aging temperature of 450°C-500°C indicate embrittlement behaviour of the material due to high hardness and strength properties. Perhaps better correlation between fractal dimension of the MBE signal for this material and material properties may be obtained if low magnetizing frequency (less than 10Hz) is used for applying the magnetic field.

## 7.5 References

1. Gianfranco Durin and Stefano Zapperi, [arXiv:cond-mat/0404512v1](https://arxiv.org/abs/cond-mat/0404512v1) [cond-mat.mtrl-sci] "The Science of Hysteresis", vol. II, G. Bertotti and I. Mayergoyz eds, Elsevier, Amsterdam(2006)181.
2. Amitava Mitra, S. Palit Sagar, and N. B. Manik: Magnetic Barkhausen Emission Study in Heat-Treated Fe–Nb–Cu–Si–B Alloy, IEEE Transaction on Magnetics, 38, 6, 3669-3674(2002).
3. S. Zapperi and G. Durin: New perspectives for the Barkhausen effect, Comp. Materials Science, 20, 436-442(2001).
4. A. Mitra and D.C. Jiles: Magnetic Barkhausen emissions in as-quenched Fe-Si-B amorphous alloy, Journal of Magnetism and Magnetic Materials 168, 169-176(1997).
5. S. K. Das, S. Tarafder, A. K. Panda, S. Chatterjee and A. Mitra: Magnetic and mechanical properties of Cu-strengthened aged HSLA-100 steel, Philosophical Magazine, 87, 32, 5065-5078 (2007).
6. A. K. Panda, S. K. Das, A. Mitra, D. C. Jiles and C. C. H. Lo: Evaluation of Deformation Behavior of HSLA-100 Steel Using Magnetic Hysteresis Technique, 42, 10, 3264-3266(2006).
7. G. Durin, A. Magni, G. Bertotti: Fractals scaling and the question of self-organized criticality in magnetization processes, Fractals , 2, 351-370 (1995).
8. G. Bertotti, G. Durin, A. Magni: Scaling aspects of domain wall dynamics and Barkhausen effect in ferromagnetic materials, J. Appl. Phys. 75, 5490-5492 (1994).
9. S. K. Das, Fracture behaviour of Copper strengthened HSLA steel, PhD Thesis, BESU, India (2007).

10. S. K. Das, S. Sivaprasad, S. Das, S. Chatterjee and S. Tarafder: The Effect of Variation of Microstructure on Fracture Mechanics Parameters of HSLA – 100 Steel, *Mat. Sci. and Engg, A*, 431, 68-79(2006).
11. S. K. Das, N. Narasaiah, S. Sivaprasad, S. Chatterjee and S. Tarafder: Effect of aging on fatigue crack growth behaviour of Cu bearing HSLA-100 steel, *Mat. Sci. and Tech.*, 23, 177-182(2007).
12. M. Pirlog, D. Schnubel, I. Altpeter and G. Dobman, ECNDT 2006, Fr. 2.4.1, <http://www.ndt.net/article/ecndt2006/doc/Fr.2.4.1.pdf>.
13. A. Ghosh, S. Chatterjee: Characterization of precipitates in an ultra low carbon Cu bearing high strength steel: A TEM study, *Materials Characterization* 55, 298-306(2005).
14. B. Tidac: Nonuniversal scaling behaviour of Barkhausen noise, *Phy Review E*, 77, 18, 3843-3846(1996).
15. P. Plewka, J.J. Zebrowski and M. Urbanski: Determinism and correlation dimension of Barkhausen noise, *Physical Review E*, 57, 6, 6422-6430(1998).
16. P. Bak, C. Tang and K. Wiesenfeld: Self-organised criticality, *Physical Review A*, 38,1, 364-374(1988).
17. J. S. Urbach, R. C. Madison, and J. T. Markert: Interface Depinning, Self-Organized Criticality, and the Barkhausen Effect, *Phys. Rev. Lett.*, 75, 276 - 279 (1995).
18. J. R. Petta, M. B. Weissman, and K. P. O'Brien: Multiple magnetization paths in Barkhausen noise, *Phys. Rev.*, E54, R1029-R1031(1996).
19. J. R. Petta, M. B. Weissman, and G. Durin: Barkhausen pulse structure in an amorphous ferromagnet: Characterization by high-order spectra, *Phys. Rev.*, E 57, 6363-6369(1998).
20. B. B. Mandelbrot, in *The Fractal Geometry of Nature* (W. H. Freeman, New York, 1983).
21. Hurst exponent. (2008, January 28). In *Wikipedia, The Free Encyclopedia*. Retrieved 10:27, June 5, 2008, from [http://en.wikipedia.org/w/index.php?title=Hurst\\_exponent&oldid=187539864](http://en.wikipedia.org/w/index.php?title=Hurst_exponent&oldid=187539864)
22. K. Falconer, in *Fractal geometry- Mathematical Foundations and Applications*, John Wiley & Sons Ltd., Baffins Lane, Chichester, West Sussex PO19 1UD, England, 1990.

# CHAPTER 8

## 8.0 Conclusions

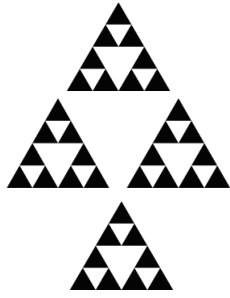
### 8.1 Future direction of work

183

To see a world in a grain of sand,  
And a heaven in a wild flower,  
Hold infinity in the palm of your hand,  
And eternity in an hour.

*"Auguries of Innocence" by William Blake*





# 8

## CONCLUSIONS

The present work was mainly aimed at investigating scale-invariant fractal properties of microstructural and fractographic images for evaluation of materials. Fractal behaviour of time domain MBE signals was also considered in order to assess their suitability as a non-destructive evaluation methodology. Low-carbon, copper-strengthened high strength low alloy (HSLA) steel, water quenched (WQ) and aged at various temperatures to exhibit a wide variation of material properties, was employed in the investigation. Amongst a wide range of methods for the determination of fractal dimension, three techniques, namely R/S, PSD and Wavelet, were selected for implementation since they are suitable for analysis of both images and signals. The endeavour was to compute fractal dimensions,  $D$ , or the Hurst exponent,  $H$ , which are quantifiers of complexity in signals and images. A systematic procedure for testing the codes developed for fractal analysis was employed in which synthetic 1D signals based on Weirestrauss cosine function (WCF) and images based on fractional Brownian motion (fBm) of various  $H$  values were used as inputs. It was shown that PSD and Wavelet analysis computed fractal dimensions for the fBm type signals correctly; however the R/S method gave equivalent fractal dimensions if

fractional Gaussian noise (fGn) signals and images, which are the gradient of the fBm type, were used. For low values of  $H$ , errors are found to be maximum since high frequency components (small length scale) are present in the signals, which make the signals too complex and anti-persistent. A set of calibration equations have been developed in this investigation that transforms  $H$  values computed from natural signals and images to the same from equivalent fBm signals.

To investigate the invariance property of fractal dimension of real microstructural images, it was necessary to find correlation between fractal dimension and magnification of the target image. An inverse correlation between fractal dimension and magnification, as reported in this work, indicates that universal values of fractal dimension for microstructural and fractographic images are not possible. As the magnification increases, the field of view decreases with increase in details. A smaller field of view reduces the global information content, and therefore the fractal dimension reduces. At lower range of magnification, since micro details are not captured, the image contains insufficient information for which fractal dimension reduces. Thus microstructural and fractographic images are found to be multi-fractals and it was important to find out the appropriate length scales within which they remain self-similar and/or self-affine fractals. Analysis at three different magnifications revealed that radially averaged power spectra of microstructural images have bilinear characteristics which distinguish two different length scales: true fractal behaviour is exhibited for length scales less than  $1\mu\text{m}$ , and “monoscale” fractal behaviour is demonstrated for length scales above  $1\mu\text{m}$ . It was interesting to find that the characteristic length scale of  $\sim 1\mu\text{m}$  corresponds to the width of lath martensites, one of the principle constituents of the microstructure of HSLA steel, which is thus of fractal nature.

In addition to the effect of magnifications on fractal dimensions, effects of spatial locations at which images were captured and the pre-processing to which images were subjected were studied. The effect of spatial location on fractal dimensions is found to be insignificant for microstructural and fractographic images of magnification greater than 1000. This indicates that the images are homogeneous and represent similar statistical similarities. Preprocessing of images changes fractal dimensions. For the binarized image, the computed fractal dimensions are the largest followed by that of histogram equalized images. The unprocessed image generates lowest fractal dimensions. The variations of fractal dimensions remain the same in unaltered as well as in preprocessed images for systematic variation of microstructural conditions.

With regard to fractal analysis methods and the types of images used for the analysis, maximum data scatter was found for the PSD analysis. Secondary electron (SE) images show more data scatter than back-scattered electron (BE) images. This indicates that noise level is higher in the former than the latter, which agrees with the general principle of electron imaging. PSD and R/S methods generate fractal dimensions which can clearly distinguish the morphological changes in microstructural as well as in fractographic images at various ageing temperatures. However Wavelet analysis has the poorest discrimination capability since the fractal dimension is found to be nearly invariant throughout the aging process.

Variations of fractal dimensions computed from microstructural images show good correlations with mechanical properties of the systematically varied microstructural conditions. While the correlations are found to be negative for hardness and strength properties, they are positive for ductility properties like percentage elongation and reduction of area. Increasing hardness signifies solid solution strengthening (through nano-size coherent copper precipitates coming out of the solid solution of steel) and an increase in the volume fraction of coherent copper precipitates. Up to aging at 550°C, there is a decreasing trend of fractal dimensions, which signifies the gradual improvement of persistent behaviour in images. Persistent behaviour in a structural sense is smoothening or ordering that can be ascribed to the increasing nano-size coherent copper precipitation occurring between 350°C-550°C. An interesting finding of the work is that the morphological changes occurring at the nano-scale level can be identified by fractal analysis of images captured at a relatively macro scale, even though conventional image analysis is unable to record any changes.

Systematic variations of fractal dimensions with ageing temperatures, estimated from the fractographic images directly, can be used for evaluation of mechanical properties of materials. Consistent trends in variation of fractal dimensions with ageing temperatures are obtained by the three methods of analysis employed, although the absolute values are different for different methods. This consistency of trend is significant, especially with regard to directly using fractographic images of SEM for fractal analysis, instead of the tedious procedure of the popular slit-island method of fractal analysis in which a set of images obtained by progressively polishing fractured specimen have to be used.

Using the concept of fractal mathematics, an expression for the particle spacing (average distance between two neighbouring void nucleating sites) has been developed, in which tensile properties like percentage area reduction ( $q$ ), elongation ( $e_f$ ) and the fractional part of the fractal

dimension ( $D^*$ ) computed from the tensile fracture surface are used. The developed expression, correlating morphological characteristics of the fractographic image with the material structural characteristics, is given by

$$\lambda = \frac{1}{k} \left( \frac{k_3 q}{(e_f + 1)(1 - q)} \right)^{\frac{1}{2D^*}}$$

The particle spacing  $\lambda$  was shown to have good correlation with the circular diameter of voids estimated from tensile fracture surfaces of HSLA steel that has been aged at various temperatures. Inverse correlation between  $\lambda$  and the increment in yield stress due to copper precipitation kinetics has been demonstrated. A model for estimating fracture toughness, named as fractal fracture toughness, has been developed in this work, based on the effectiveness of fractal dimensions in characterizing fracture surfaces. For computing fractal fracture toughness, the micro-roughness of the fracture surface ( $M$ ), obtained from  $\lambda$  and  $D$ , and the volume fraction of void nuclei  $V_f$ , estimated using the circular diameter of voids on a tensile fracture surface, has been employed to determine the local strain responsible for fracture initiation to give the relation

$$J_f = \sigma_0 \lambda \left( \ln \left( \frac{M^2}{3V_f} \right) \right)^3$$

The agreement between experimentally determined fracture toughness and the same predicted using the proposed model has endorsed the applicability of fractals for evaluation of materials.

To develop a non-destructive protocol for evaluation of material, MBE signals were used as 1D time series signals. To estimate the variation of local pinning fields originating from the presence of microstructural constituents responsible for impediment of domain wall (DW) motion, the power law exponents of the decaying Barkhausen spectra were estimated from the MBE signals captured from specimens of HSLA steel at variously aged conditions. An inverse correlation between  $\gamma$  exponent and the strength of local pinning interactions was observed for this steel. The reduced strength of local DW pinning interactions increases the MBE voltage which also increases the DW velocity. Fractal dimensional analysis of MBE signals showed that the MBE signal is anti-persistent in nature since the Hurst exponent is less than 0.5. Anti-persistent fractal behaviour is expected due to the fact that Barkhausen Jumps (BJ) have high frequency harmonic characteristics that lead to BJ activity at high magnetizing field rate being stochastic for the

HSLA material. The cross-correlation between fractal dimensions computed by the R/S method and magnetic properties of the steel is found to be high, while mechanical properties have weak correlations. Nevertheless, the data shows certain trends, especially the inflection at the ageing temperature of 450°C-500°C, which indicates the manifestation of embrittlement that is supported by mechanical behaviour of the material.

## **8.1 Future direction of work**

There are a number of aspects remaining to be investigated to get a complete understanding of fractal behaviour of microstructural and fractographic images, and its application for the evaluation of materials. It is required to know how fractal dimensions vary with various operating parameters (time and concentration of etchants) for metallographic sample preparation. Classification of fractal dimensions needs to be attempted, focusing on the development of various constituent phases in case of microstructural images and on fracture mechanisms for fractographic images. Fractal dimensions, obtained by three methods, show similar trend and ensure that the parameter is quite relevant, especially when correlations with material properties have been demonstrated. However, it would be appropriate to obtain fractal dimensions by conventional area-parameters correlations, and validate the results presented in this work. Variations of fractal dimensions for two simple image pre-processing techniques have been reported. Pre-processing using filters and its effect on fractal dimension could have been an additional direction of research.

For the analysis of MBE signals, effects of the frequency of magnetization on fractal dimensions need to be evaluated for establishing a non destructive protocol for quantifying microstructural damages in materials.

Finally, it is clear that for the use of fractal based analysis for the evaluation of materials, careful calibrations are required to develop a technological tool for real life application. This has to be carried out for specific material systems, with appropriate consideration of statistical variability and personal subjectivity. Such an endeavour is yet to be undertaken.



# APPENDICES

## A Appendices

A1	HSLA steel and its properties	185
A2	Algorithms for fractal analysis	188
A3	Expression for void volume fraction	193



# APPENDIX-1: HSLA steel and its properties

## A1.1 About HSLA steel

High strength steel was first developed in the 1960's for naval applications. Low carbon, Cu containing high strength low alloy (HSLA) steels are emerging materials for naval and other structural applications due to their good combination of strength and toughness and excellent weldability. The improved weldability is achieved through lower concentrations of carbon. The copper addition provides the required strength through aging. These steels can provide different combinations of strength and toughness in a wide range of plate thickness by different heat treatments. So appropriate selection of heat treatment is possible to obtain the best strength-toughness combination in these steels.

## A1.2 Chemical composition

Table-A.1: Chemical composition of HSLA steels in weight percent

<i>Steel</i>	<i>C</i>	<i>Mn</i>	<i>P</i>	<i>S</i>	<i>N</i>	<i>Si</i>	<i>Cr</i>	<i>Mo</i>	<i>Ti</i>	<i>V</i>	<i>Nb</i>	<i>Ni</i>	<i>Cu</i>
HSLA-100	0.04	0.90	0.01	0.005	0.015	0.25	0.6	0.60	0.02	0.03	0.03	3.50	1.60

## A1.3 Aging or heat treatment

In order to obtain a homogeneous microstructure, the specimens of HSLA steel were austenitised for 1h at 910°C and then water quenched (WQ). “Austenitizing is the process of holding the ductile iron casting like HSLA steel above the critical temperature for a sufficient period of time to ensure that the matrix is fully transformed to austenite”[1]. This is like refreshing the microstructure and then new desired microstructures are developed through tempering. In metallurgy “Quenching and Tempering are the standard heat treatments applied to ductile iron castings requiring maximum strength and wear resistance”[1]. To obtain different strength-toughness combination, the WQ specimens were tempered at 350°C to 700°C at an interval of 50°C with an additional temperature of 675°C. Tempering gives age hardening treatment to the material and alters the microstructural morphology progressively. Figure A.1 shows the heat-treatment diagram.

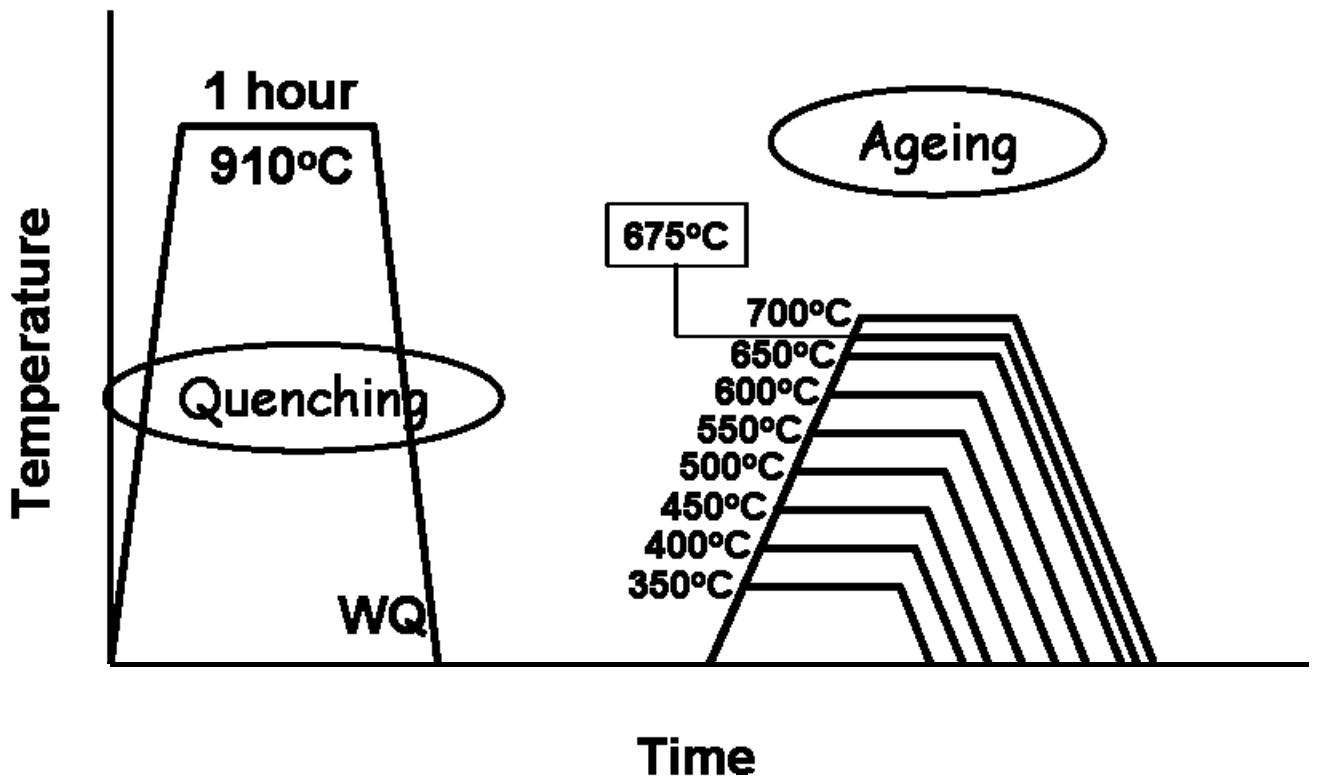


Figure A.1: Heat-treatment diagram of HSLA steel

### A1.4 Magnetic properties

The magnetic hysteresis loop (MHL) and magnetic Backhouse (MBE) emission were measured using a surface probe for different heat-treated materials. Coercivity is estimated from the MHL and root mean square value of the induced voltage ( $V_{RMS}$ ) is estimated from MBE measurement shown in Table A.2.

Table A.2: Magnetic properties of the HSLA steels

Aging Temp(°C)	350	400	450	500	550	600	650	675	700
Coercivity	4.8703	4.6475	4.5693	4.5281	4.4724	4.4167	4.6952	5.1488	5.2602
$V_{RMS}$	26.8	27.5	27.7	31.37	36.7	40.4	21.83	24.93	15.37

## A1.5 Mechanical and fracture properties

The mechanical and fracture properties of HSLA steels are dependent on the chemistry of materials, process parameters, rolling condition, aging or heat-treated condition *etc.* that influences the resultant microstructure. Round tensile specimens of 5 mm diameter and 25 mm gauge length, tempered at different temperatures, were used for evaluating the tensile properties as per ASTM standard E-8M using a 100kN Instron servohydraulic testing system.

For experimental determination of initiation fracture toughness,  $J_i$ , three-point bend (TPB) specimen machined as per ASTM standard E-1820. All specimens were pre-cracked to  $a/W = 0.5$  in a EMR machine at 75 Hz frequency. Tests were conducted in a 100 kN Instron servo hydraulic testing system equipped with a digital controller that was interfaced to a computer for test control and data acquisition. A displacement rate of  $3 \times 10^{-3}$  mm/s was used for applying loads on the specimen. A 10 mm COD gauge was used for Load-Line-Displacement (LLD). Software was used for test control and data acquisition and the raw data was analysed off-line to get the load-load line displacement (P-LLD) and  $J$ - $R$  curve as per ASTM E-1820.  $J_i$  was computed from the  $J$ - $R$  curve. Table A.3 presents the mechanical and fracture properties of this steel.

Table-A.3: Mechanical properties of the WQ and aged HSLA steel

Heat-treated condition / Aging temperature	Hardness (Hv)	E (GPa)	YS (MPa)	UTS (MPa)	% EI	%RA	$J_i$ (kJ/m <sup>2</sup> )
WQ	296	195.0	818	1004	9.38	69.54	299
350 °C	300	203.3	886	1056	8.49	67.88	231
400 °C	321	191.5	957	1076	7.70	62.56	69
450 °C	331	195.7	968	1098	6.46	61.26	207
500 °C	343	200.0	1034	1121	5.9	61.75	22
550 °C	312	192.7	927	1011	14.69	65.09	500
600 °C	271	187.7	698	955	15.92	69.63	493
650 °C	263	192.5	643	934	17.71	70.11	725
675 °C	252	175.4	640	921	19.84	73.27	649
700 °C	280	203.6	831	983	19.12	73.90	896

## APPENDIX-2: Algorithms for fractal analysis

### A2.1: Rescaled range analysis

a) 1D implementation

**Input:** 1D signal

**Output:** D

- Initiate level,  $n = 1$
- Input 1D signal  $Y(t)$  with  $N = \text{length}(Y(t))$
- Divide the signal into  $T = 2^{(n-1)}$  parts
- Each part has signal length  $= N/T$
- Compute a set of mean value  $\{\bar{Y}_1, \bar{Y}_2, \dots, \bar{Y}_k\}_{0 < k < T}$
- Compute the accumulated departure from the mean

$$X(t, j) = \left. \sum_{t=(j-1)*N/T+1}^{j*(N/T)} (Y(t) - \bar{Y}_j) \right|_{0 < j \leq T}$$

- Compute range  $R(j)$

$$R(n, j) = \max(X(t, j) - \min(X(t, j)) \Big|_{(j-1)*N/T+1 \leq t \leq j*(N/T)}) \Big|_{0 < j \leq T}$$

- Compute standard deviation  $S(j)$

$$S(n, j) = \left[ \frac{1}{N/T} \sum_{t=(j-1)*N/T+1}^{j*(N/T)} ((Y(t) - \bar{Y}_j)^2) \right]^{1/2} \Big|_{0 < j \leq T}$$

- Compute R/S ( $n, j$ ) value

$$R/S(n, j) = \frac{R(n, j)}{S(n, j)}$$

- Compute the average R/S value

$$R/S(n) = \frac{1}{T} \sum_{j=1}^T R/S(n, j)$$

- Go to the next level,  $n = n + 1$
- Compute  $\log(R/S(n))$  and  $\log(n)$  and get the slope of the linear fit of the log-log plot. The slope is the Hurst exponent  $H_r$  as given in the power law correlation

$$\langle R/S(n) \rangle \Big|_{N/T > \text{Threshold}} = C n^{H_r} \text{ as } n \rightarrow \infty$$

- Compute  $D = 2 - H_r$

b) 2D implementation

**Input:** Intensity image

**Output:** D

- Initiate level,  $n = 1$
- Input image  $f(x,y)$  with  $M$ =Image width and  $N$ =Image height
- Divide the signal into  $T=4^{(n-1)}$  parts
- Each part has image dimension,  $M1=M/2^{(n-1)}$  and  $N1=N/2^{(n-1)}$
- Compute a set of mean value  $\{\bar{Y}_1, \bar{Y}_2, \dots, \bar{Y}_k\}_{0 < k < T}$
- Compute the accumulated departure from the mean

$$X(i, j) = \left. \sum_{i, j=(k-1)*N/T+1}^{k*(N/T)} (Y(i, j) - \bar{Y}_k) \right|_{0 < k < T}$$

- Compute range  $R(j)$

$$R(n, k) = \max(X(i, j) - \min(X(i, j))) \Big|_{\substack{(j-1)*N/T+1 \leq i, j \leq j*(N/T) \\ 0 < k \leq T}}$$

- Compute standard deviation  $S(j)$

$$S(n, k) = \left[ \frac{1}{N/T} \sum_{i, j=(k-1)*N/T+1}^{k*(N/T)} ((Y(i, j) - \bar{Y}_j)^2) \right]^{1/2} \Big|_{0 < k \leq T}$$

- Compute  $R/S(n, k)$  value

$$R/S(n, k) = \frac{R(n, k)}{S(n, k)}$$

- Compute the average  $R/S$  value

$$R/S(n) = \frac{1}{T} \sum_{k=1}^T R/S(n, k)$$

- Go to the next level,  $n=n+1$
- Compute  $\log(R/S(n))$  and  $\log(n)$  and get the slope of the linear fit of the log-log plot. The slope is the Hurst exponent  $H_r$  as given in the power law correlation

$$\langle R/S(n) \rangle \Big|_{N/T > Threshold} = Cn^{H_r} \text{ as } n \rightarrow \infty$$

- Compute  $D=3-H_r$

## A2.2: PSD analysis

### a) 1D implementation

**Input:** 1D signal

**Output:** D

- Read the signal  $X(t)$
- Crop the signal and get the length  $N$
- Supply sampling frequency,  $f_s$
- Do fast Fourier transformation of the signal

$$X_k = \text{fft}(X(1:N), f_s);$$

- Compute power spectral density and corresponding frequency by

$$P = X_k .* \text{conj}(X_k) / N;$$
$$f = f_s * (1:f_s) / N;$$

- The frequency range obtained is  $f_s/2$
- Get  $\log P(f)$  vs  $\log(f)$  plot and compute the slope,  $\beta$  using the following correlation

$$P(f) \propto \frac{1}{f^\beta}$$

- Compute  $H = \frac{\beta - 1}{2}$  and  $D = 2 - H$

### 3.2.2 b) 2D implementation

**Input:** Intensity image

**Output:** D

- Read image file  $f(i,j)$
- Crop image to remove text from the image and get the final image dimensions  $N = \text{Image width}$  and  $N = \text{Image height}$
- Compute FFT of the image
- Do FFT shift to bring the spectrum at the centre
- Calculate power spectral density

$$P(u, v) = \frac{|G(u, v)|^2}{N * N}$$

- Convert the Cartesian co-ordinate system to Polar coordinate system for the frequency components,  $f$  and  $\theta$

$$f = \text{int}(\sqrt{u^2 + v^2})$$

$$\text{where } \theta = \tan^{-1} \frac{v}{u}$$

- Compute average power for  $f=1$  to  $N/4$

$$P(f) = \langle P(u, v) \rangle_{f=\text{int}(\sqrt{u^2+v^2})}$$

- Get log P(f) vs log(f) plot and compute the slope,  $\beta$  using the following correlation

$$P(f) \propto \frac{1}{f^\beta}$$

- Compute  $H = \frac{\beta-2}{2}$  and  $D=3-H$

### A2.3: Discrete wavelet analysis

#### a) 1D implementation

**Type:** Haar (db1), Daubachi (db2, db4, db8)

**Input:** 1D signal

**Output:** D

- Read the signal X(t)
- Do wavelet decomposition using

$$[C, L] = \text{wavedec}(X, \log(\text{double}(N)) / \log(2), 'Type');$$

where C is the co-efficient vector and L is the level vector.

- Get detailed coefficient vector Cd for all levels using

$$Cd = \text{detcoef}(C, L, 'cells');$$

- For each level compute power by taking summation of Cd vector using

$$Ed(k) = \text{sum}(Cd\{k\}.^2) / (2^{(M+1-k)});$$

where k is the level and  $M = \text{length}(L) - 2$ ;

- Get log (Ed(k) vs log(k) plot and compute the slope,  $\beta$  using the following correlation

$$Ed(k) \propto \frac{1}{k^\beta}$$

- Compute  $H = \frac{\beta-1}{2}$  and  $D=2-H$

*b) 2D implementation*

**Type:** Haar (db1), Daubachi (db2, db4, db8)

**Input:** 1D signal

**Output:** D

- Read the image  $I(i,j)$
- Get length of the image  $L=length(I)$ ;
- Do wavelet decomposition using  
 $[C, L] = wavedec2(B1, \log(double(N))/\log(2), 'Type');$   
where C is the co-efficient vector and L is the level vector.
- Get detailed coefficient matrix in horizontal, vertical and diagonal directions,  
 $[chd2, cvd2, cdd2]$ , for each level, k using  
 $[chd2, cvd2, cdd2] = detcoef2('all', C, L, k);$
- For each level compute summation for each of the  $[chd2, cvd2, cdd2]$  components  
 $ch = \text{sum}(\text{sum}(chd2.^2));$   
 $cv = \text{sum}(\text{sum}(cvd2.^2));$   
 $cd = \text{sum}(\text{sum}(cdd2.^2));$
- For each level compute power by taking summation of Cd vector using  
 $Ed(k) = (ch+cv+cd) / (M*M)$   
where k is the level and  $M = \text{length}(chd2);$
- Get  $\log(E_d(k))$  vs  $\log(k)$  plot and compute the slope,  $\beta$  using the following correlation  
$$E_d(k) \propto \frac{1}{k^\beta}$$
- Compute  $H = \frac{\beta-2}{2}$  and  $D=3-H$

## APPENDIX-3: Expression for void volume fraction

Void volume fraction,  $V_f$ , can be given by

$$V_f = \frac{K_v^3 \cdot V_v}{V_s} \quad (1)$$

where  $K_v$  is the number of dimples on the fracture surface,  $V_v$  is the volume of a void and  $V_s$  is the volume of the cylindrical specimen. Shape of the void is assumed as spheroid.

For cylindrical specimens,

$$V_s = \pi \left( \frac{D_0}{2} \right)^2 \cdot h \quad (2)$$

where  $h$  is the gauge length of the specimen. Since  $h$  is a linear function of  $D_0$ ,

$$V_s \propto \pi \left( \frac{D_0}{2} \right)^3 \quad (3)$$

For a spheroid void,  $V_v$

$$V_v = \frac{4}{3} \pi \left( \frac{x_c}{2} \right)^3 \quad (4)$$

where  $x_c$  is the critical diameter of average void nuclei, at which the voids start coalescence.

Assuming  $x_c$ , the critical diameter of average void nuclei, as a function of the number of dimples on the fracture surface and the average diameter of the initial void nuclei, it can be written as

$$x_c \propto K_v \cdot x_0 \quad (5)$$

Substituting  $x_c$  from equation (5) in equation (4), the volume fraction of voids become

$$V_v = \frac{4}{3} \pi \left( \frac{K_v \cdot x_0}{2} \right)^3 \quad (6)$$

Substituting equations (6) and (3) in equation (1), we get the expression for the void volume fraction as

$$V_f \propto K_v^6 \left( \frac{x_0}{D_0} \right)^3 \quad (7)$$

